

UNCLASSIFIED

AD NUMBER

AD893660

LIMITATION CHANGES

TO:

Approved for public release; distribution is unlimited.

FROM:

Distribution authorized to U.S. Gov't. agencies only; Test and Evaluation; APR 1972. Other requests shall be referred to Space and Missile Systems Organization, Los Angeles, CA 90045.

AUTHORITY

SAMSO ltr 27 Jan 1978

THIS PAGE IS UNCLASSIFIED



FORCE AND PRESSURE TESTS ON CONES WITH SIMULATED ABLATED NOSES AT MACH NUMBERS 8 AND 16

J. S. Hahn and H. R. Little

ARO, Inc.

April 1972



Distribution limited to U.S. Government agencies only; this report contains information on test and evaluation of military hardware; April 1972; other requests for this document must be referred to Space and Missile Systems Organization/TRD-STINFO, AF Unit Post Office, Los Angeles, California 90045.

**VON KÁRMÁN GAS DYNAMICS FACILITY
ARNOLD ENGINEERING DEVELOPMENT CENTER
AIR FORCE SYSTEMS COMMAND
ARNOLD AIR FORCE STATION, TENNESSEE**

NOTICES

When U. S. Government drawings specifications, or other data are used for any purpose other than a definitely related Government procurement operation, the Government thereby incurs no responsibility nor any obligation whatsoever, and the fact that the Government may have formulated, furnished, or in any way supplied the said drawings, specifications, or other data, is not to be regarded by implication or otherwise, or in any manner licensing the holder or any other person or corporation, or conveying any rights or permission to manufacture, use, or sell any patented invention that may in any way be related thereto.

Qualified users may obtain copies of this report from the Defense Documentation Center.

References to named commercial products in this report are not to be considered in any sense as an endorsement of the product by the United States Air Force or the Government.

FORCE AND PRESSURE TESTS ON
CONES WITH SIMULATED ABLATED NOSES
AT MACH NUMBERS 8 AND 16

J. S. Hahn and H. R. Little
ARO, Inc.

Distribution limited to U.S. Government agencies only; this report contains information on test and evaluation of military hardware; April 1972; other requests for this document must be referred to Space and Missile Systems Organization/TRD-STINFO, AF Unit Post Office, Los Angeles, California 90045.

FOREWORD

The work reported herein was done at the request of the Space and Missile Systems Organization (SAMSO), Air Force Systems Command (AFSC), for the Aerospace Corporation, under Program Element 63311F, System 627A.

The results of the tests were obtained by ARO, Inc. (a subsidiary of Sverdrup & Parcel and Associates, Inc.), contract operator of the Arnold Engineering Development Center (AEDC), AFSC, Arnold Air Force Station, Tennessee, under Contract F40600-72-C-0003. The tests were conducted from May 10 to September 7, 1971, under ARO Project No. VT0190, and the final data package was completed on October 21, 1971. The manuscript was submitted for publication on February 9, 1972.

The Tunnel B and Tunnel F tests were conducted by J. S. Hahn and H. R. Little, respectively.

This technical report has been reviewed and is approved.

Emmett A. Niblack, Jr.
Lt Colonel, USAF
AF Representative, VKF
Directorate of Test

Frank J. Passarello
Colonel, USAF
Acting Director
Directorate of Test

ABSTRACT

Results are presented from static-force tests and pressure distribution tests of conical bodies with various nose shapes which were chosen to simulate the estimated shapes obtained after significant ablation of the nose had taken place. The basic cone half-angle is 6.3 deg, and the nominal bluntness ratio is 0.25. Nose shapes tested consisted of symmetrical biconics with nose angles of 30, 40, and 50 deg and asymmetrical noses derived from the 50-deg biconic. Results were also obtained for a 50-deg symmetric biconic nose on 4.0- and 9.0-deg cones. The effect of changing the nose-to-cone shoulder radius was investigated on several configurations. Most of the data were obtained at Mach 8, and a limited amount of data was taken at Mach 16. The nominal Reynolds number was 3.1×10^6 based on the sharp cone length of the 6.3-deg pressure model. For the force tests, the angle-of-attack range was from -5 to 11 deg, and for the pressure tests, the angles of attack included the configuration trim angle and up to 4 deg on either side of the trim angle in increments of generally 1 deg. At Mach 8, data are given for the ablated nose shapes with the vehicle rolled -30, -60, and -90 deg. The primary effects of the various nose shapes were found to be in the axial-force coefficient, and for the asymmetrical shapes, the pitching moment. For these asymmetric shapes, trim angles of up to 6 deg were obtained with a corresponding normal-force coefficient of about 0.45. Comparisons of symmetric- and asymmetric-biconic pressure data made at the asymmetrical trim angle demonstrated that trim angle was primarily governed by the contributions of differential pressures in the region between the shoulder and about one base diameter downstream of the shoulder.

Distribution limited to U.S. Government agencies only; this report contains information on test and evaluation of military hardware; April 1972; other requests for this document must be referred to Space and Missile Systems Organization/TRD-STINFO, AF Unit Post Office, Los Angeles, California 90045.

CONTENTS

	<u>Page</u>
ABSTRACT	iii
NOMENCLATURE	vii
I. INTRODUCTION	1
II. APPARATUS	
2.1 Models	1
2.2 Wind Tunnels	2
2.3 Instrumentation	3
III. PROCEDURES	
3.1 Test Conditions	5
3.2 Tunnel B Test Techniques	5
3.3 Tunnel F Data Acquisition and Techniques	6
3.4 Data Precision	7
IV. RESULTS AND DISCUSSION	
4.1 Static-Force Tests	10
4.2 Pressure Tests	11
V. CONCLUDING REMARKS	13
REFERENCES	14

APPENDIXES

I. ILLUSTRATIONS

Figure

1. Photographs of Selected Models	19
2. Photographs of Noses for Force Models	21
3. Photographs of Noses for Pressure Model	23
4. Details of Models	25
5. Details of Noses	26
6. Pressure Model Orifice Location for $\Delta\phi = 0$	28
7. Typical Tunnel B Shadowgraphs for $\alpha = \phi_m = 0$	29
8. Typical Monitor Data Traces and Tunnel Conditions for Tunnel F	30
9. Tunnel F Static-Force Data Acquisition	31
10. Typical Viscous Interaction Corrections of Tunnel F Axial-Force Data	33

<u>Figure</u>	<u>Page</u>
11. Effects of Cone Angle (θ_c) on the Normal-Force, Pitching-Moment, and Axial-Force Characteristics, $M_\infty = 8$	34
12. Effects of Nose Angle (θ_n) on the Normal-Force, Pitching-Moment, and Axial-Force Characteristics of Symmetrical Biconics, $M_\infty = 8$	36
13. Comparison of the Normal-Force, Pitching-Moment, and Axial-Force Characteristics of the Symmetrical Configurations Tested at $M_\infty = 16$	37
14. Effects of Nose Cant Angle (δ_n) on the Normal-Force, Pitching-Moment, and Axial-Force Characteristics of the Asymmetrical Biconics Tested at $M_\infty = 16$	38
15. Effects of Nose Cant Angle (δ_n) on the Normal-Force, Pitching-Moment, and Axial-Force Characteristics of Asymmetrical Biconics, $M_\infty = 8$	40
16. Effects of Shoulder Radius (r_s) on the Normal-Force, Pitching-Moment, and Axial-Force Characteristics, $M_\infty = 8$	47
17. Variations of C_{N_α} , C_{m_α} , $C_{A_{\alpha=0}}$, and x_{cp}/l for Symmetrical Shapes, $M_\infty = 8$	49
18. Variations of C_{N_α} , C_{m_α} , $C_{A_{\alpha=0}}$, x_{cp}/l and α_t for Asymmetrical Biconics	51
19. Nose Cone Pressure Data at $M_\infty = 16$, 50-deg Biconic	53
20. Aft-Cone Pressure Distributions at $M_\infty = 16$, 50-deg Biconic	54
21. Nose Cone Circumferential Pressure Distributions for Symmetrical Biconics, $M_\infty = 8$	56
22. Nose Cone Circumferential Pressure Distributions for Asymmetrical Biconics, $M_\infty = 8$	59
23. Aft-Cone Longitudinal Pressure Distributions for Symmetrical Biconics, $M_\infty = 8$	71
24. Aft-Cone Longitudinal Pressure Distributions for Asymmetrical Biconics, $M_\infty = 8$	81
25. Effects of Nose Cone Angle (θ_n) on the Main-Cone Windward and Leeward Pressure Distributions, $M_\infty = 8$	102

<u>Figure</u>	<u>Page</u>
26. Effects of Shoulder Radius (r_s) on the Main-Cone Windward and Leeward Pressure Distributions, $M_\infty = 8$	106
27. Effects of Deviations from Trim Condition on the Main-Cone Differential Pressure Distributions for Asymmetrical Biconics, $M_\infty = 8$	109
28. Comparisons of Aft-Cone Differential Pressure Distributions for Trimmed Asymmetrical Biconics, $M_\infty = 8$	112
29. Comparisons of Aft-Cone Differential Pressure Distributions for Symmetrical and Asymmetrical Biconics at the Asymmetrical Trim Angle, $M_\infty = 8$ and $\phi_m = 0$	113

II. TABLES

I. Tunnel B Static-Force Test Summary	116
II. Tunnel B Pressure Test Summary, Symmetrical Configurations	117
III. Tunnel B Pressure Test Summary, Asymmetrical Configurations	118
IV. Tunnel F Static-Force Test Condition	119
V. Tunnel F Pressure Test Conditions	120

NOMENCLATURE

A	Reference area (model base area, see Fig. 4), in. ²
C_A	Forebody axial-force coefficient, $C_{A_t} - C_{A_b}$
C_{A_b}	Base axial-force coefficient, $-(p_b - p_\infty)/q_\infty$
C_{A_t}	Total axial-force coefficient, total axial force/ $q_\infty A$
$C_{A_{\alpha=0}}$	Forebody axial-force coefficient at zero angle of attack
C_m	Pitching-moment coefficient, pitching moment (about $x = 0.65\ell$)/ $q_\infty A \ell$
C_{m_α}	Initial slope of pitching-moment coefficient curve, $(dC_m/d\alpha)_{\alpha=0}$, deg ⁻¹

C_N	Normal-force coefficient, normal force/ $q_\infty A$
C_{N_α}	Initial slope of normal-force coefficient curve, ($dC_N/d\alpha$) $_{\alpha=0}$, deg^{-1}
C_ω	Chapman-Rubesin viscosity coefficient, $(\mu_w/\mu_\infty)(T_\infty/T_w)$
d_b	Model base diameter (see Fig. 4), in.
H_0	Tunnel F stagnation enthalpy, Btu/lbm
ℓ	Reference length (model sharp cone length, see Fig. 4), in.
M_∞	Free-stream Mach number
P	Nose cone aft shoulder point (see Figs. 4 and 5)
p	Model surface pressure, psia
p_b	Model base pressure, psia
p_0	Tunnel stilling- or arc-chamber pressure, psia
p'_0	Tunnel F test section pitot pressure, psia
p_∞	Free-stream static pressure, psia
\dot{q}_0	Stagnation point heat-transfer rate on a 1-in. -diam hemisphere-cylinder probe, Btu/ft ² -sec
q_∞	Free-stream dynamic pressure, psia
Re_ℓ	Free-stream Reynolds number based on the reference length
Re_∞	Free-stream unit Reynolds number, ft ⁻¹
r_b	Model base radius (see Fig. 4), in.
r_n	Model nose radius (see Fig. 5a), in.
r_s	Model shoulder radius (see Fig. 5a), in.
s	Surface distance measured downstream of the $x = 0.25\ell$ station (see Fig. 5a), in.
\bar{s}	Surface distance measured upstream of the model shoulder when $r_s = 0$ but along rays of the model frustum (see Fig. 5a), in.
T_0	Tunnel stilling-chamber temperature, °R
T_w	Model wall temperature, °R
T_∞	Free-stream static temperature, °R
t	Tunnel F run time, msec
U_∞	Free-stream velocity, ft/sec

\bar{v}_ℓ	Viscous interaction parameter, $M_\infty(C_\infty/Re_\ell)^{1/2}$
x	Longitudinal distance from sharp cone apex (see Fig. 4), in.
x_{cp}	Longitudinal center of pressure at $\alpha = 0$ measured from sharp cone apex, $\ell(0.65 - C_{m\alpha}/C_{N\alpha})$, in.
α	Angle of attack, deg
α_t	Trim (zero pitching moment) angle of attack, deg
Δp	Pressure differential between windward ($\phi = 0$) and leeward ($\phi = 180$) sides of the model, psia
$\Delta\phi$	Roll orientation of the nose relative to the main cone (see Fig. 4), deg
δ_n	Nose cant angle (see Fig. 5a), deg
θ_c	Main cone half-angle, deg
θ_n	Nose tip half-angle (see Fig. 5a), deg
μ_w	Viscosity at model wall temperature, lb-sec/ft ²
μ_∞	Viscosity at free-stream temperature, lb-sec/ft ²
ρ_∞	Free-stream density, lbm/ft ³
ϕ	Circumferential orientation relative to the free-stream wind vector (see Fig. 4), positive clockwise when looking upstream, deg
ϕ_m	Model resultant roll angle (roll orientation of P), $\phi_t + \Delta\phi$ (see Fig. 4), deg
ϕ_t	Tunnel roll-mechanism angle (see Fig. 4), deg
ω	Circumferential location of any pressure orifice from P when $\Delta\phi = 0$ (see Figs. 4 and 6), positive clockwise when looking upstream, deg

NOTE: Force and moment coefficients in this report are in the nonrolling body-axis system.

SECTION I INTRODUCTION

The aerodynamic performance of the slender conical shapes prevalent in unmanned reentry vehicles has been shown by experimental and analytical methods to be highly sensitive to nose geometry. Consequently, the nose configuration for a particular vehicle may be dictated by the reentry mission trajectory. However, during reentry the nose shape is often altered by ablation, which must be considered by the designer but is usually not amenable to analytic methods.

The primary objective of the tests reported herein was to obtain experimental data on the aerodynamic characteristics of slender cones with several simulated ablated nose shapes. This data may be used to check or improve existing analytical theories or, at least, as a basis for the development of semi-empirical correlations. Another objective of these tests was to provide sufficient pressure data for use in determining the factors governing trim of the asymmetrical configurations.

Static-force data were obtained for an angle-of-attack range from -5 to 11 deg; pressure data were obtained at angles of 0, ± 1 , ± 2 , and ± 4 deg relative to a configuration's trim angle. Testing was conducted in the Hypersonic Wind Tunnel (B) and the Hypervelocity Wind Tunnel (F) of the von Kármán Gas Dynamics Facility (VKF) at Mach numbers 8 and 16, respectively, for a nominal free-stream unit Reynolds number of 10^6 per foot and zero sideslip.

The test models were mainly 6.3-deg half-angle cones fitted with various symmetrical and asymmetrical noses; however, static-force data at Mach number 8 were also obtained for one 9-deg and two 4-deg half-angle cone configurations.

SECTION II APPARATUS

2.1 MODELS

Photographs and details of the models and various nose configurations are shown in Figs. 1 through 5 (Appendix I). The five models (see Fig. 4) consisted of 4.0-, 6.3-, and 9.0-deg half-angle cones fitted with one of eleven nose configurations (Fig. 5b). The Tunnel B models consisted of three force models with the aforementioned frustum

half-angles and a 6.3-deg pressure model (Fig. 1a), which was also used as the Tunnel F pressure model. The 6.3-deg frustum of the Tunnel F force model (Fig. 1b) was fabricated (in the VKF) from balsa wood, sheathed with a fiber glass and epoxy skin, and fitted with interchangeable magnesium noses (Fig. 2b). Frustums of the other models were fabricated from stainless steel and furnished by the Reentry and Environmental Systems Division of the General Electric Company for use in previous VKF tests.

The eleven nose configurations (Fig. 5b) consisted of 5 symmetrical biconics, 4 asymmetrical biconics, a spherically blunted cone, and a sharp cone. A radius ratio (r_n/r_b) of 0.25 was maintained for all biconics; whereas, r_n/r_b was $(0.25 \cos \theta_c)$ for the spherically blunted cone configuration. The equations used in designing the noses (Fig. 5a) were furnished by the Aerospace Corporation. All noses were fabricated in the VKF and, except for the Tunnel F force-model noses, were fabricated from stainless steel.

Aft of the nose joint (see Fig. 4), the pressure model was instrumented with a total of 60 static-pressure orifices, consisting of 4 orifices equally spaced in the circumferential direction, at each of the 15 axial stations. Pressure instrumentation forward of the nose joint varied, depending on the configuration; however, each configuration had pressure orifices on the nose cone and just aft of the nose cone shoulder. Detailed pressure orifice locations for each configuration are given in Fig. 6.

2.2 WIND TUNNELS

2.2.1 Tunnel B

Hypersonic Wind Tunnel (B) is a continuous flow, closed-circuit, variable density wind tunnel with an axisymmetric contoured nozzle and a 50-in. -diam test section. The tunnel can be operated at a nominal Mach number of 6 or 8 at stagnation pressures from 20 to 300 and 50 to 900 psia, respectively, and at stagnation temperatures up to 1350°R. The model may be injected into the tunnel for a test run and then retracted for model cooling or model changes without interrupting the tunnel flow. A more complete description of the tunnel may be found in the Test Facilities Handbook (Ref. 1).

2.2.2 Tunnel F

The Hypervelocity Wind Tunnel (F) is an arc-driven wind tunnel of the hotshot type (Refs. 1 through 4) having 54- and 108-in. -diam test

sections. Schlieren and shadowgraph optical coverage is available for both test sections. The test gas, nitrogen or air, is initially confined in an arc chamber by a diaphragm located near the throat of an attached 4-deg half-angle conical nozzle. The gas is heated and compressed by an electric arc discharge. The increased pressure ruptures the diaphragm, and the gas is released to expand through the nozzle to the test section. Typically, run times from 0.1 to 0.2 sec are obtained. Mach number is determined by the throat size, and the Reynolds number by the electric arc energy and the initial arc chamber density.

2.3 INSTRUMENTATION

2.3.1 Tunnel B Tests

Model forces and moments were measured with a six-component, moment-type, strain-gage balance supplied and calibrated by VKF. Before testing, static loads in each plane and combined static loads were applied to the balance, simulating the range of model loads anticipated for the test. The following uncertainties represent the bands for 95 percent of the measured residuals based on the differences between the applied loads and the corresponding values calculated from the final data reduction equations.

<u>Balance Component</u>	<u>Design Load</u>	<u>Range of Static Loadings</u>	<u>Measurement Uncertainty</u>
Normal force, lb	200	±60	±0.35
Pitching moment*, in.-lb	680	±265	±1.45
Side force, lb	100	±60	±0.40
Yawing moment*, in.-lb	300	±265	±1.35
Rolling moment, in.-lb	100	±6.4	±0.17
Axial force, lb	50	0 to 30	±0.10

*About balance forward moment bridge.

The transfer distance from the balance to the model moment reference point was -0.872 in. (for the 6.3-deg cone), which was measured with an estimated precision of ±0.01 in.

Pressures on the nose cone were measured with 15-psid transducers, whereas all other surface pressures (including base pressures) were measured with one of two types of 1-psid transducers. All transducers were referenced to a near vacuum. Based on periodic comparisons with secondary standards, the precisions (bands which include 95 percent

of the residuals) of the 1-psid transducers are estimated to be ± 0.001 psia or ± 0.003 psia; whereas the 15-psid transducers have an estimated precision of ± 0.015 psia.

Stilling-chamber pressure was measured with a 1000-psid transducer referenced to a near vacuum. Based on periodic comparisons with secondary standards, the precision of this transducer is estimated to be ± 0.2 percent of full scale. Stilling-chamber temperature was measured with a Chromel[®]-Alumel[®] thermocouple to a precision of $\pm 9^{\circ}\text{R}$ based on manufacturers' specifications for the thermocouple wire and instrument slide wire error.

Model flow field shadowgraphs were obtained on each configuration at selected angles of attack. Typical shadowgraphs at $M_{\infty} = 8$ are presented in Fig. 7 to show the influence of nose shape.

2.3.2 Tunnel F Tests

In Tunnel F, model pressures were measured with internally mounted miniature pressure transducers with elastic diaphragms. For low pressures, the transducer used was a 0- to 0.5-psid variable reluctance device, while for the higher pressures, flexure-mounted strain gages capable of ranges from 0 to 1.0 and 0 to 10 psid were employed. Test section pitot pressures (p'_0) were measured with 0- to 15-psid strain-gage transducers, and the arc-chamber pressures (p_0) were measured with 40,000-psid transducers. Test section stagnation point heat-transfer rates were measured using resistance thermometer slug calorimeter heat-transfer transducers. The estimated precision of all types of pressure transducers within the Tunnel F data acquisition system is ± 3 percent, and the precision of the heat-transfer instrumentation system is ± 5 percent.

The aerodynamic forces and moments were measured using a six-component force balance developed specifically for use in the hotshot tunnel. Accelerometers are mounted in plane with each load cell to allow compensation for inertial loads which result from vibrations of the model and support system during the tunnel test period. The estimated precision of the force measuring system is ± 3 percent. Discussions of the various instrumentation components and their use are contained in Refs. 5 and 6.

SECTION III PROCEDURES

3.1 TEST CONDITIONS

Nominal tunnel conditions at which the tests were conducted are given below.

Tunnel	M_∞	p_o , psia	T_o , °R	q_∞ , psia	p_∞ , psia	Re_∞ /ft
B	7.96	200	1215	0.94	0.021	10^6
F	16	13,000	4000	2.0	0.011	10^6

Tunnel B test summaries are presented in Tables I through III (Appendix II). Tunnel conditions for the Tunnel F tests are shown in Tables IV and V.

3.2 TUNNEL B TEST TECHNIQUES

The force and pressure models were scribed and aligned optically at zero angle of attack under air load conditions.

The static-force data were obtained using the pitch-pause technique, and measured axial force was corrected to zero base axial force using the measured base pressure and the model base area. The fixed moment reference point was located on the sharp cone axis of symmetry at 65 percent of the sharp cone length. Any reference to the static stability and trim angle characteristics in the report will apply only to the vehicle with a center of gravity at the same location.

Each asymmetrical configuration was injected into the tunnel at a fixed roll angle (ϕ_m) of 0, -30, -60, and -90 deg, the angle of attack was varied, and the force and moment data obtained were converted into the nonrolling body-axis system. This resulted in a total test matrix of four configurations for each asymmetrical biconic listed in Fig. 5b.

Although the pressure orifices aft of the nose joint were 90 deg apart peripherally, pressure data were acquired in 30-deg increments around the model. To accomplish this for the asymmetrical configurations, an indexing arrangement, located at the nose joint, was used to roll the nose -30, 0, and 30 deg relative to the frustum ($\Delta\phi$). In order to maintain the desired model roll attitude (ϕ_m), the tunnel roll-mechanism angle (ϕ_t) was set at ($\phi_m - \Delta\phi$).

The desired angles of attack for each pressure model configuration were 0, ± 1 , ± 2 , and ± 4 deg relative to its trim angle (angle of attack for zero pitching moment), which was determined from the static-force data.

3.3 TUNNEL F DATA ACQUISITION AND TECHNIQUES

Timewise measurements of the test section pitot pressure and hemisphere stagnation heat-transfer rates were used in conjunction with the Fay-Riddell stagnation point heat-transfer theory (Ref. 7) to infer the reservoir enthalpy. By using this total enthalpy and the measured reservoir and pitot pressures, the test section free-stream conditions were calculated, assuming isentropic flow as described in Ref. 8. A discussion of this method of calculation is presented in Ref. 9.

Acquisition of test data in Tunnel F was accomplished using a digital system with concomitant oscillographs for analogue records. The digital data system is capable of scanning 70 data channels in one millisecond and storing up to 150 scans of data. Basic data reduction is done on an off-line digital computer.

Figure 8a presents examples of the analogue records for tunnel monitor information (p_o , p_o') and model base pressure p_b . Calculated values of free-stream unit Reynolds number (Re_∞) and Mach number (M_∞) are also shown to illustrate timewise variations of test conditions. The data shown are typical of the Mach number 16 test conditions reported herein; for other test conditions variations may occur in the run time, nozzle starting time, and starting loads. Note that there is a 45-msec delay from the initial pressure rise to the start of the useful run, a time which is consumed by the nozzle starting process and the increase in T_o to saturation conditions. The termination of the useful portion of the run is signaled by the breakdown of the base pressure. On the force model, estimates of the source flow effects were made by calculating the apparent shift in the center-of-pressure location ($\Delta x_{cp}/\ell$) by the formula

$$\Delta x_{cp}/\ell = (2/9)(0.8/\cos^2 \theta_c)(\ell/L)$$

where

L = nozzle length

0.8 - is the source flow reduction
factor as obtained from corre-
lations of experimental data

This gave a 0.2-percent forward shift. Since this is well within the uncertainty of the center-of-pressure location (± 0.5 percent) the effect was

neglected. The pressure model, being much larger than the force model, was subject to small source flow effects. The effect of source flow was to apply a negative pressure gradient over the length of the model. No attempt was made to assess the magnitude of the gradient for the biconic model; however, for a sharp cone of the same length, with flow conditions defined by the monitor probes at the model midpoint, the effect would be a +5-percent bias at the model nose and a -5-percent bias at the base.

The force data were obtained using the variable angle-of-attack mechanism, a torsion-bar-driven device which carried the model through a pitch sweep of about 15 deg. The mechanism, shown in Fig. 9a, was initially tethered at some preset angle of attack. At the beginning of the useful run time the tether was released, leaving the mechanism free to sweep. The sweep cycle had a period of about 150 msec which allowed useful data to be taken, in general, from the maximum, or initial angle of attack, to the minimum angle obtained. Typical timewise variations of the angle of attack and force coefficients are shown in Fig. 9b. Data acquisition at the rate of one loop per millisecond produced about 3 points per degree of angle change near the midpoint of the sweep; near the extremes the number of points increased greatly. The changing test conditions caused by the decay of the reservoir pressure made it necessary to adjust the axial force for viscous interaction effects. All axial-force data have therefore been adjusted to a common test condition ($M_\infty = 16$, $Re_\infty = 0.9 \times 10^6$) for which the viscous interaction parameter $\bar{v}_\ell = 0.015$. Examples of the viscous interaction correction are shown in Fig. 10. The slopes used for the corrections to the blunted configuration data correspond to the slope of the sharp cone line at the same angle of attack. For the condition variations encountered in the present tests, the maximum axial-force correction was about ± 3 percent. No variations in the normal-force or pitching-moment coefficients were discernible for the present range of \bar{v}_ℓ .

All pressure data were obtained on a fixed-sting installation; therefore, only one pitch and roll position could be set for any one test run. No variation in pressure ratio (p/p'_0) was seen for the timewise change in run conditions; therefore, only one time point is presented for each run.

3.4 DATA PRECISION

3.4.1 Tunnel B Tests

Uncertainties (bands which include 95 percent of the calibration data) in the basic tunnel parameters (p_0 , T_0 , and M_∞) were estimated

from repeat calibrations of the instrumentation and from the repeatability and uniformity of the test section flow during tunnel calibrations. These uncertainties were then used to estimate the uncertainties in other free-stream properties, using the Taylor series method of error propagation.

Uncertainty, percent					
M_∞	p_o	T_o	q_∞	p_∞	Re_∞
± 0.1	± 1.0	± 0.7	± 1.1	± 1.3	± 1.5

The Tunnel B pitch and roll mechanisms are precise within ± 0.05 and ± 0.1 deg, respectively, based on repeat calibrations. During the force tests, model attitude corrections were made for model-balance deflections under air load. The precision of the final model angle of attack is estimated to be ± 0.1 deg in either case.

The balance uncertainties listed in Section 2.3.1 were combined with uncertainties in the tunnel parameters, assuming a Taylor series error propagation, to estimate the precision of the aerodynamic coefficients. The following representative uncertainties were obtained for the 6.3-deg cone model:

Coefficient	Uncertainties	
	Near Minimum Load	Near Maximum Load, percent
C_N	± 0.0027	± 1.5
C_m	± 0.0003	± 2.8
C_A	± 0.0025	± 2.1

The parameters C_{N_α} and C_{m_α} were evaluated from a least-squares curve fit of the data for $-2.5 \leq \alpha \leq 2.5$ deg; x_{cp}/ℓ was computed using these two parameters. Using the aforementioned precisions of C_N , C_m , and α , the estimated propagated uncertainties of C_{N_α} and C_{m_α} are ± 2.5 and ± 5.2 percent, respectively; the estimated uncertainties of α_t and x_{cp}/ℓ are ± 0.3 deg and ± 0.04 , respectively.

An evaluation of the influence of random pressure-measurement errors is presented below. The precisions of the pressure data were estimated using the instrument precisions quoted in Section 2.3.1 and the aforementioned uncertainties in free-stream conditions, assuming the propagation of these independent measurement errors is closely approximated by a Taylor series expansion.

Parameter	Surface Location	Transducer Uncertainty, psia	Uncertainties	
			Near Minimum Value	Near Maximum Value, percent
p/p_∞	Nose Cone	± 0.015	± 0.76	± 1.7
p/p_∞	$s < 4$ in.	± 0.003	± 0.14	± 2.2
p/p_∞	$s > 4$ in.	± 0.001	± 0.05	± 1.6
$\Delta p/p_\infty$	$s < 4$ in.	± 0.003	± 0.20	± 4.5
$\Delta p/p_\infty$	$s > 4$ in.	± 0.001	± 0.07	± 2.0

3.4.2 Tunnel F Tests

The results of an assessment of the experimental uncertainties in the measured data and the calculated test section conditions are as follows:

<u>Parameter</u>	<u>Uncertainty</u>
<u>Pressure Data</u>	<u>Pressure Ratio Uncertainty</u>
p/p_o'	± 8 percent at all pressure levels (± 5 -percent experimental uncertainty; ± 5 -percent source flow)
<u>Force Data</u>	<u>Coefficient Value Uncertainty</u> (Except as Otherwise Noted)
C_A	± 0.0056 (sharp cone) (N11) ± 0.0091 (Configurations N3, N7, N8, N9, N10)
C_N	± 7 percent ($\alpha > 5^\circ$) ± 0.01 ($\alpha < 5^\circ$)
C_m	± 0.002 (near maximum angle of attack)
α	± 0.4 deg
	<u>Uncertainty, percent</u>
<u>Free Stream</u>	<u>M_∞</u> <u>Re_∞</u> <u>q_∞</u> <u>p_∞</u> <u>p_o'</u> <u>p_o</u> <u>\dot{q}_o</u>
	± 2 ± 15 ± 5 ± 7 ± 5 ± 3 ± 10

SECTION IV RESULTS AND DISCUSSION

4.1 STATIC-FORCE TESTS

Asymmetry-produced side-force, yawing-moment, and rolling-moment data were obtained during these tests. However, measured rolling moments and the side-force and yawing-moment variations with angle of attack were less than their estimated measurement precisions. Therefore, these data have been omitted from the report, since side-force and yawing-moment levels may be obtained from the data presented herein.

Variations in the normal-force coefficient, C_N , pitching-moment coefficient, C_m , and axial-force coefficient, C_A , with angle of attack are presented in Figs. 11 through 16. Summary plots showing the effects of various configurations on the important parameters at zero angle of attack are given in Figs. 17 and 18.

Effects of the cone angle may be seen in Fig. 11a for the hemispherically blunted cones and in Fig. 11b for the 50-deg symmetrical biconics. The most noticeable effect is the almost constant displacement of the axial force. There are some effects on C_N and C_m at the higher angles of attack.

Effects of the nose angle, θ_n , for the symmetrical biconics are given in Fig. 12. There is the expected influence on the axial-force coefficient. At the higher angles of attack, there is a considerable effect on the normal-force coefficient without a corresponding effect on the pitching moment. This implies that the effect of the nose extends considerably downstream, since if the effect were concentrated in the region of the nose, there would be more effect on the pitching moment than is shown.

Figure 13 gives results for different nose shapes at $M_\infty = 16$. The 50-deg biconic and the hemispherically blunted cone have very similar characteristics except for the axial-force coefficients.

Effects of the nose cant angle (δ_n) are given in Fig. 14 for $M_\infty = 16$ for the unrolled vehicle. Figure 15 gives the corresponding results for $M_\infty = 8$ and several roll angles. The primary effect of the cant angle is the introduction of a pitching moment at zero angle of attack or, equivalently, the trim angle is different from zero. Figures 14 and 15a give a direct comparison of Mach number effects. Figures 15b, c, and d

show that as the model is rolled the effect of the cant angle on the moment is significantly reduced. These effects are discussed later in conjunction with Fig. 18.

Figure 16 presents the effects of shoulder radius, r_s . There are small effects on the axial-force coefficient, but little effect on the normal-force coefficient and the pitching-moment coefficient.

Figure 17 summarizes the important parameters for symmetrical shapes at zero angle of attack. Figure 17a presents the effects of cone angle, θ_c , and Fig. 17b gives the effect of the nose angle, θ_n , for the symmetrical biconics. The variation of the axial-force coefficient with cone angle and nose angle is as would be expected. The increase in $C_{N\alpha}$, $C_{m\alpha}$, and x_{cp}/ℓ of the 50-deg biconic as the cone angle is increased from 6.3 to 9 deg in Fig. 17a is a bit larger than would be expected for a hemispherically blunted cone.

The effects of nose cant angle for the asymmetrical biconics are given in Fig. 18a. The effects on $C_{N\alpha}$, $C_{m\alpha}$, and x_{cp}/ℓ are rather small at any given Mach number. There are some slight Mach number effects. The trim angle of attack is given in the lower portion of the figure and shows the expected trends; i. e., an increasing trim angle with increasing cant angle, with the value of the trim angle varying approximately as the cosine of the roll angle. Figure 18b gives the effect of shoulder radius, and the only significant effect is on the axial-force coefficient.

4.2 PRESSURE TESTS

The pressure distribution data are presented in Figs. 19 through 24. The results for the 50-deg biconic at $M_\infty = 16$ are given in Fig. 19 for the nose cone and Fig. 20 for the aft cone. The results at Mach 8 for the symmetrical biconics are given in Fig. 21 for the nose and Fig. 23 for the aft cone. The Mach 8 results for the asymmetrical biconics are given in Fig. 22 for the nose portion and in Fig. 24 for the aft cone. Data were obtained at 30-deg increments in the circumferential direction, but for clarity, values for only the four orthogonal locations are given.

The circumferential pressure distributions on the nose cone of the symmetrical 50-deg biconic at $M_\infty = 16$ are presented in Fig. 19. Also shown are inviscid values for a sharp cone as computed by the method of Jones (Ref. 10). The results agree satisfactorily except at an angle

of attack of 2 deg near the windward streamline ($\phi = 0$). Pressure distributions on the aft cone are given in Fig. 20.

The remainder of the basic pressure data are from Tunnel B at Mach 8. Figure 21 gives the circumferential pressure distributions on the nose of the symmetrical biconics. Also shown are the inviscid sharp cone values calculated using the method of Jones (Ref. 10). Experimental values and calculated values generally agree within the precision of the data (± 1.7 percent).

The nose pressure distributions for the asymmetrical noses are given in Fig. 22 for nose cant angles of 6, 12, and 18 deg. For each cant angle, results are presented for roll angles (ϕ_m) of 0, -30, -60, and -90 deg. For each combination the trim angle as given by Fig. 18 was included as one of the angles of attack, and other angles of attack were selected in increments of ± 1 deg from the trim angle. Longitudinal pressure distributions on the aft cone are given in Fig. 23 for the symmetrical biconics and in Fig. 24 for the asymmetrical biconics.

In view of the large amount of data presented, extended discussion of the results is inappropriate. Studies are being made at other centers with the purpose of comparing the results from the force tests with the results obtained by integrating the pressure distributions. In addition, it is planned to make comparisons between the experimental pressure distributions and results of various 3-dimensional characteristics computer programs. There are, however, a few points that should be made.

The effects of the various model configuration variables on longitudinal surface pressure distributions downstream of the shoulder are presented in Figs. 25 through 29. From the vast amount of distribution data obtained, only the windward ($\phi = 0$) and leeward ($\phi = 180$) surface pressure distributions are shown. Effects of the nose cone angle on downstream surface pressure distributions of the symmetrical biconics are shown in Fig. 25 for angles of attack of 0, 1, 2, and 4 deg. The pressure distribution produced by the 50-deg conical nose became characteristically different from the other two on the windward side with increasing angle of attack, in that a plateau was not achieved.

The effects of shoulder radius (r_s) on the longitudinal surface pressure distributions are presented in Fig. 26 for the symmetrical 50-deg biconic at $\alpha = 0$ and 4 deg. Also included is the difference between the windward and leeward pressure ratios, which may be used as a rough indication of the loading distribution. The data show that shoulder radius had relatively insignificant effects on the absolute and differential distributions for either angle of attack.

Longitudinal-differential pressure distributions for the various asymmetric biconics are presented in Figs. 27 through 29. Comparisons of these distributions for angles of attack on either side of the trim angle are made in Fig. 27 at $\phi_m = 0$ and -60 deg for each basic cant angle. Recalling that the moment reference point location is at $s = 14.81$ in. and viewing the differential pressure values relative to $\Delta p/p_\infty$ at $s = 14.81$ in., the region which caused a net positive pitching moment for $\alpha < \alpha_t$ is seen to have been $0 < s < \approx 7$ in. As α was increased, however, the increasing differential pressure loading over approximately the aft 2/3 of the cone resulted in larger negative (opposing) moments. Differential pressure distributions for the three trimmed asymmetrical configurations are compared in Fig. 28 at two roll angles. Although the levels are different because of angle-of-attack effects, the distributions are remarkably similar in shape. The direct effects of the three basic cant angles on the surface pressure distributions are shown in Fig. 29, where data for the comparable symmetric biconic (N3) are presented at the trim angles of the asymmetrical configurations. Upon examination of these differential pressure data it is even more evident that trim angle was primarily governed by the contributions of differential pressures downstream of the shoulder but upstream of $s \approx 7$ in.

SECTION V CONCLUDING REMARKS

From the results of static-force and pressure tests conducted on a 6.3-deg cone at $M_\infty = 8$ and 16 and $Re_\infty = 10^6$ per foot, the following general remarks may be made regarding the effects of the various noses:

1. Windward-surface pressure distributions produced by a symmetrical 50-deg conical nose on the 6.3-deg cone became characteristically different with increasing angle of attack from those produced by 30- and 40-deg cones. Circumferential pressure distributions just upstream of the 50-deg cone shoulder agreed well with inviscid sharp cone theory for $0 \leq \alpha \leq 4$ deg. Increasing the cone angle from 30 to 50 deg significantly decreased C_{N_α} and uniformly (approximately) increased C_A by about 55 percent.
2. Shoulder radius variations (from 0 to $0.6 r_n$) had almost insignificant effects on absolute and differential (windward-leeward) pressure distributions and on the aerodynamic coefficients, except for a small decrease in C_A with increasing radius.

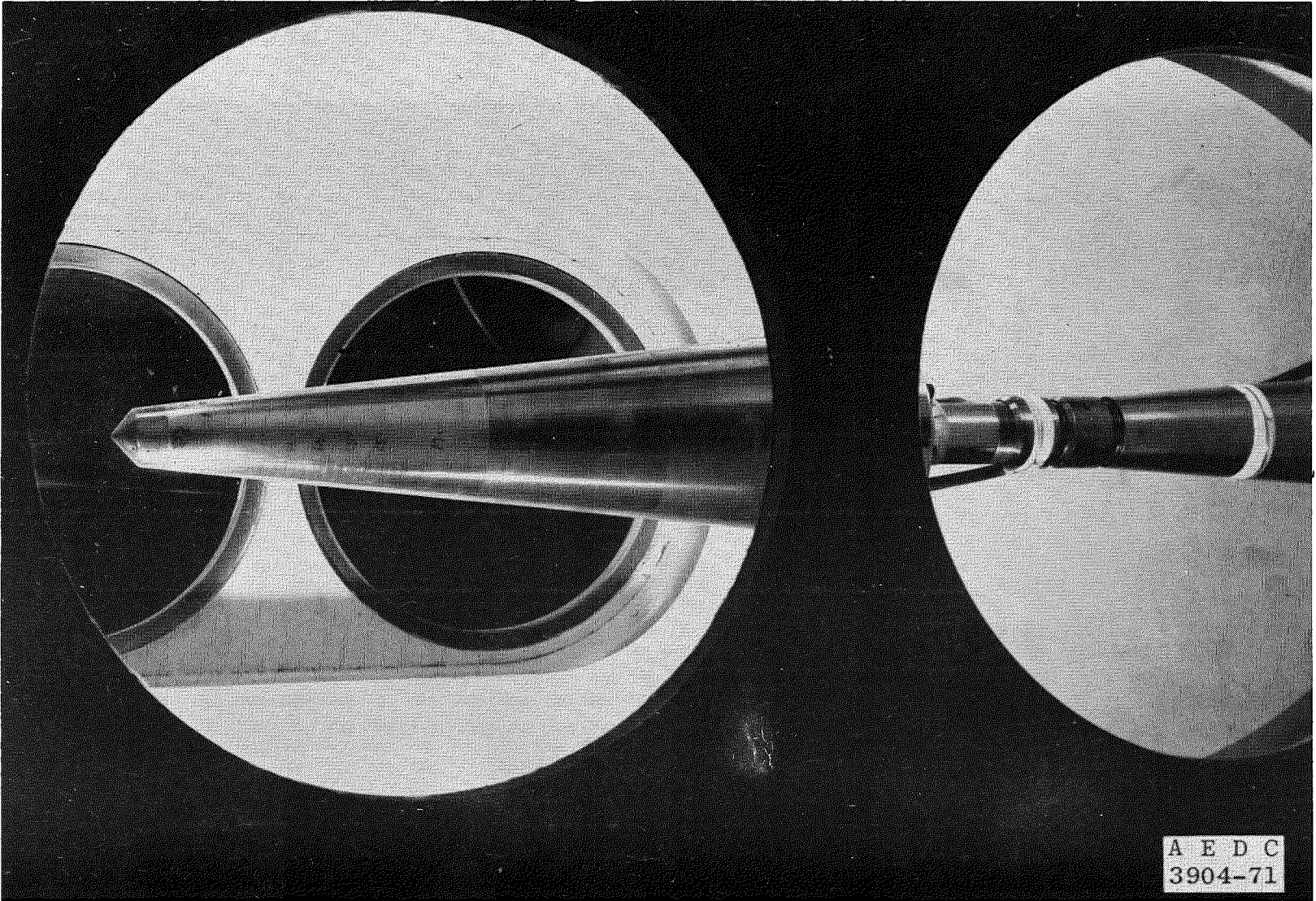
3. Center of pressure (and hence pitching moment) was greatly affected by model asymmetries, which were produced by three basic canted nose angles (δ_n) of 6, 12, and 18 deg. Trim angles as large as 5 and 6 deg were obtained at $M_\infty = 8$ and 16, respectively, for $\delta_n = 18$ deg. Measured rolling moment and side-force and yawing-moment variations with angle of attack were negligible, even when the asymmetries were located in the yaw plane. Differential (windward-leeward) pressure distributions viewed relative to the moment reference point showed that the region $0 < s < \approx 7$ in. produced the net positive pitching moment when $\alpha < \alpha_t$ for the asymmetrical configurations. As α was increased, however, the increasing differential pressure loading over approximately the aft 2/3 of the cone resulted in larger negative (opposing) moments. Comparisons of symmetric- and asymmetric-biconic pressure data made at the asymmetrical trim angle demonstrated that trim angle was primarily governed by the contributions of differential pressures downstream of the shoulder, but upstream of $s \approx 7$ in.

REFERENCES

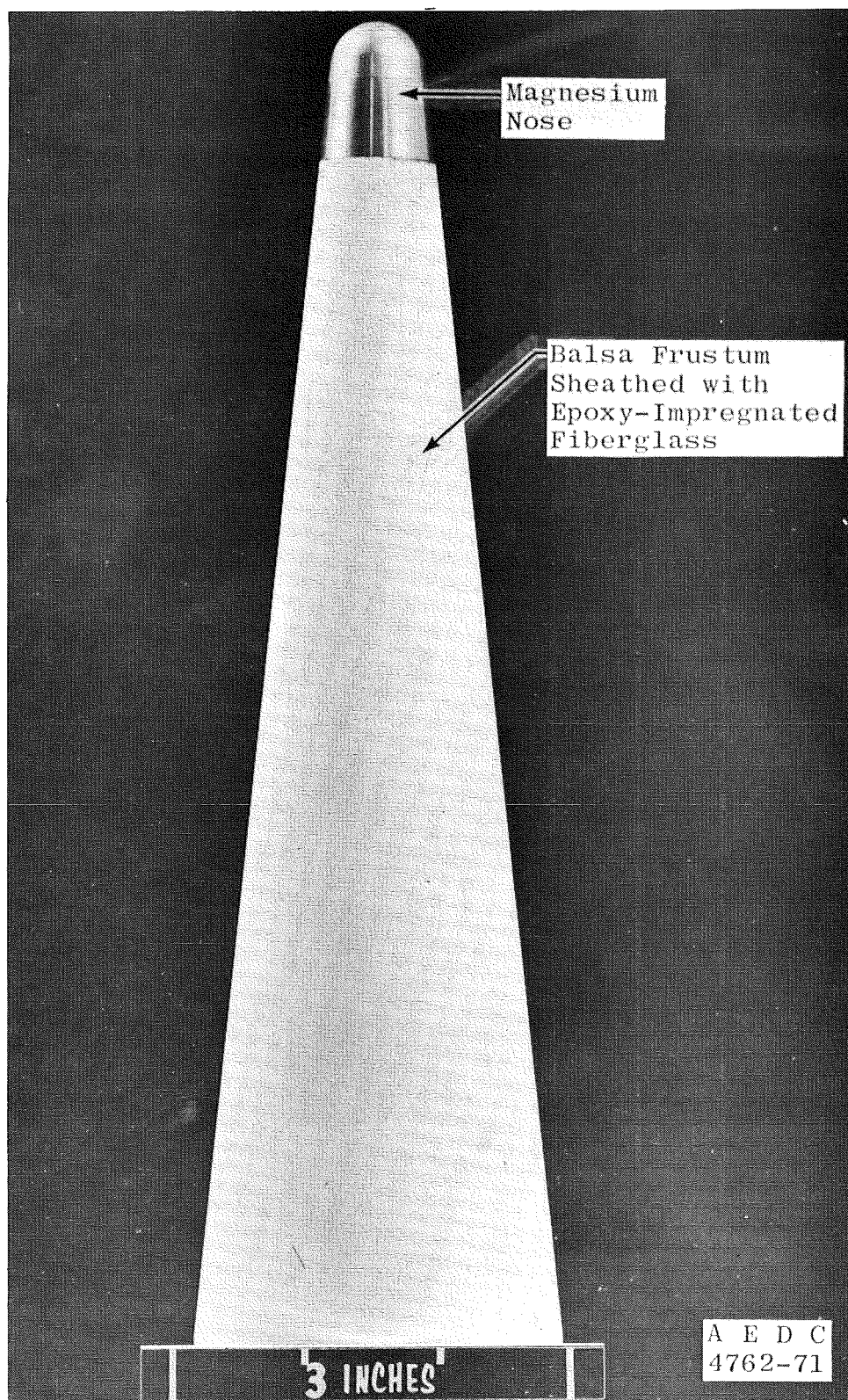
1. Test Facilities Handbook (Ninth Edition). "Von Kármán Gas Dynamics Facility, Vol. 3." Arnold Engineering Development Center, July 1971.
2. Weddington, E. D. and Griffith, B. J. "Recent Refinements and Advancements of Hypersonic Testing Techniques for the 100-in. Tunnel F of the von Kármán Gas Dynamics Facility." Fourth Hypervelocity Techniques Symposium, Arnold Engineering Development Center, November 15-16, 1965. Also Weddington, E. D. and Griffith, B. J. "Calibration and Status of the AEDC-VKF 100-Inch Hotshot Tunnel." AEDC-TR-66-191 (AD8000778), October 1966.
3. Lukasiewicz, J., Jackson, R., and Whitfield, Jack D. "Status of Development of Hotshot Tunnels at AEDC." The High Temperature Aspects of Hypersonic Flow, Pergamon Press, 1964, pp. 323-356.
4. Eaves, R. H., Jr., Griffith, B. J., and Buchanan, T. D. "Design and Initial Calibration of the AEDC-VKF Tunnel F with an Enlarged Arc Chamber." AEDC-TR-69-122 (AD862975), December 1969.

5. Bynum, D. S. "Instrumentation for the AEDC/VKF 100-Inch Hot-shot Tunnel F." AEDC-TR-66-209 (AD804567), January 1967.
6. Ledford, R. L., Smotherman, W. E., and Kidd, C. T. "Recent Developments in Heat-Transfer Rate, Pressure, and Force Measurements for Hotshot Tunnels." AEDC-TR-66-228 (AD645764), January 1967.
7. Fay, J. A. and Riddell, F. R. "Theory of Stagnation Point Heat Transfer in Dissociated Air." Journal of Aerospace Sciences, Vol. 25, No. 2, February 1958, pp. 73-85, 121.
8. Grabau, Martin, Smithson, H. K., Jr., and Little, Wanda J. "A Data Reduction Program for Hotshot Tunnels Based on the Fay-Riddell Heat-Transfer-Rate Using Nitrogen at Stagnation Temperatures from 1500 to 5000°K." AEDC-TR-64-50 (AD601070), June 1964.
9. Griffith, B. J. and Lewis, C. H. "A Study of Laminar Heat Transfer to Spherically Blunted Cones and Hemisphere-Cylinders at Hypersonic Conditions." AEDC-TDR-63-102 (AD408568), June 1963. Also AIAA Journal, Vol. 2, No. 3, March 1964, pp. 438-444.
10. Jones, D. J. "Numerical Solutions of the Flow Field for Conical Bodies in a Supersonic Stream." National Research Council of Canada, Report LR-507, July 1968.

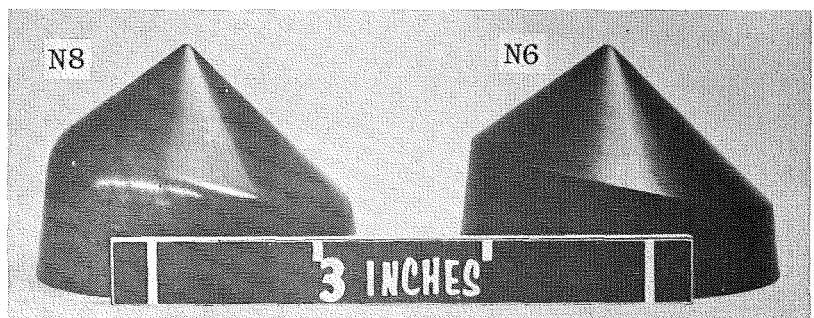
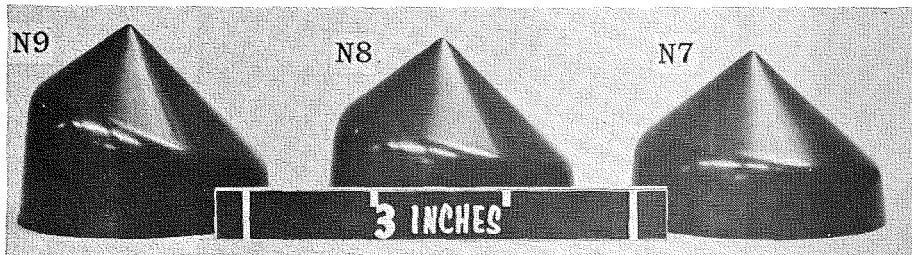
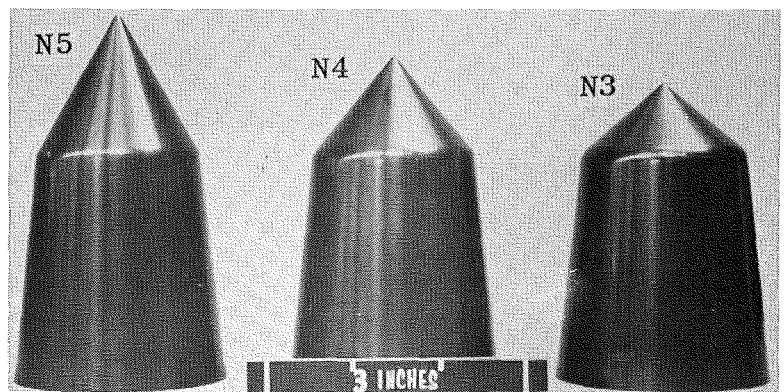
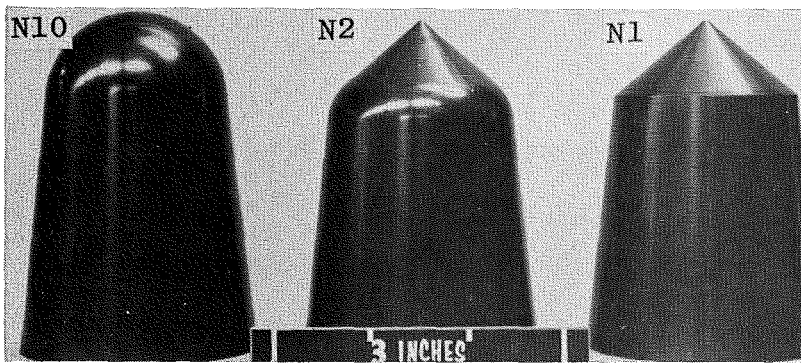
APPENDIXES
I. ILLUSTRATIONS
II. TABLES



a. Pressure Model Installed in Tunnel B
Fig. 1 Photographs of Selected Models

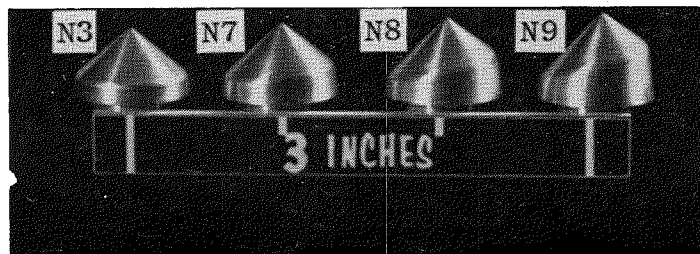


b. Tunnel F Force Model
Fig. 1 Concluded

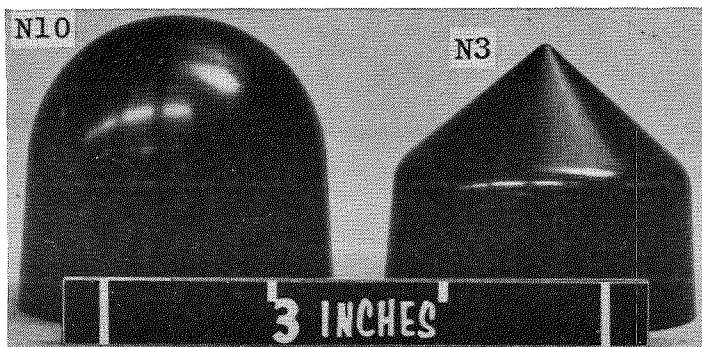


a. 6.3-deg Cone Noses Used in Tunnel B
 Fig. 2 Photographs of Noses for Force Models

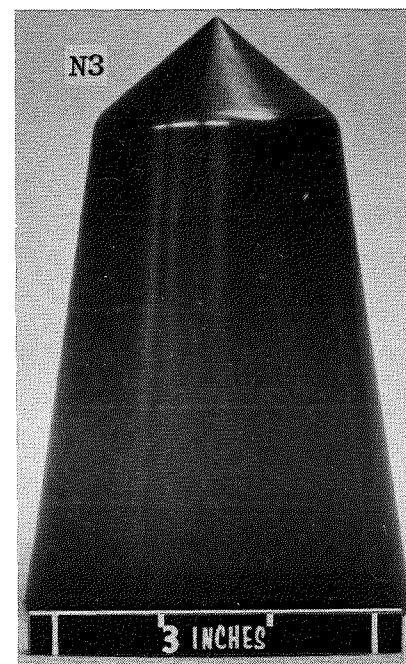
Note: N10 and N11 are omitted here,
but N10 is shown in Fig. 1b.



b. 6.3-deg Cone Noses Used in Tunnel F

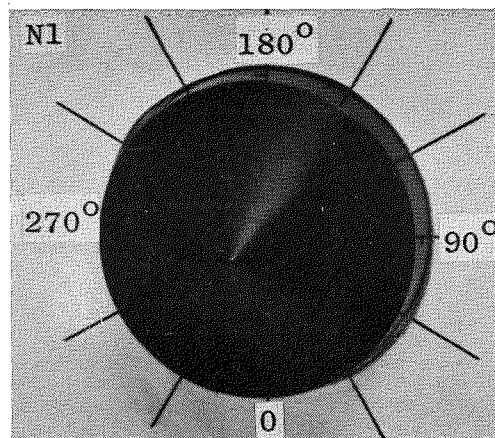
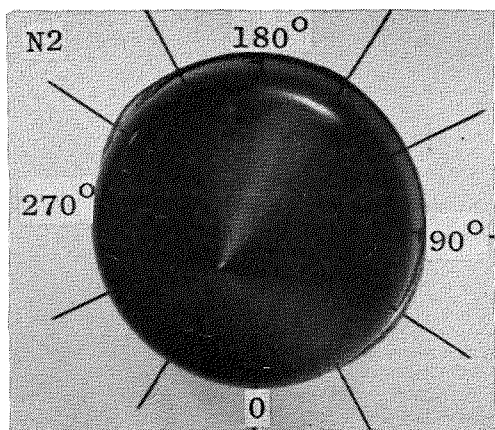
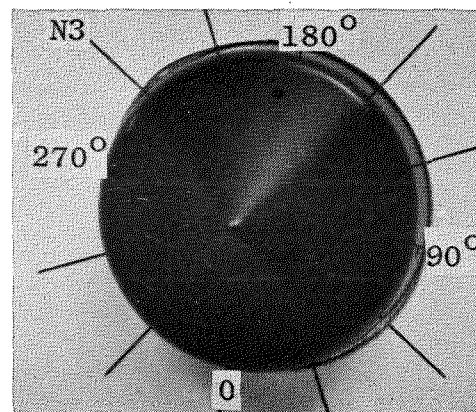
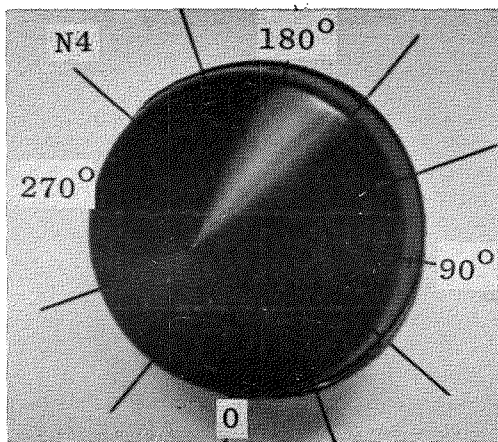
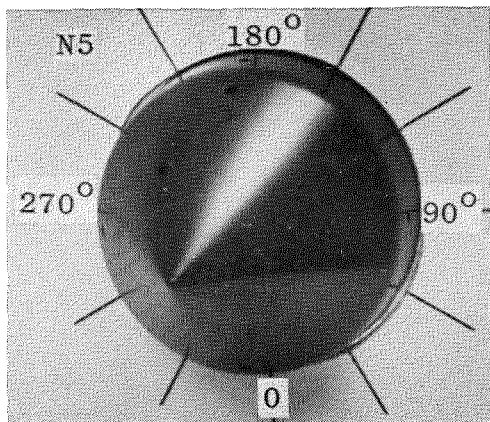


4.0-deg Cone Noses

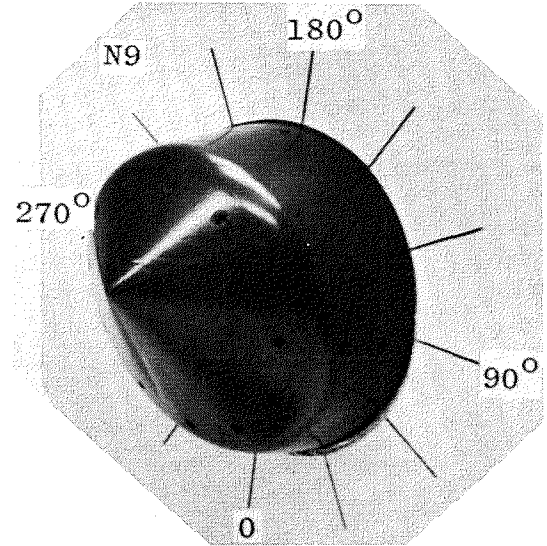
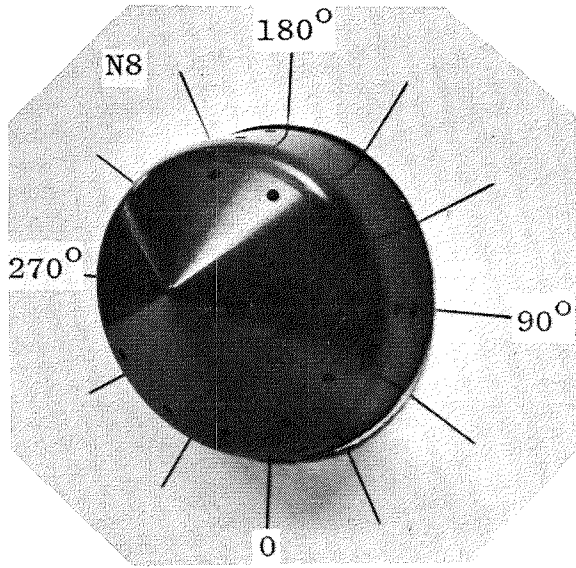
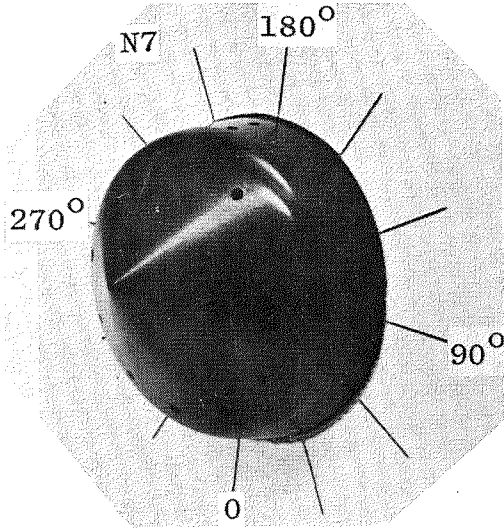


9.0-deg Cone Nose

c. 4.0- and 9.0-deg Cone Noses Used in Tunnel B
Fig. 2 Concluded



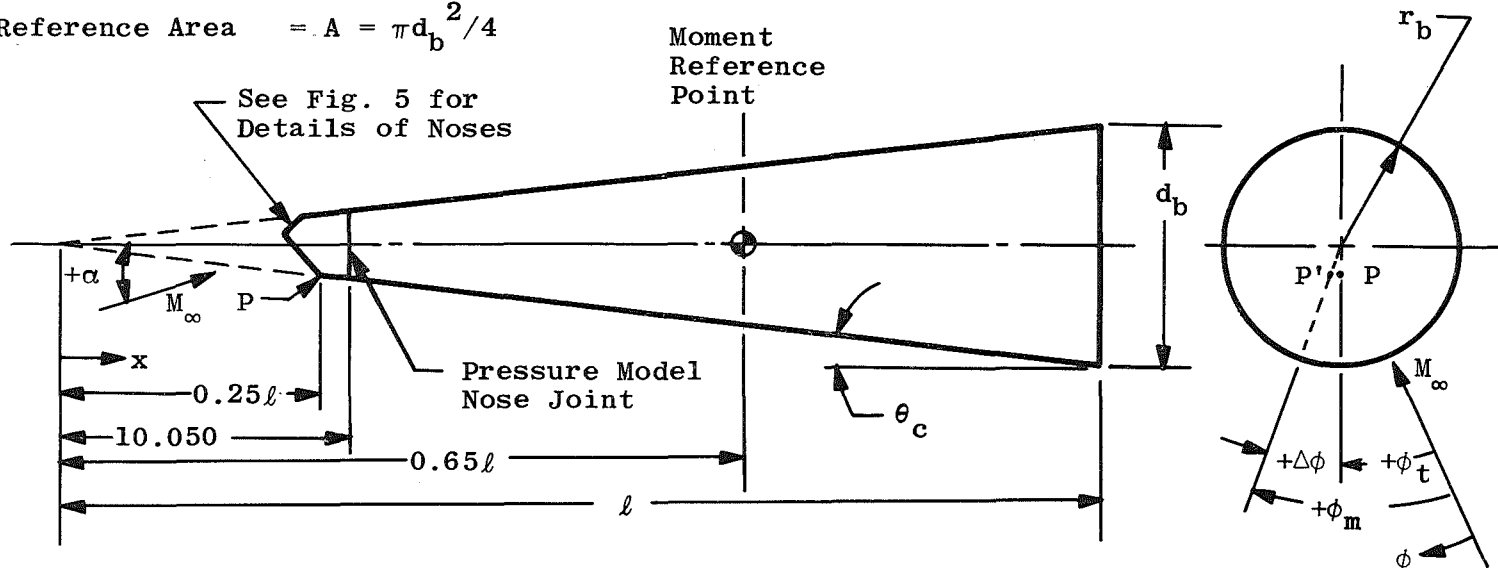
a. Symmetrical Noses
 Fig. 3 Photographs of Noses for Pressure Model



b. Asymmetrical Noses
Fig. 3 Concluded

Reference Length = ℓ

Reference Area = $A = \pi d_b^2/4$

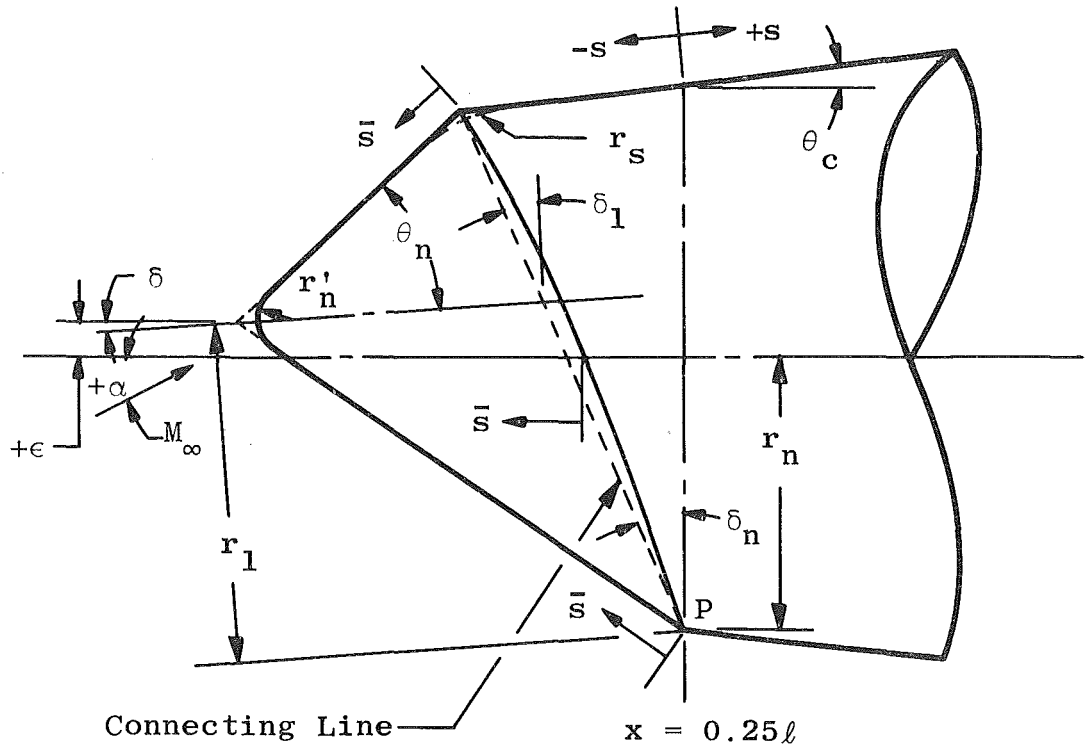


Model Type	θ_c , deg	M_∞	ℓ , in.	A , in. ²	r_b , in.	d_b , in.	0.25ℓ , in.	0.65ℓ , in.	Configurations Tested
Force ↓	4.0	8	57.203	50.265	4.000	8.000	14.301	37.182	N3, N10
	6.3	8	36.798	51.849	4.062	8.125	9.200	23.919	N1-N10
	6.3	16	13.586	7.069	1.500	3.000	3.396	8.831	N3, N7-N11
	9.0	8	31.569	78.540	5.000	10.000	7.892	20.520	N3
Pressure	6.3	8; 16	36.798	51.849	4.062	8.125	9.200	23.919	N1-N5, N7-N9; N3

Note: P' is the location of the nose cone aft shoulder point (P) when the nose cone is rolled relative to the frustum ($\Delta\phi$).

$\phi_m = \phi_t$ when $\Delta\phi = 0$

Fig. 4 Details of Models



For Biconic Configurations:

$$r_n = 0.25 r_b$$

$$r'_n = 0.05 r_n$$

$$\delta_l = \cos^{-1} \left[\sqrt{(\tan^2 \theta_n + \cos^2 \delta_n - \tan^2 \theta_c \sin^2 \delta_n) / \sec^2 \theta_n} \right]$$

$$r_l = [r_n \cos \theta_c \cos (\theta_n - \delta_l)] / [\cos \theta_n \cos (\theta_c - \delta_n)]$$

$$\delta = \delta_n - \delta_l$$

$$\epsilon = (r_l \cos \delta) [1 - (\tan \delta / \tan \theta_n)] - r_n$$

For Spherically Blunted Cone Configuration:

$$r_s = r'_n = 0.25 r_b$$

$$r_n = (0.25 r_b) \cos \theta_c$$

a. Geometry
Fig. 5 Details of Noses

Configuration	Shape	θ_n , deg	r_s/r_n	δ_n , deg	θ_c , deg			
					$M_\infty = 8$		$M_\infty = 16$	
					Force	Pressure	Force	Pressure
N1	Symmetrical Biconic	50	0	0	6.3	6.3	---	---
N2	↓	↓	0.6	↓	6.3	6.3	---	---
N3		↓	0.3	↓	4.0	---	---	---
↓		↓	↓	↓	6.3	6.3	6.3	6.3
N4		↓	↓	↓	9.0	---	---	---
N5		↓	↓	↓	6.3	6.3	---	---
N6	Asymmetrical Biconic	50	0	12	↓	6.3	---	---
N7	↓	↓	0.3	6	↓	6.3	6.3	---
N8		↓	↓	12	↓	↓	↓	---
N9		↓	↓	18	↓	↓	↓	---
N10	Spherically Blunted Cone	--	$1/\cos \theta_c$	--	4.0	---	---	---
N10	Spherically Blunted Cone	--	$1/\cos \theta_c$	--	6.3	---	6.3	---
N11	Sharp Cone	6.3	0	0	---	---	6.3	---

b. Nose Configuration Coding
Fig. 5 Concluded

See Nose Nomenclature in Fig. 5a

On Nose Cone:

(Note: $\phi = \phi_m + \omega$)

Conf.	ω	\bar{s}
N1	ω_1	0.31
N2	↓	↓
N3		↓
N4		0.26
N5		0.23
N7	ω_2	0.25
N8	↓	↓
N9		↓

On Nose Frustum:

(Note: $\phi = \phi_m + \omega$)

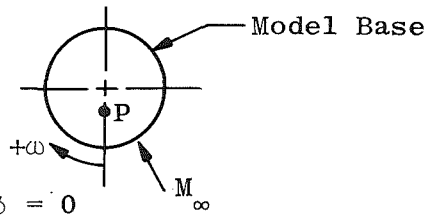
Conf.	ω	s
N1	ω_1	0.20
N2	↓	0.30
N3		0.20
N4		↓
N5		↓
N7		↓
N8	↓	↓
N9		↓
N7	180	-0.01
N8	90	-0.02
N8	180	-0.23
N8	270	-0.03
N9	90	-0.14
N9	270	-0.14

On Body Frustum, but

Aft of Nose Joint:

(Note: $\phi = \phi_t + \omega$)

Conf.	ω	s
+A11	ω_1	1.006
↓	↓	1.509
		2.012
		2.515
		3.018
		4.024
		5.030
		6.036
		*7.043
		8.049
		*10.061
		13.079
		16.600
		21.128
		26.158



Note: $\Delta\phi = 0$

Upstream View

+A11: Configurations N1,N2,N3,N4,N5,N7,N8, and N9

ω_1 : $\omega = 0, 90, 180, \text{ and } 270 \text{ deg}$

ω_2 : $\omega = 0, 30, 60, 90, 120, 150, 180, 210, 240, 270, 300, \text{ and } 330 \text{ deg}$

*Pressure taps at these stations were not used for the Tunnel F ($M_\infty = 16$) tests.

Note: All model pressure orifice diameters were 0.063 in.

Fig. 6 Pressure Model Orifice Location for $\Delta\phi = 0$

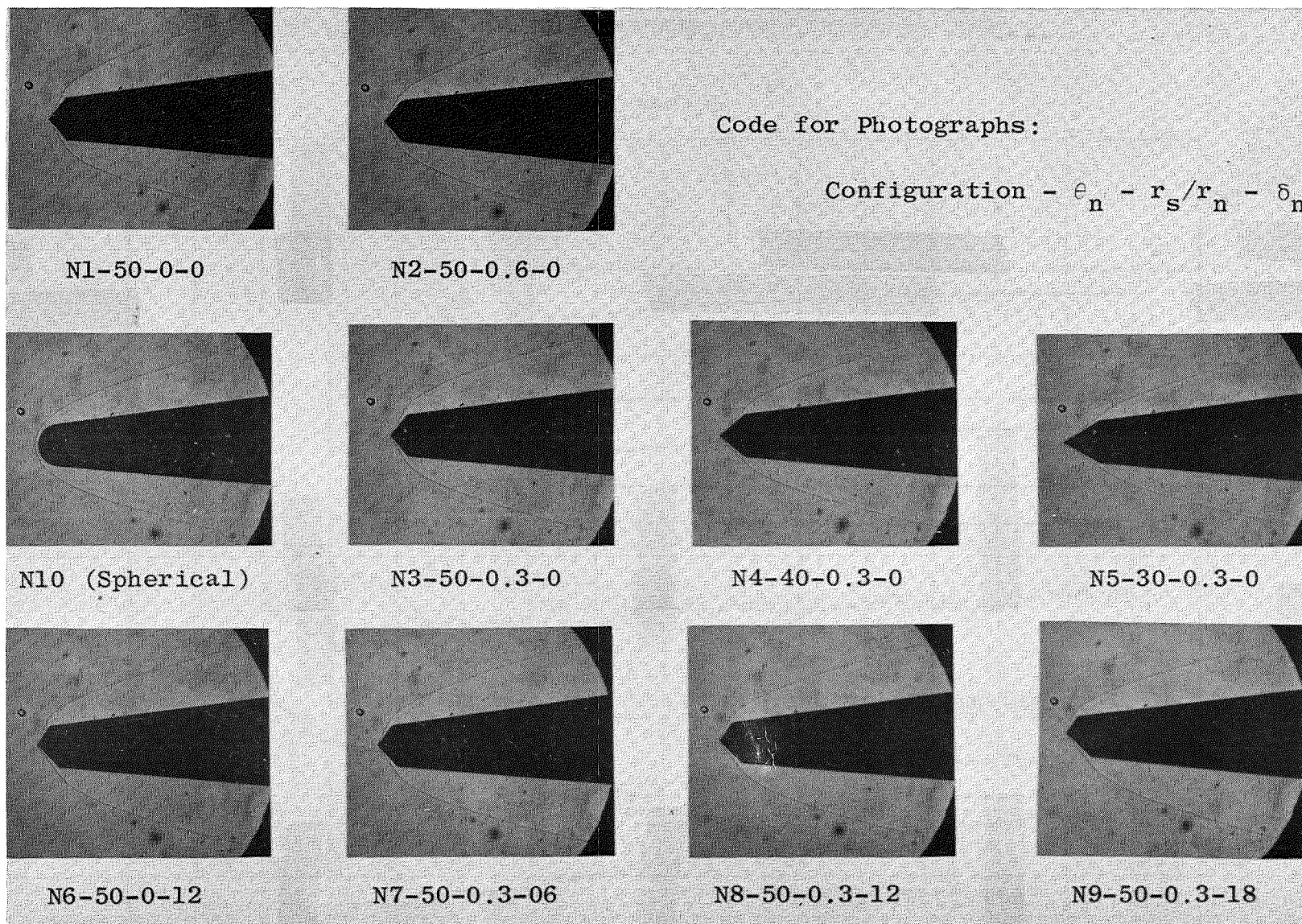


Fig. 7 Typical Tunnel B Shadowgraphs for $\alpha = \phi_m = 0$

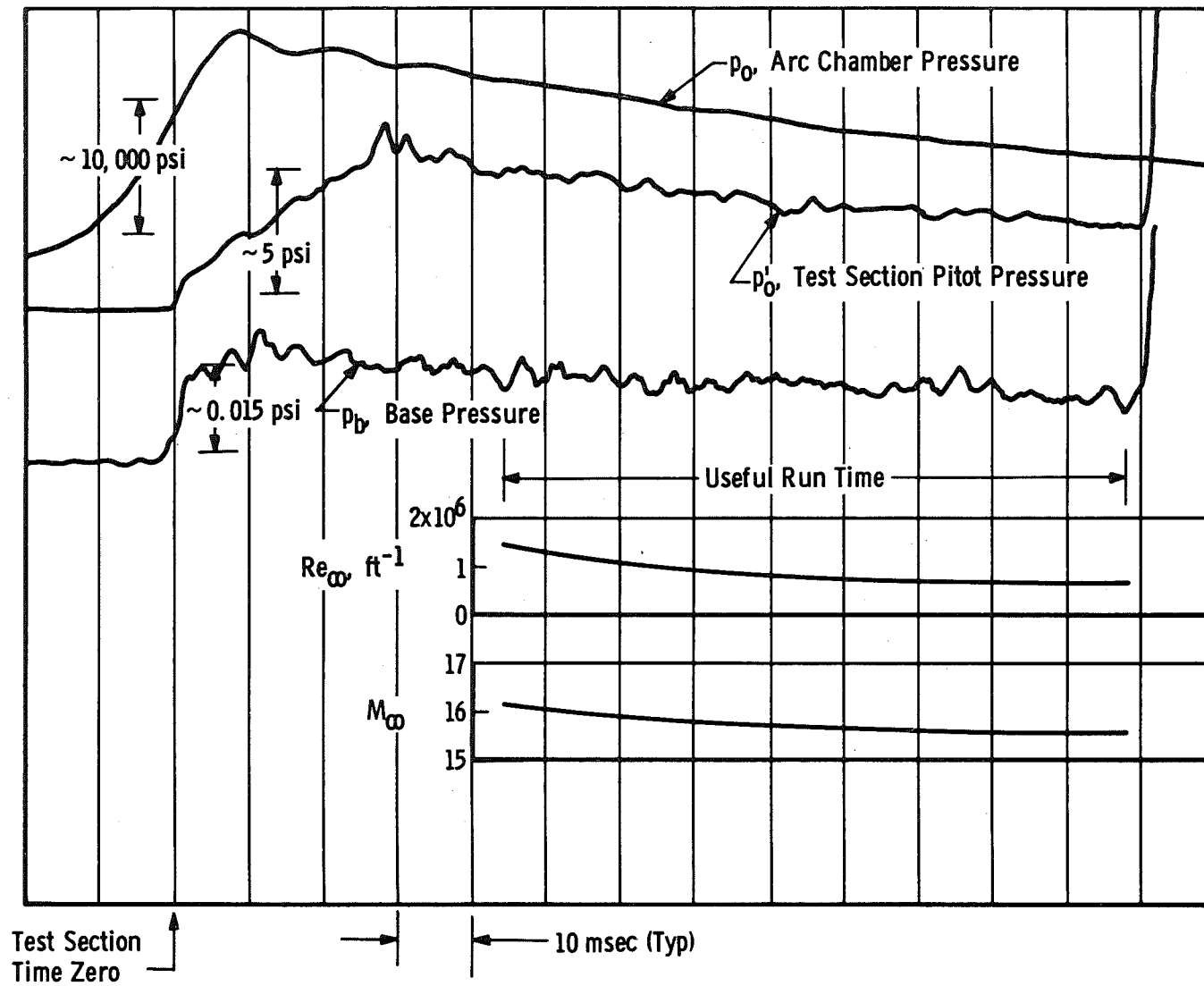
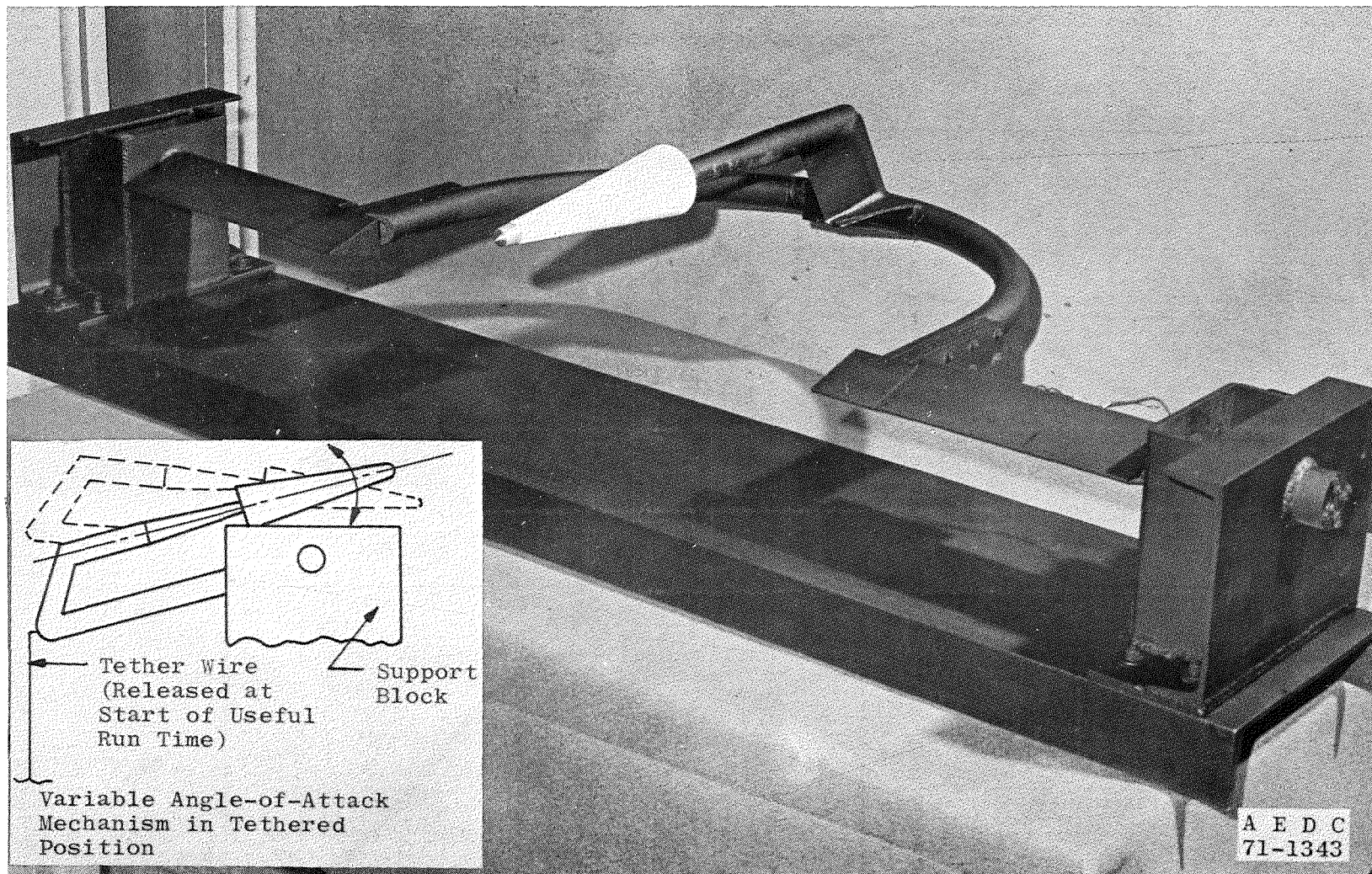
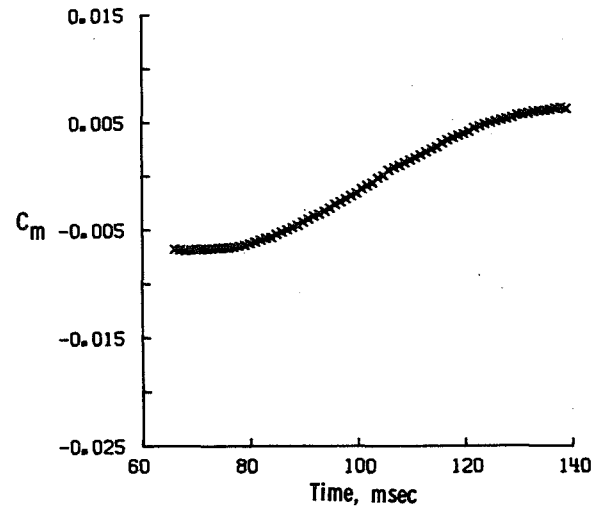
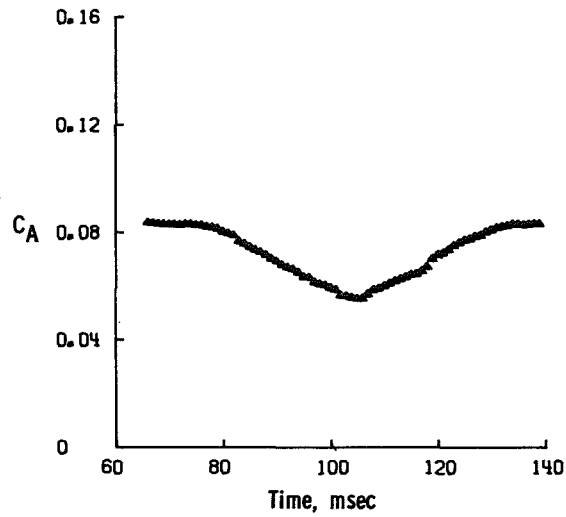
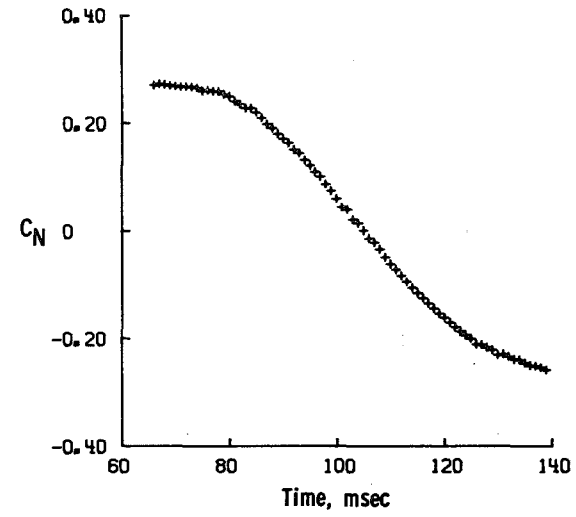
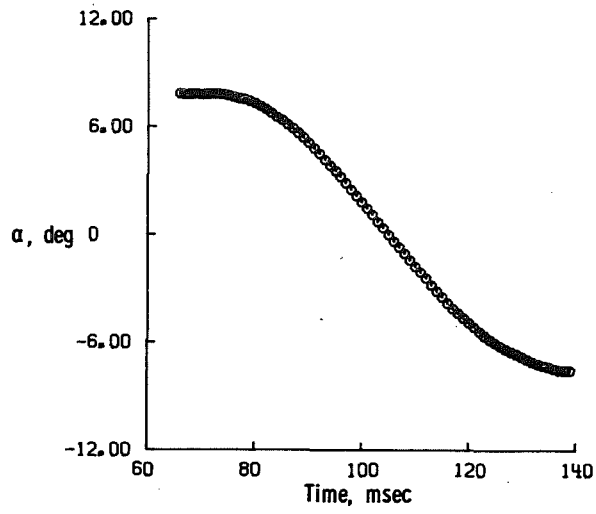


Fig. 8 Typical Monitor Data Traces and Tunnel Conditions for Tunnel F



a. Variable Angle-of-Attack Mechanism
Fig. 9 Tunnel F Static-Force Data Acquisition



b. Typical Static-Force Data
Fig. 9 Concluded

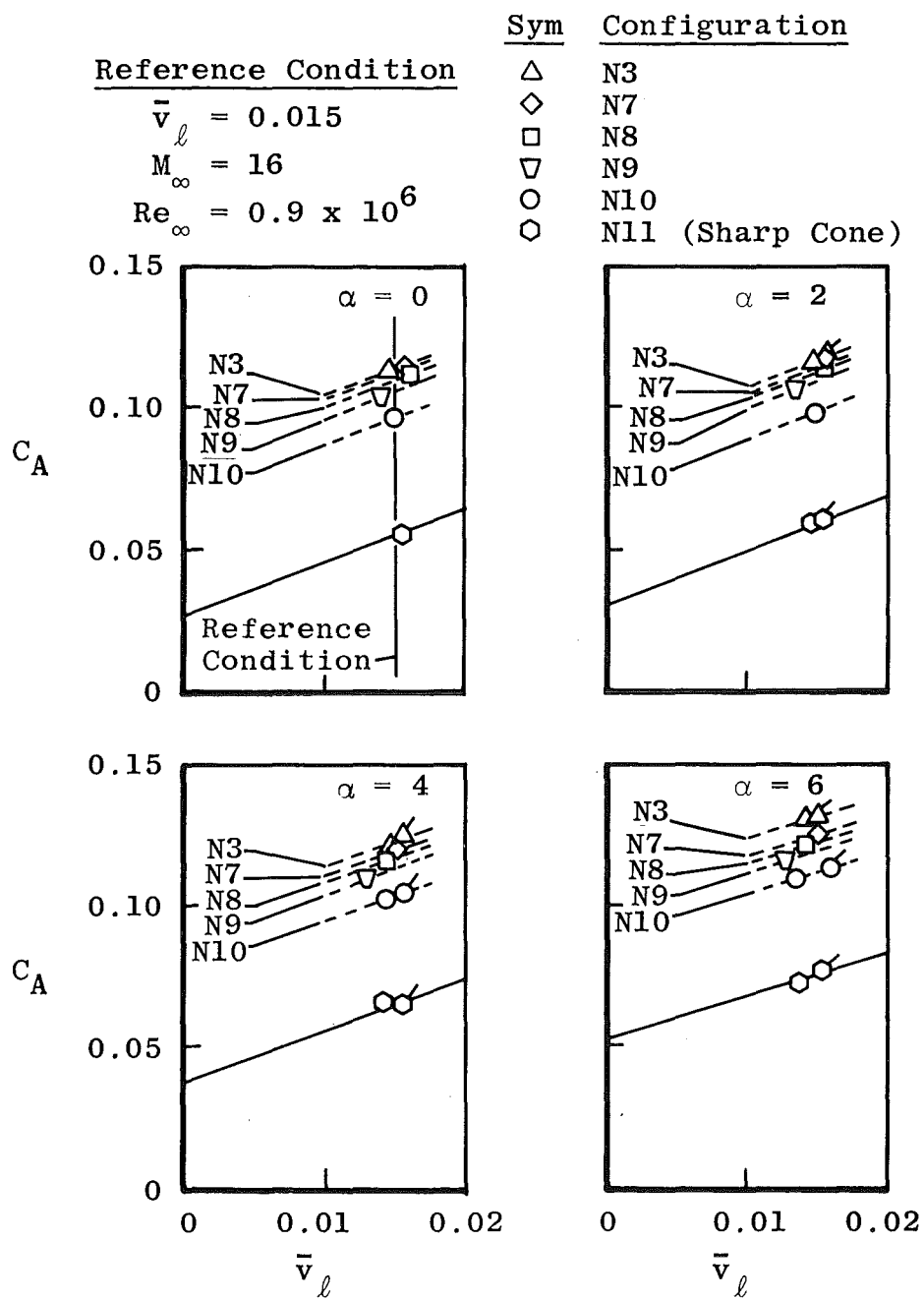
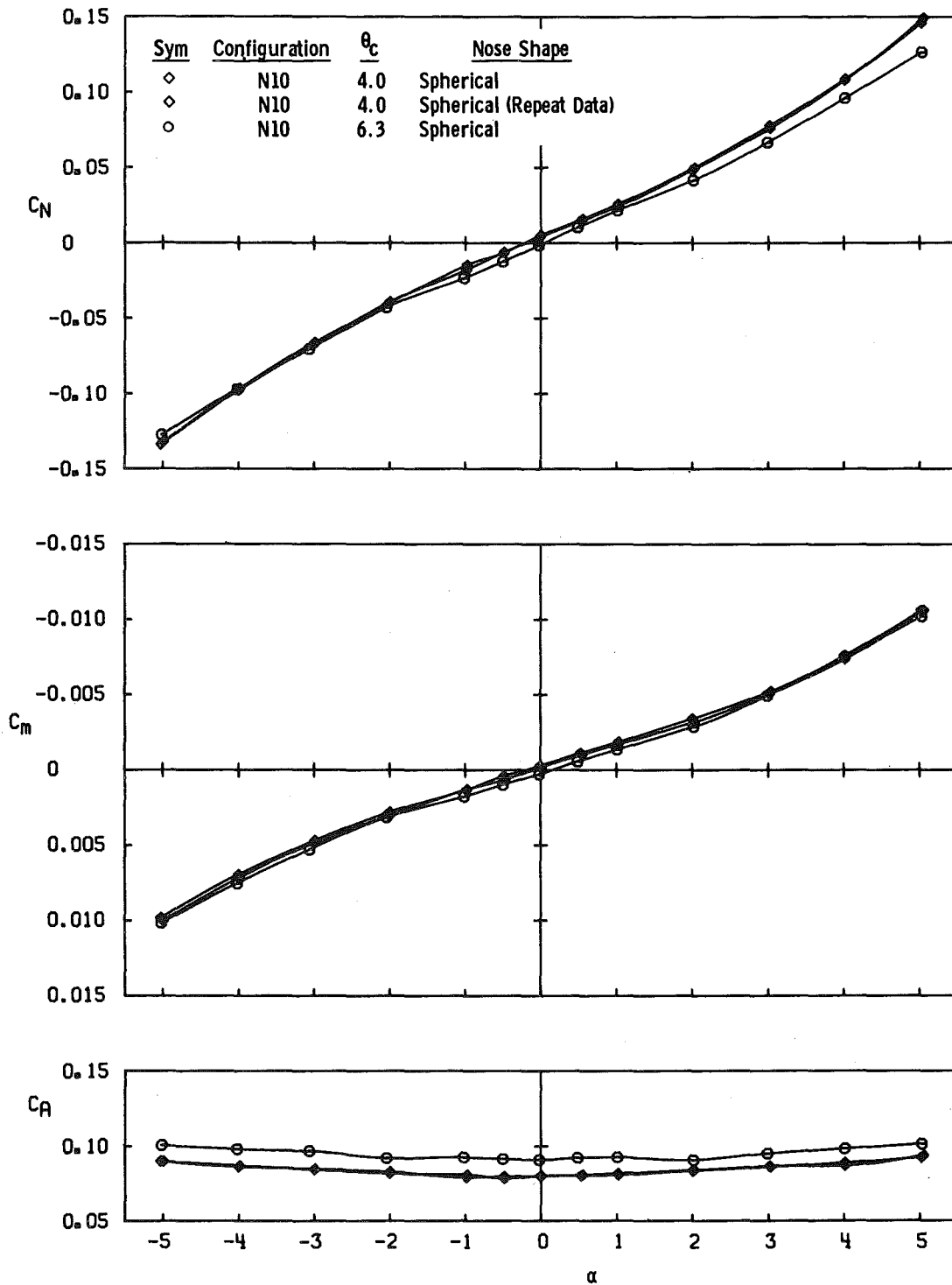
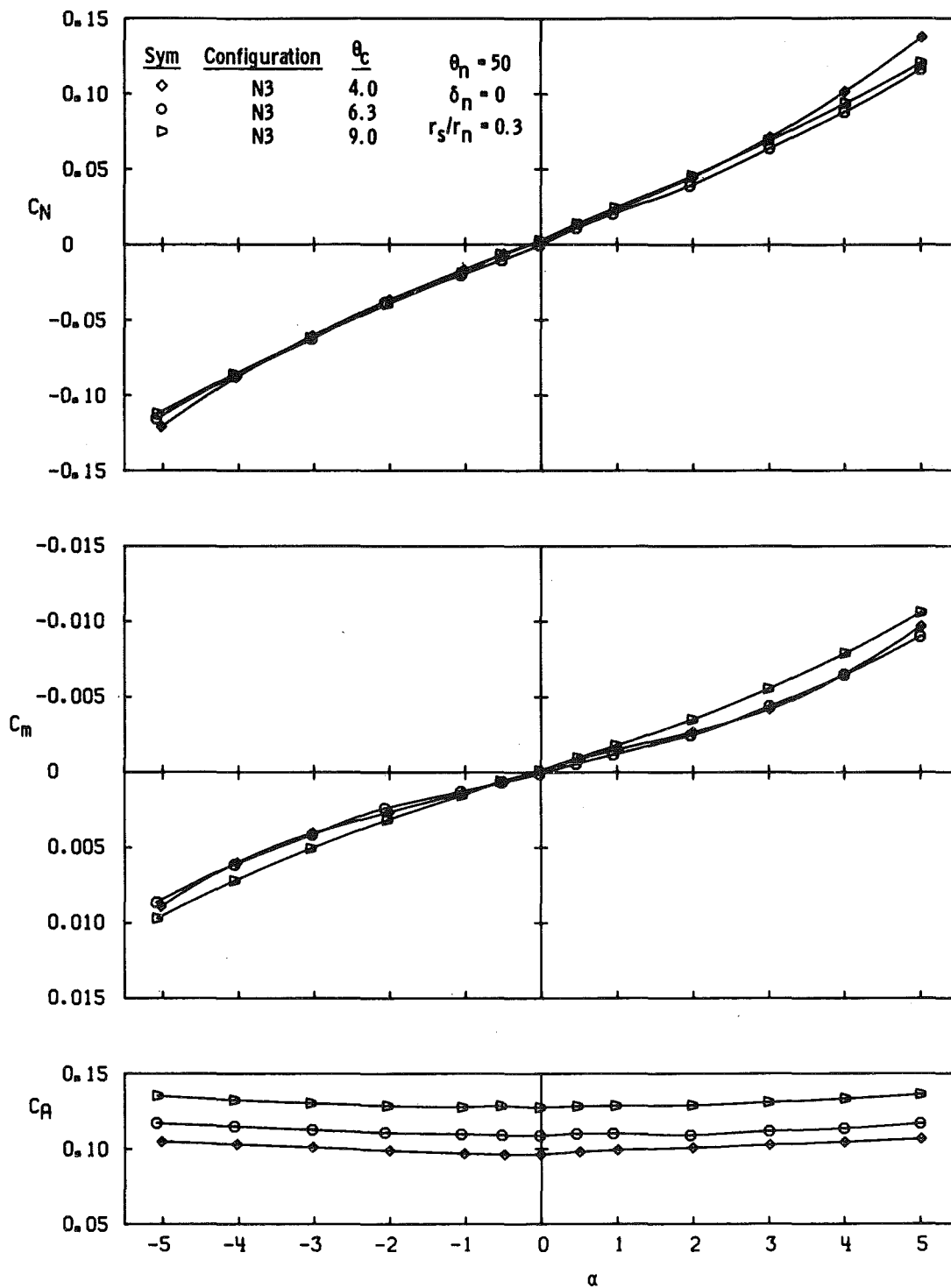


Fig. 10 Typical Viscous Interaction Corrections of Tunnel F Axial-Force Data



a. Spherically Blunted Cones

Fig. 11 Effects of Cone Angle (θ_c) on the Normal-Force, Pitching-Moment, and Axial-Force Characteristics, $M_\infty = 8$



b. Symmetrical 50-deg Biconics
Fig. 11 Concluded

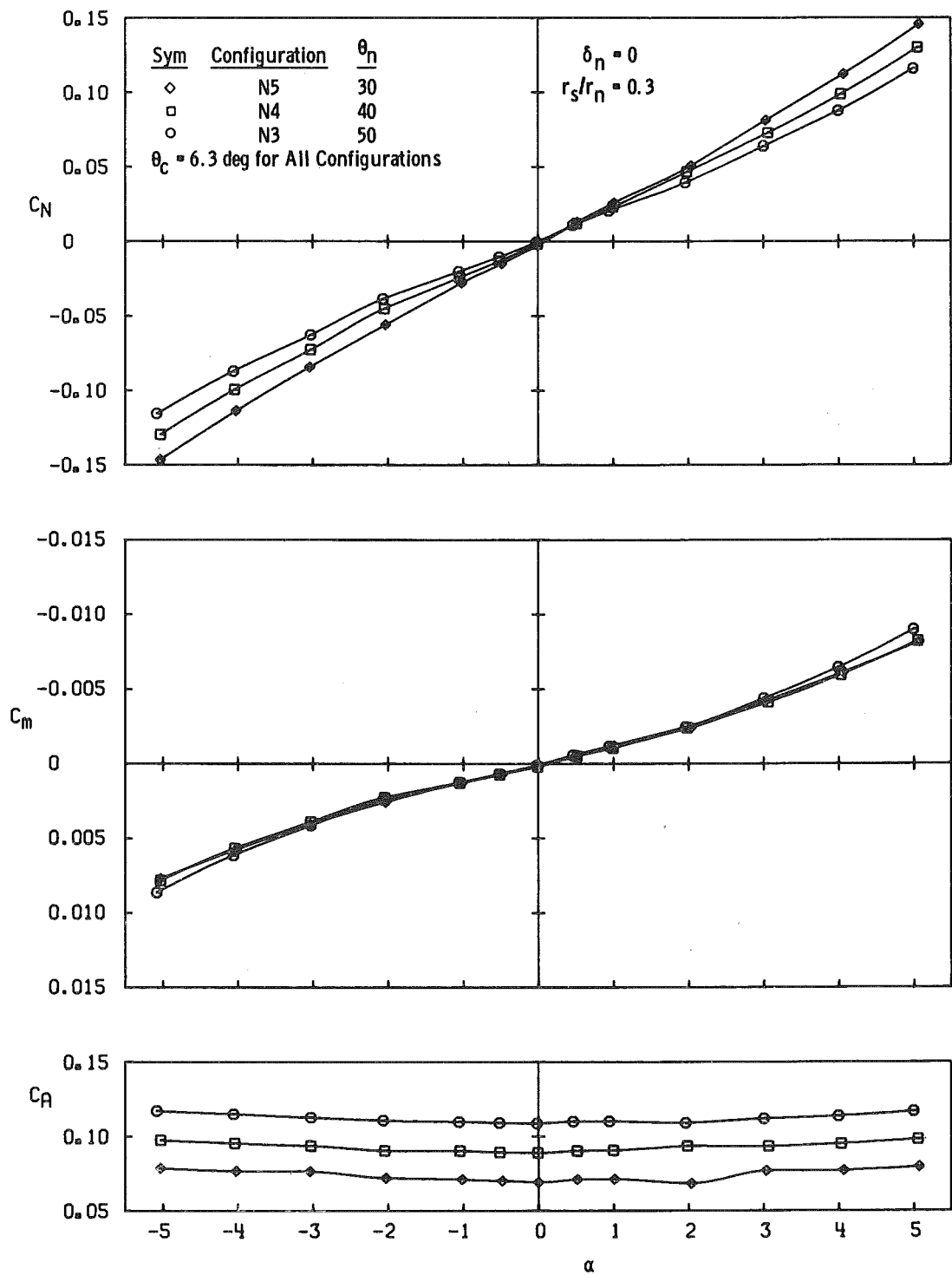


Fig. 12 Effects of Nose Angle (θ_n) on the Normal-Force, Pitching-Moment, and Axial-Force Characteristics of Symmetrical Biconics, $M_\infty = 8$

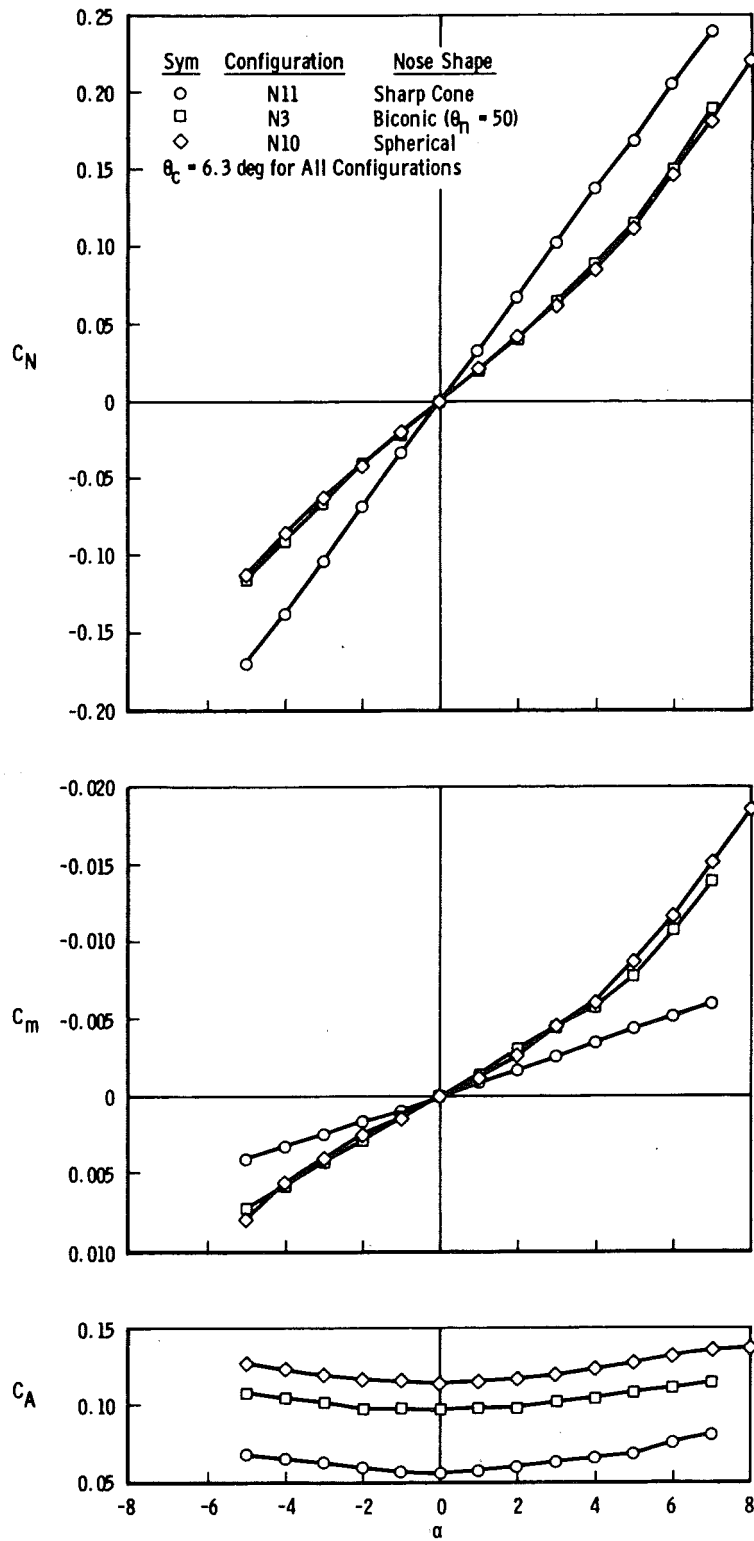


Fig. 13 Comparison of the Normal-Force, Pitching-Moment, and Axial-Force Characteristics of the Symmetrical Configurations Tested at $M_\infty = 16$

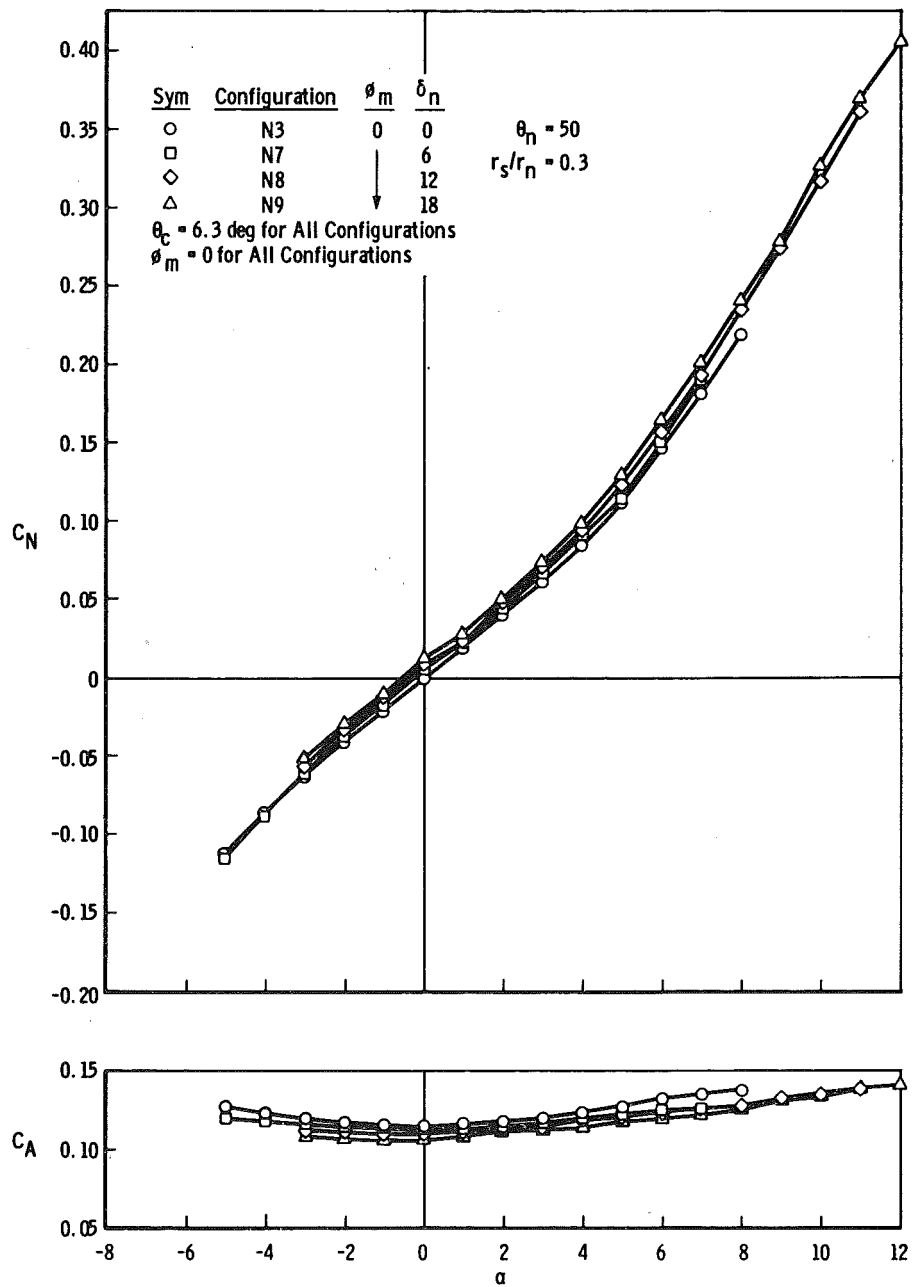


Fig. 14 Effects of Nose Cant Angle (δ_n) on the Normal-Force, Pitching-Moment, and Axial-Force Characteristics of the Asymmetrical Biconics Tested at $M_\infty = 16$

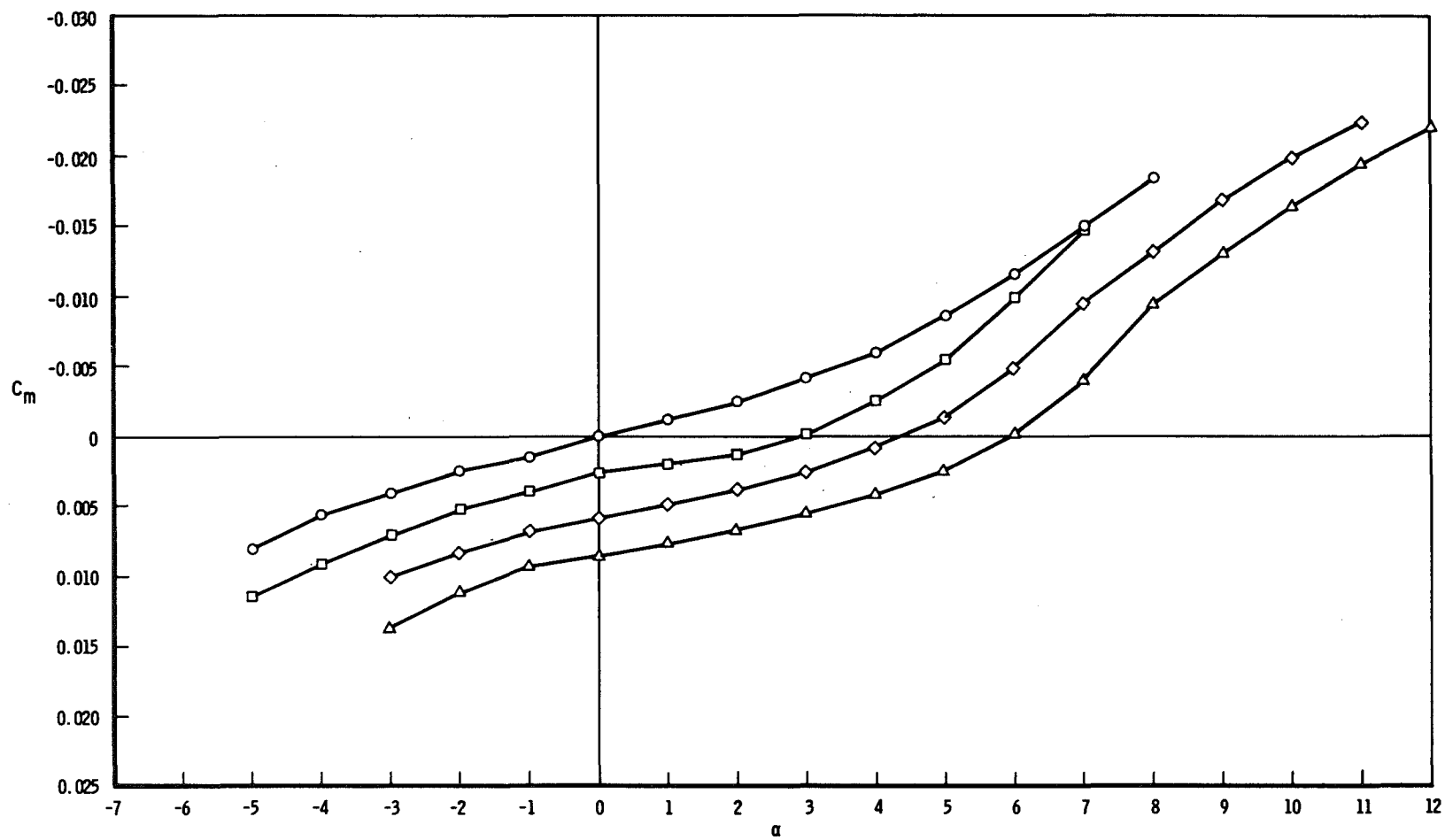
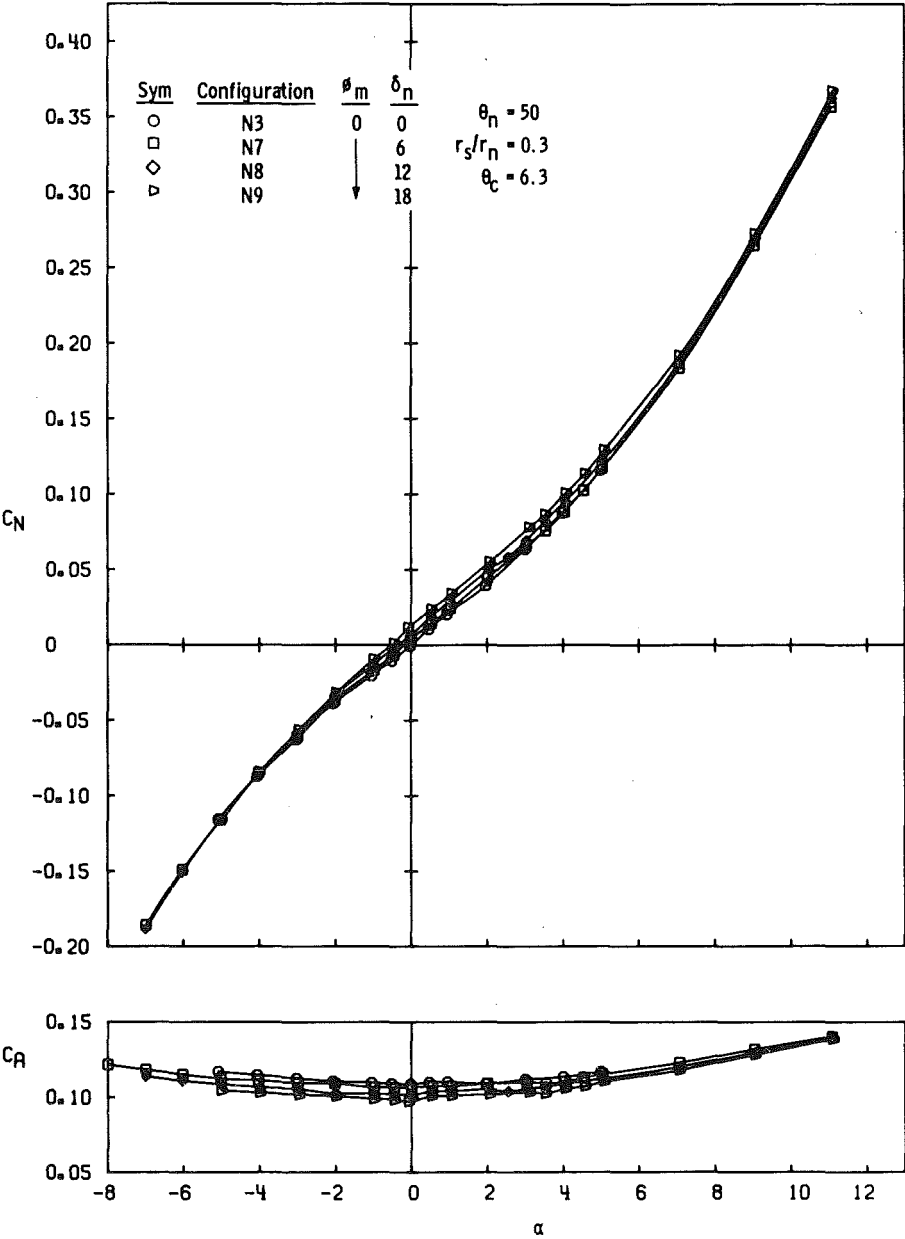
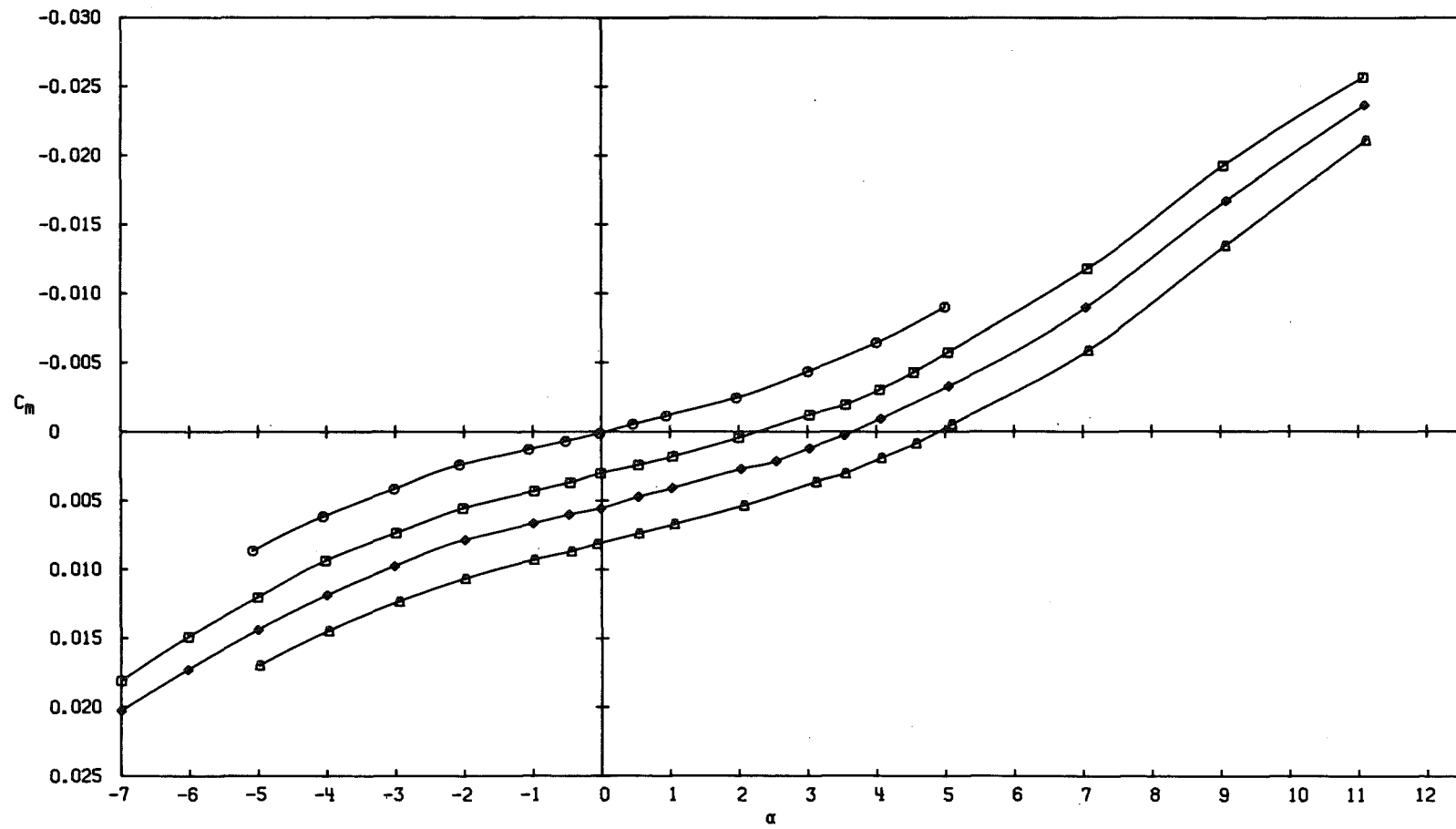


Fig. 14 Concluded

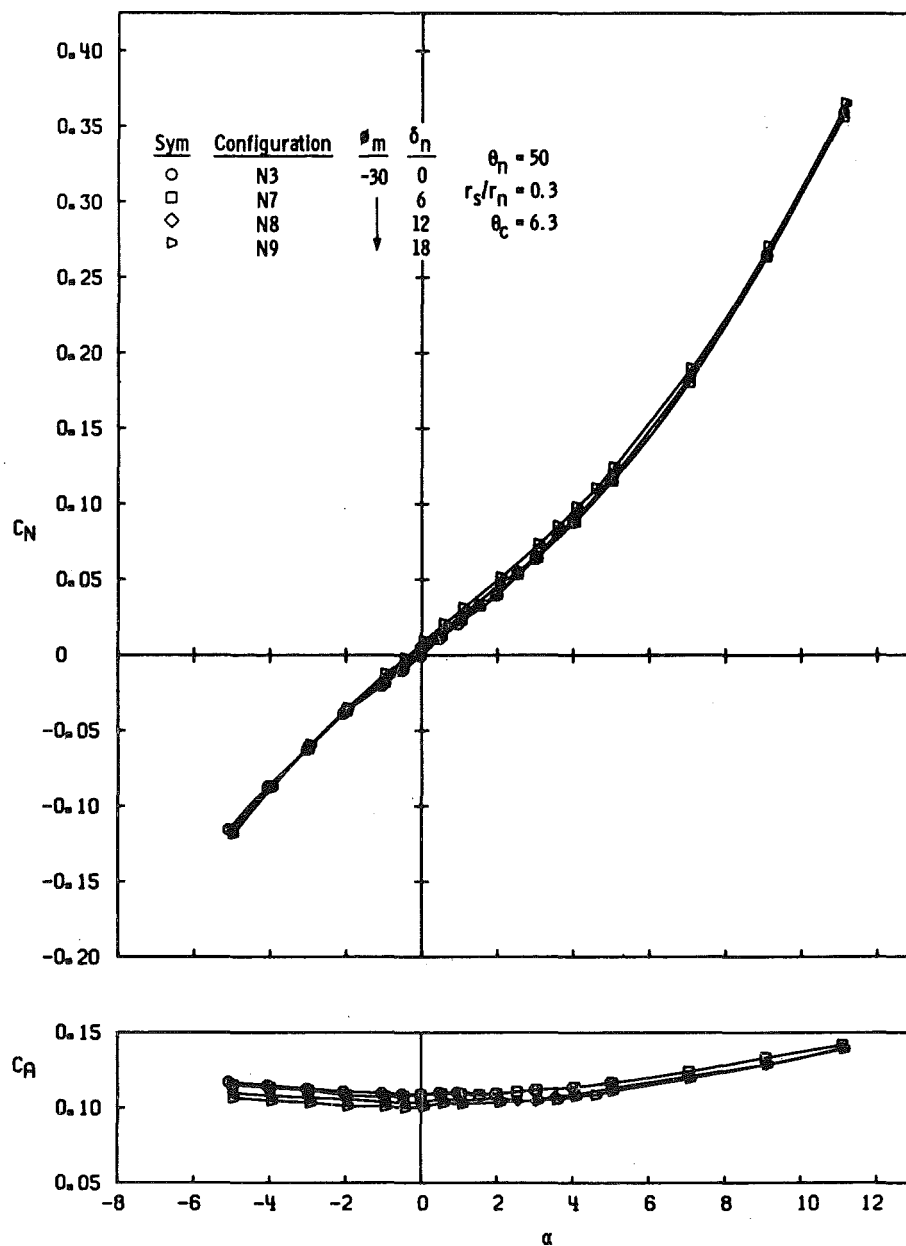


a. $\phi_m = 0$

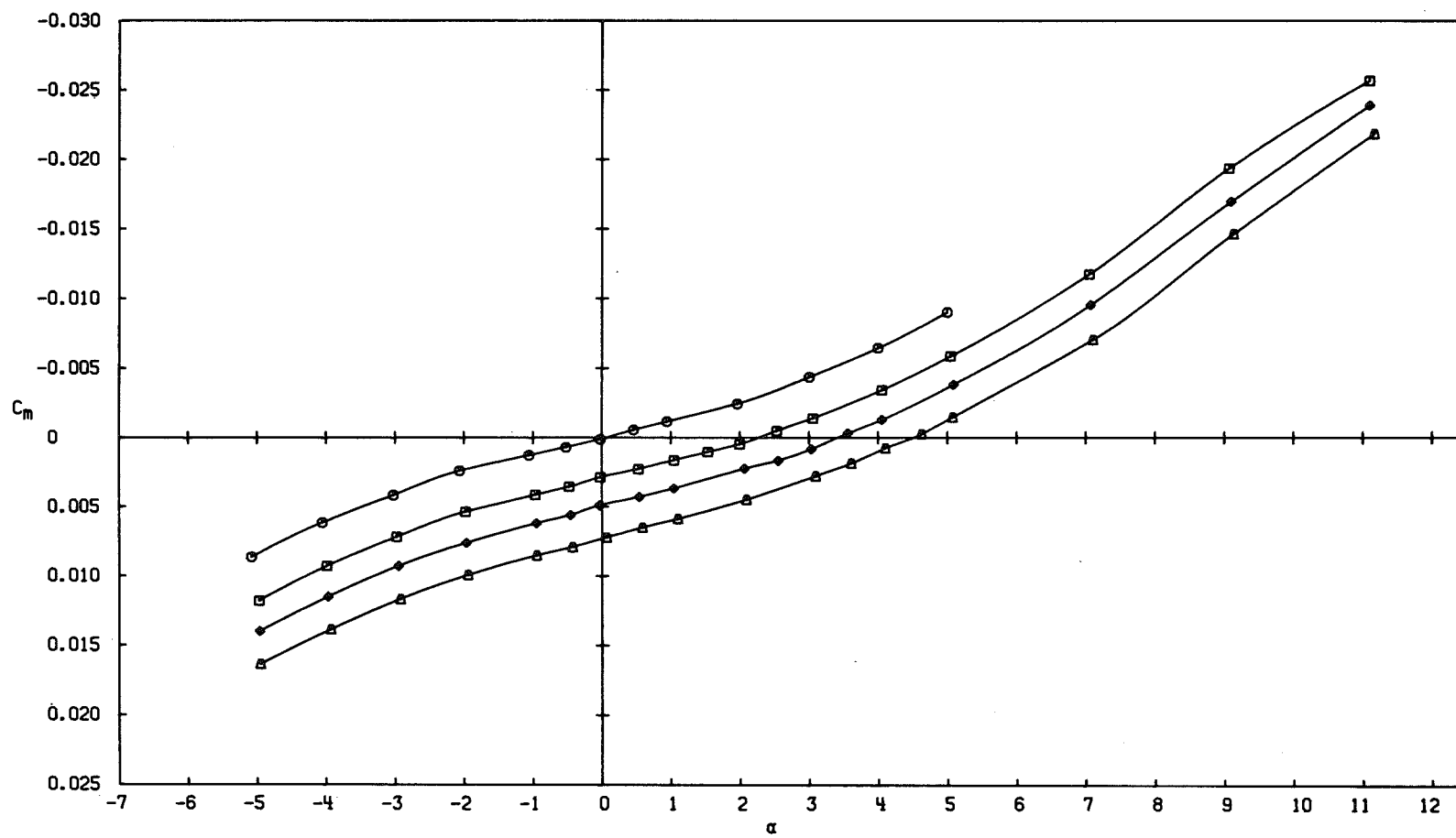
Fig. 15 Effects of Nose Cant Angle (δ_n) on the Normal-Force, Pitching-Moment, and Axial-Force Characteristics of Asymmetrical Biconics, $M_\infty = 8$



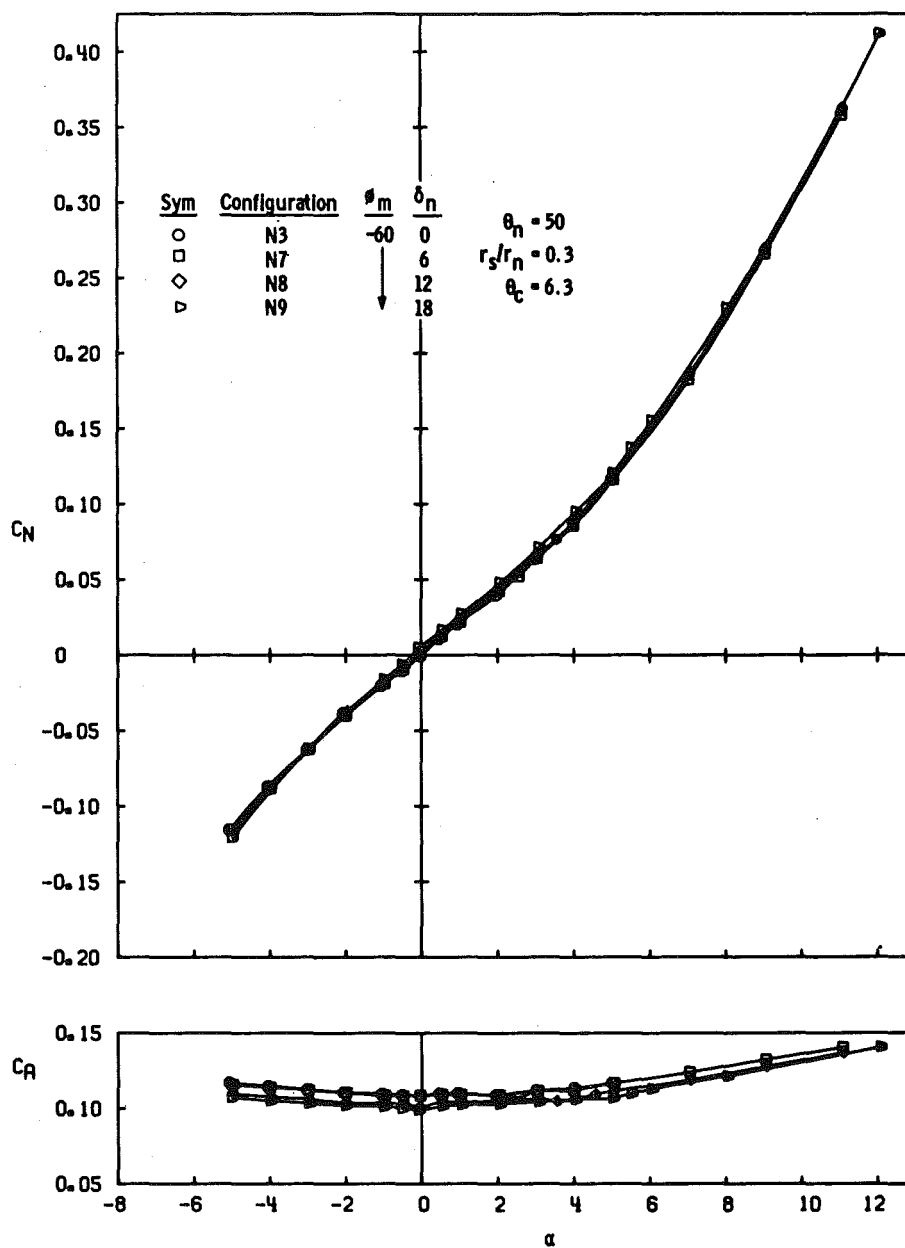
a. Concluded
Fig. 15 Continued



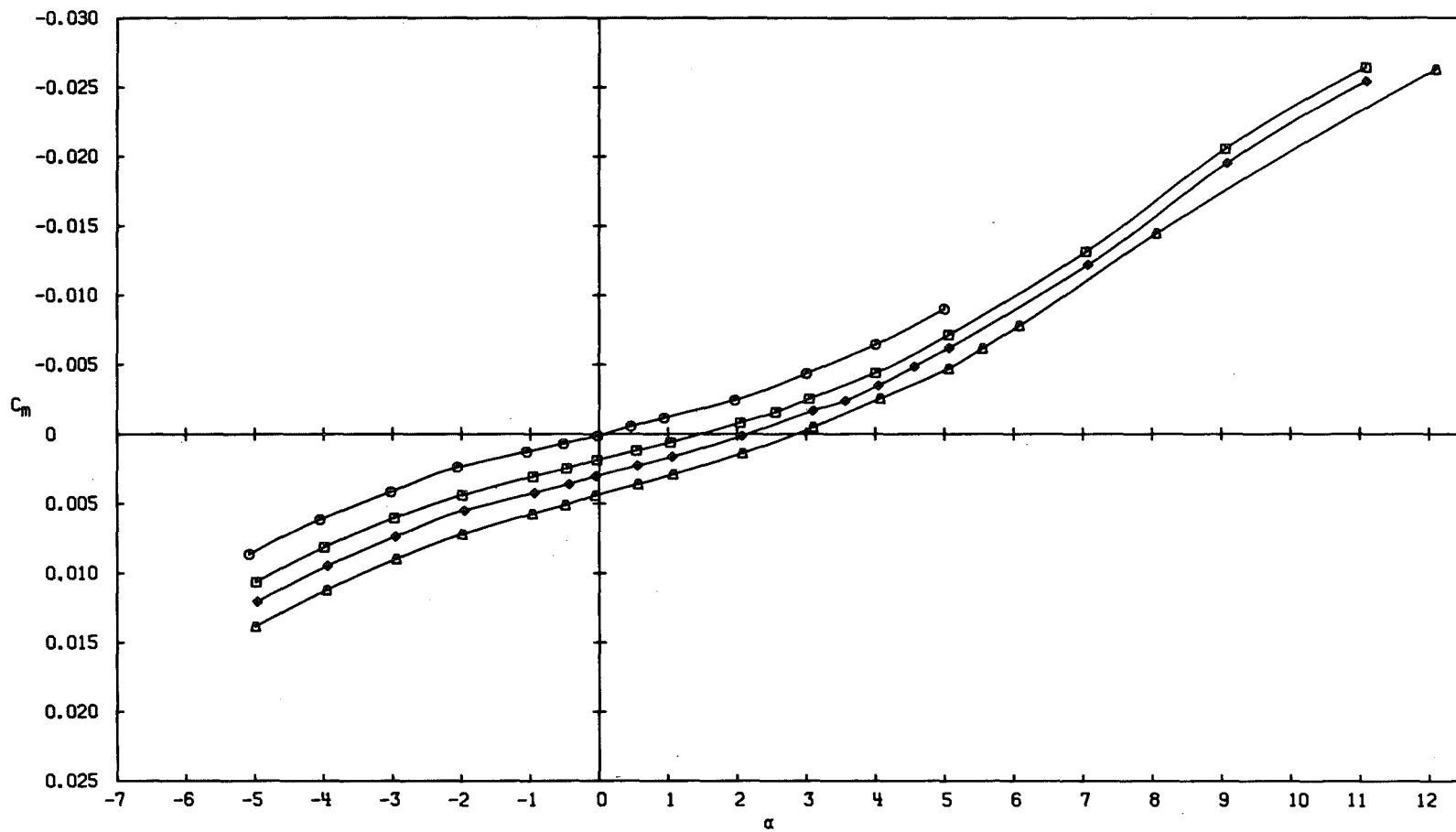
b. $\phi_m = -30$ deg
 Fig. 15 Continued



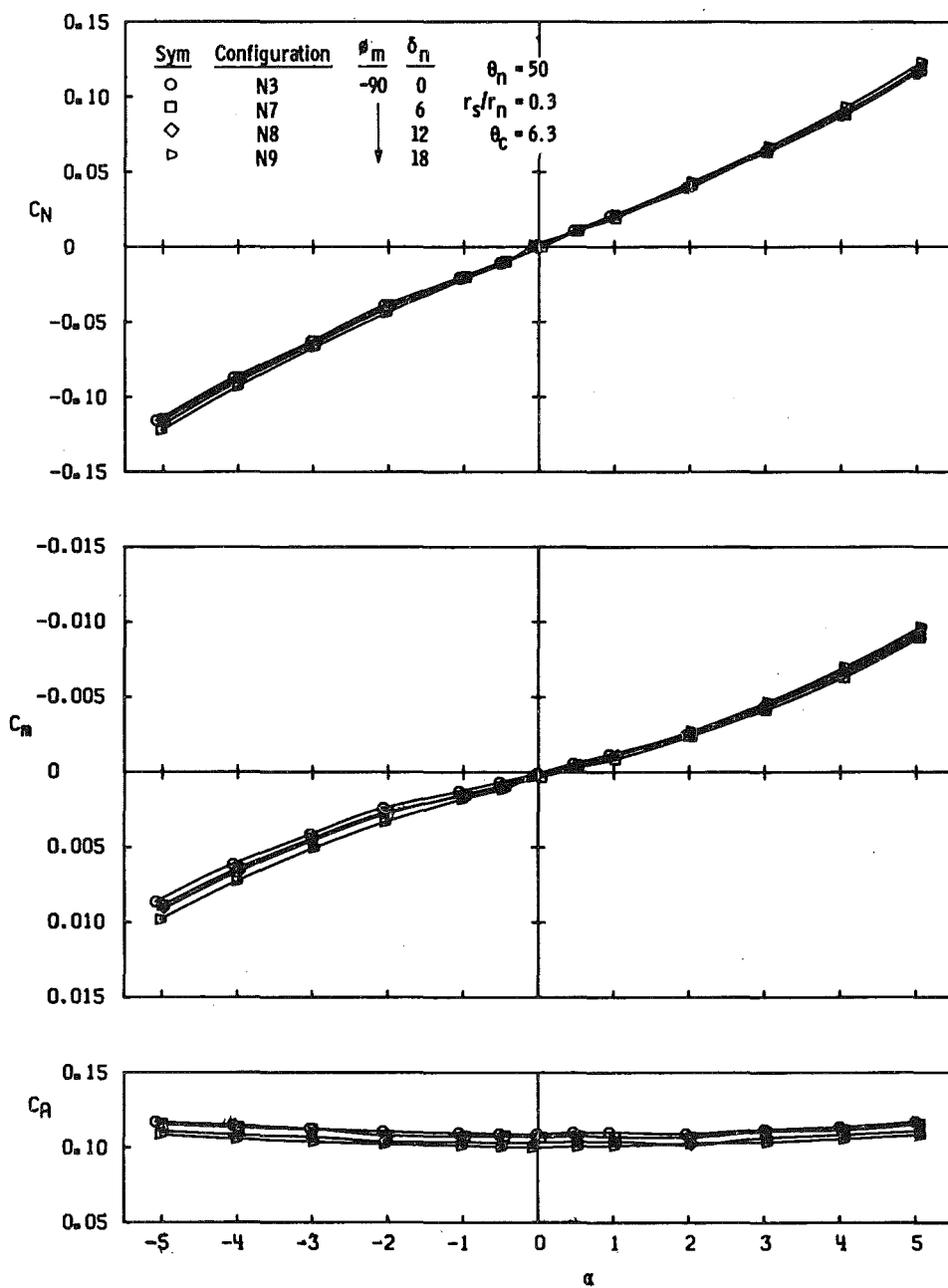
b. Concluded
Fig. 15 Continued



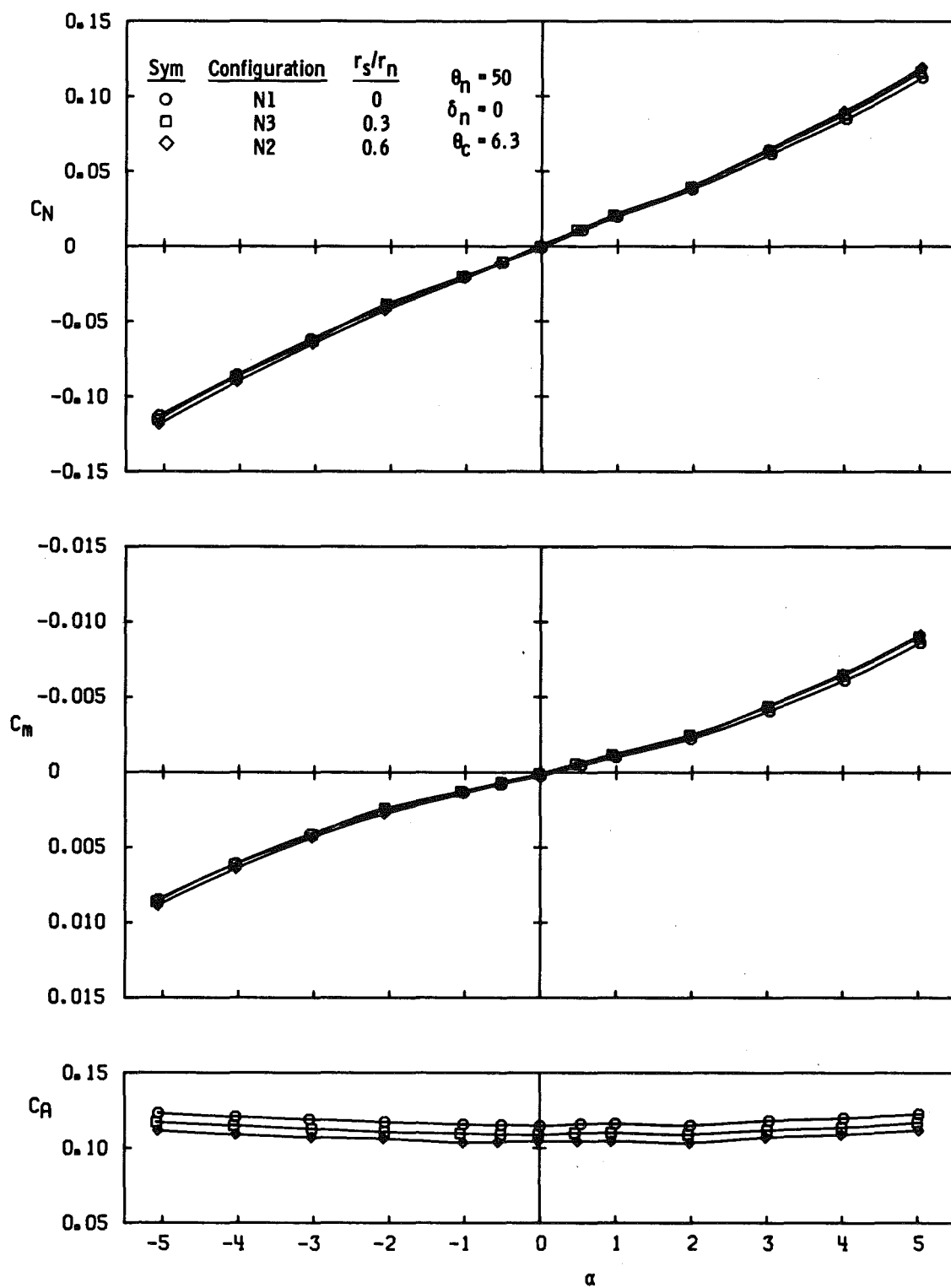
c. $\phi_m = -60$ deg
 Fig. 15 Continued



c. Concluded
Fig. 15 Continued

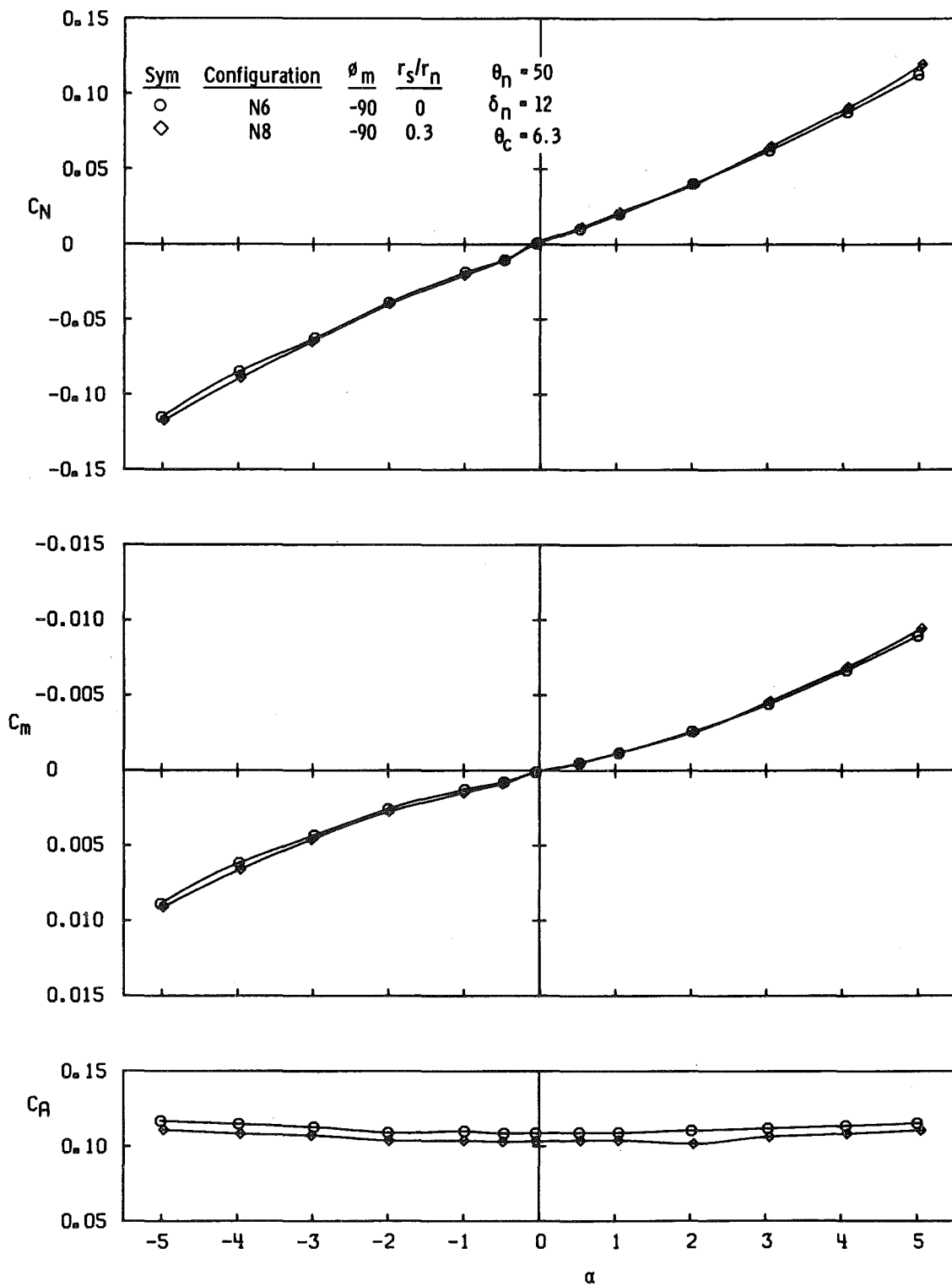


d. $\phi_m = -90$ deg
Fig. 15 Concluded

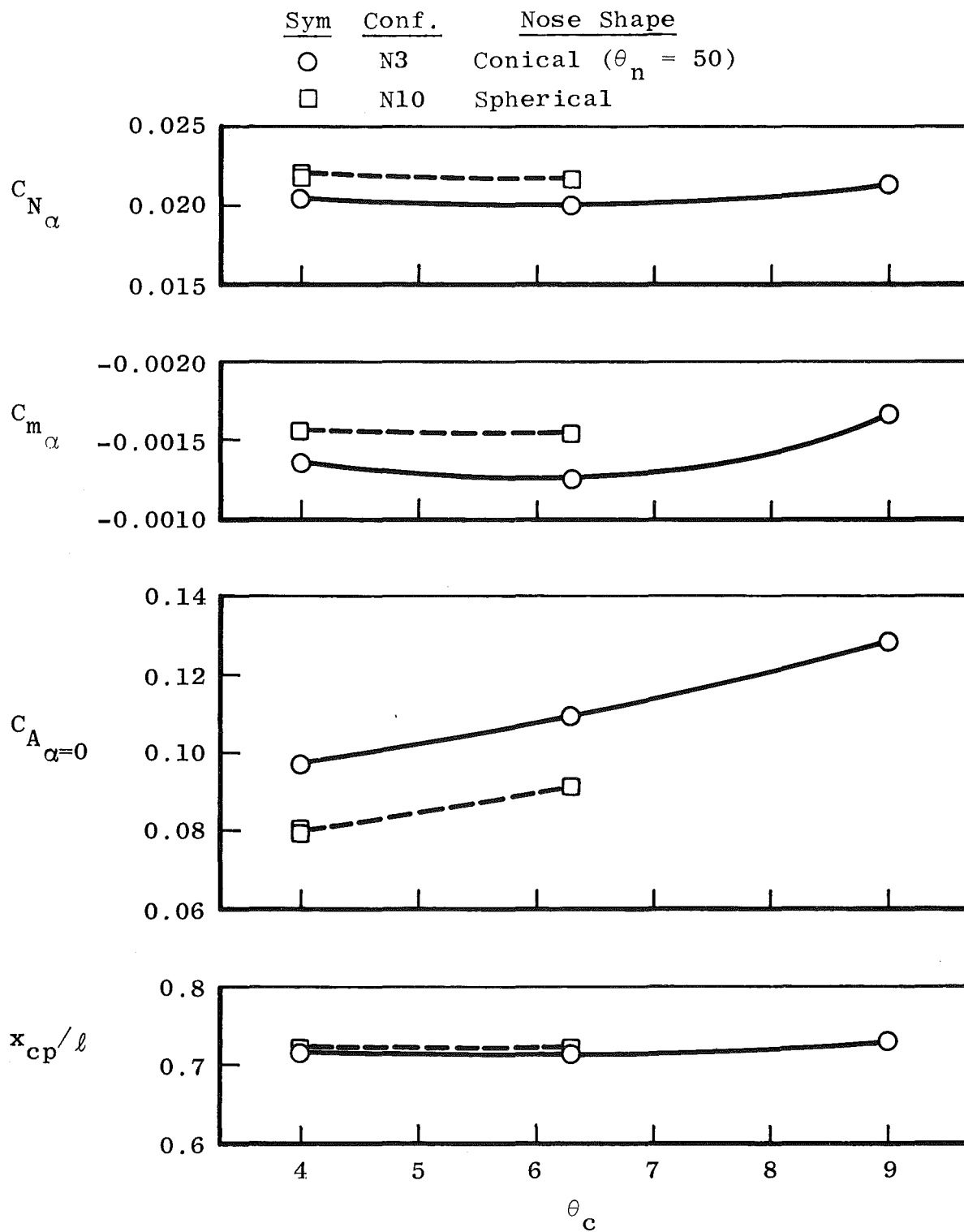


a. Symmetrical Biconics

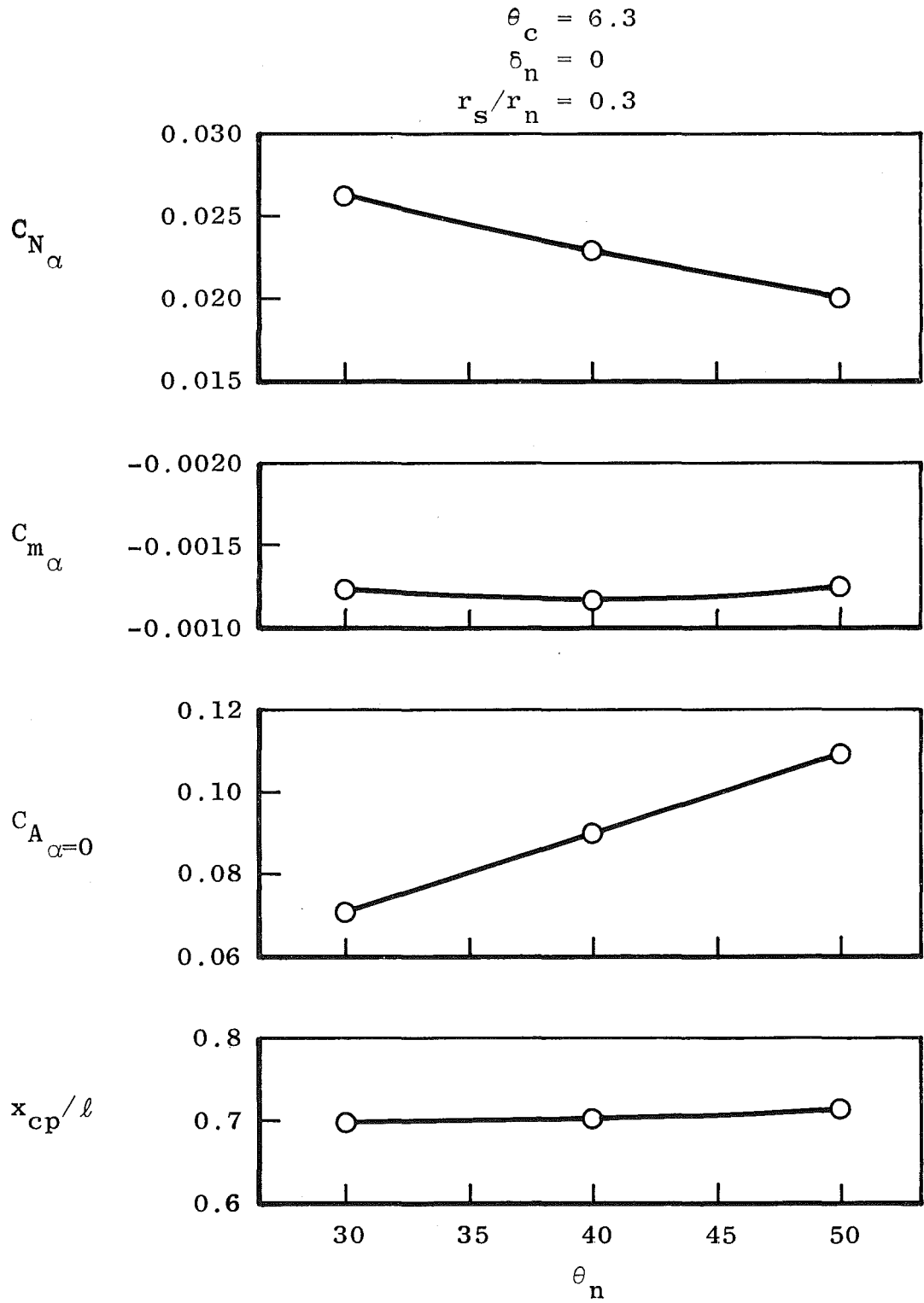
Fig. 16 Effects of Shoulder Radius (r_s) on the Normal-Force, Pitching-Moment, and Axial-Force Characteristics, $M_\infty = 8$



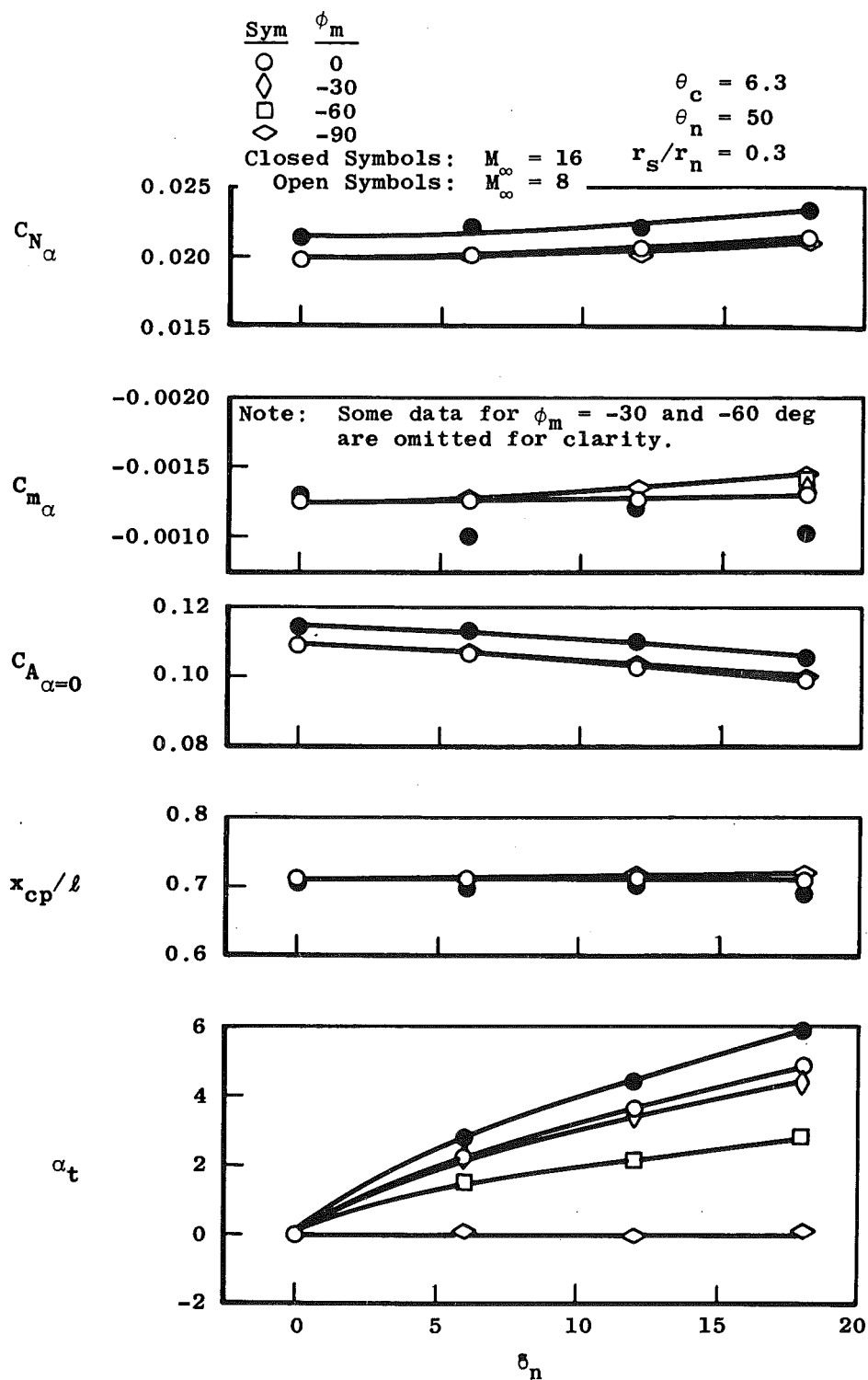
b. Asymmetrical Biconics, $\phi_m = -90$ deg
Fig. 16 Concluded



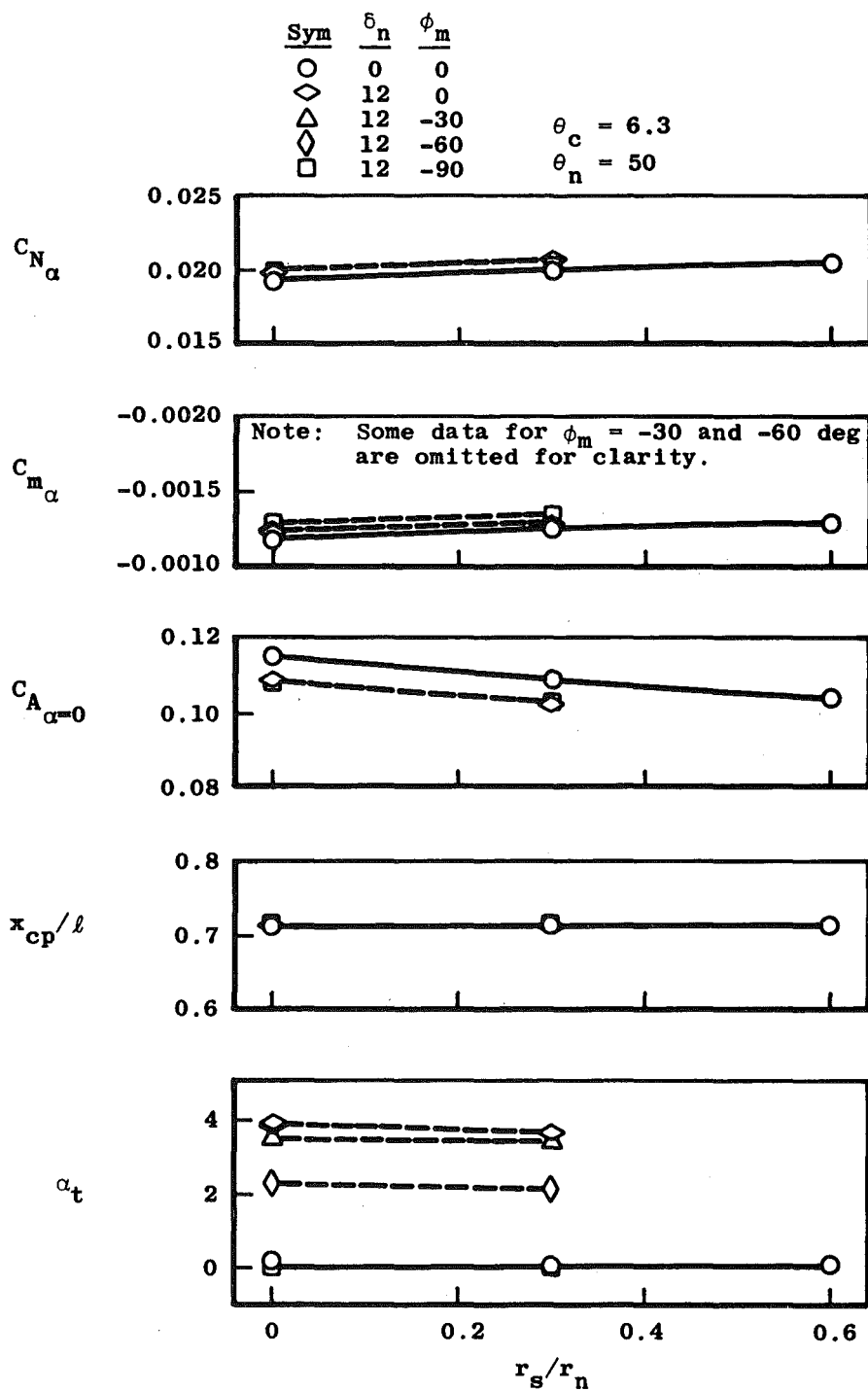
a. Effects of Cone Angle, θ_c
 Fig. 17 Variations of C_{N_α} , C_{m_α} , $C_{A_{\alpha=0}}$, and x_{cp}/ℓ
 for Symmetrical Shapes, $M_\infty = 8$



b. Effects of Nose Angle, θ_n
Fig. 17 Concluded



a. Effects of Cant Angle, δ_n
 Fig. 18 Variations of C_{N_α} , C_{m_α} , $C_{A_{\alpha=0}}$, x_{cp}/l and α_t for Asymmetrical Biconics



b. Effects of Shoulder Radius, r_s
 Fig. 18 Concluded

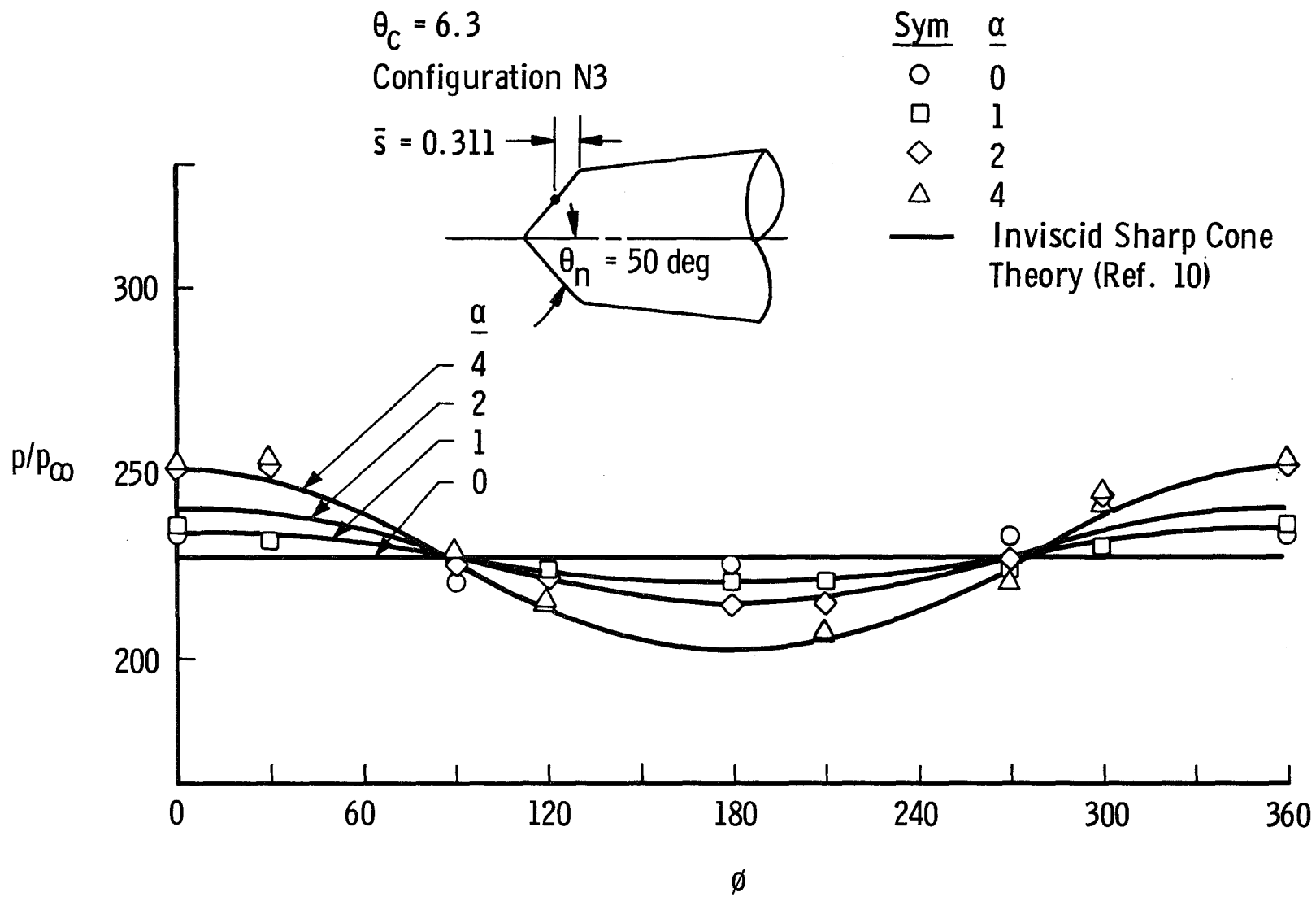


Fig. 19 Nose Cone Pressure Data at $M_\infty = 16$, 50-deg Biconic

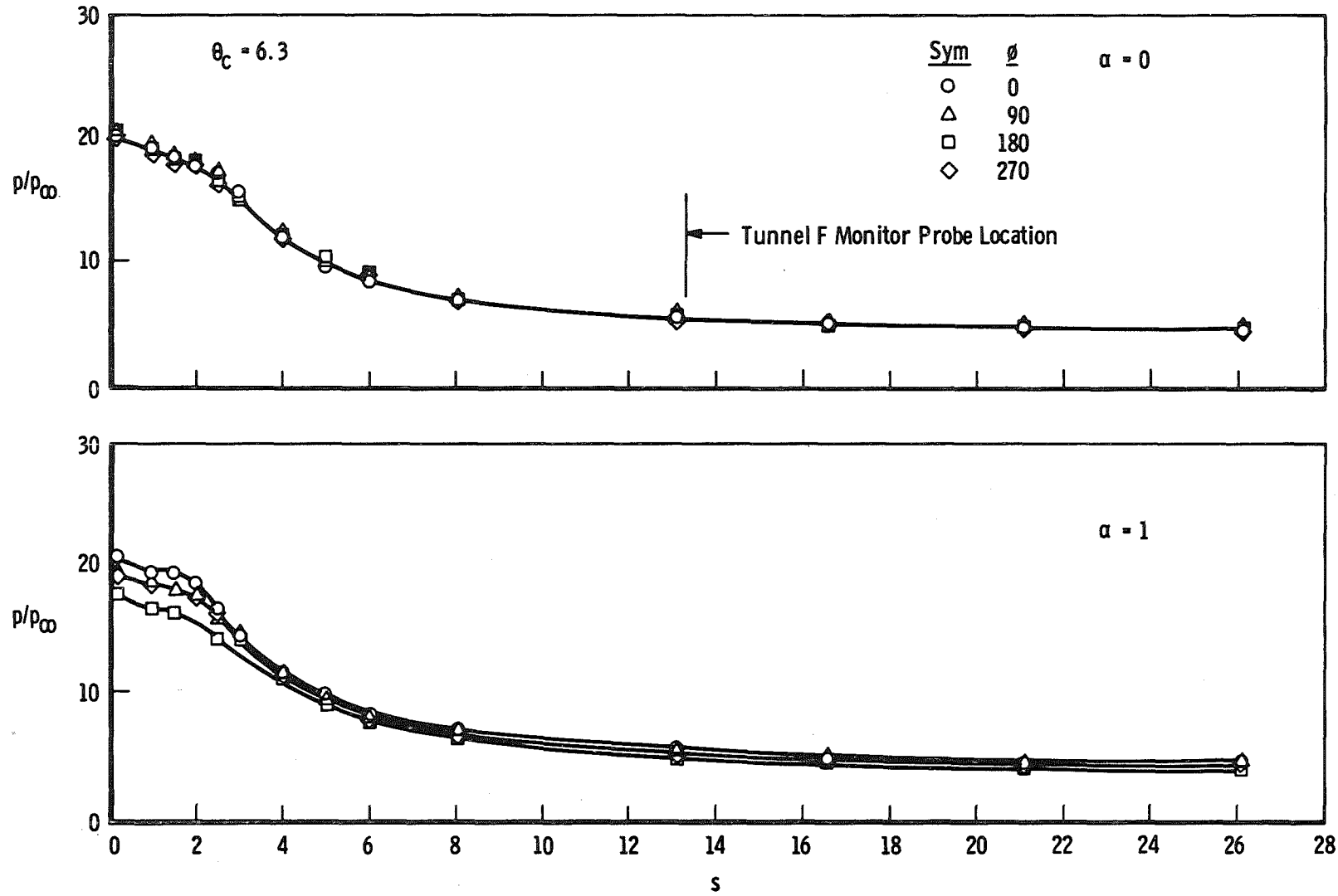


Fig. 20 Aft-Cone Pressure Distributions at $M_\infty = 16$, 50-deg Biconic

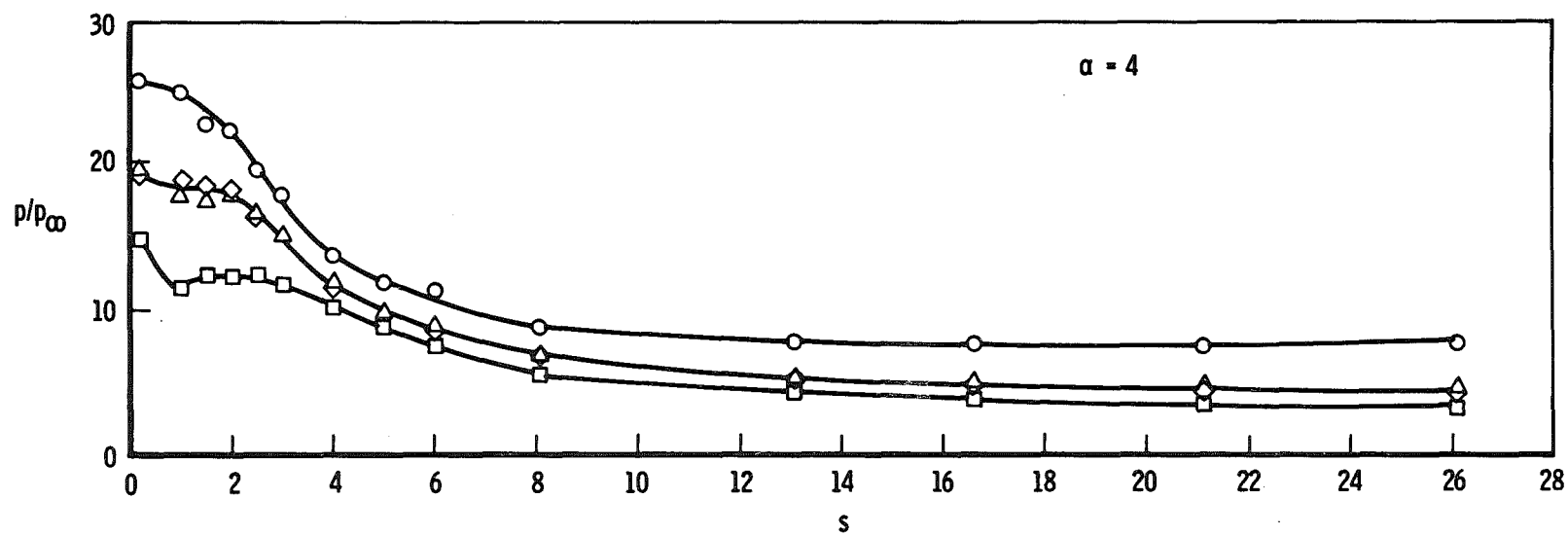
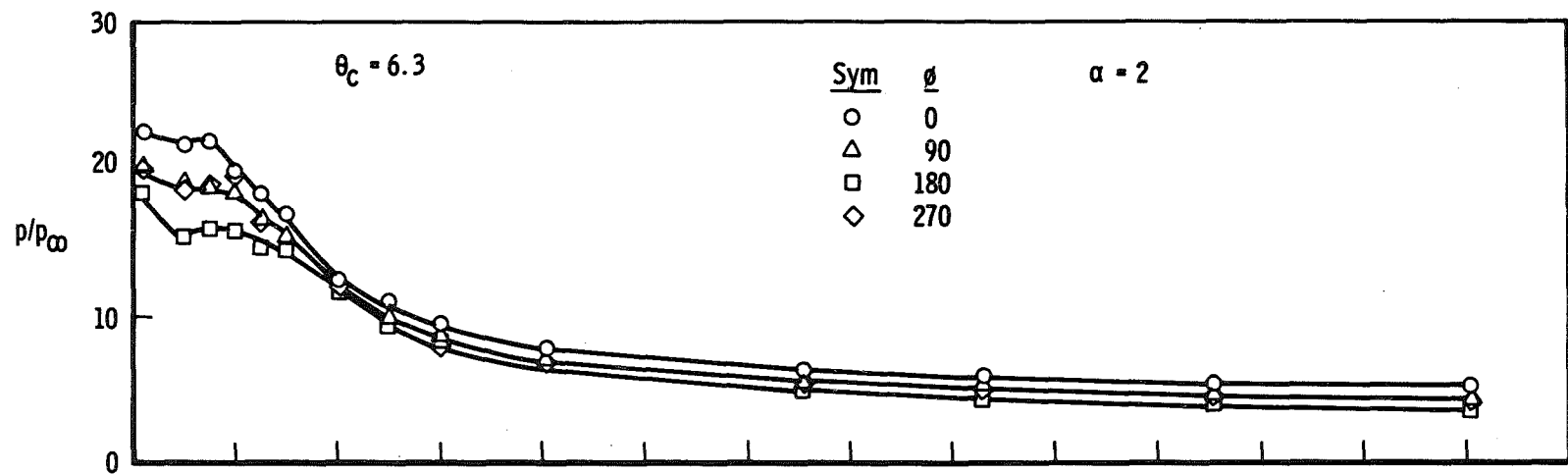
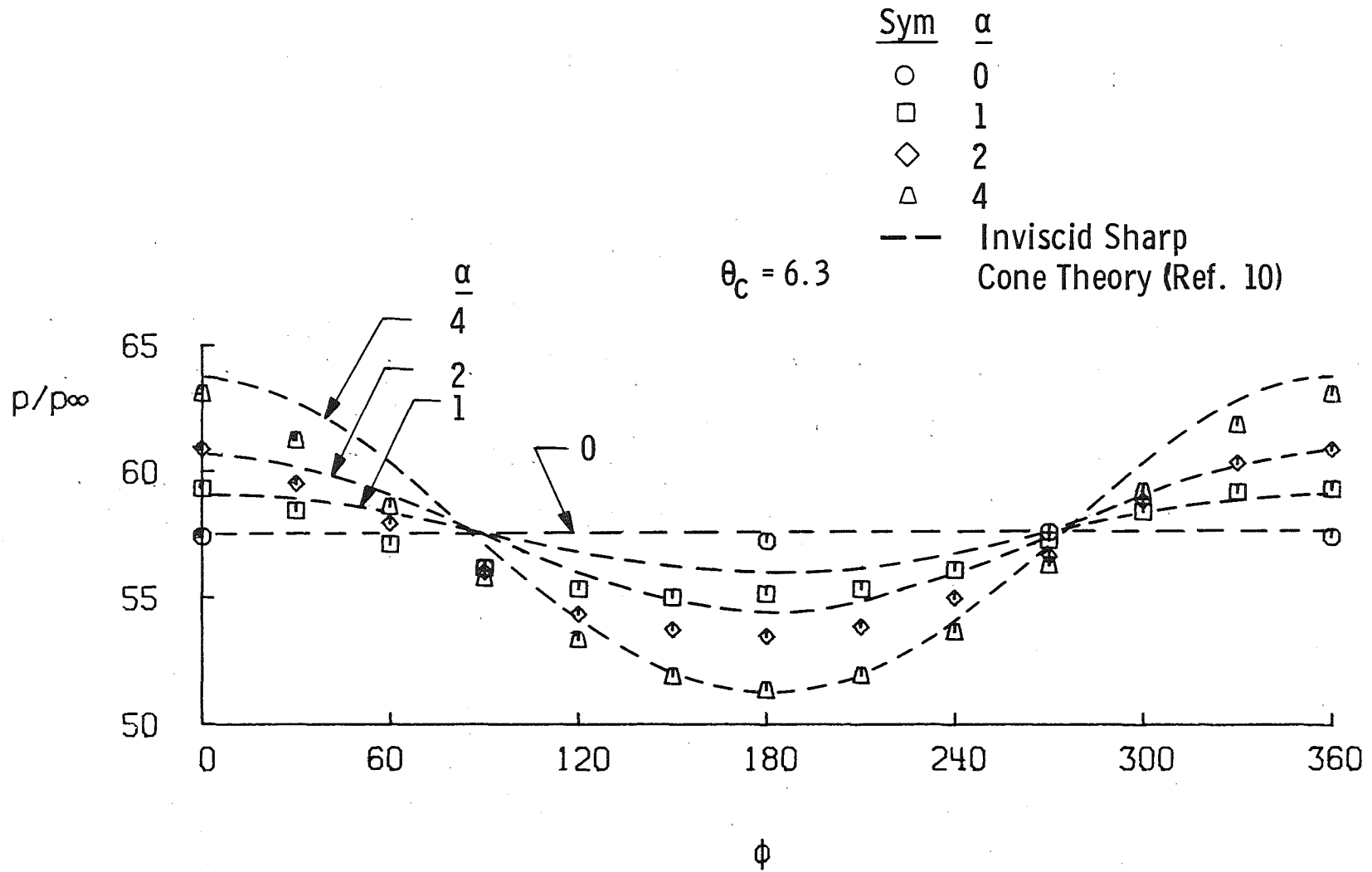
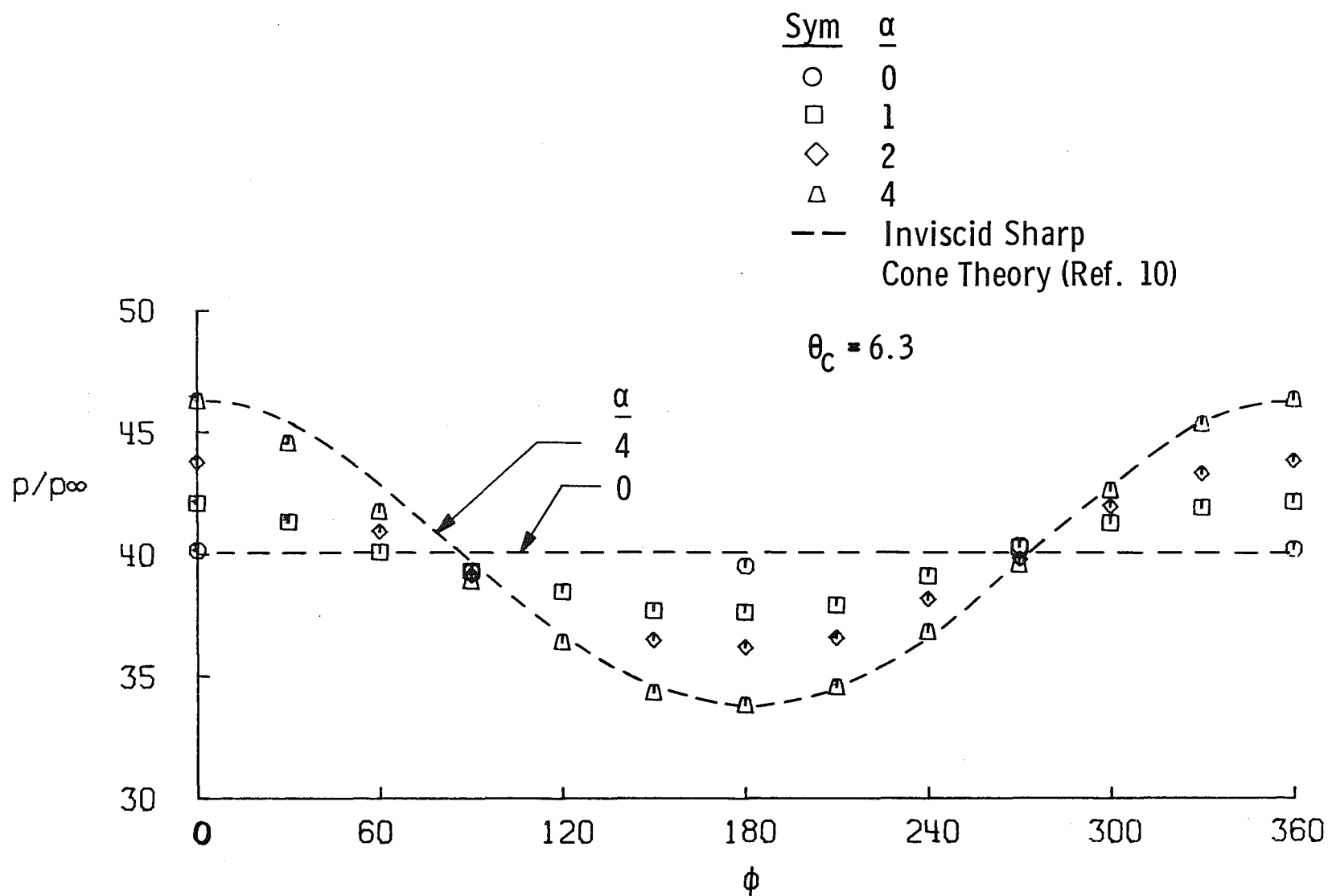


Fig. 20 Concluded

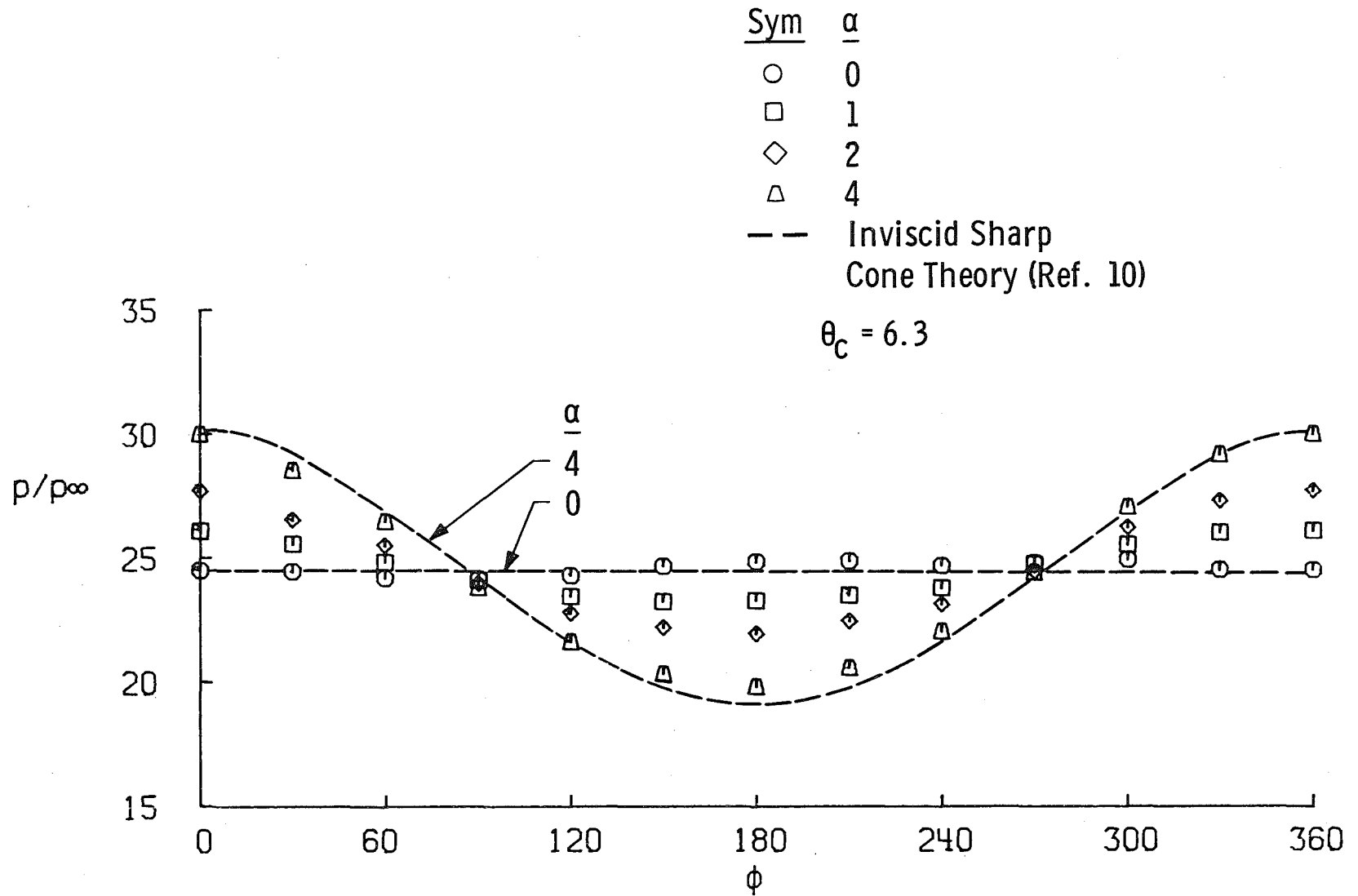


a. 50-deg Biconic

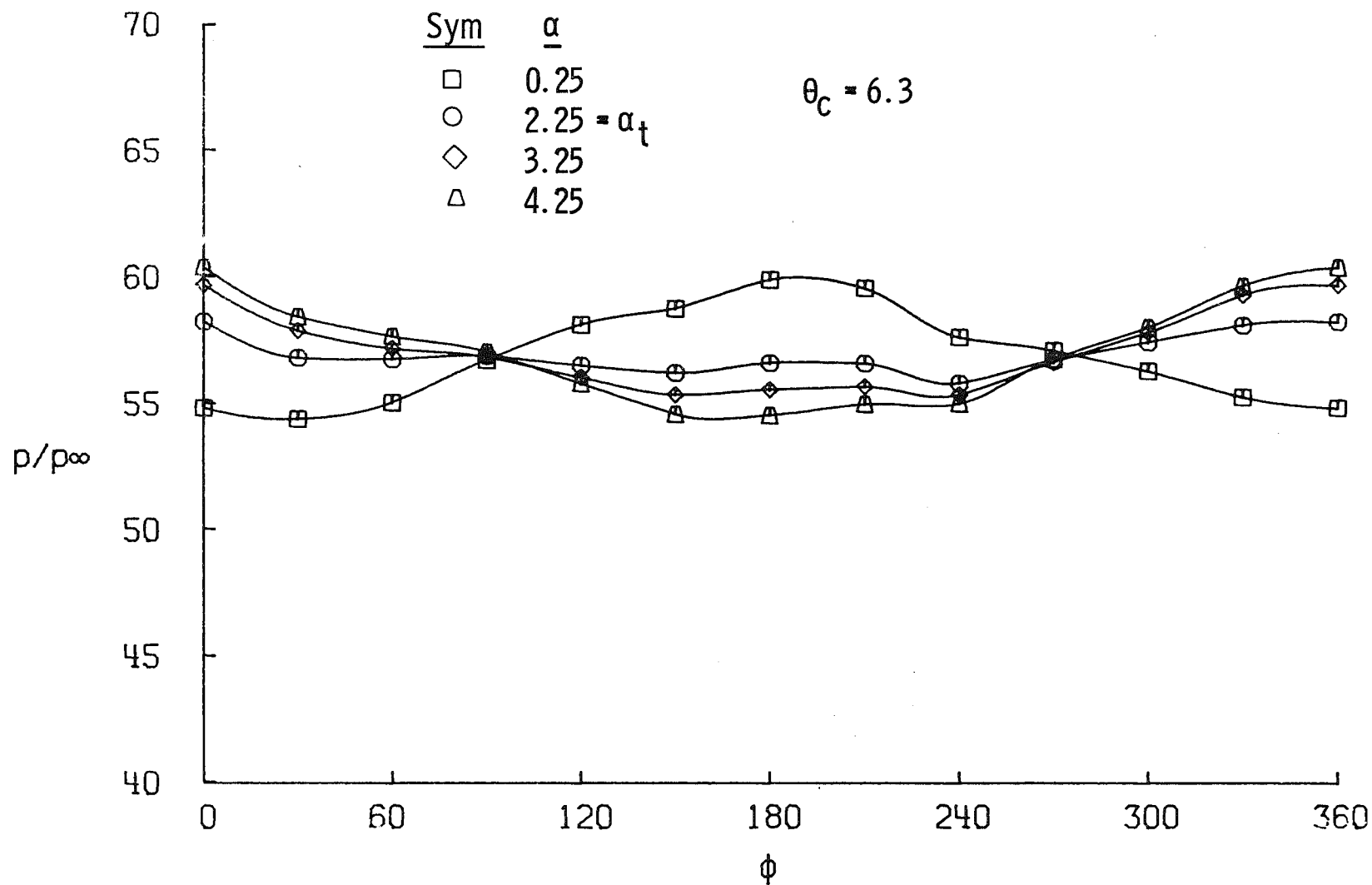
Fig. 21 Nose Cone Circumferential Pressure Distributions for Symmetrical Biconics, $M_\infty = 8$



b. 40-deg Biconic
Fig. 21 Continued

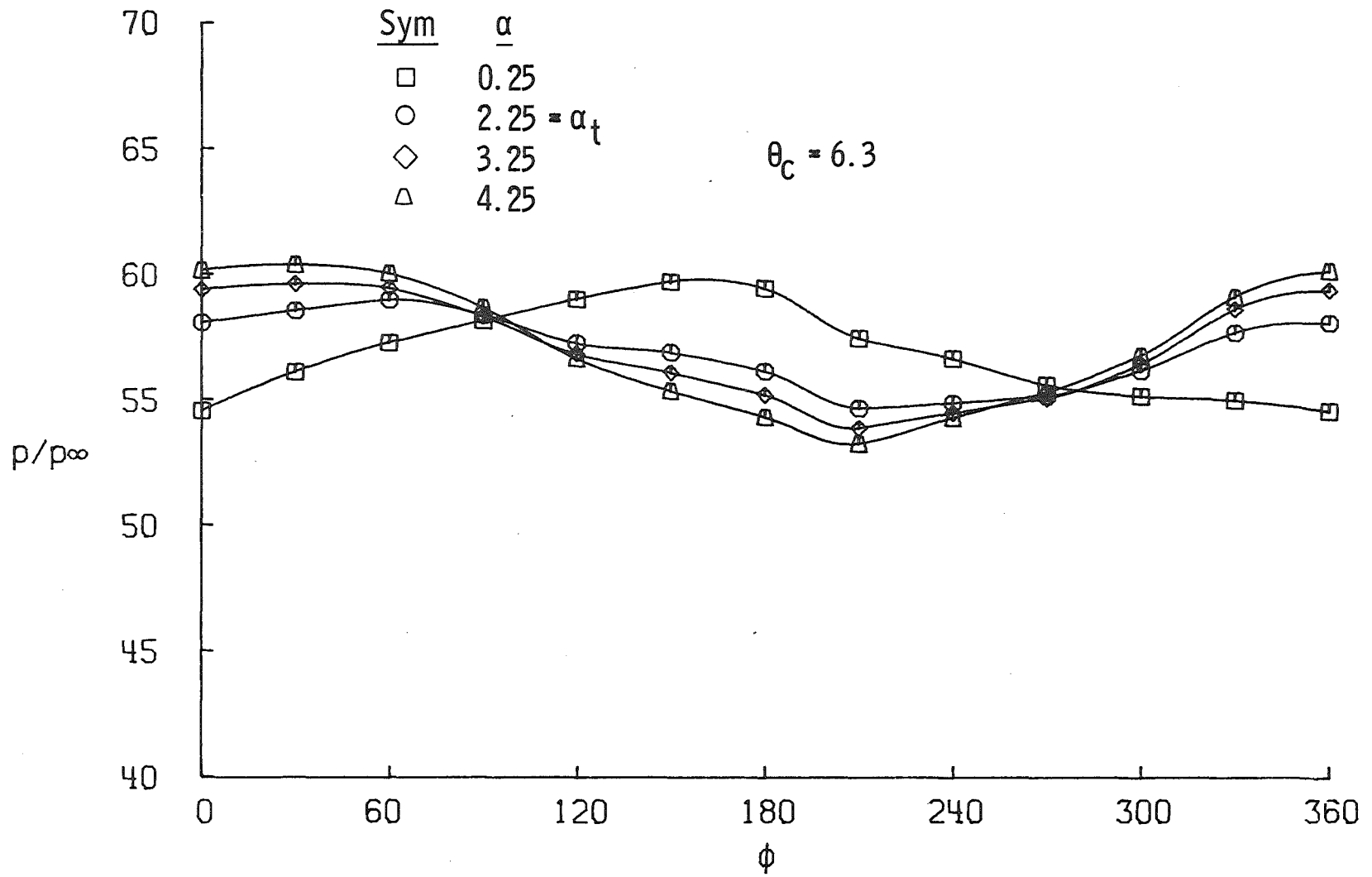


c. 30-deg Biconic
Fig. 21 Concluded

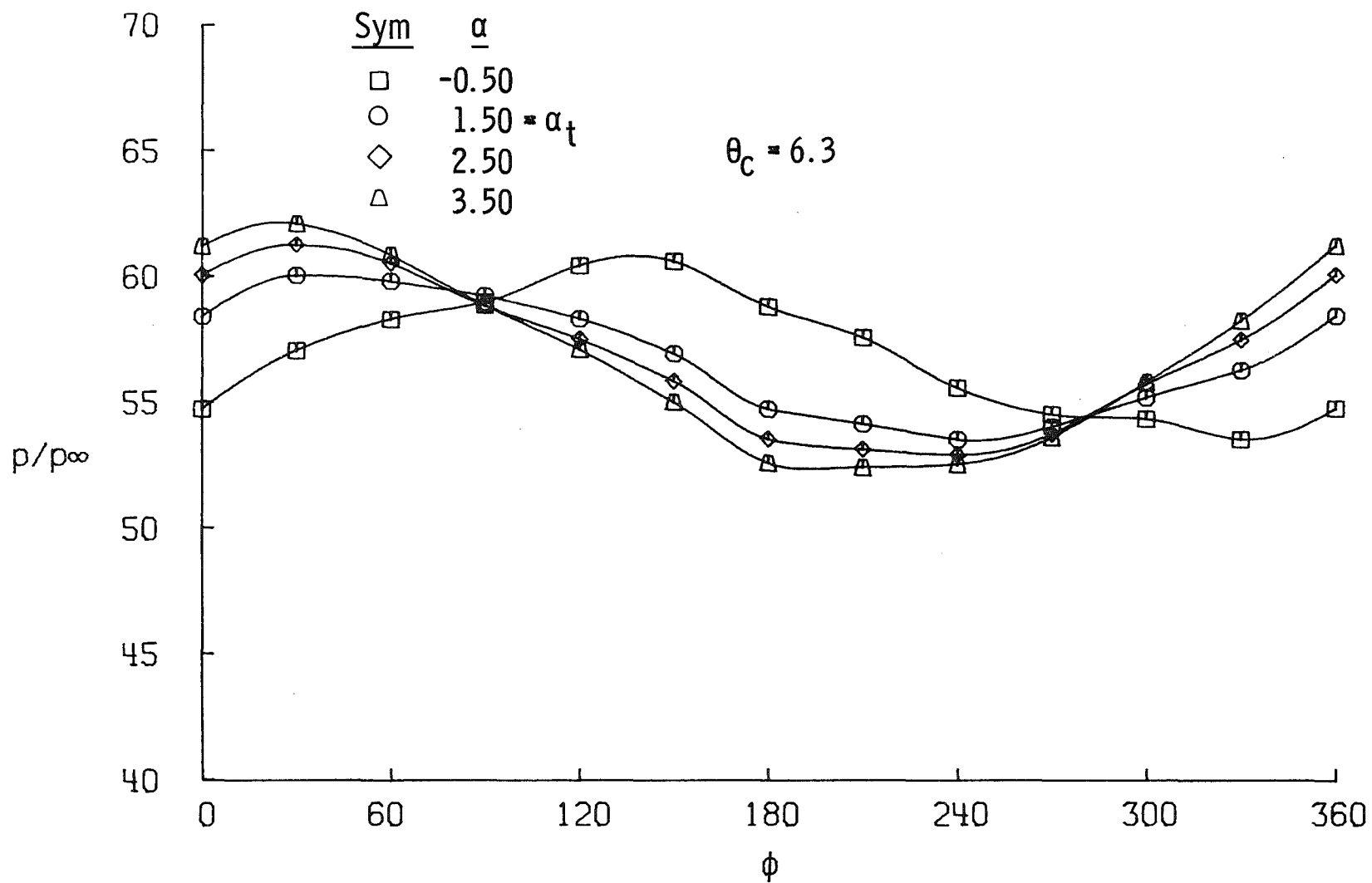


a. Configuration N7 ($\delta_n = 6$), $\phi_m = 0$

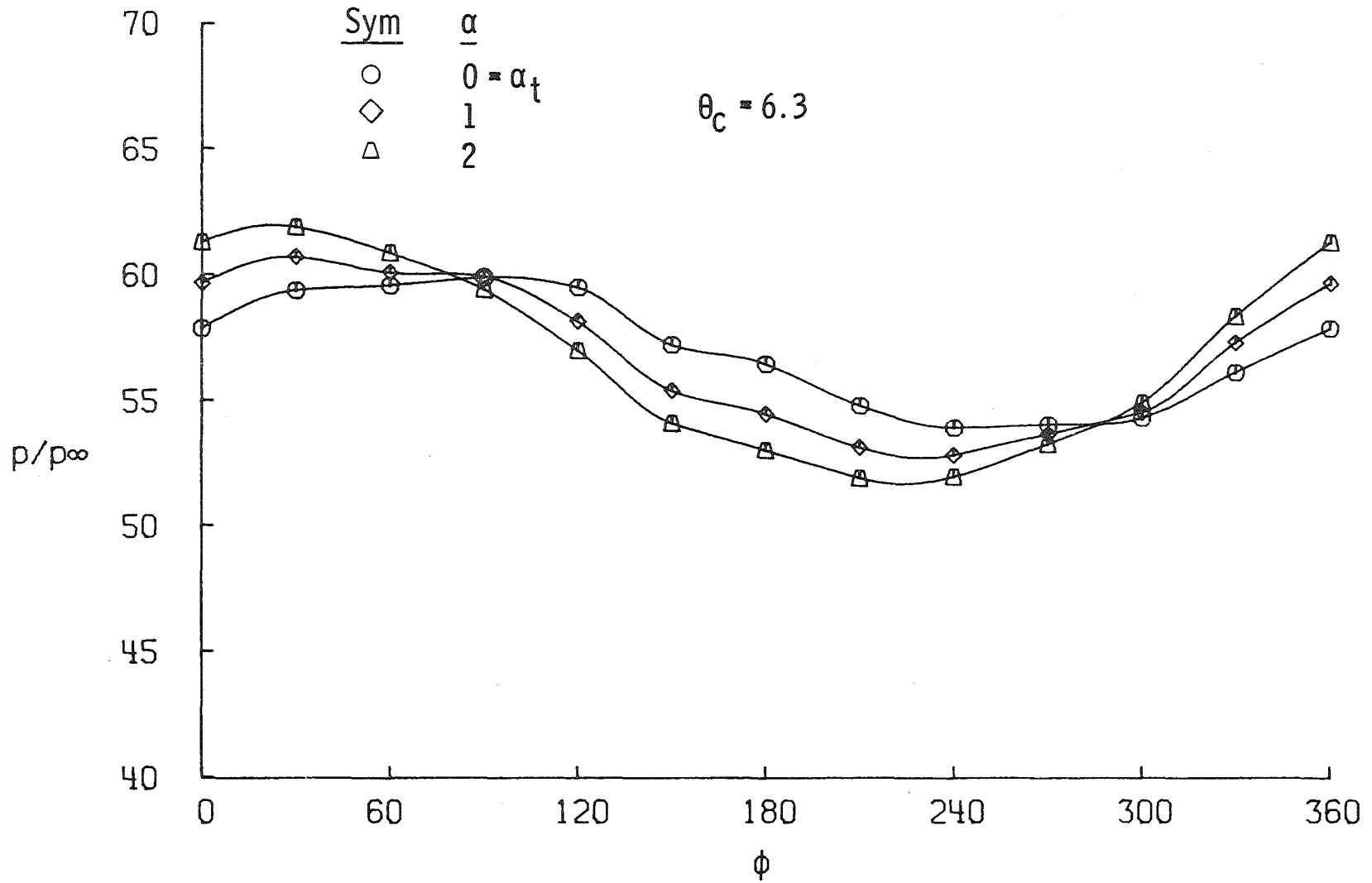
Fig. 22 Nose Cone Circumferential Pressure Distributions for Asymmetrical Biconics, $M_\infty = 8$



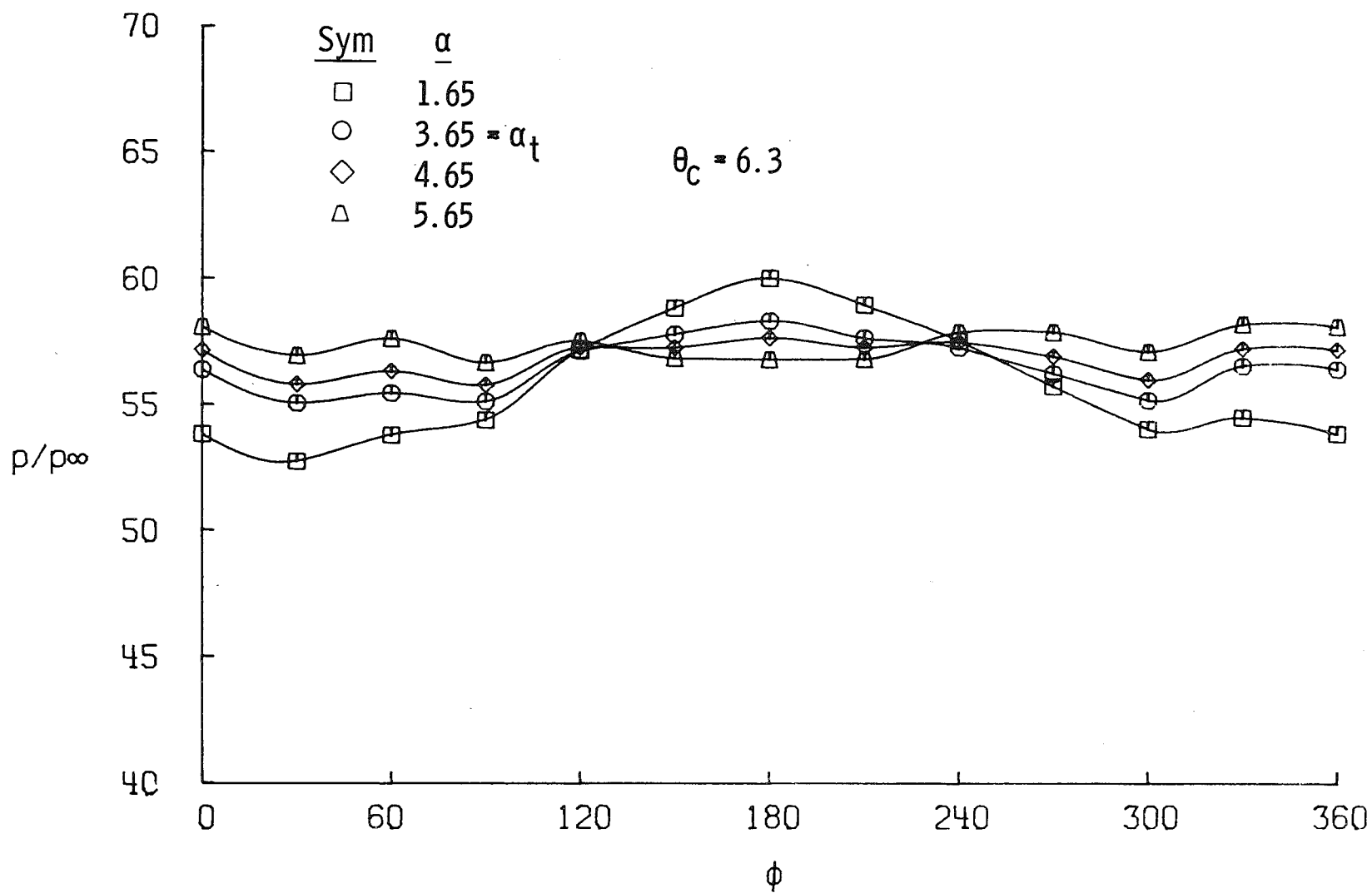
b. Configuration N7 ($\delta_n = 6$), $\phi_m = -30$
Fig. 22 Continued



c. Configuration N7 ($\delta_n = 6$), $\phi_m = -60$
Fig. 22 Continued



d. Configuration N7 ($\delta_n = 6$), $\phi_m = -90$
Fig. 22 Continued



e. Configuration N8 ($\delta_n = 12$), $\phi_m = 0$
Fig. 22 Continued

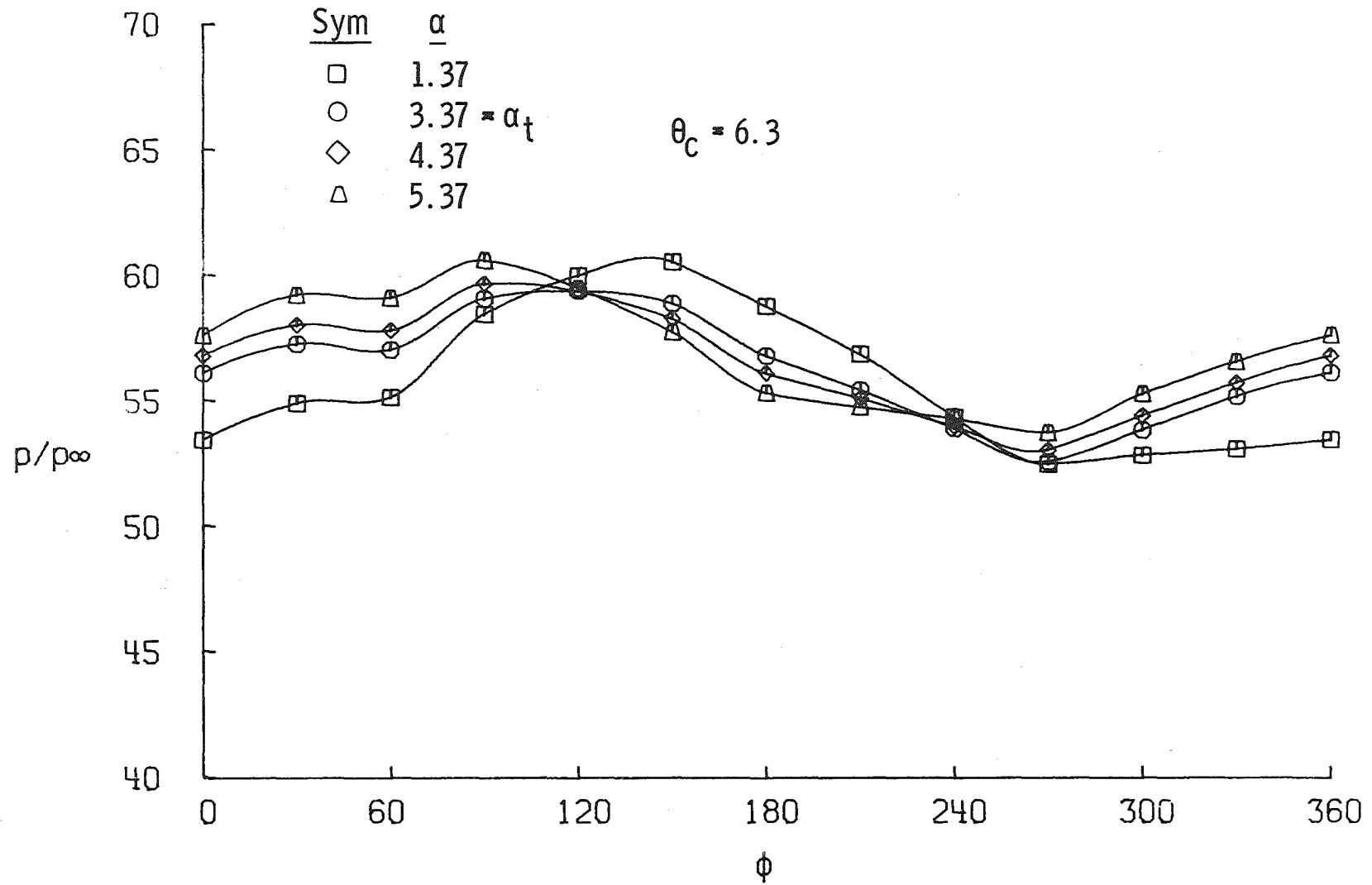
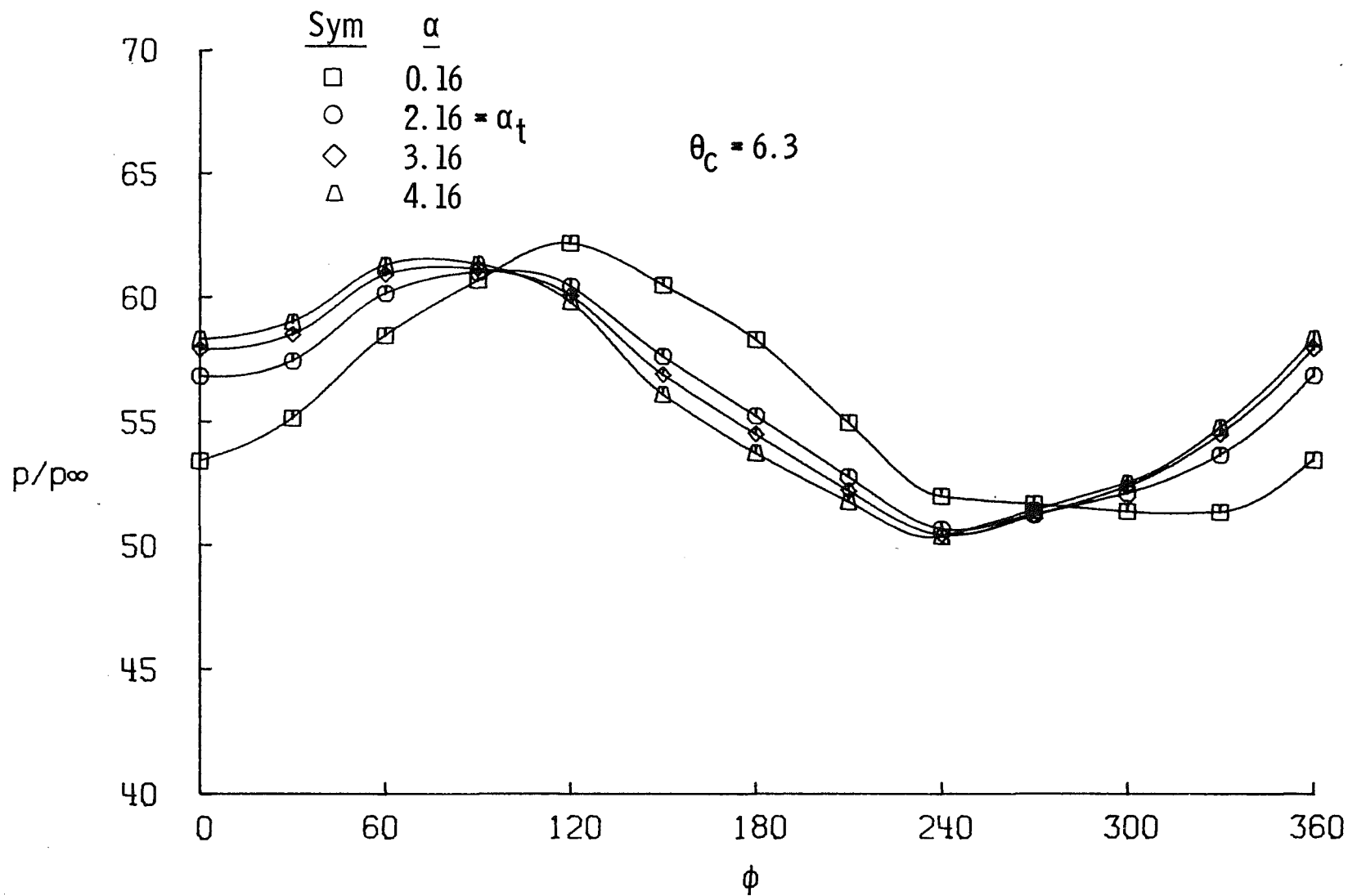
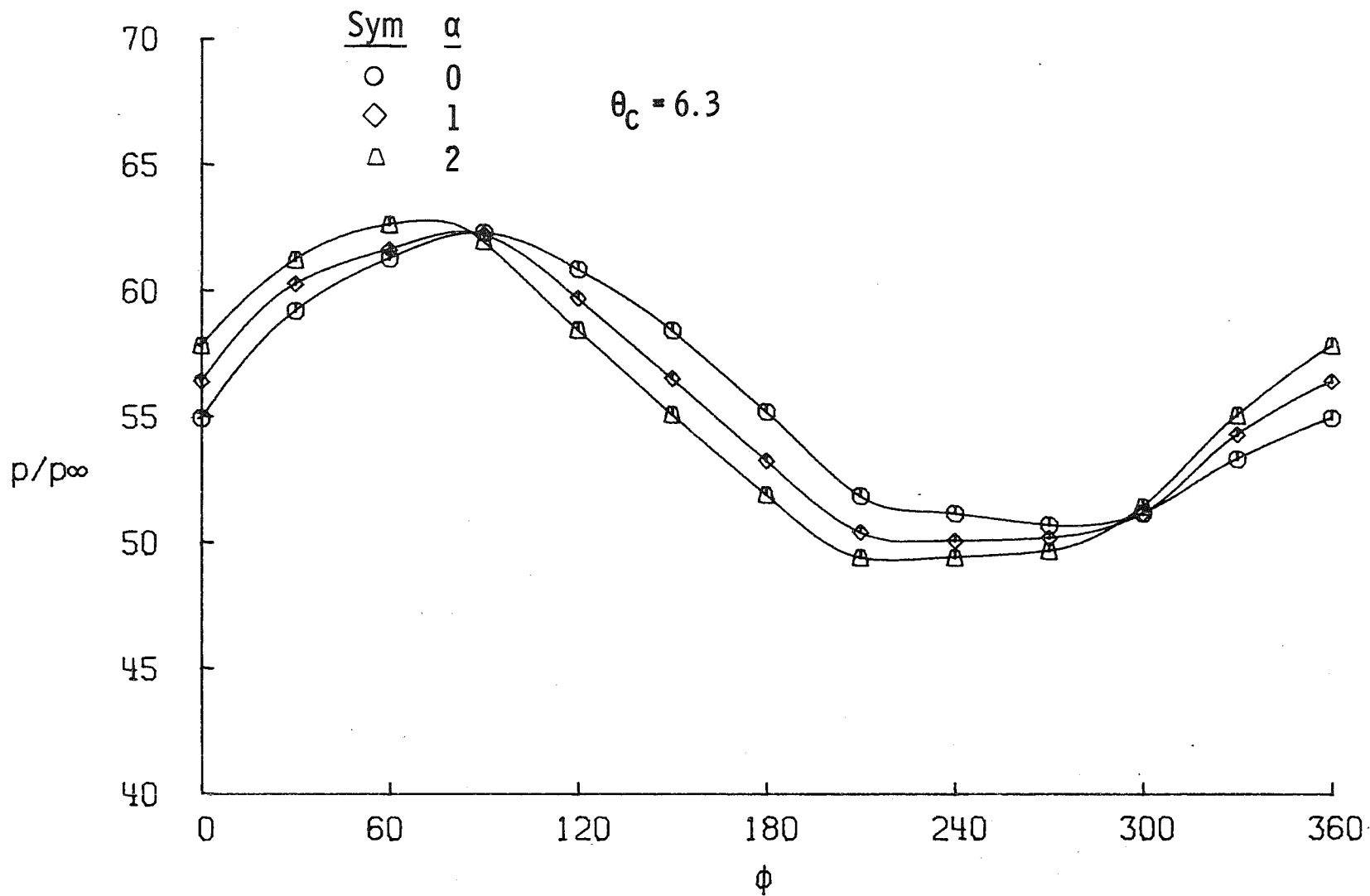
f. Configuration N8 ($\delta_n = 12$), $\phi_m = -30$

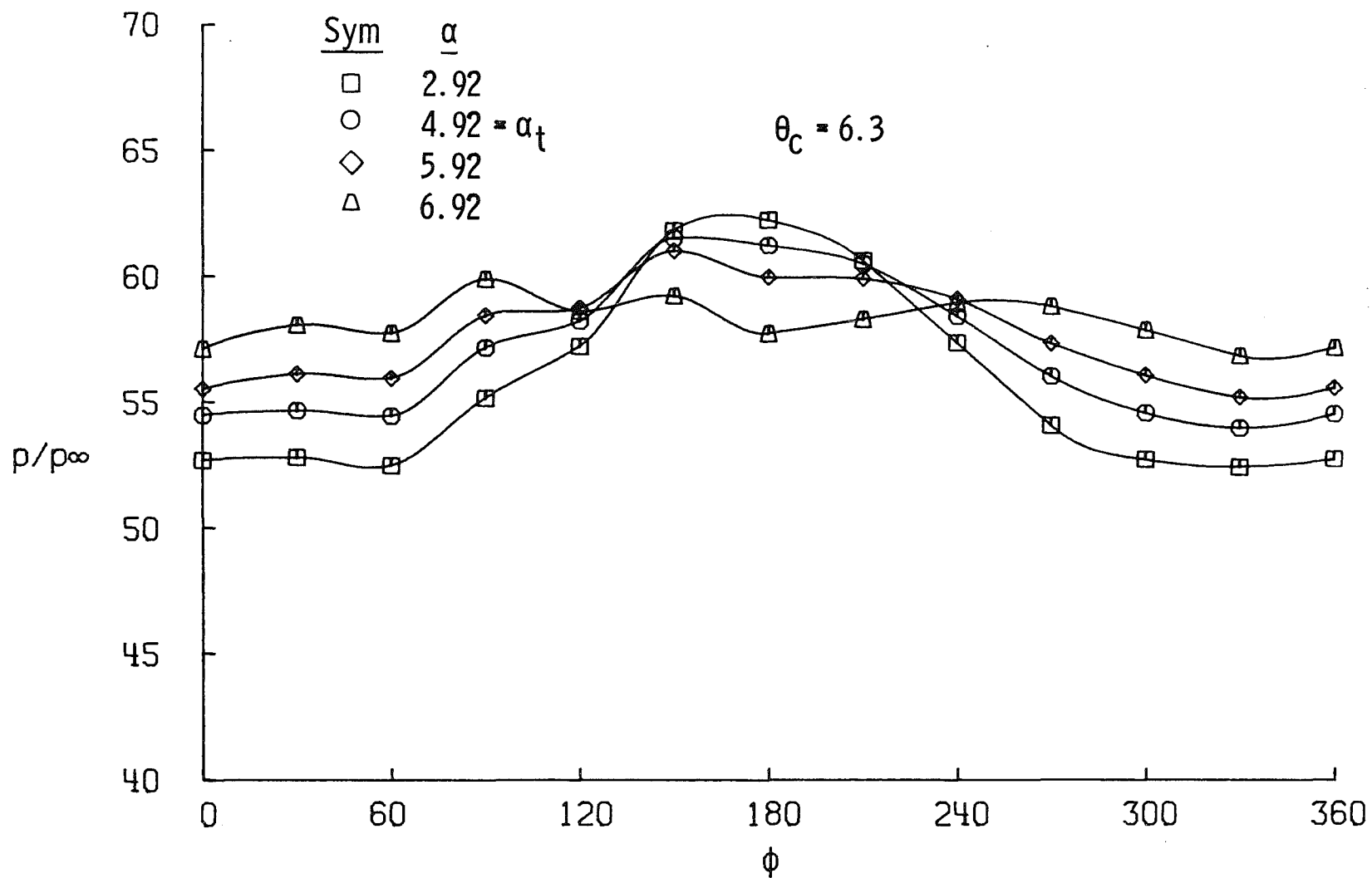
Fig. 22 Continued



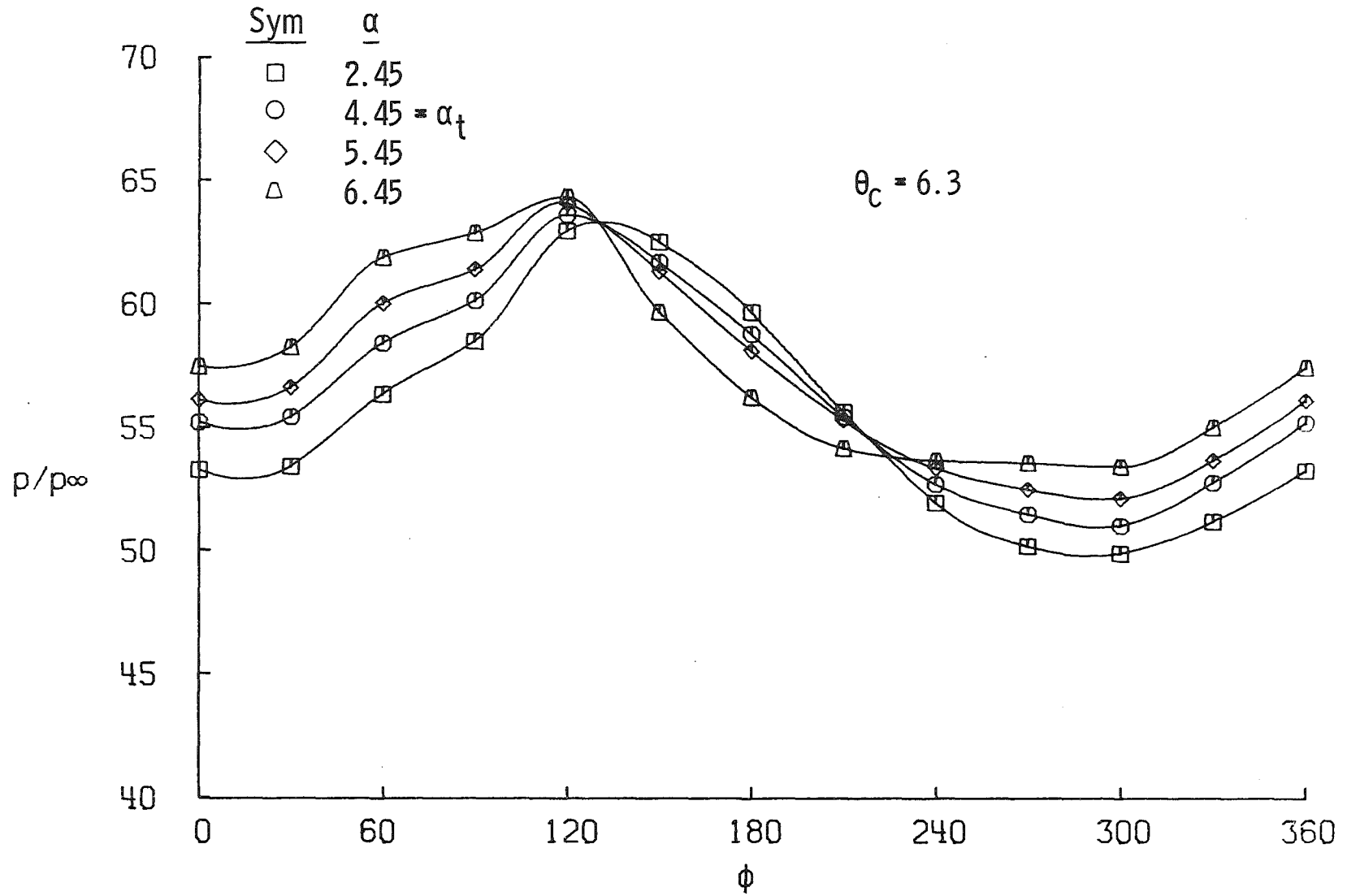
g. Configuration N8 ($\delta_n = 12$), $\phi_m = -60$
Fig. 22 Continued



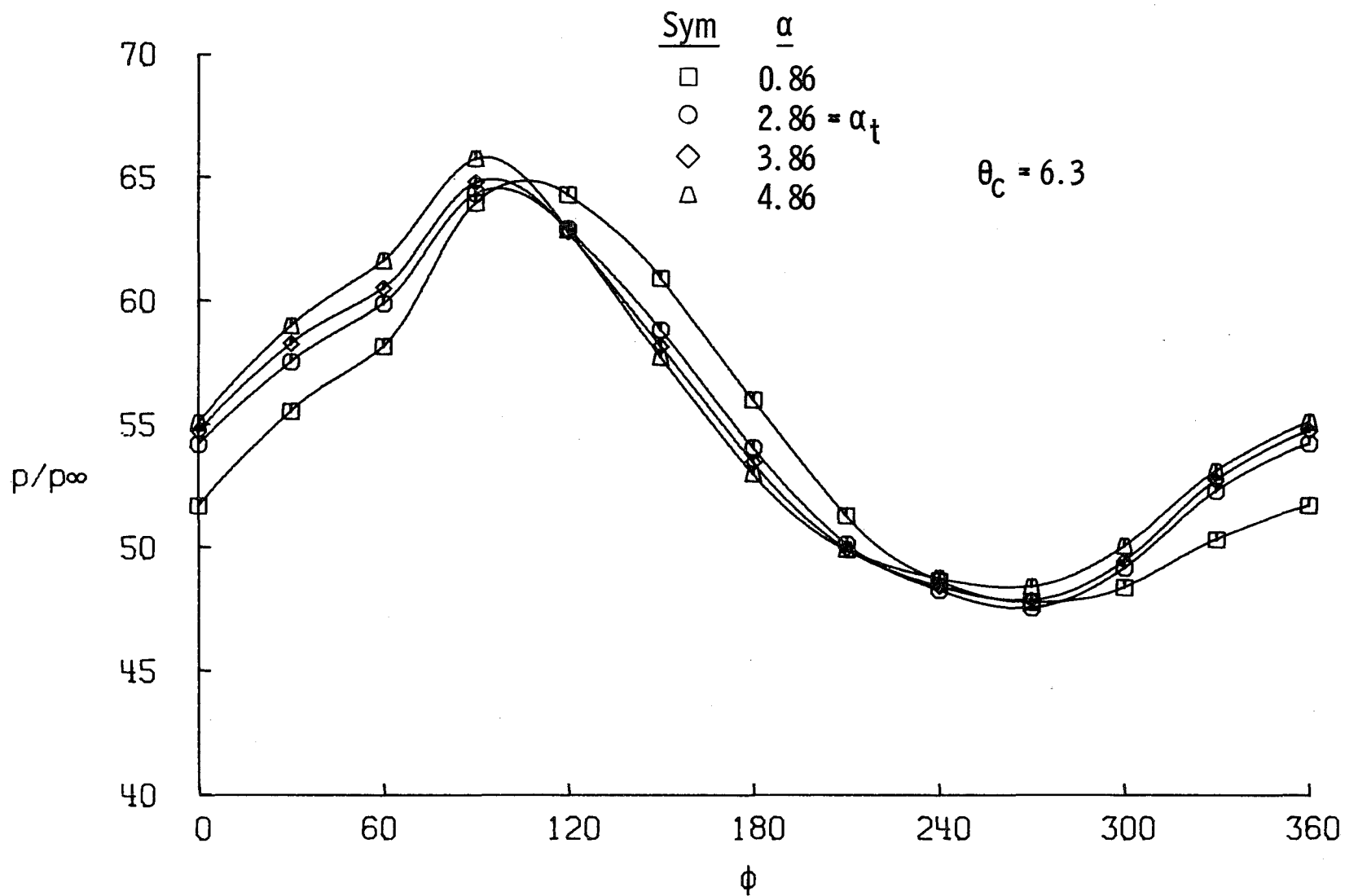
h. Configuration N8 ($\delta_n = 12$), $\phi_m = -90$
Fig. 22 Continued



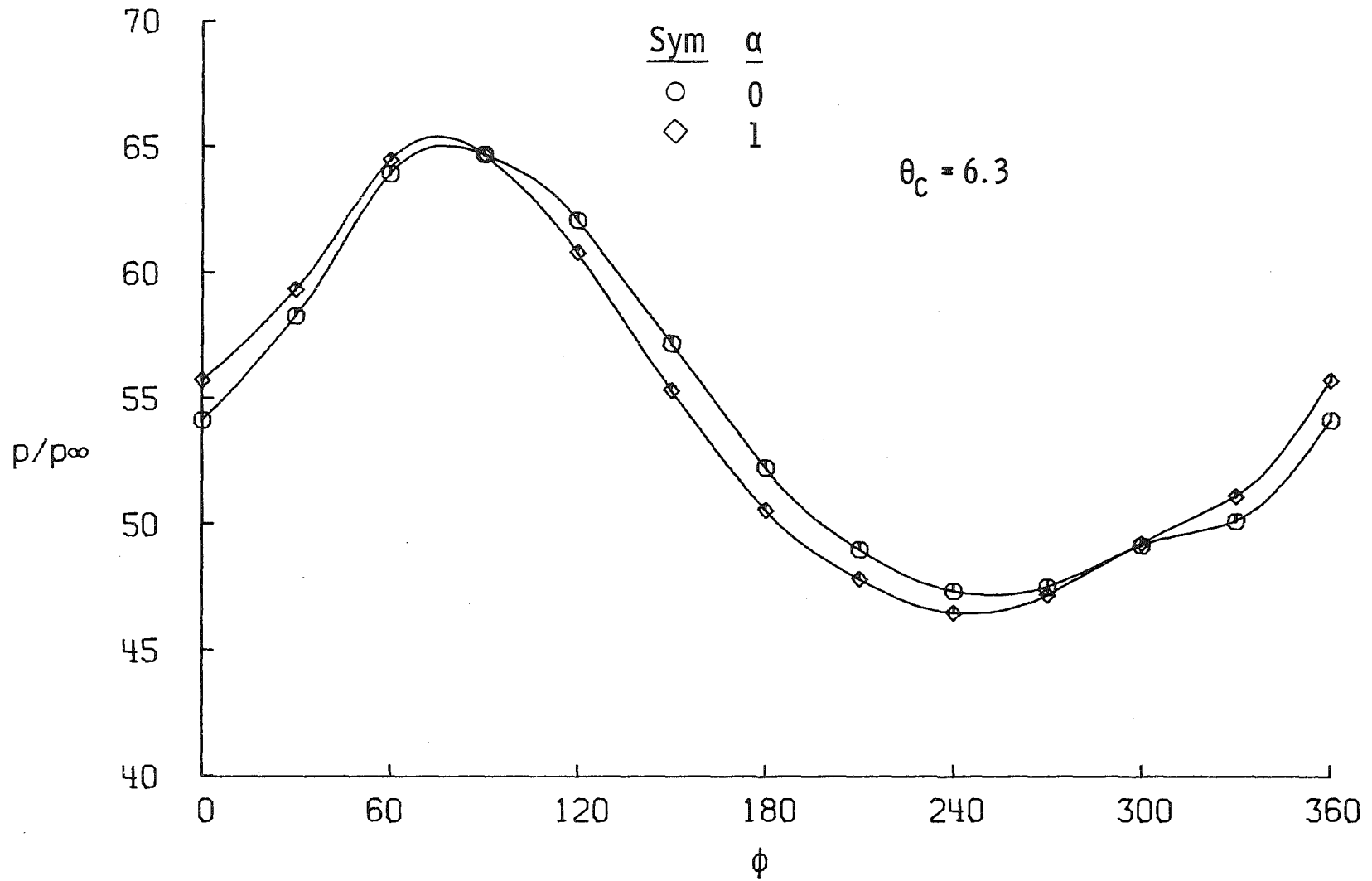
i. Configuration N9 ($\delta_n = 18$), $\phi_m = 0$
Fig. 22 Continued



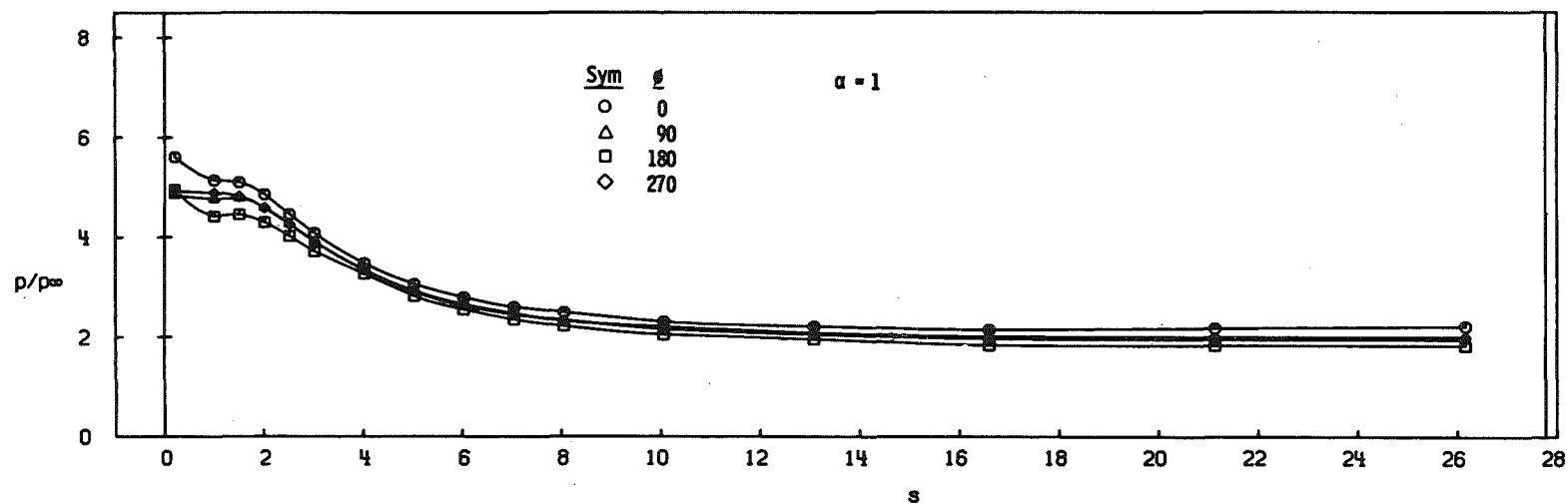
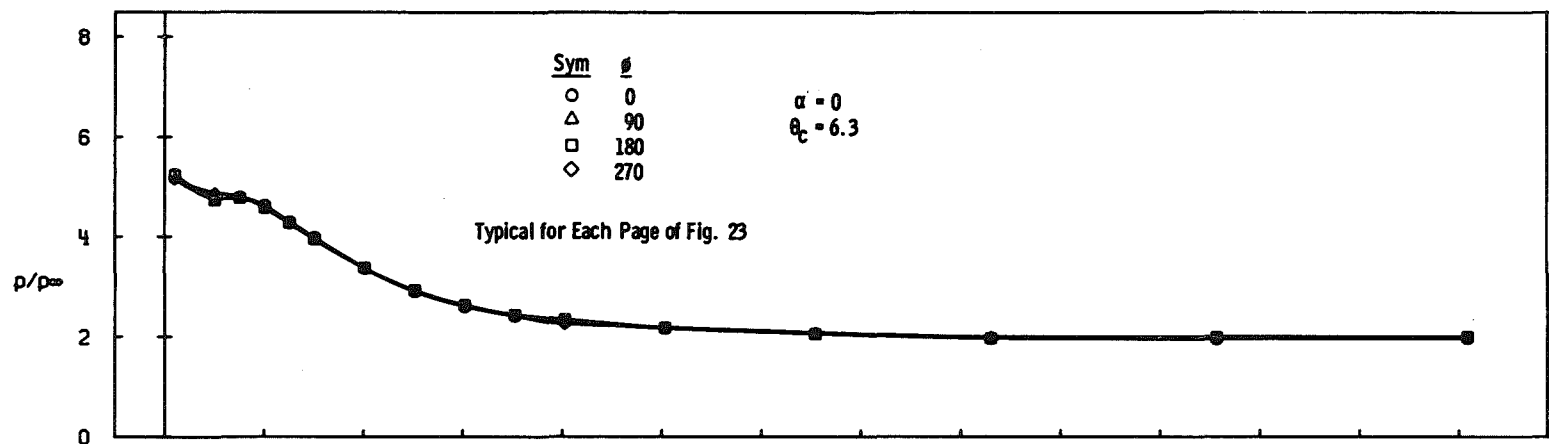
j. Configuration N9 ($\delta_n = 18$), $\phi_m = -30$
Fig. 22 Continued



k. Configuration N9 ($\delta_n = 18$), $\phi_m = -60$
Fig. 22 Continued

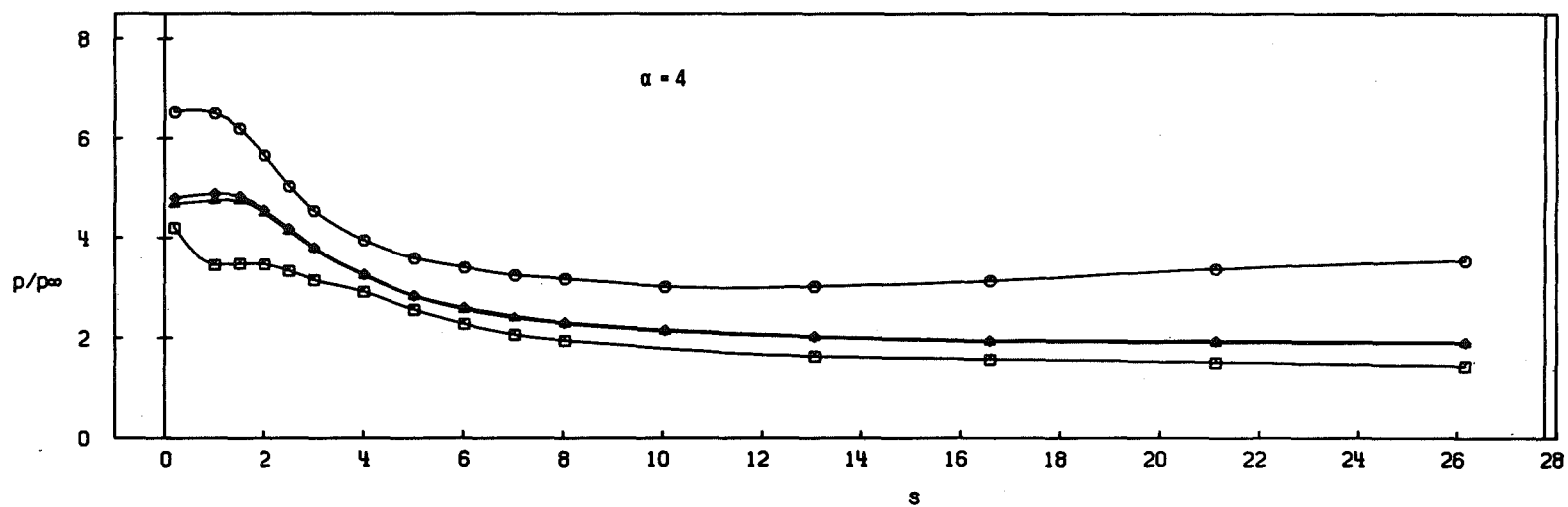
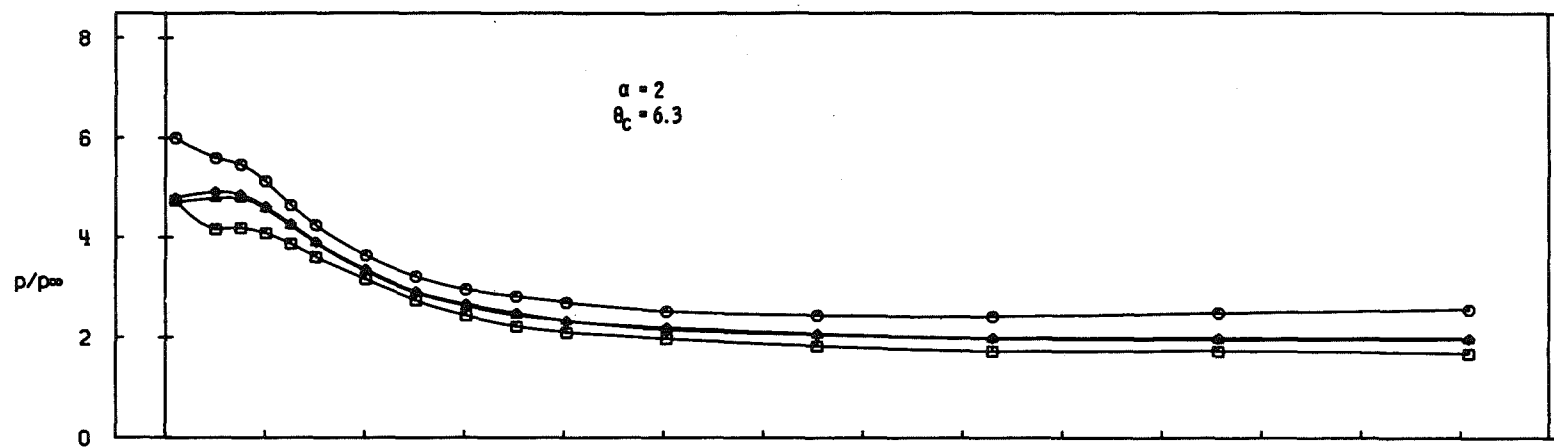


I. Configuration N9 ($\delta_n = 18$), $\phi_m = -90$
 Fig. 22 Concluded

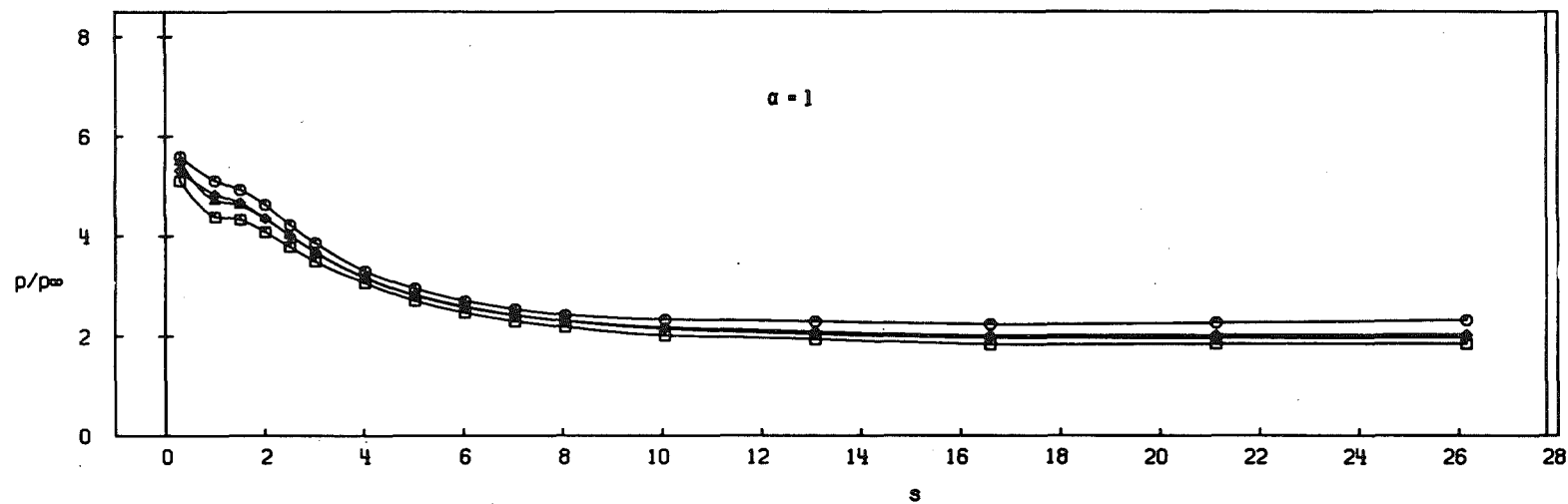
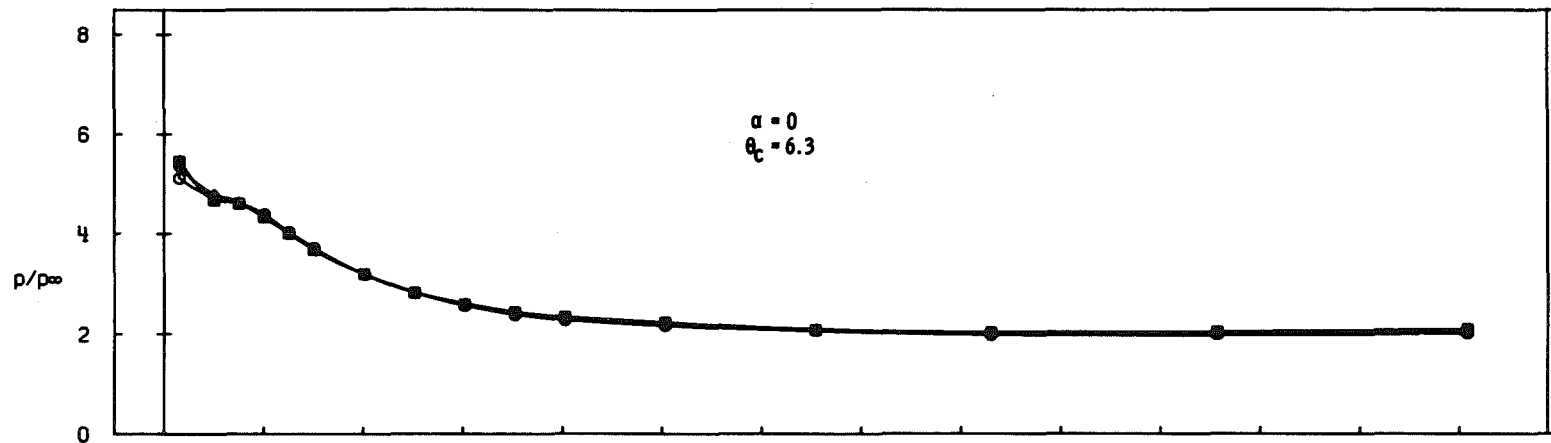


a. Configuration N1 ($\theta_n = 50$, $r_s/r_n = 0$)

Fig. 23 Aft-Cone Longitudinal Pressure Distributions for Symmetrical Biconics, $M_\infty = 8$

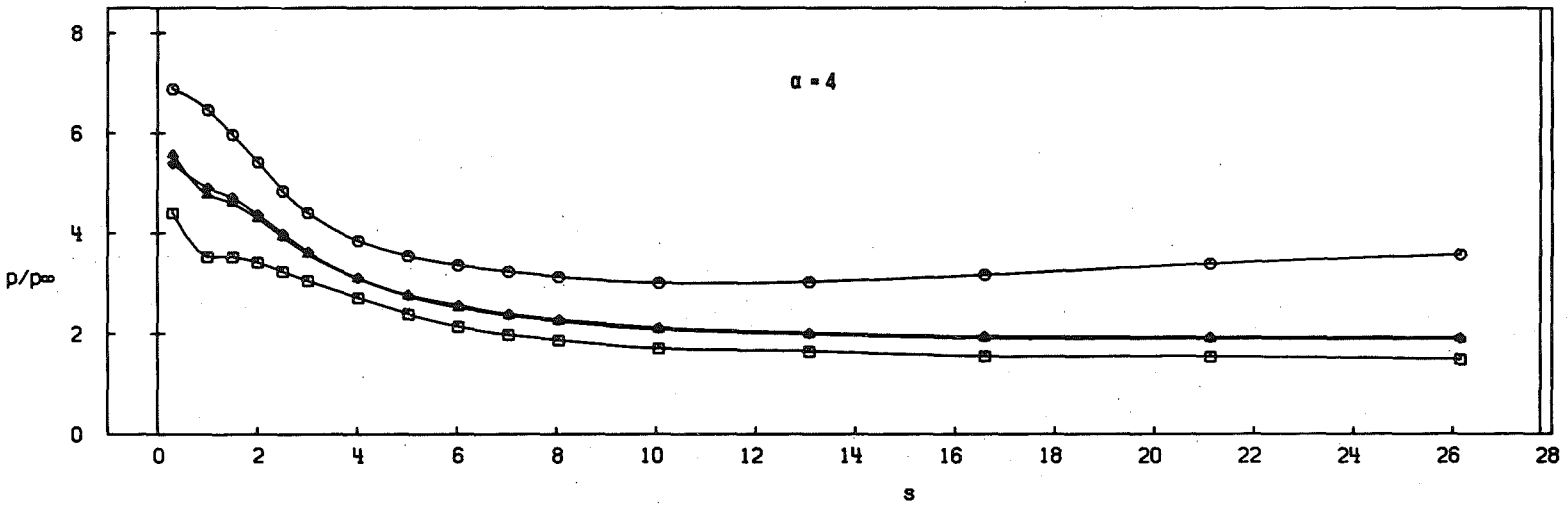
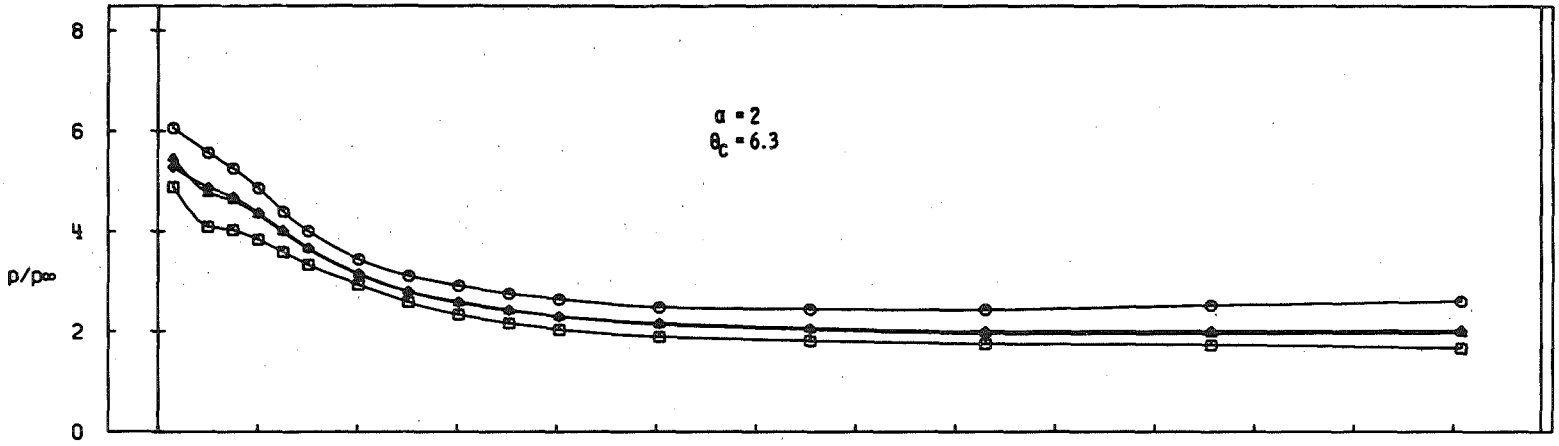


a. Concluded
Fig. 23 Continued

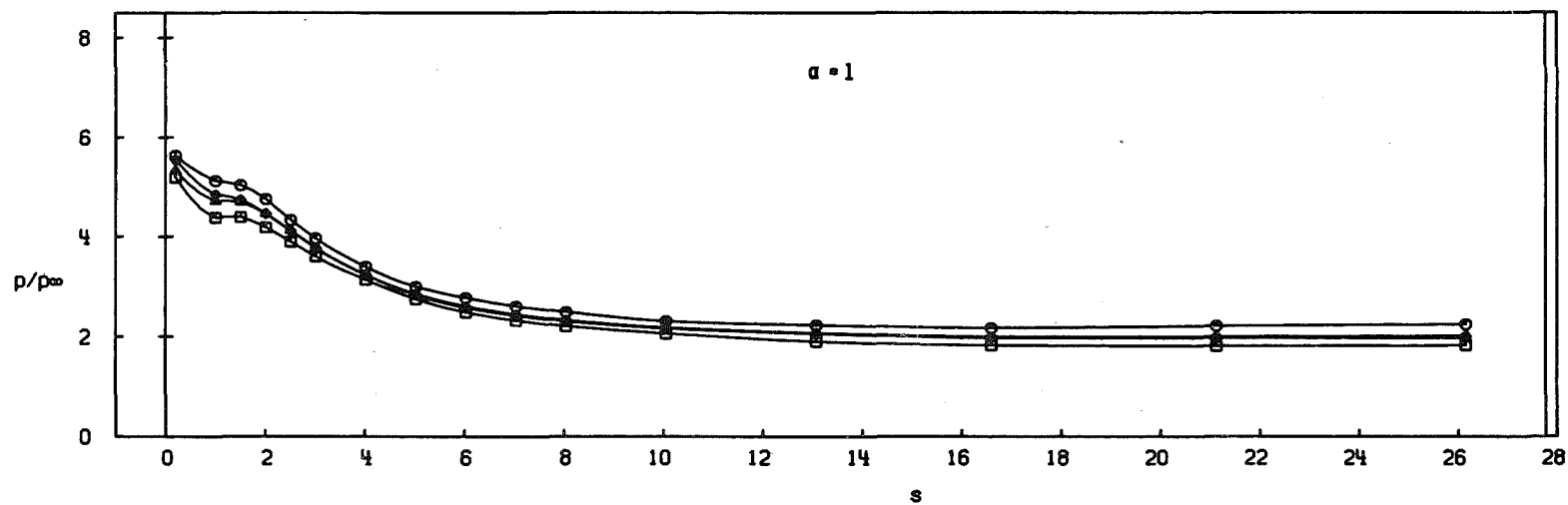
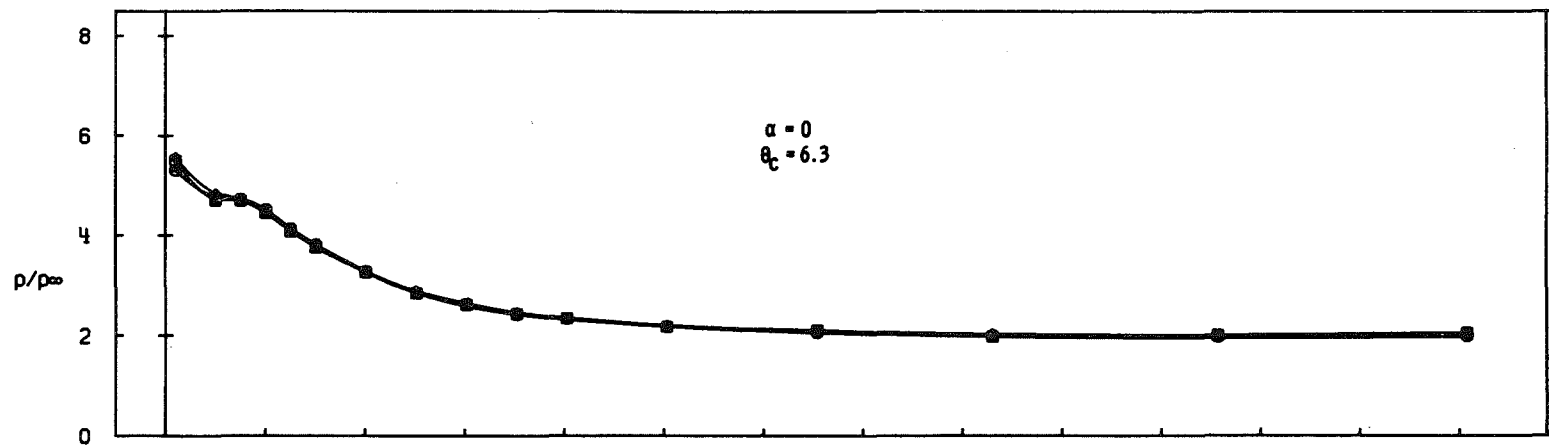


b. Configuration N2 ($\theta_n = 50, r_s/r_n = 0.6$)

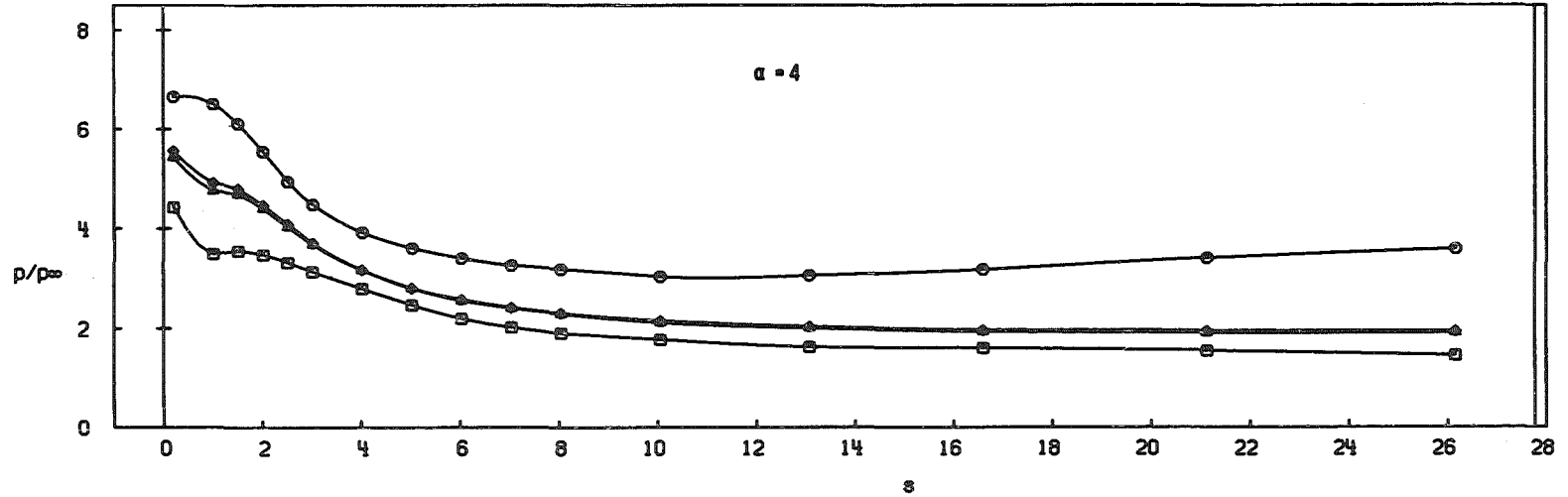
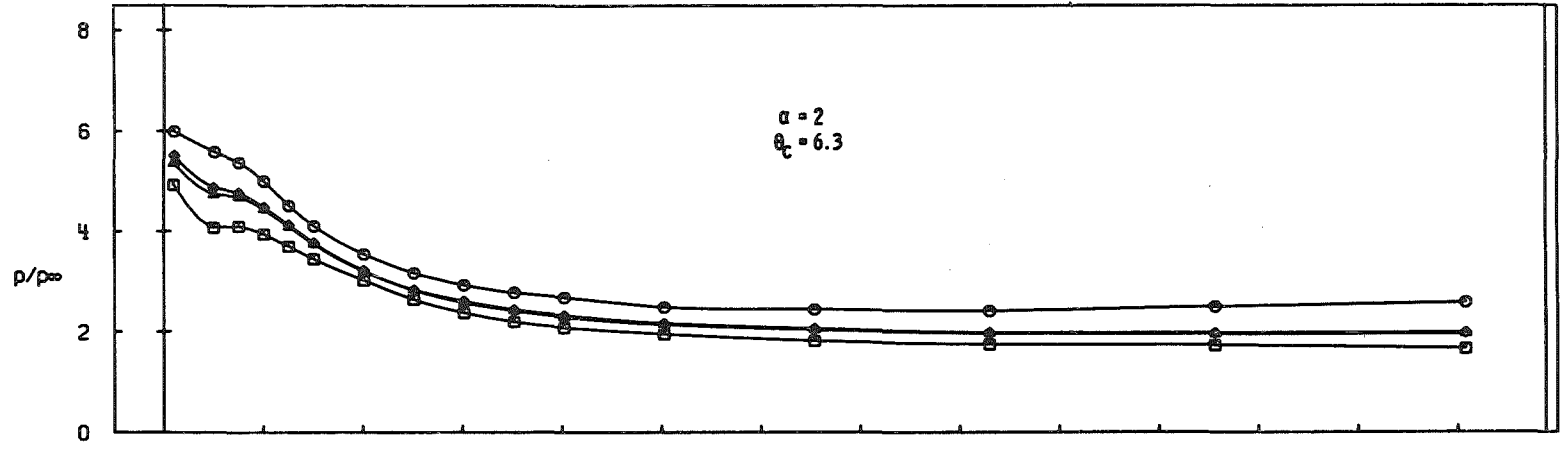
Fig. 23 Continued



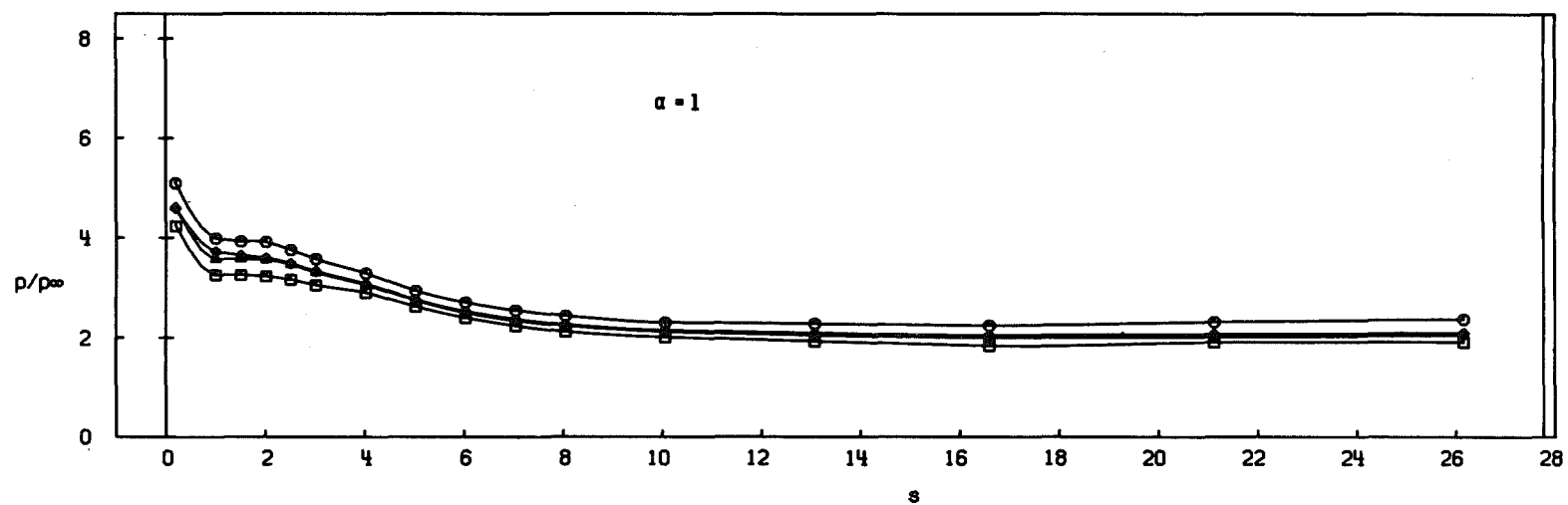
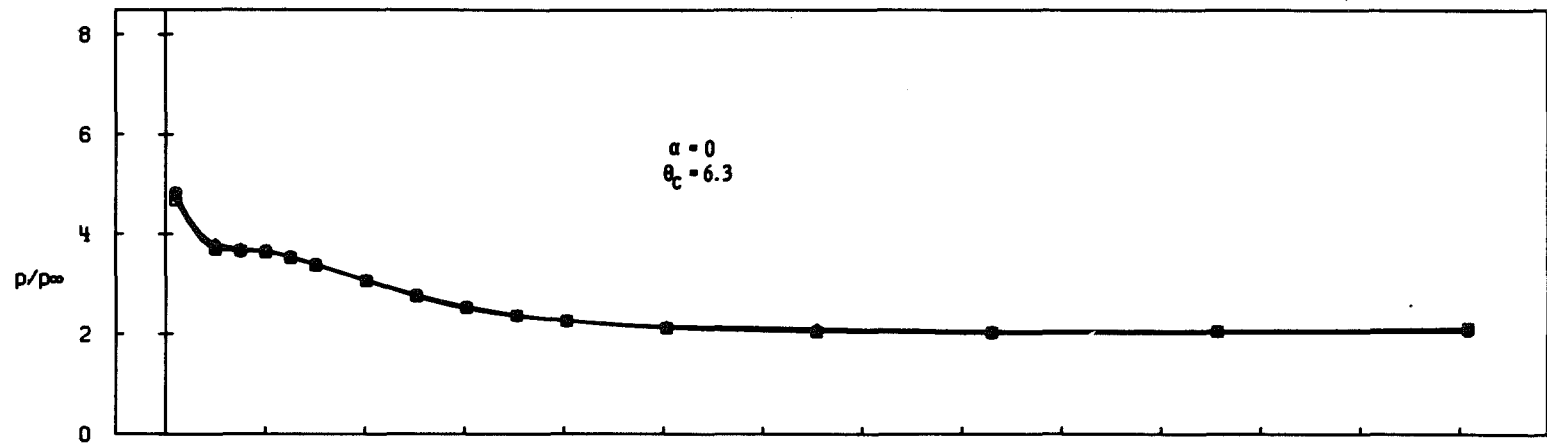
b. Concluded
Fig. 23 Continued



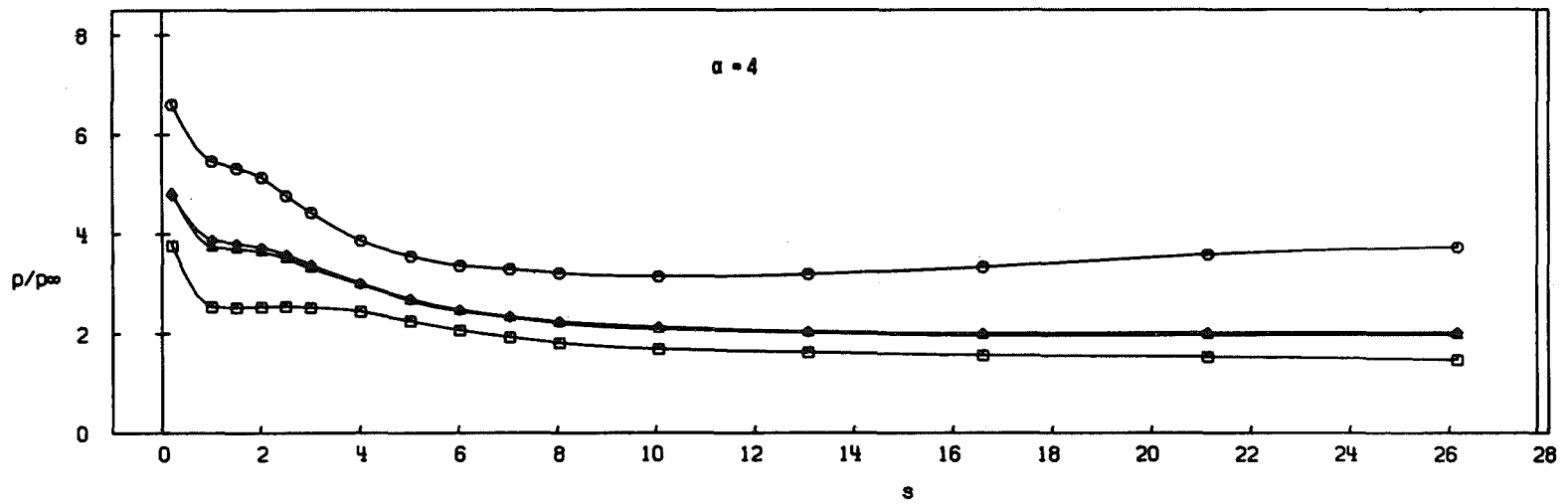
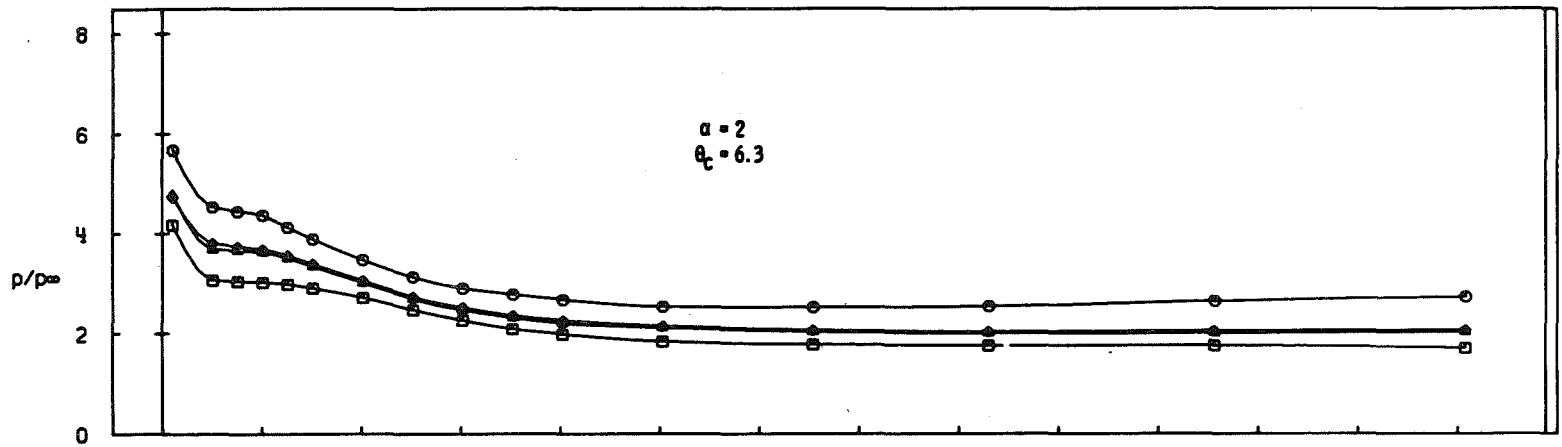
c. Configuration N3 ($\theta_n = 50, r_s/r_n = 0.3$)
Fig. 23 Continued



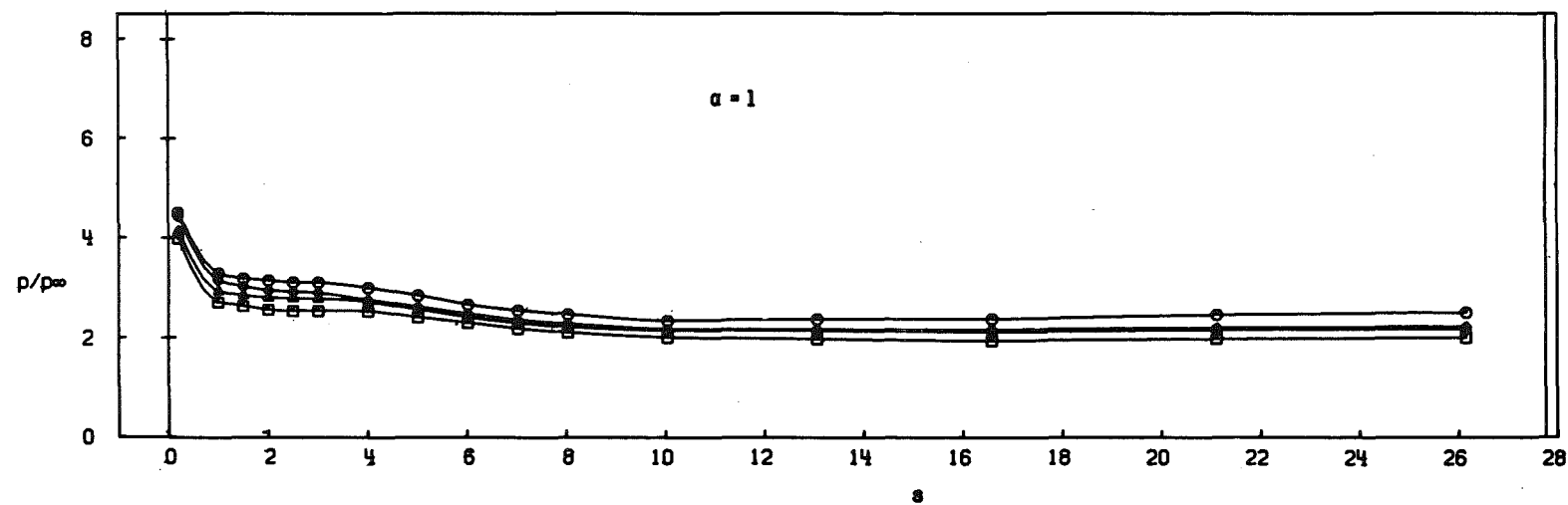
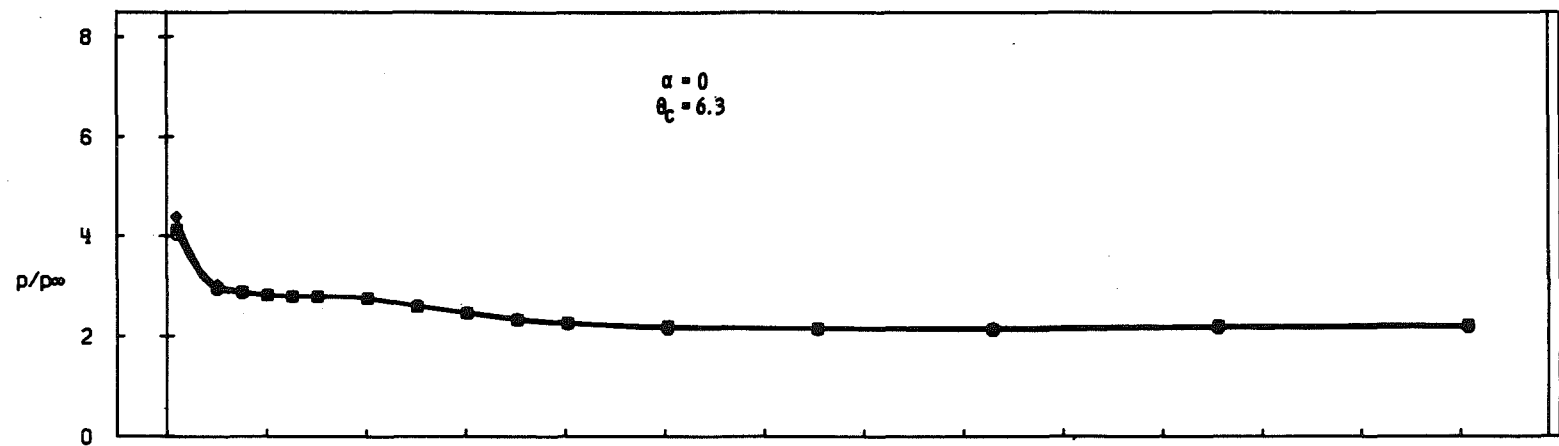
c. Concluded
Fig. 23 Continued



d. Configuration N4 ($\theta_n = 40$, $r_s/r_n = 0.3$)
Fig. 23 Continued

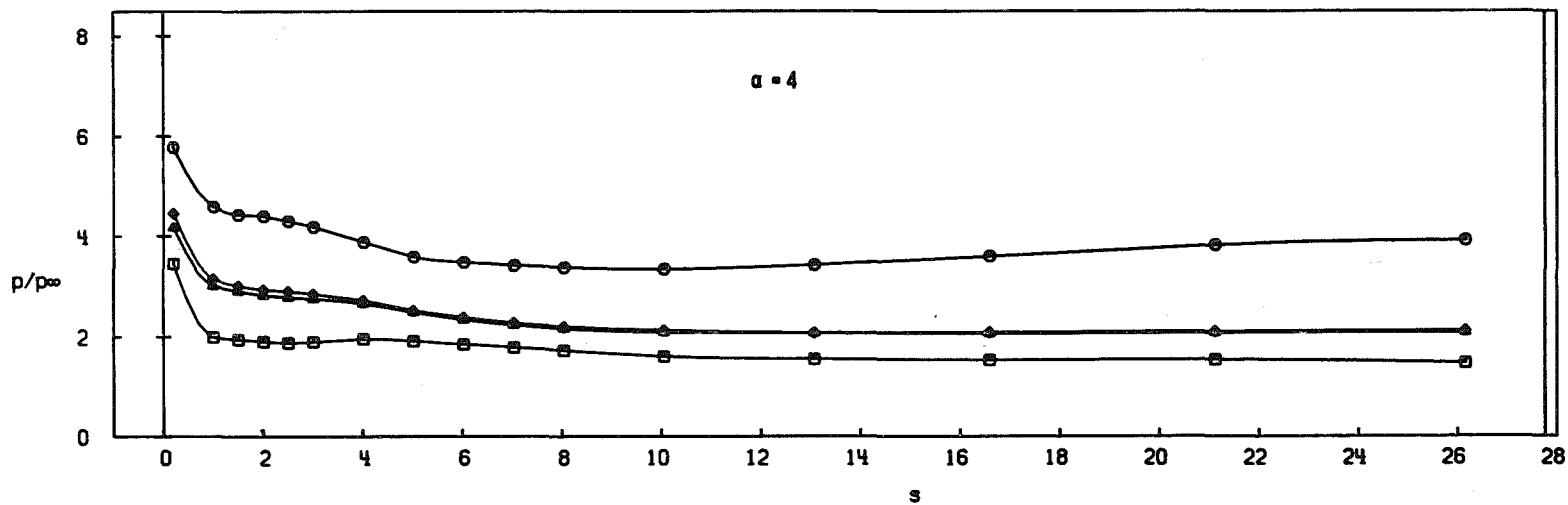
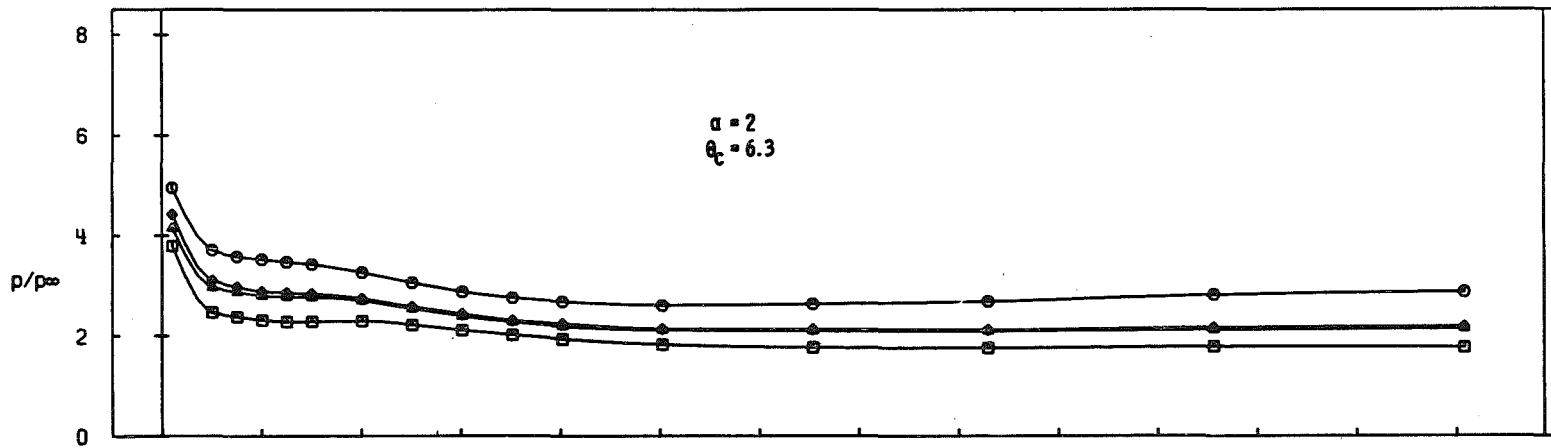


d. Concluded
Fig. 23 Continued

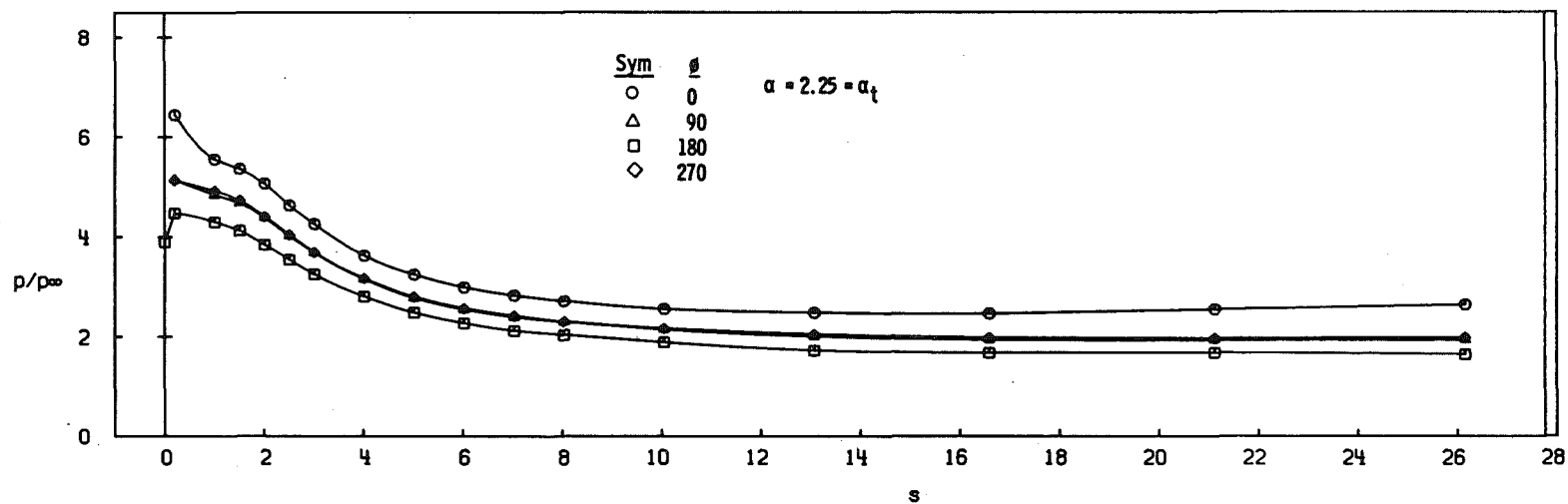
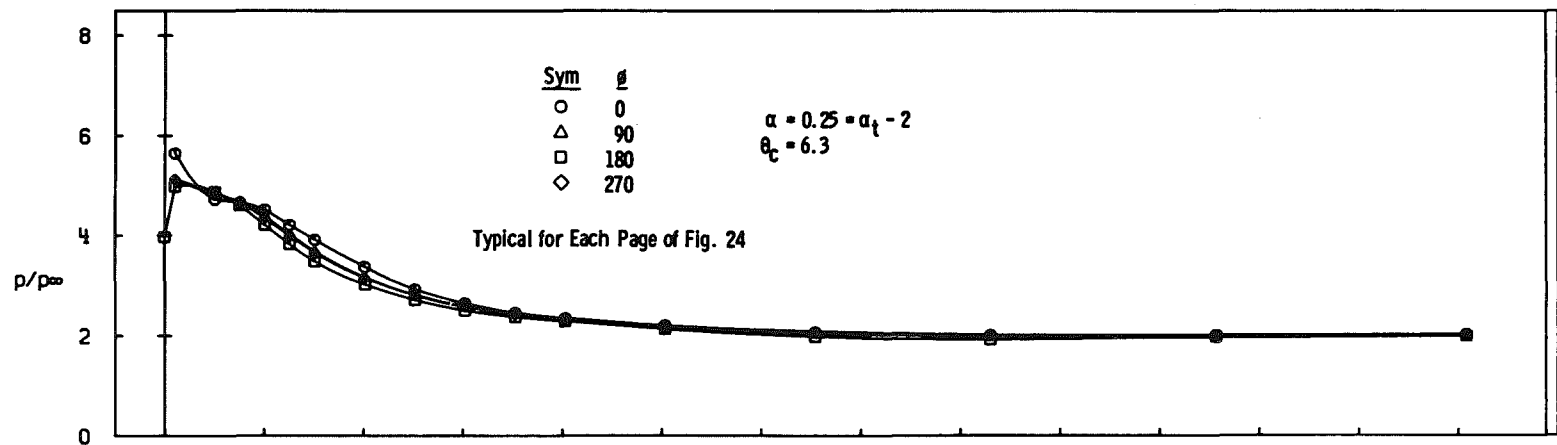


e. Configuration N5 ($\theta_n = 30$, $r_s/r_n = 0.3$)

Fig. 23 Continued

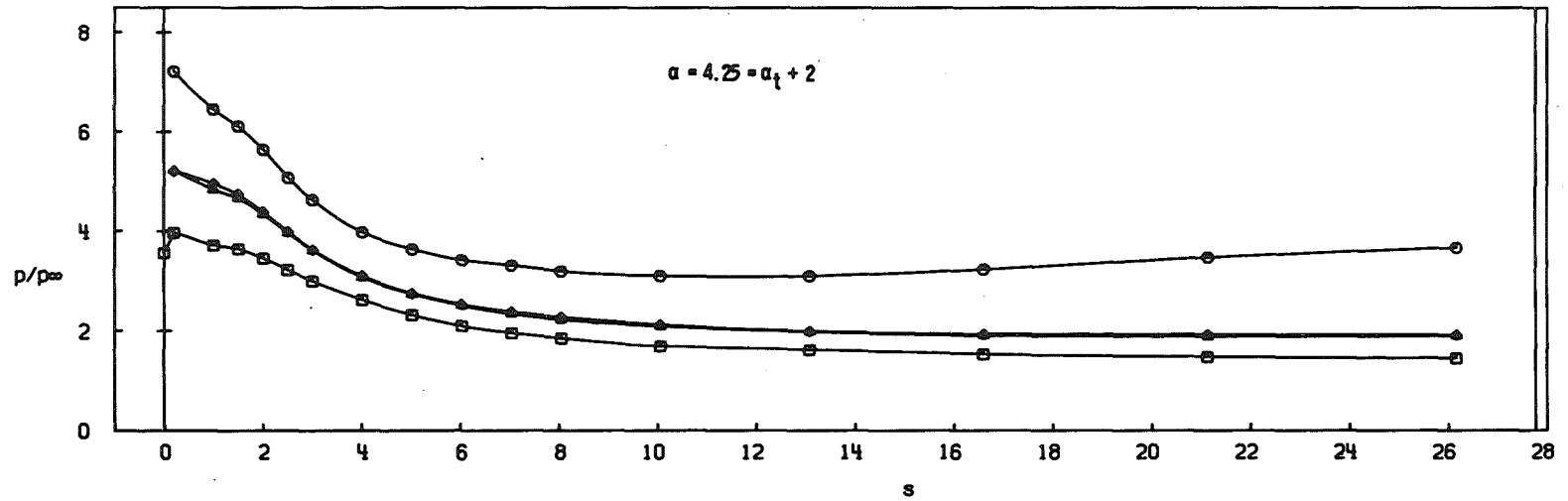
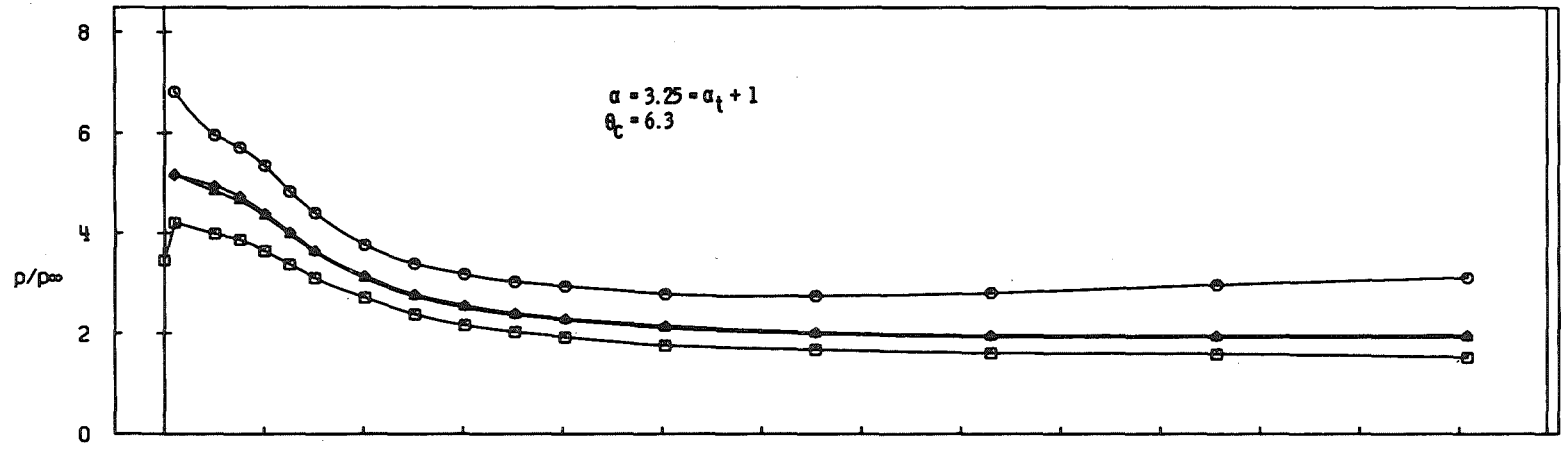


e. Concluded
Fig. 23 Concluded

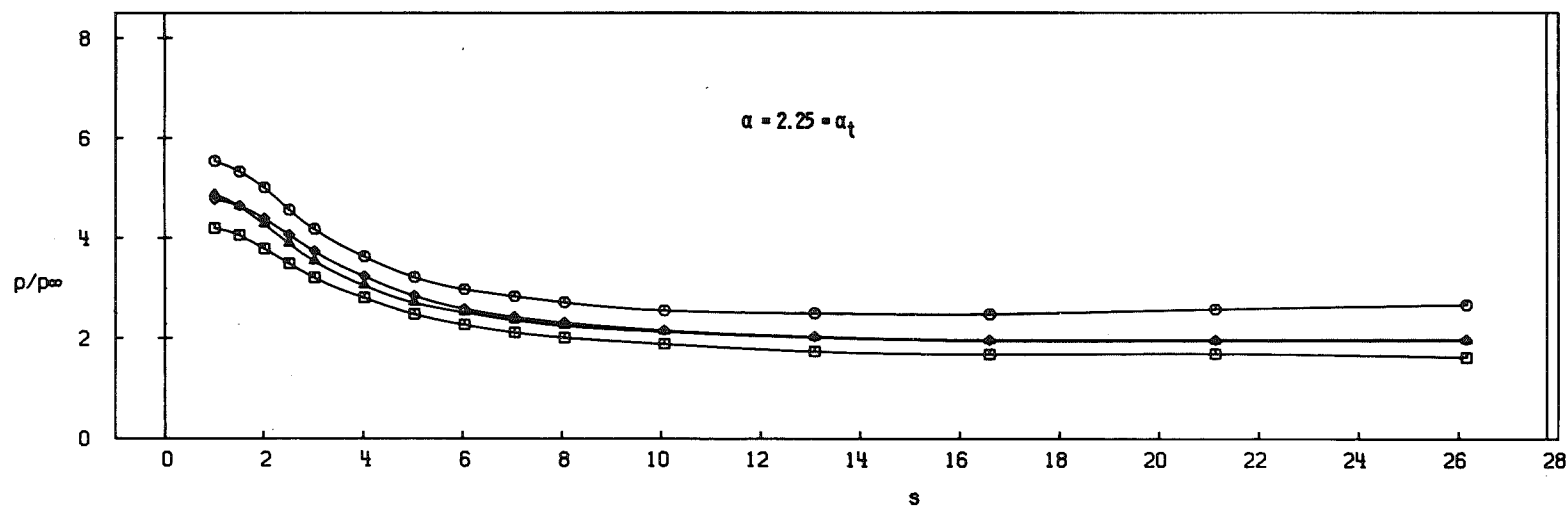
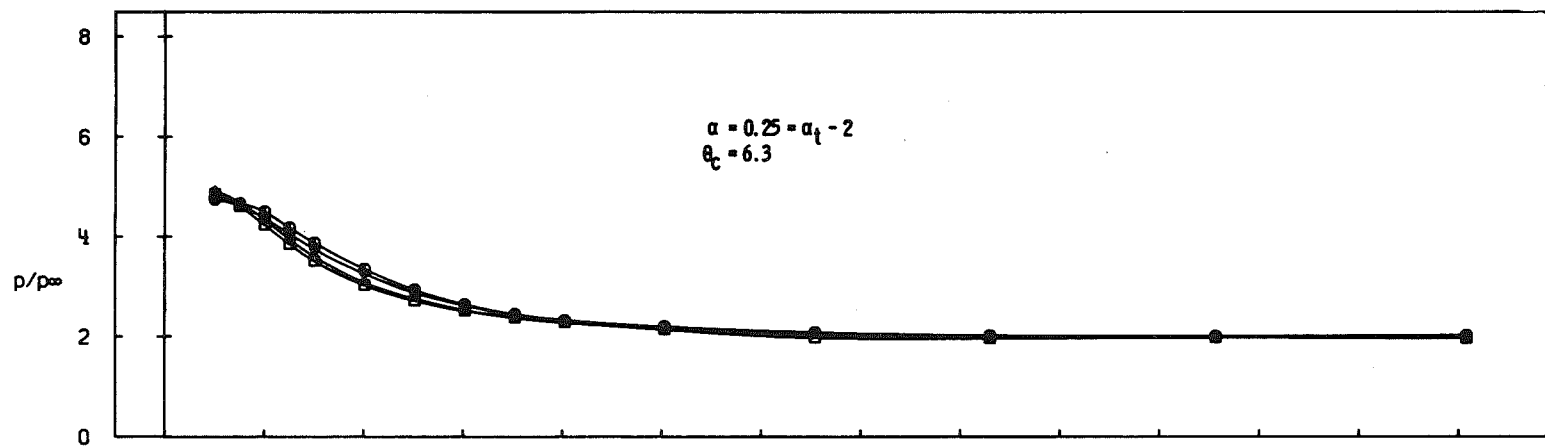


a. Configuration N7 ($\delta_n = 6$), $\phi_m = 0$

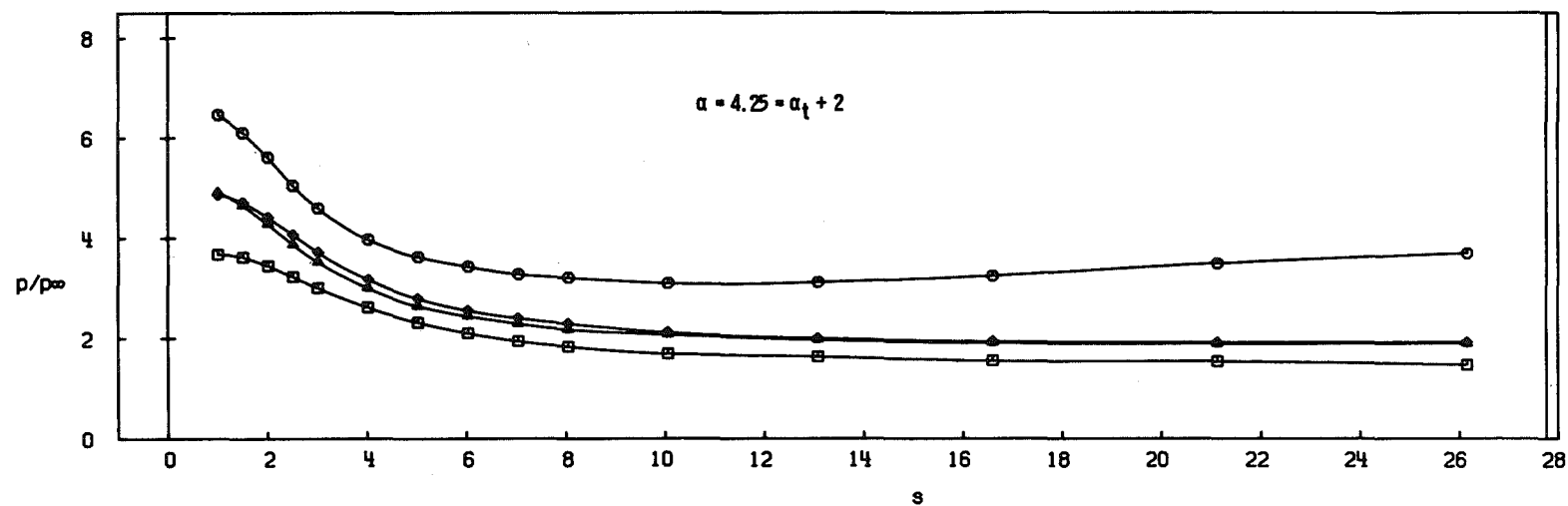
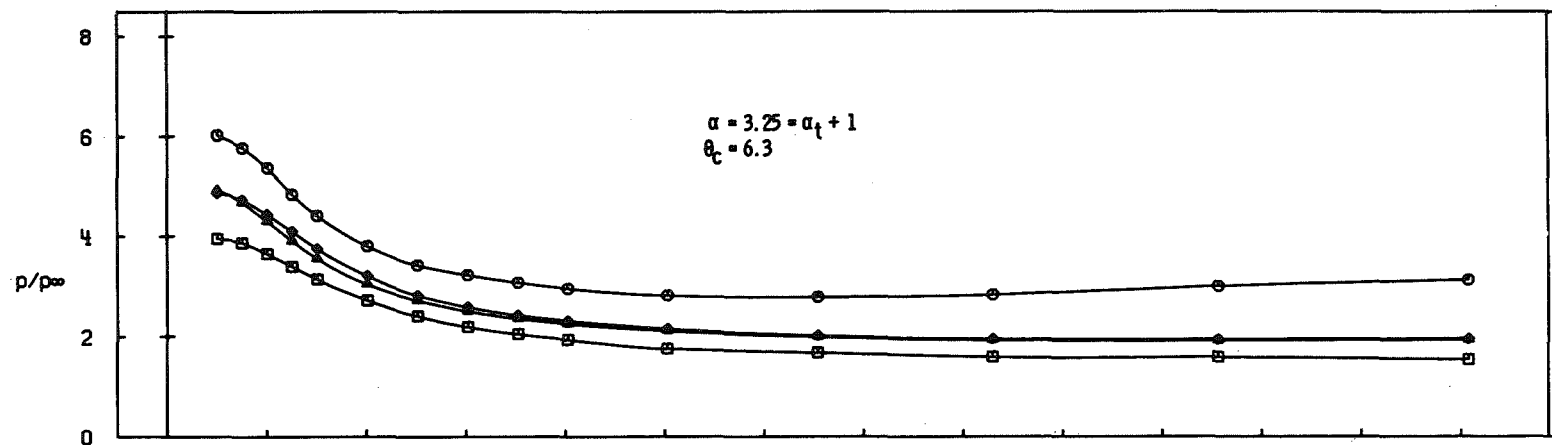
Fig. 24 Aft-Cone Longitudinal Pressure Distributions for Asymmetrical Biconics, $M_\infty = 8$



a. Concluded
 Fig. 24 Continued



b. Configuration N7 ($\delta_n = 6$), $\phi_m = -30$
 Fig. 24 Continued



b. Concluded
 Fig. 24 Continued

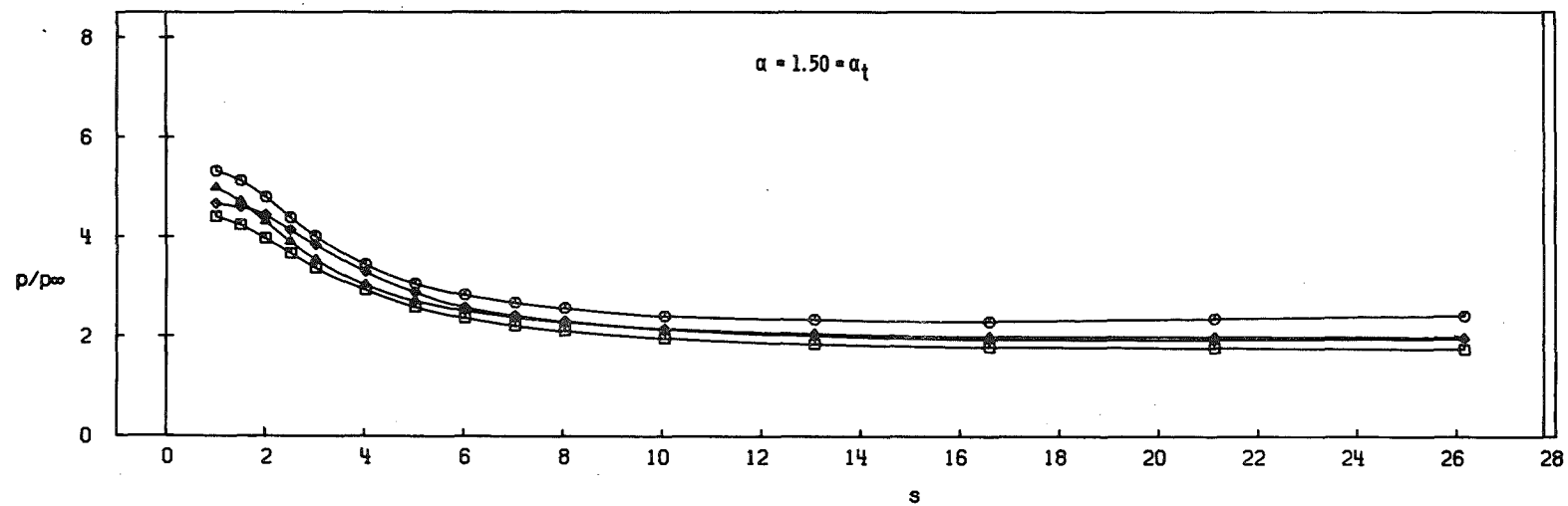
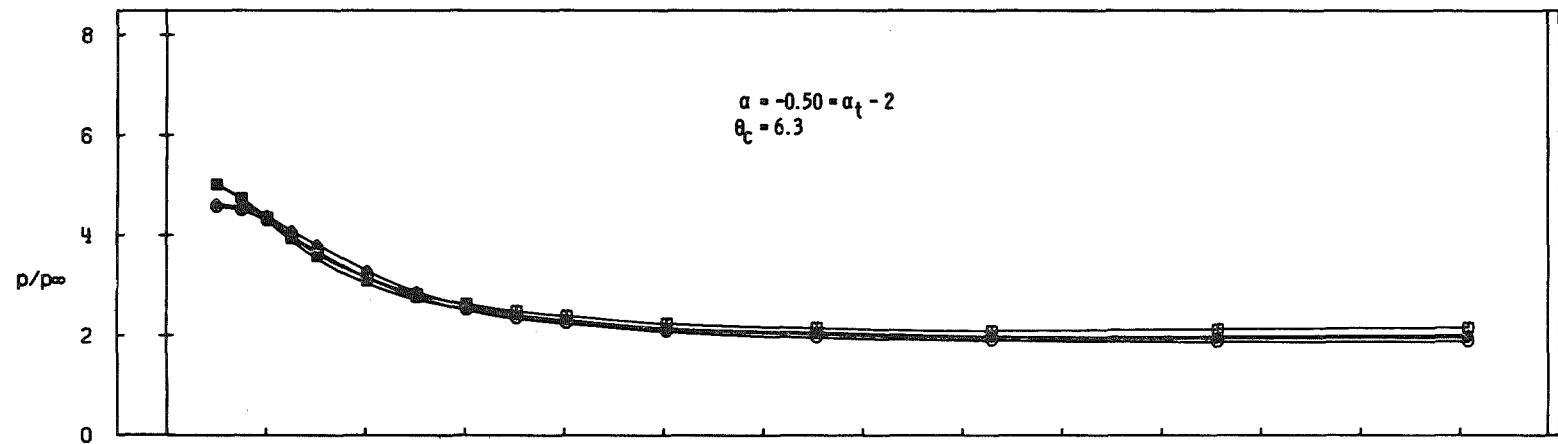
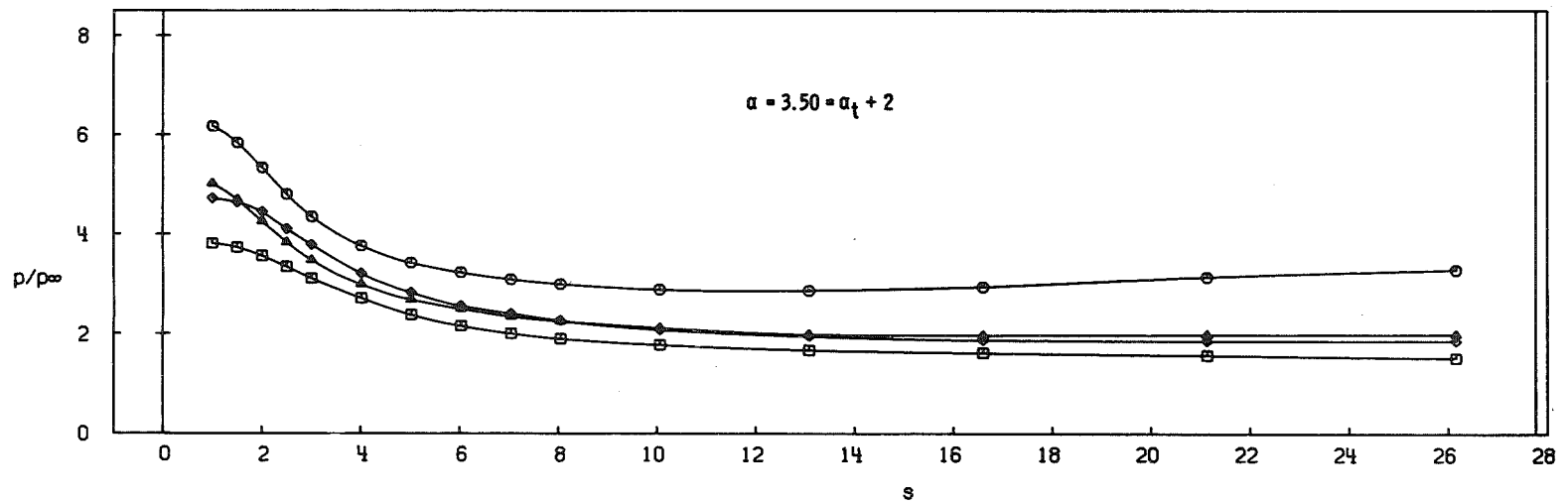
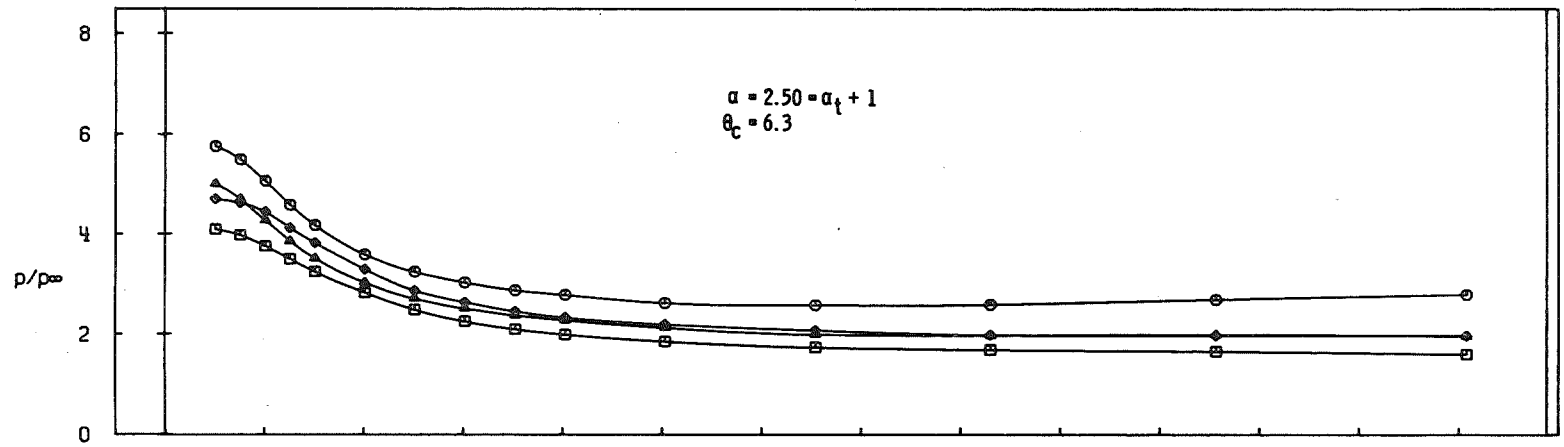
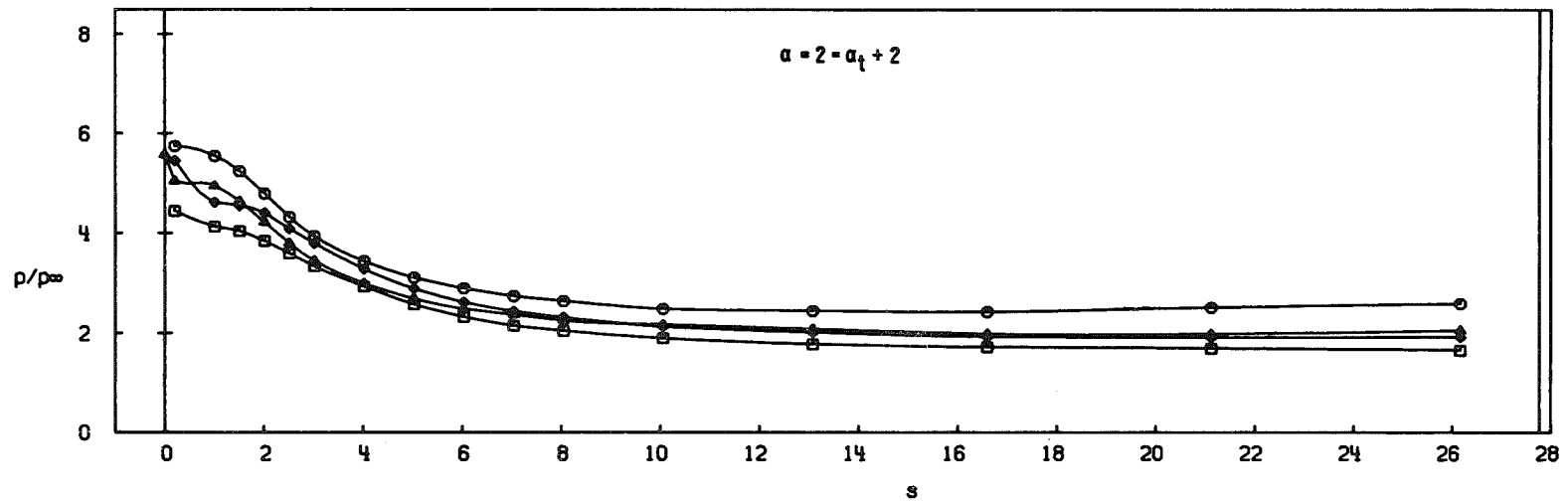
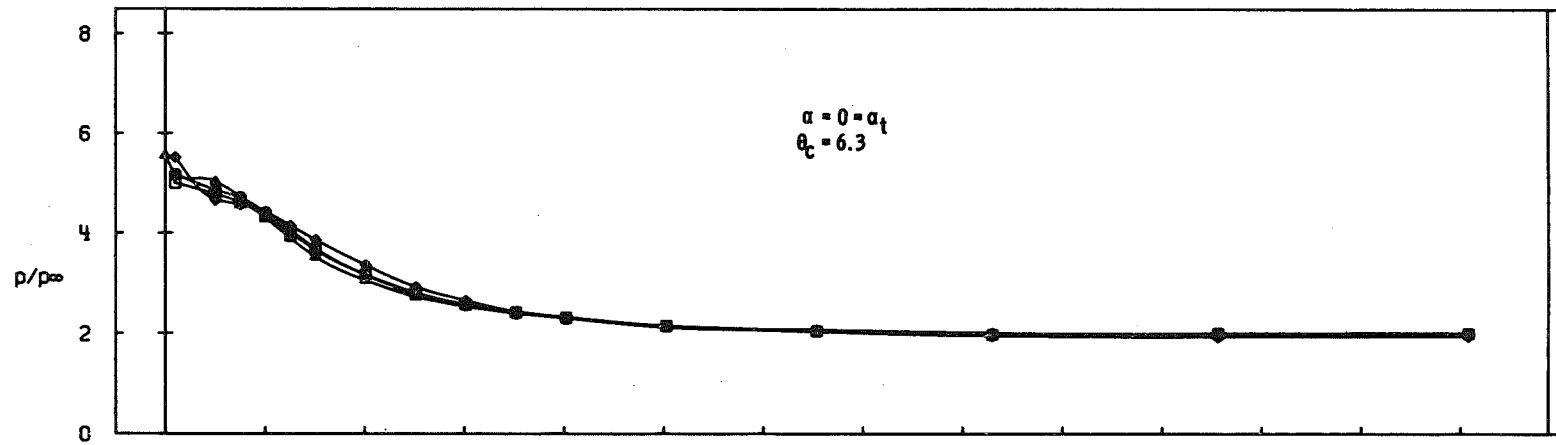
c. Configuration N7 ($\delta_n = 6$), $\phi_m = -60$

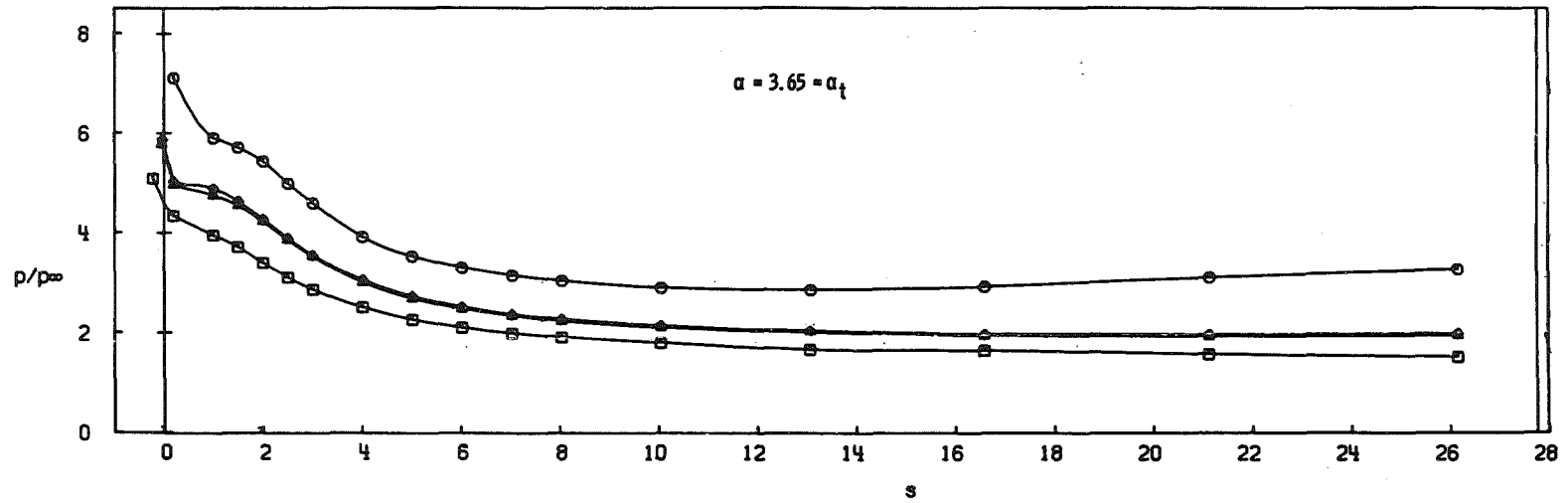
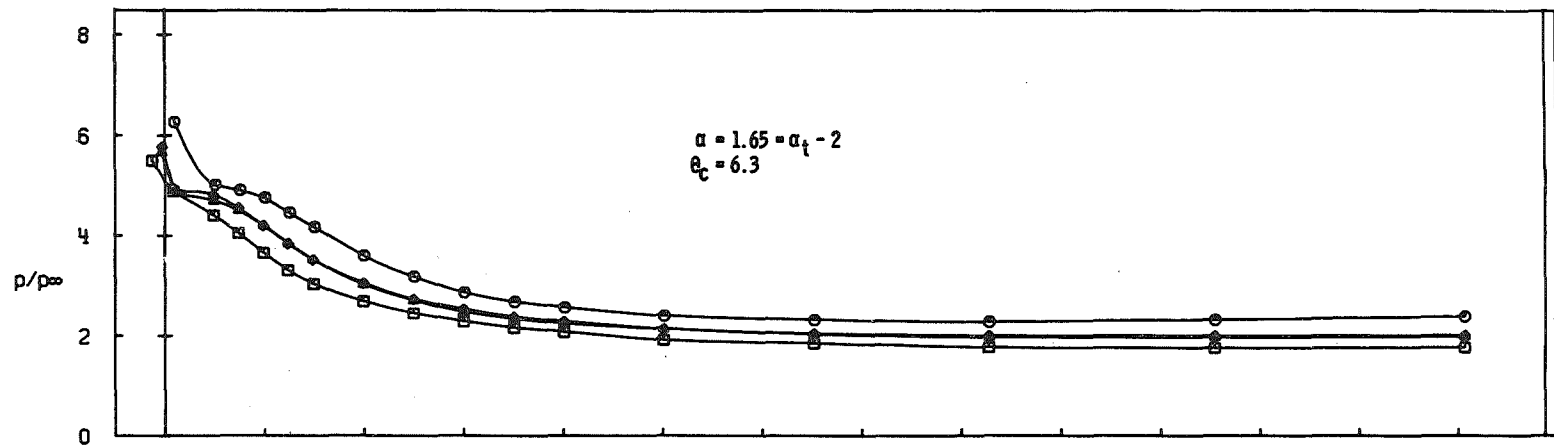
Fig. 24 Continued



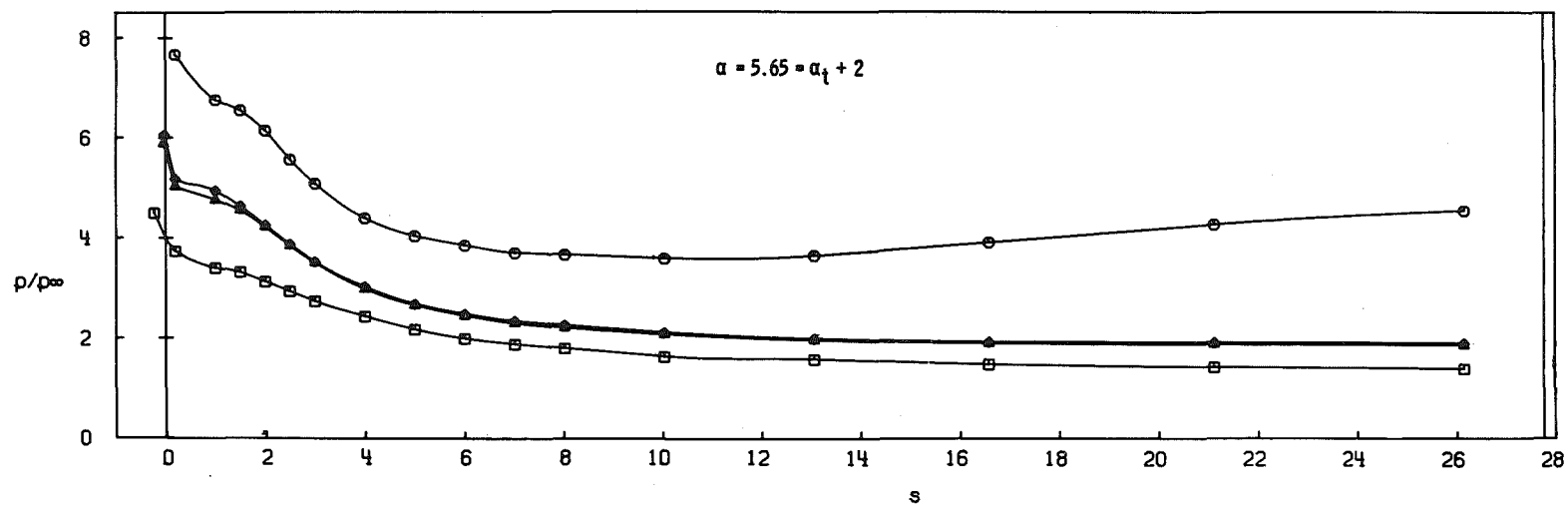
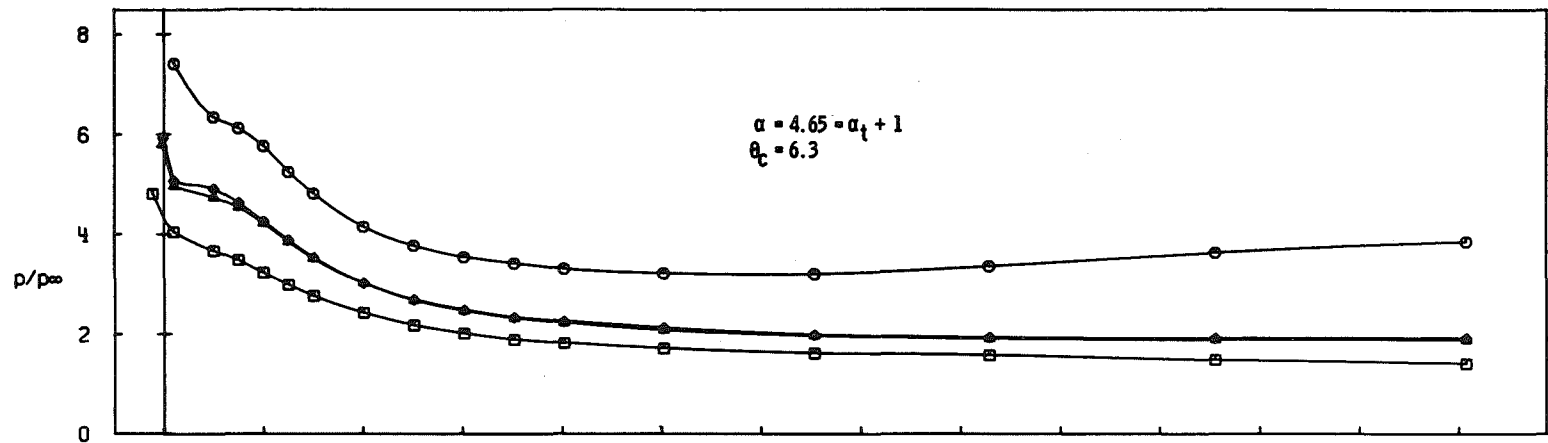
c. Concluded
 Fig. 24 Continued



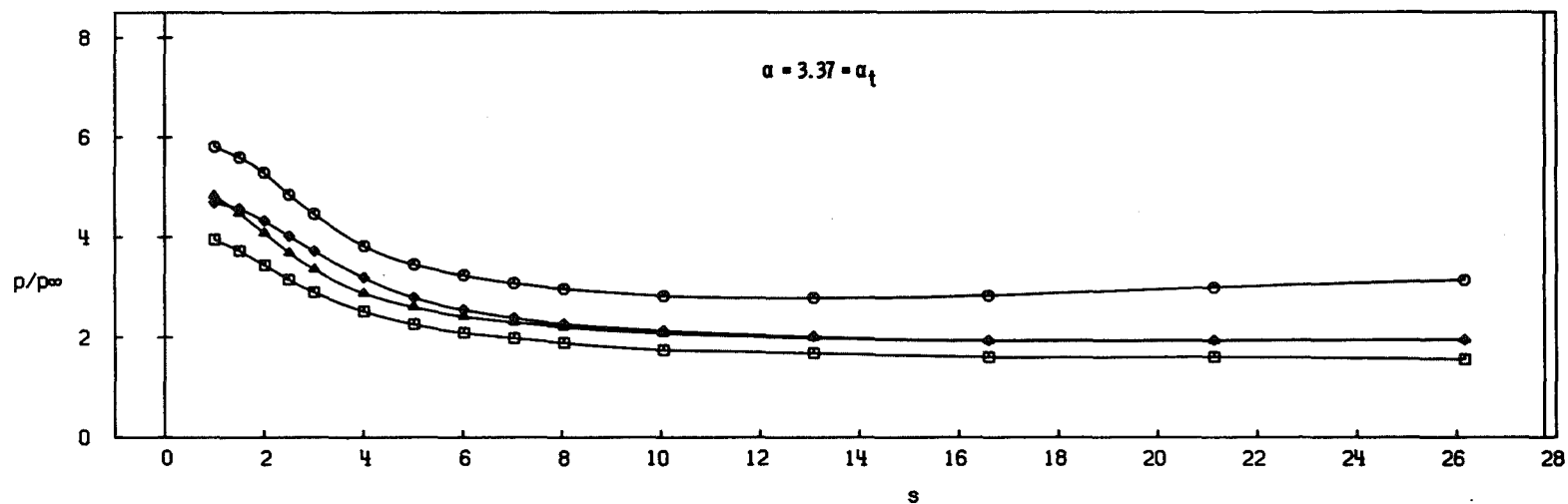
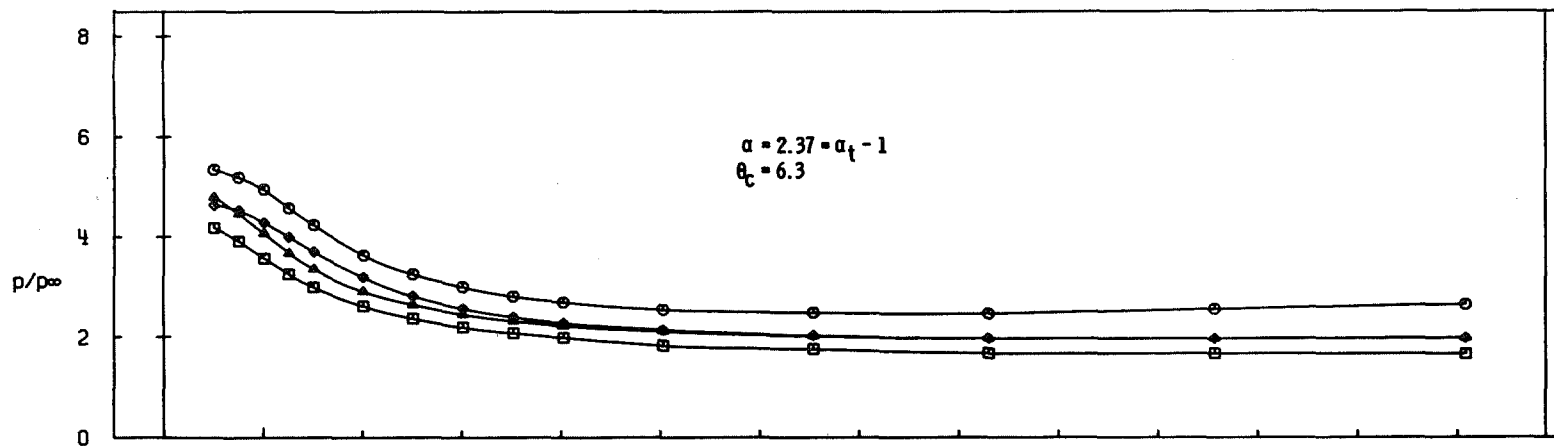
d. Configuration N7 ($\delta_n = 6$), $\phi_m = -90$
 Fig. 24 Continued



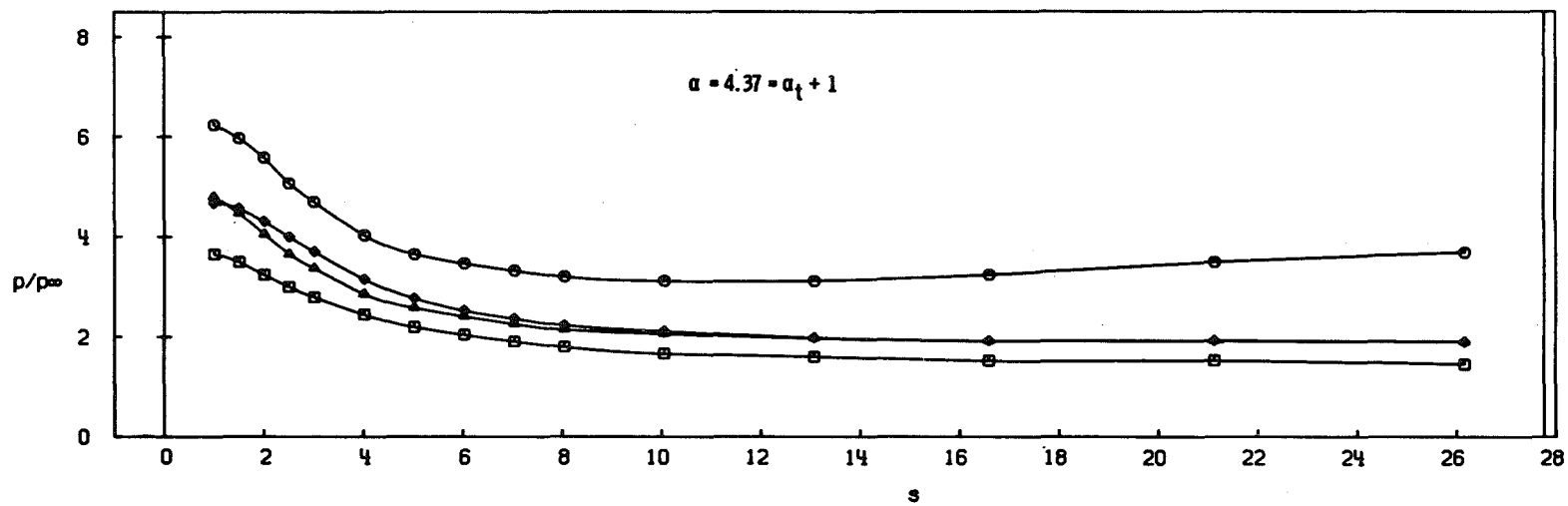
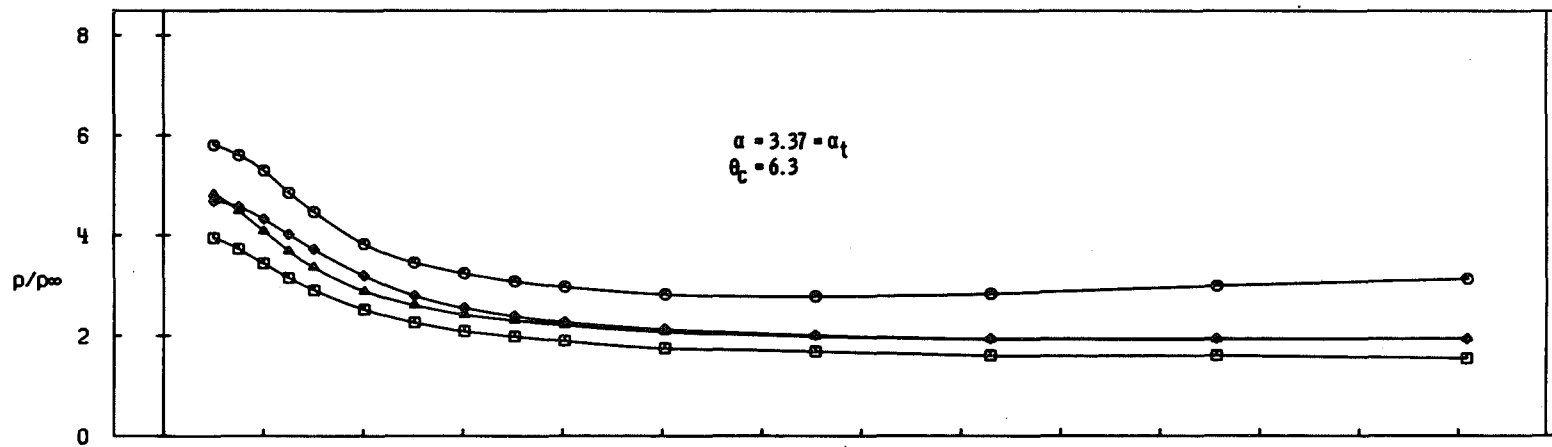
e. Configuration N8 ($\delta_n = 12$), $\phi_m = 0$
 Fig. 24 Continued



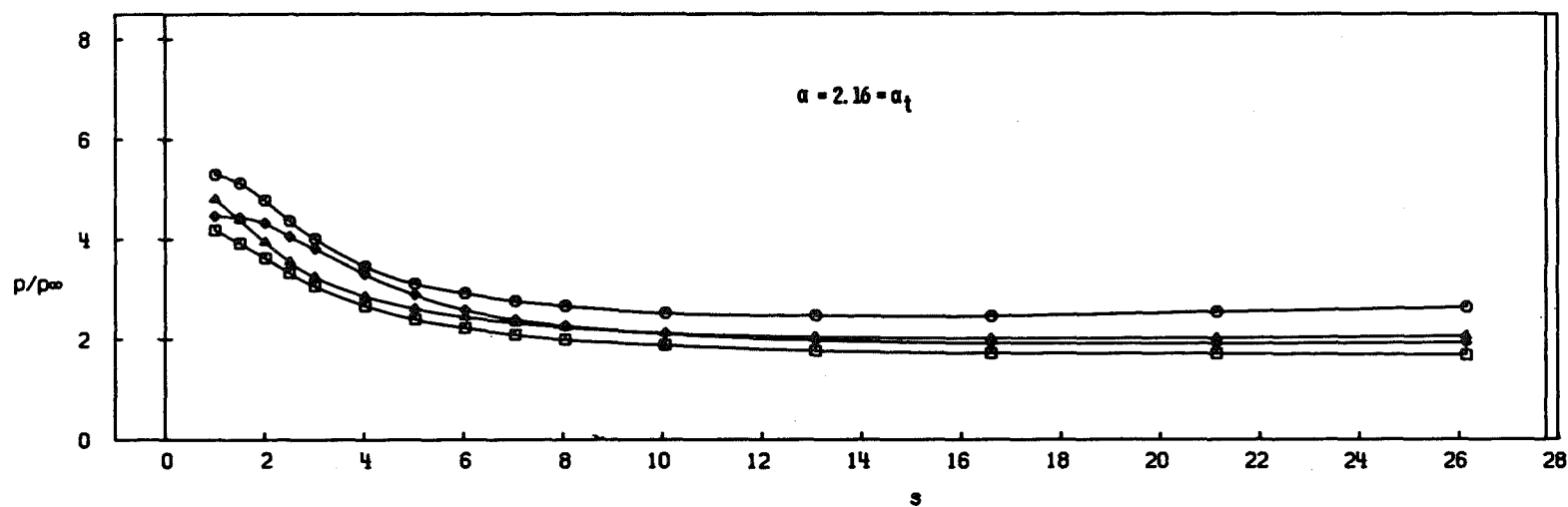
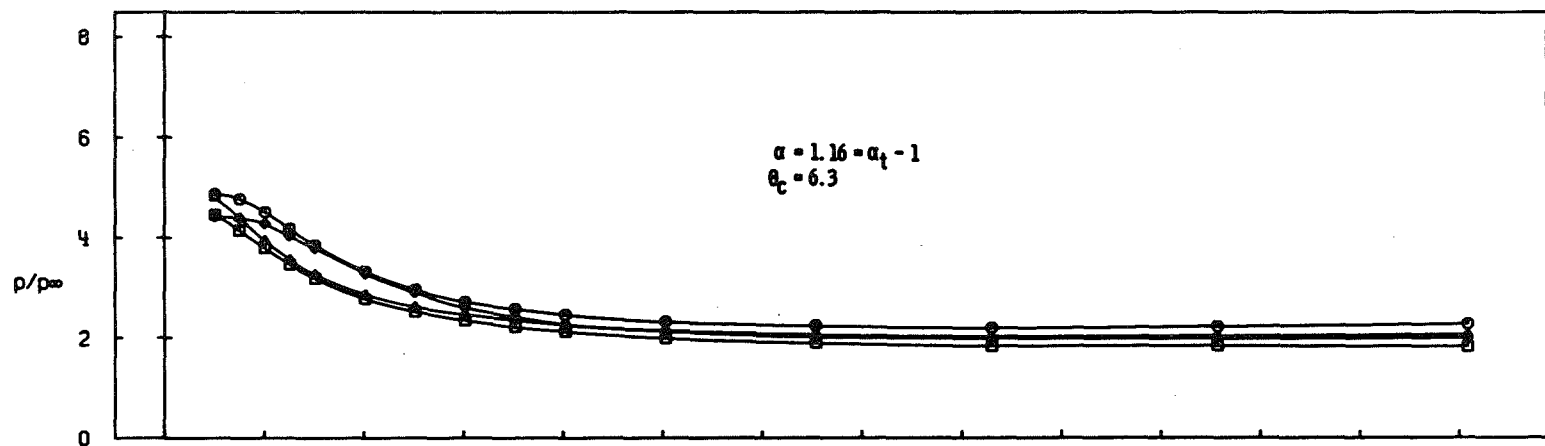
e. Concluded
 Fig. 24 Continued



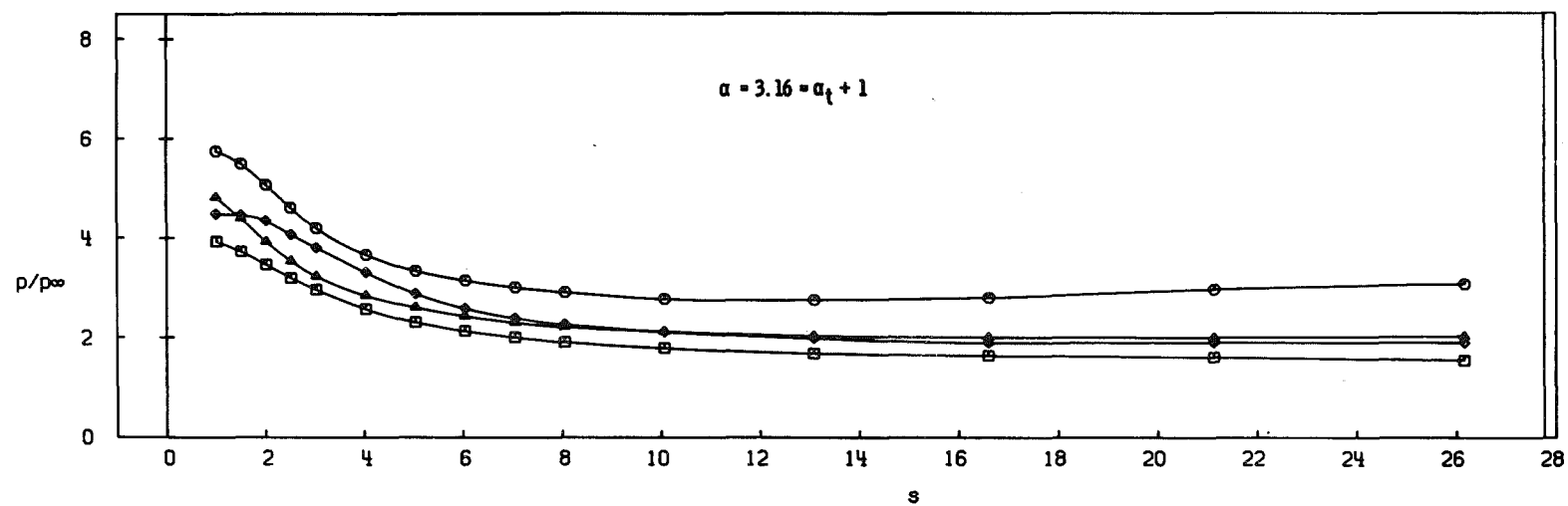
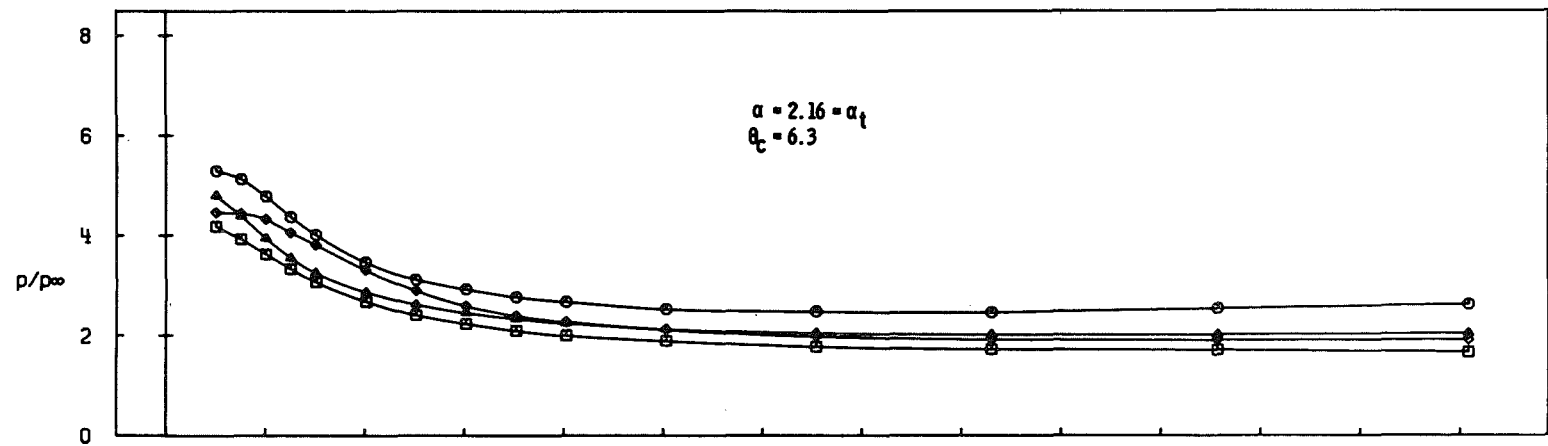
f. Configuration N8 ($\delta_n = 12$), $\phi_m = -30$
Fig. 24 Continued



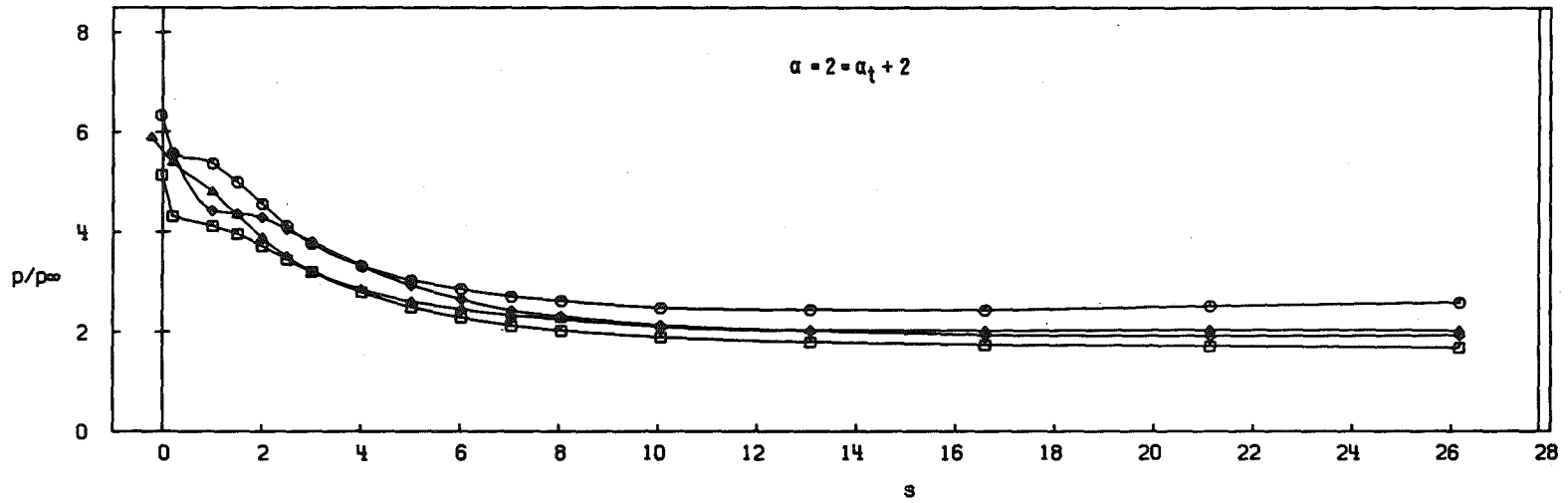
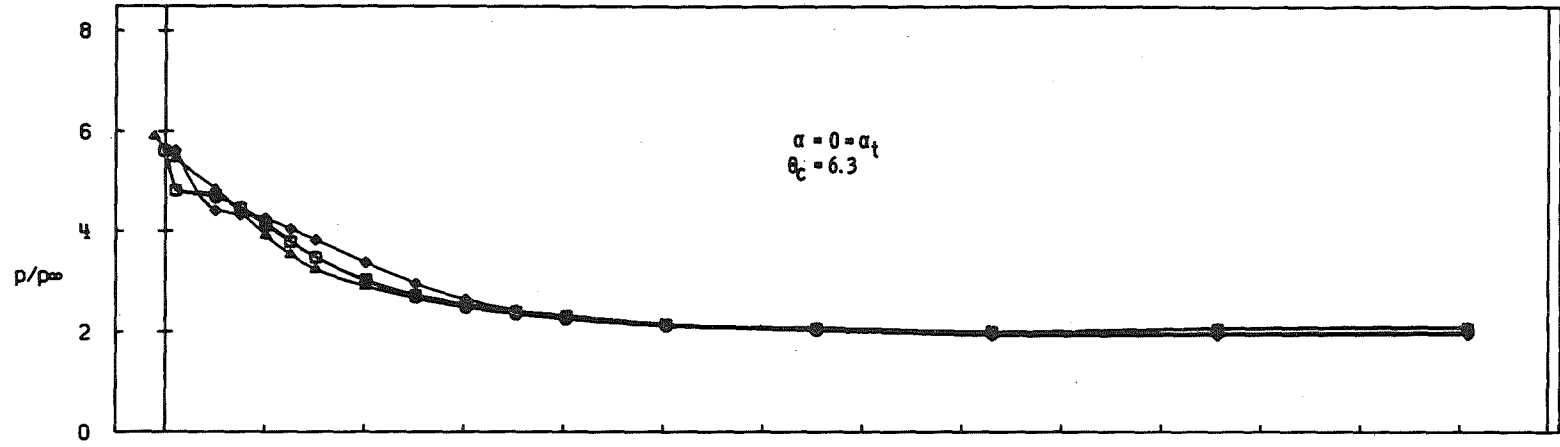
f. Concluded
Fig. 24 Continued



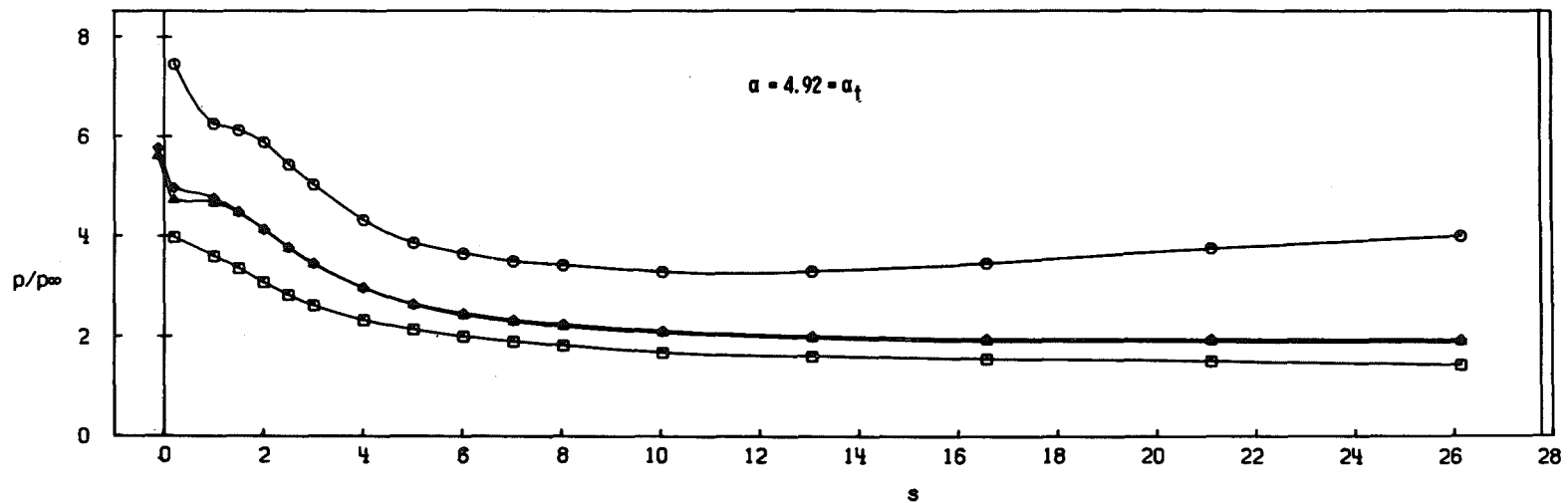
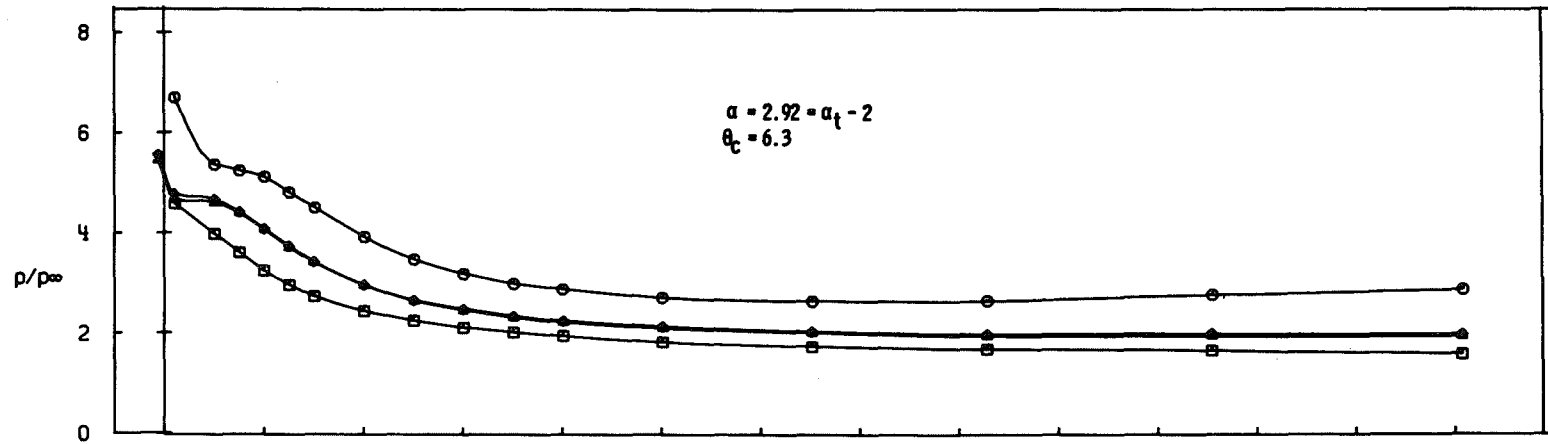
g. Configuration N8 ($\delta_n = 12$), $\phi_m = -60$
Fig. 24 Continued



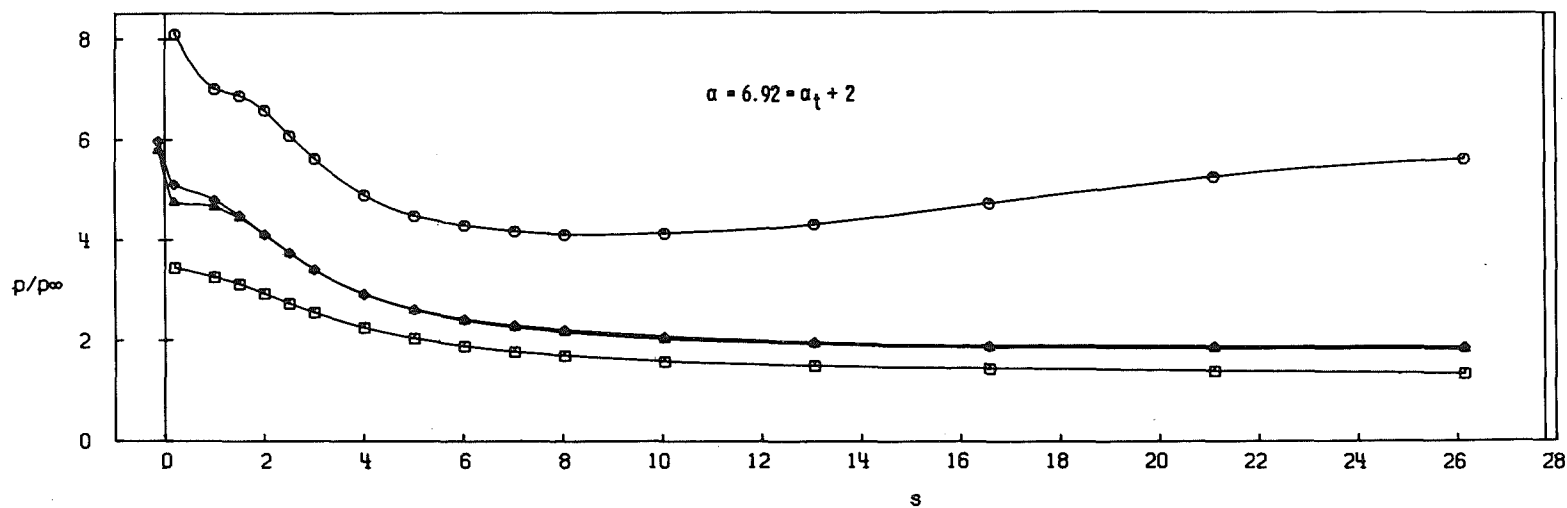
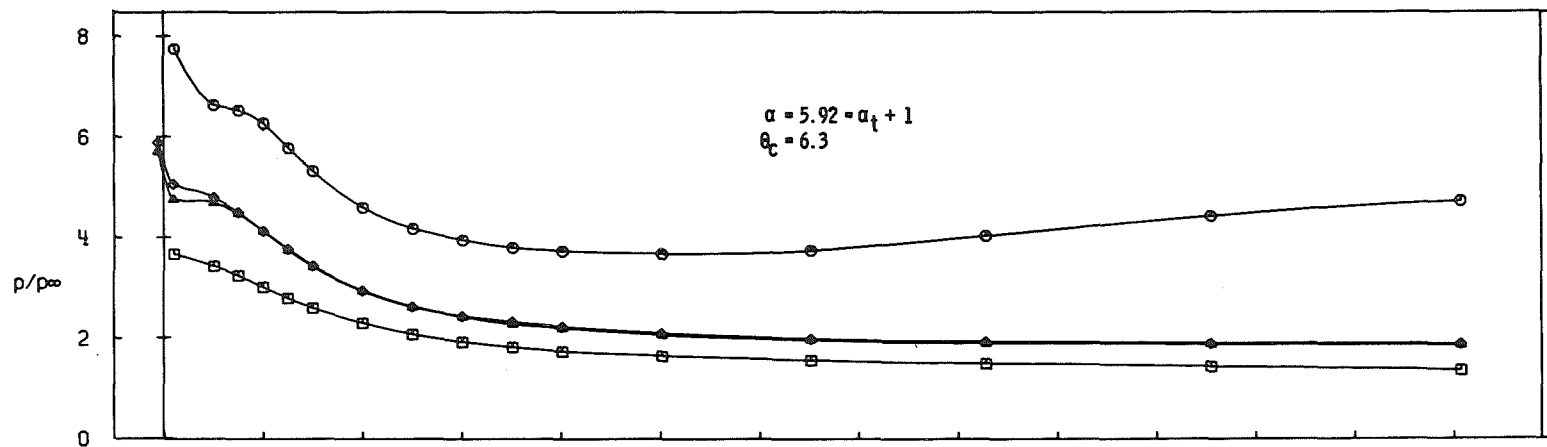
g. Concluded
Fig. 24 Continued



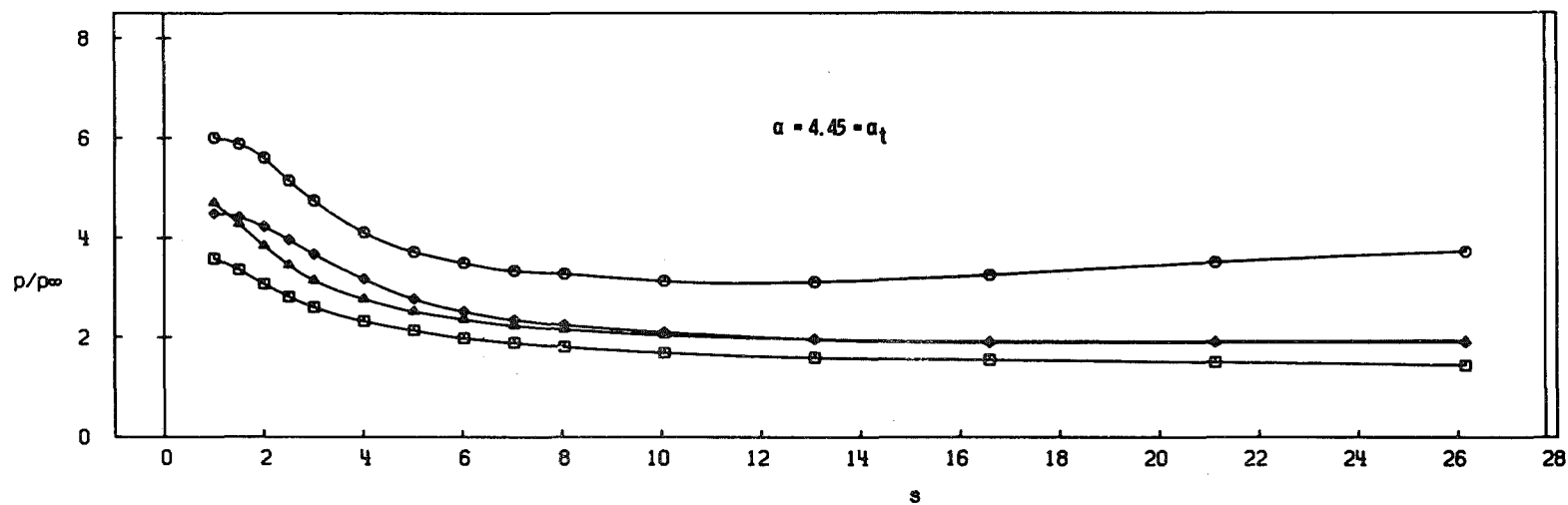
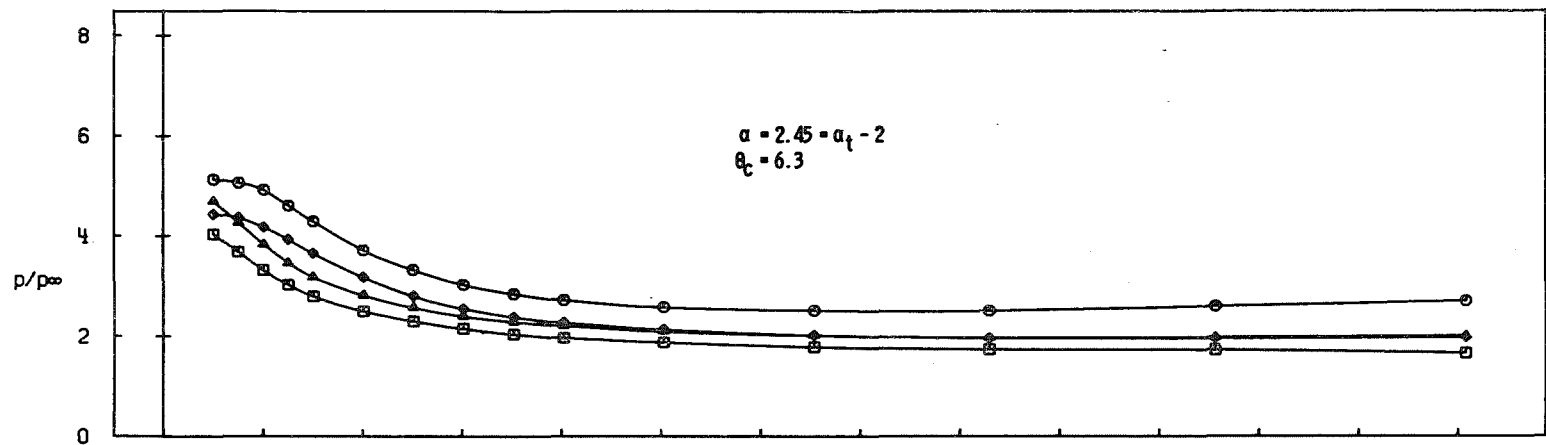
h. Configuration N8 ($\delta_n = 12$), $\phi_m = -90$
 Fig. 24 Continued



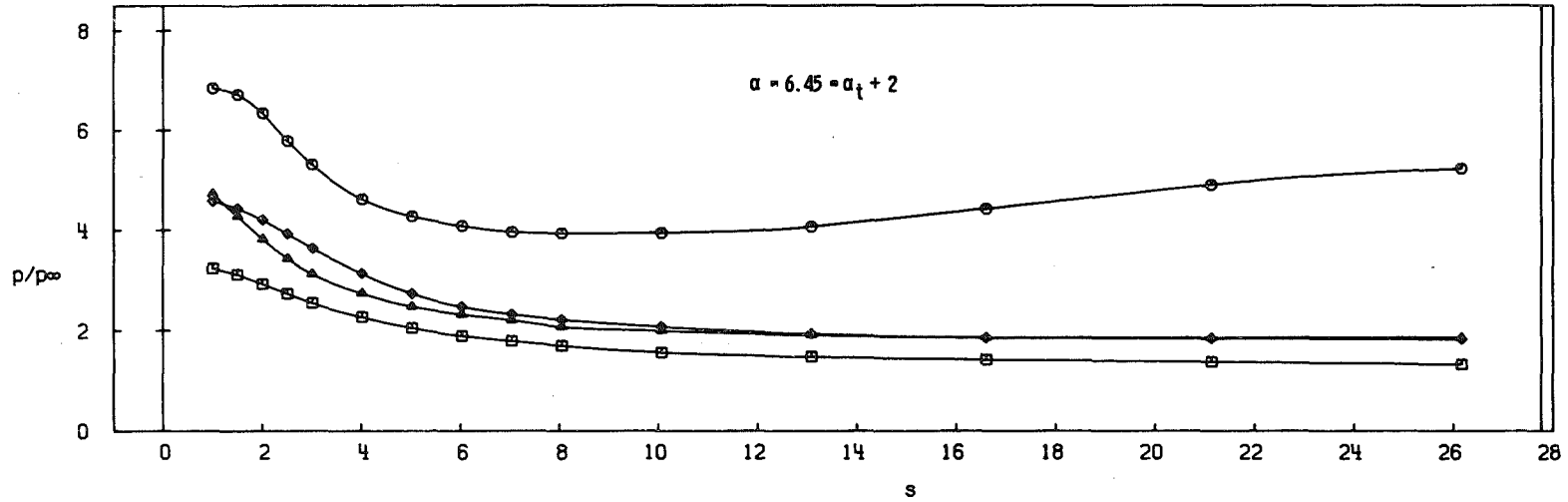
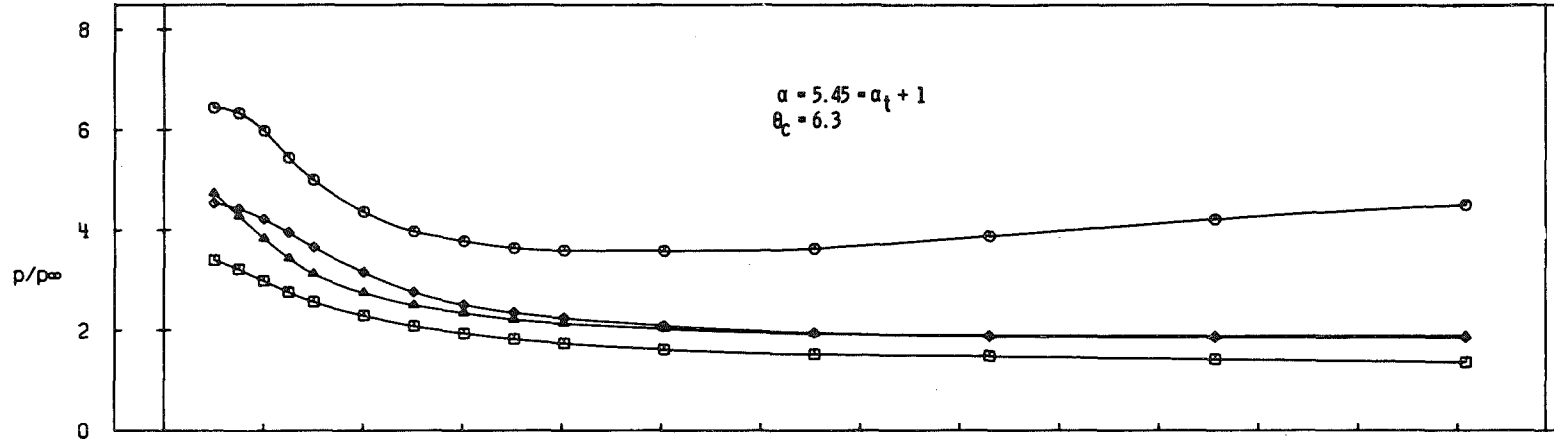
i. Configuration N9 ($\delta_n = 18$), $\phi_m = 0$
 Fig. 24 Continued



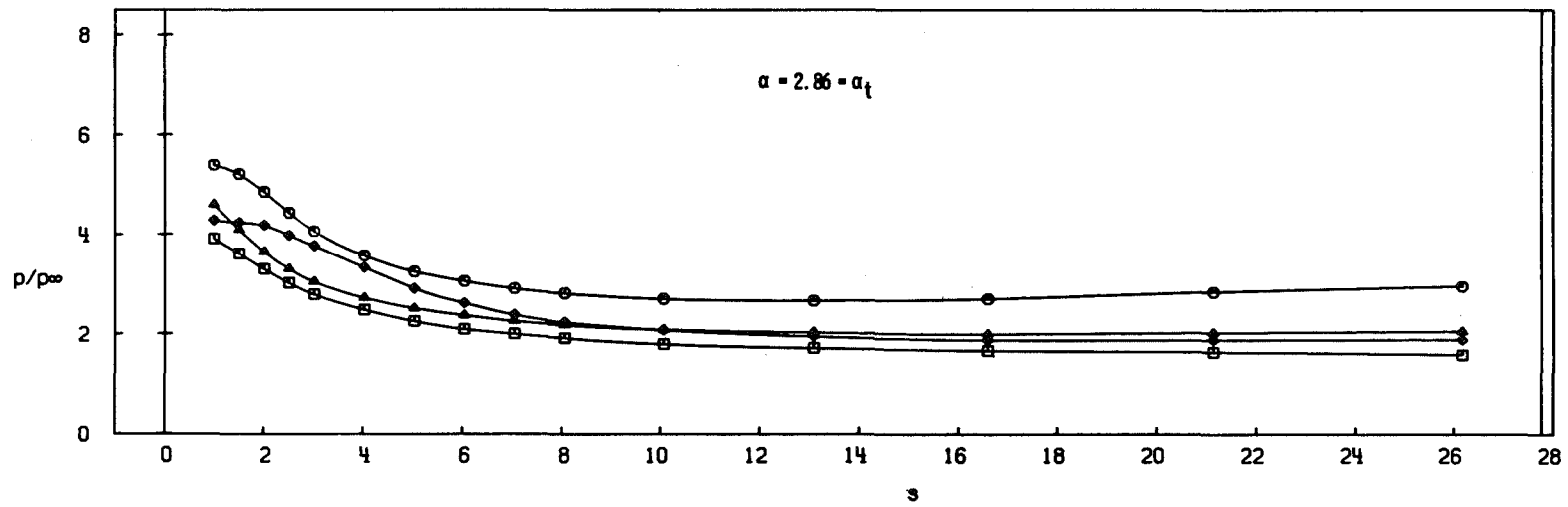
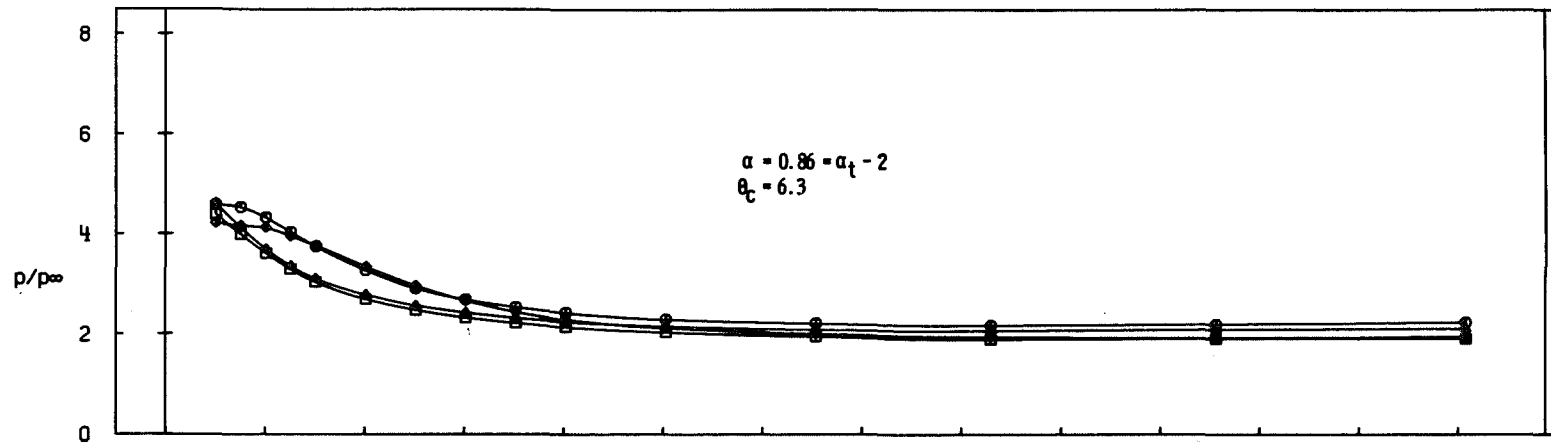
i. Concluded
 Fig. 24 Continued



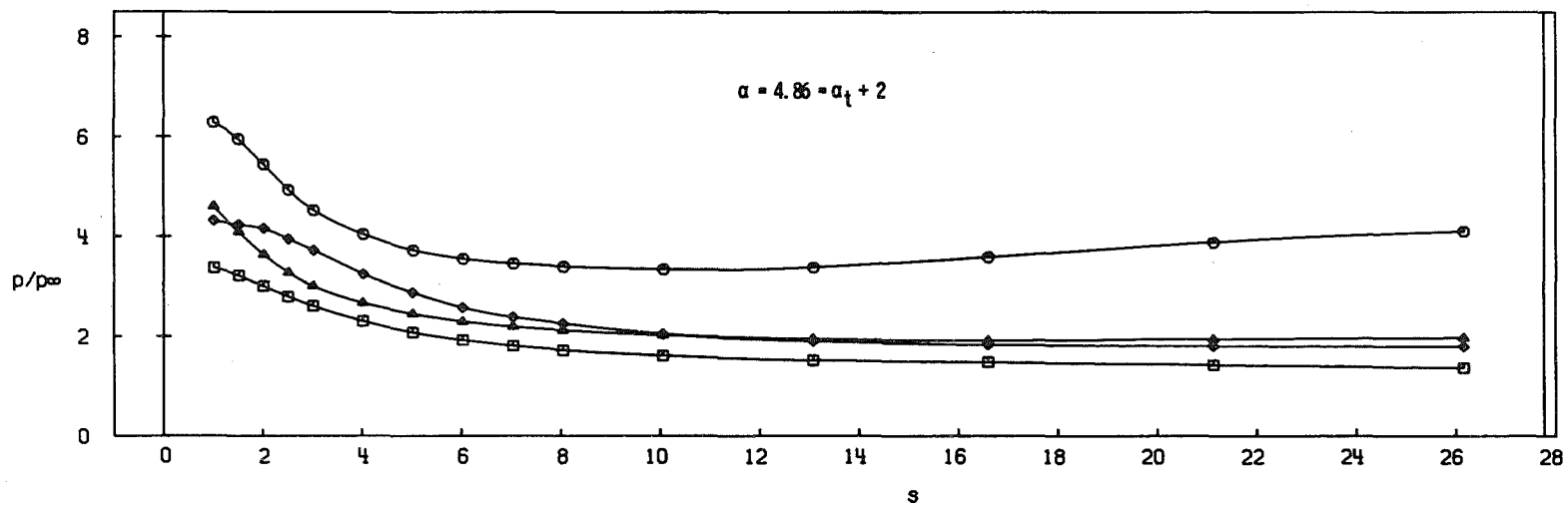
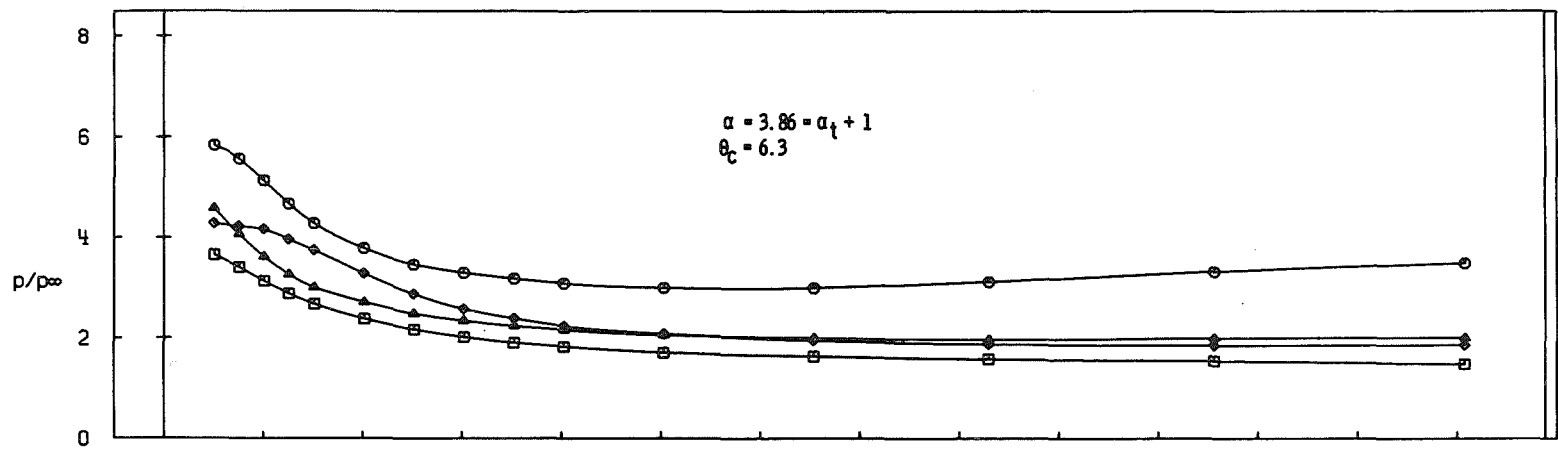
j. Configuration N9 ($\delta_n = 18$), $\phi_m = -30$
 Fig. 24 Continued



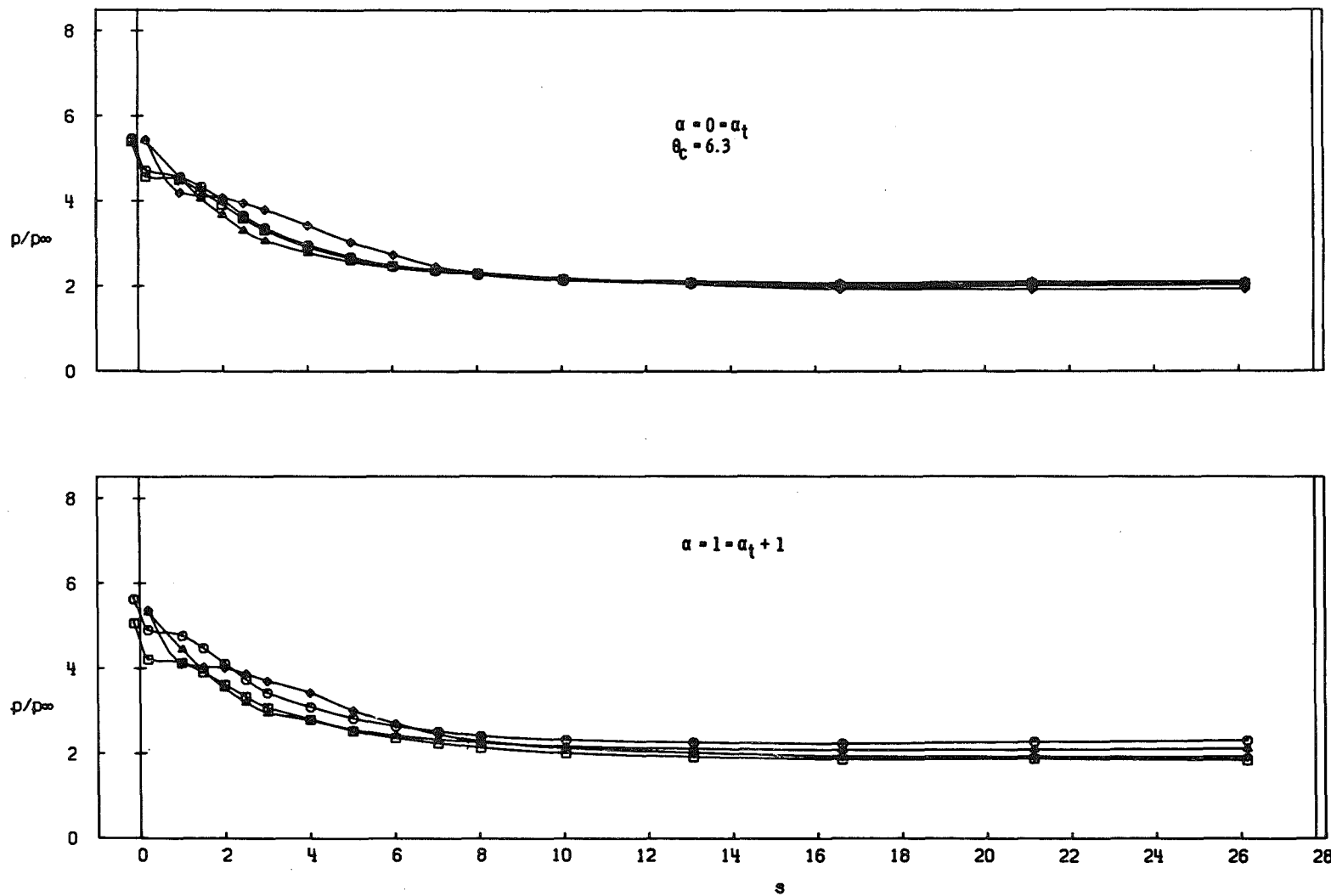
j. Concluded
 Fig. 24 Continued



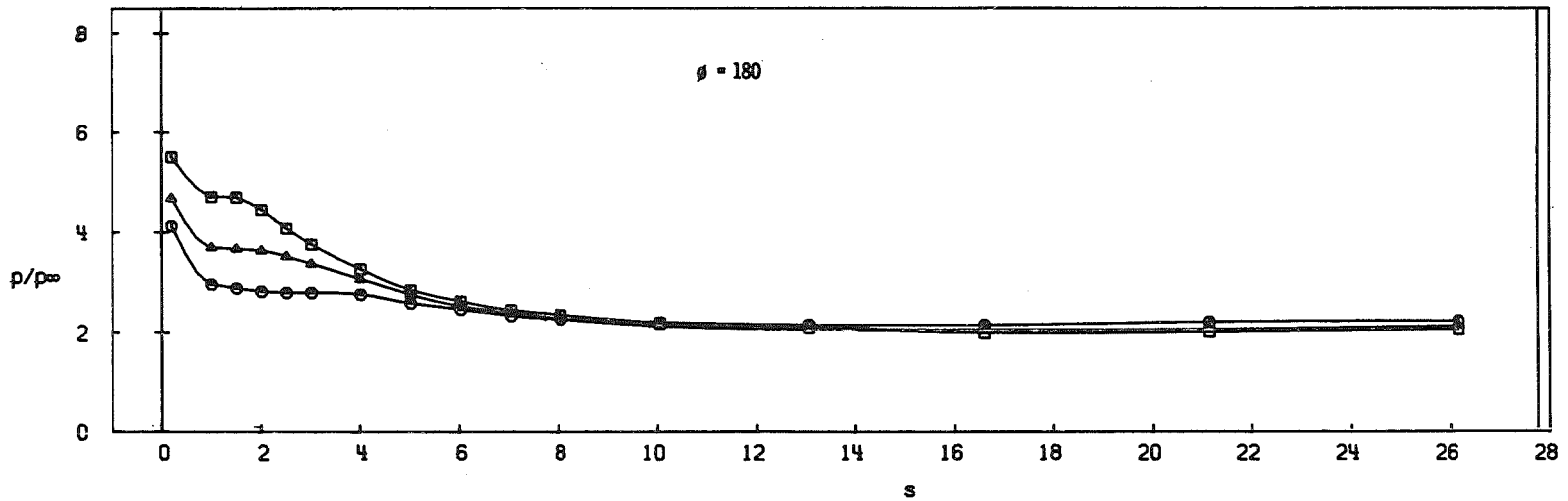
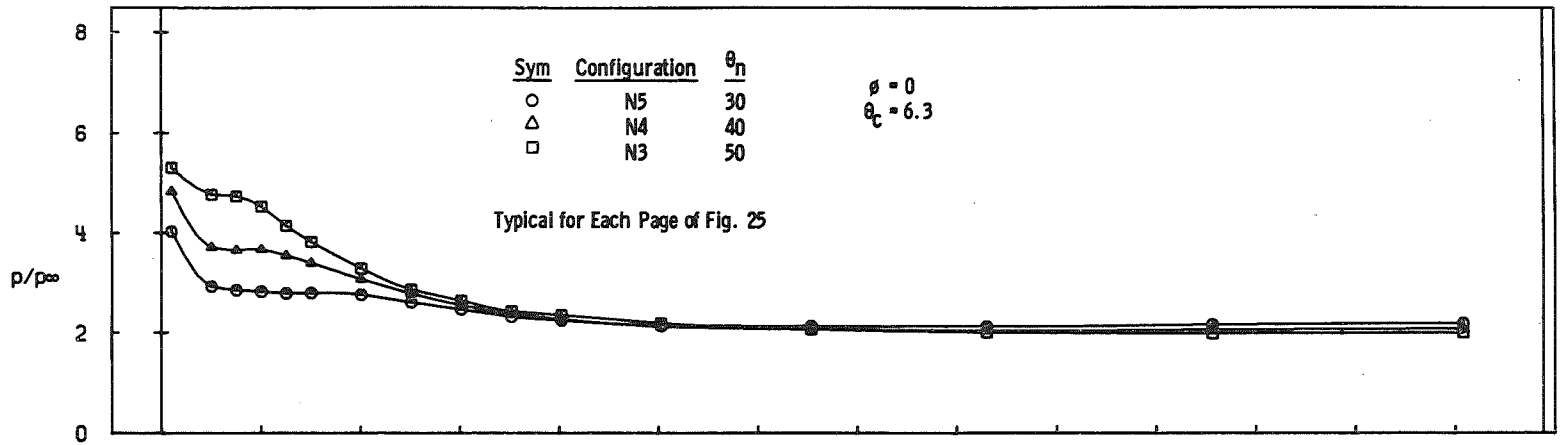
k. Configuration N9 ($\delta_n = 18$), $\phi_m = -60$
 Fig. 24 Continued



k. Concluded
 Fig. 24 Continued

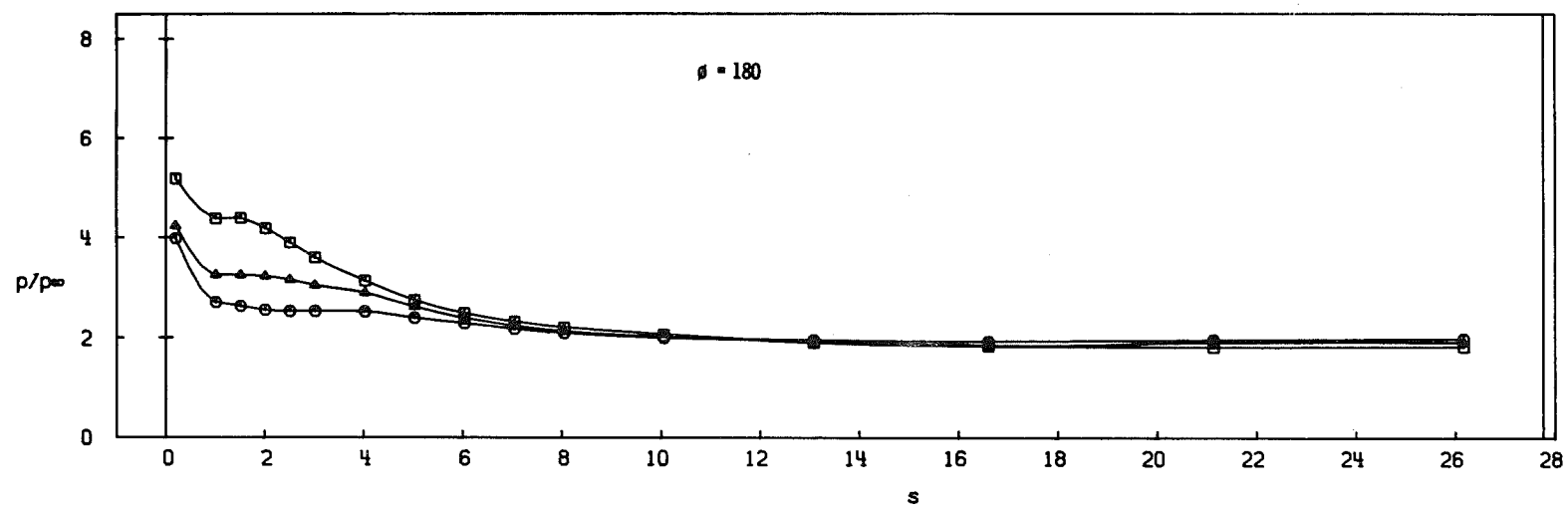
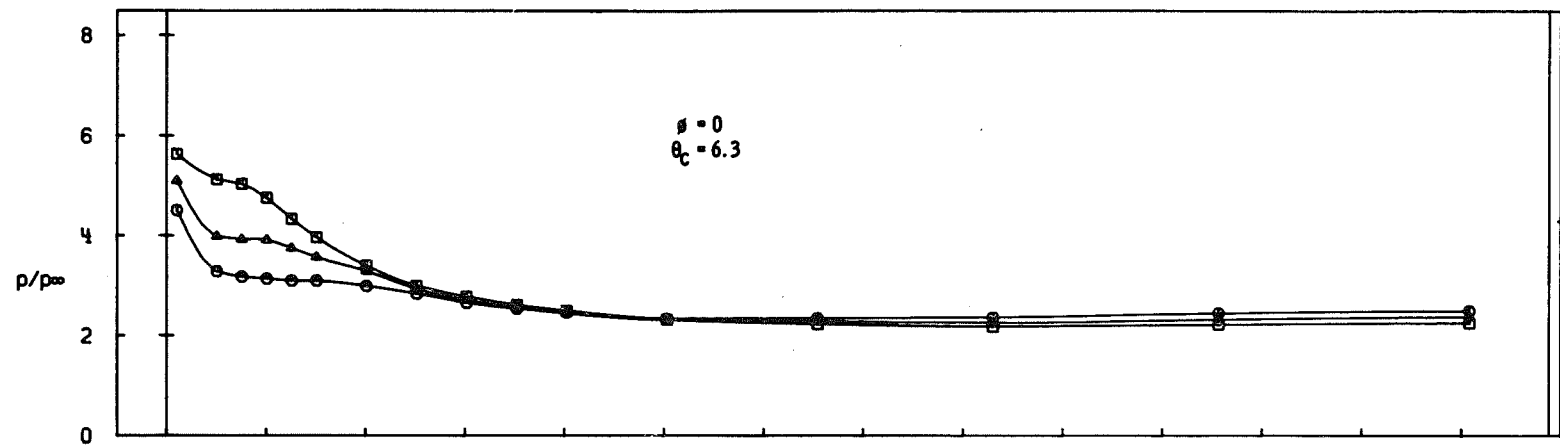


I. Configuration N9 ($\delta_n = 18$), $\phi_m = -90$
 Fig. 24 Concluded

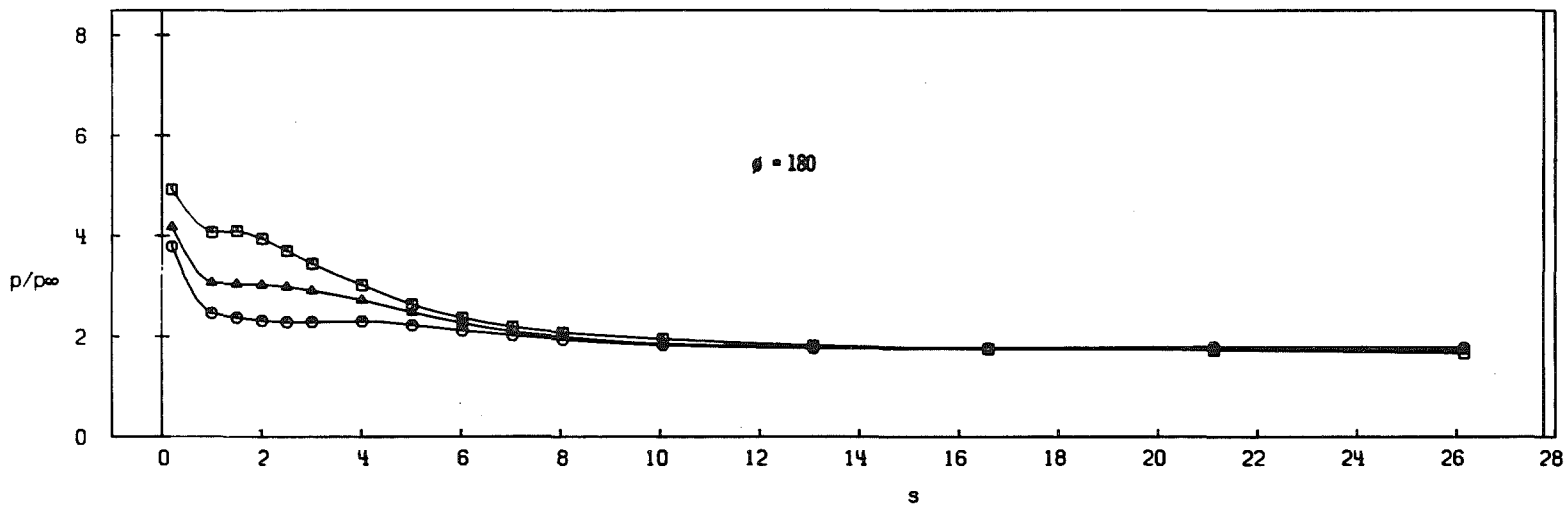
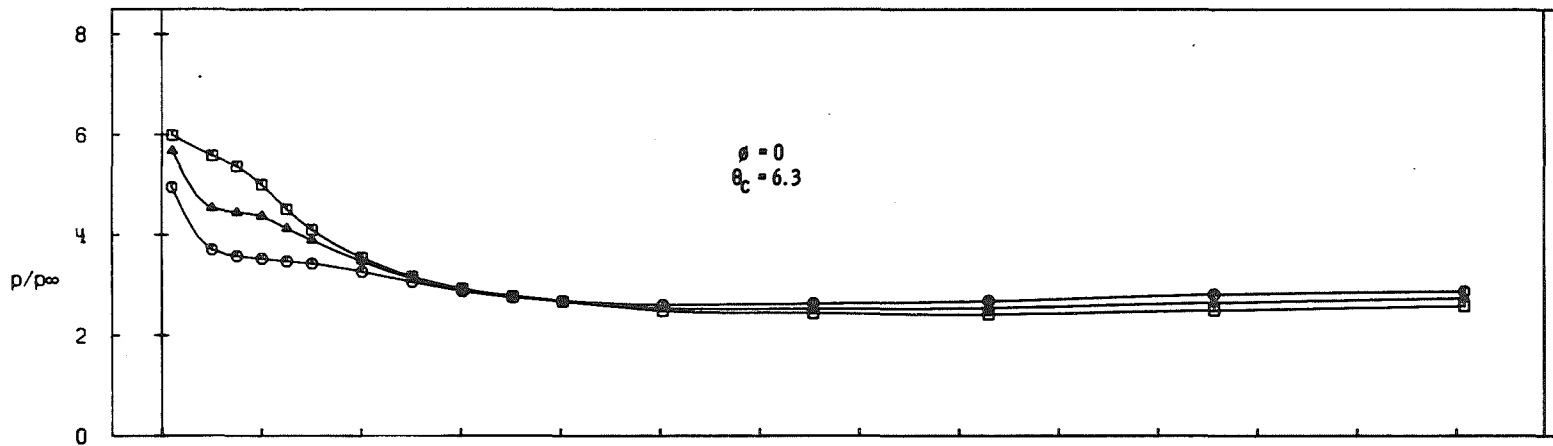


a. $\alpha = 0$

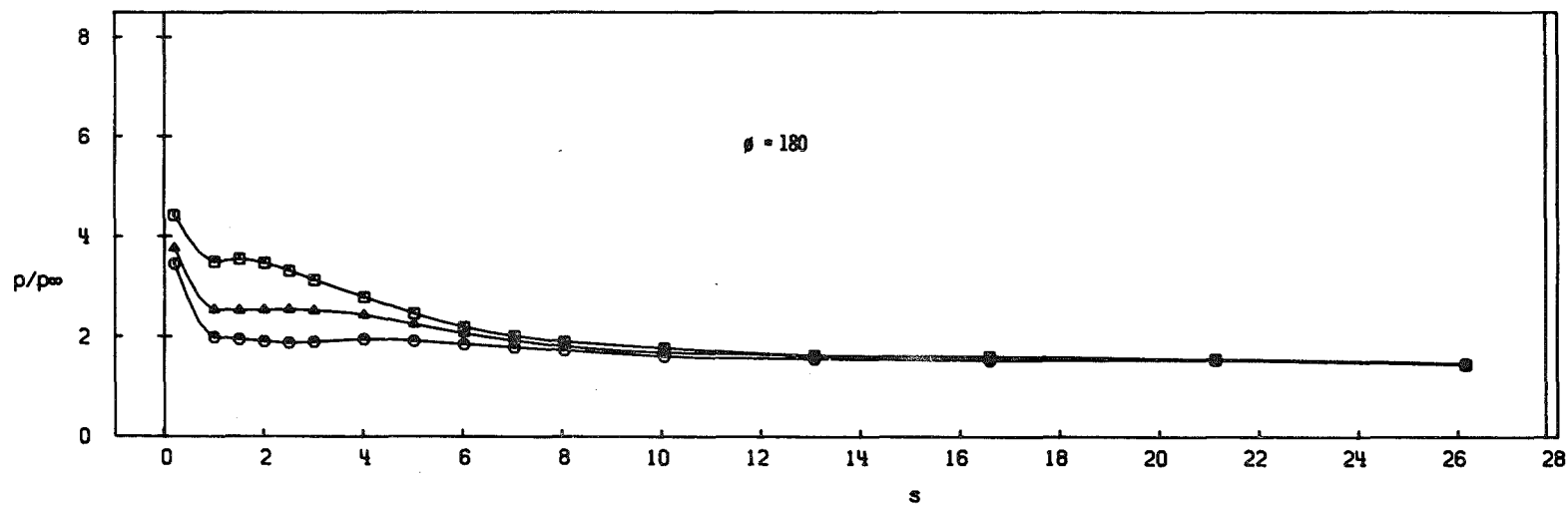
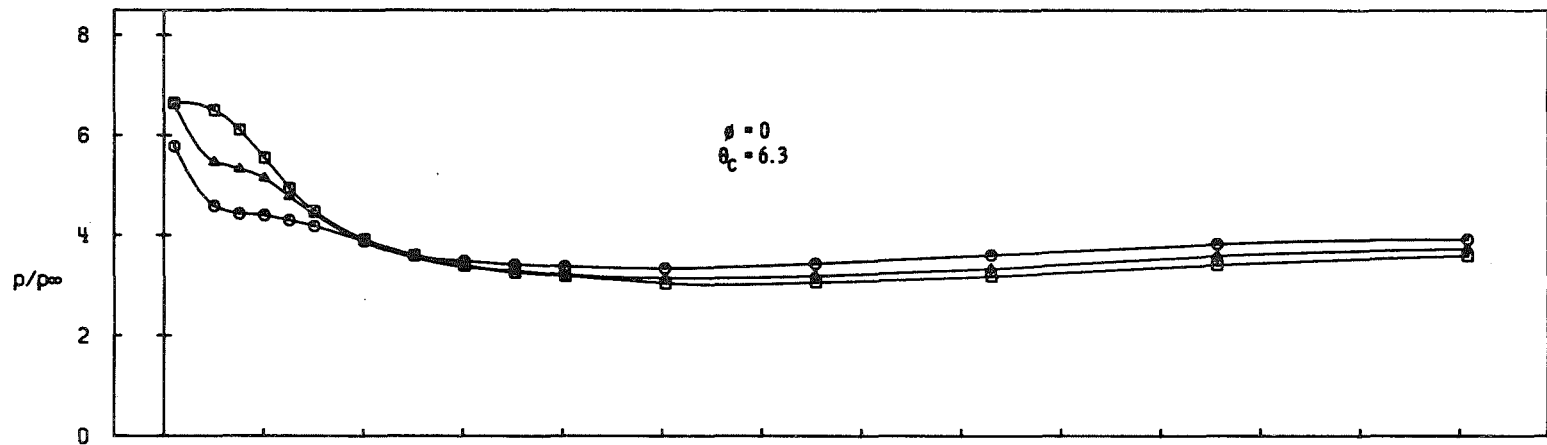
Fig. 25 Effects of Nose Cone Angle (θ_n) on the Main-Cone Windward and Leeward Pressure Distributions, $M_\infty = 8$



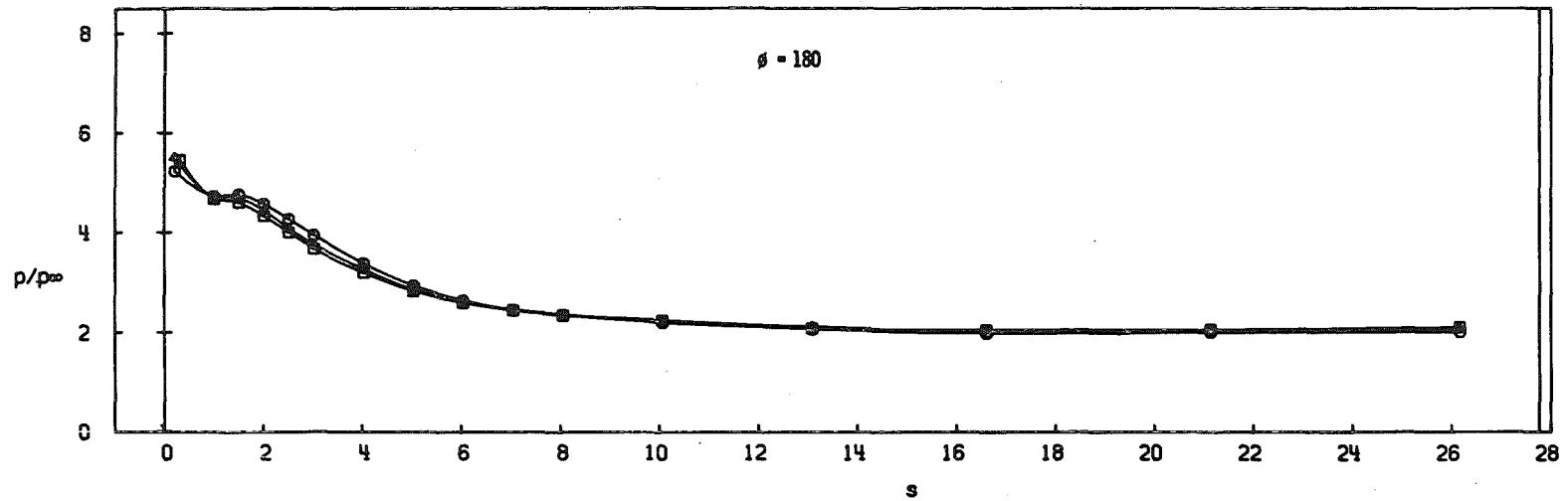
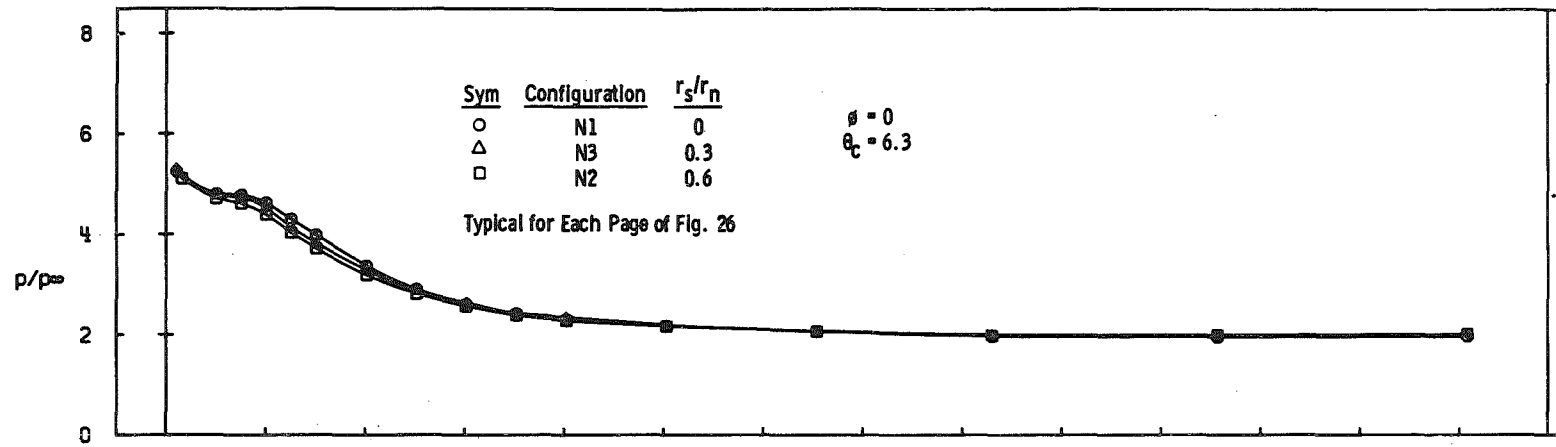
b. $\alpha = 1$
Fig. 25 Continued



c. $a = 2$
Fig. 25 Continued

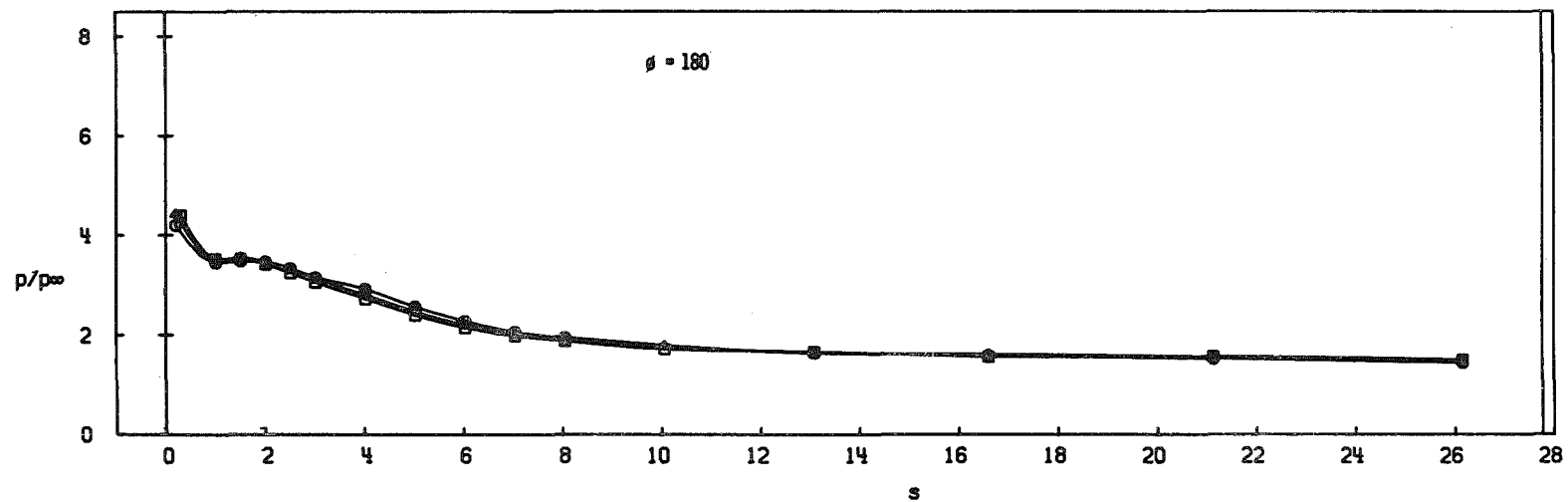
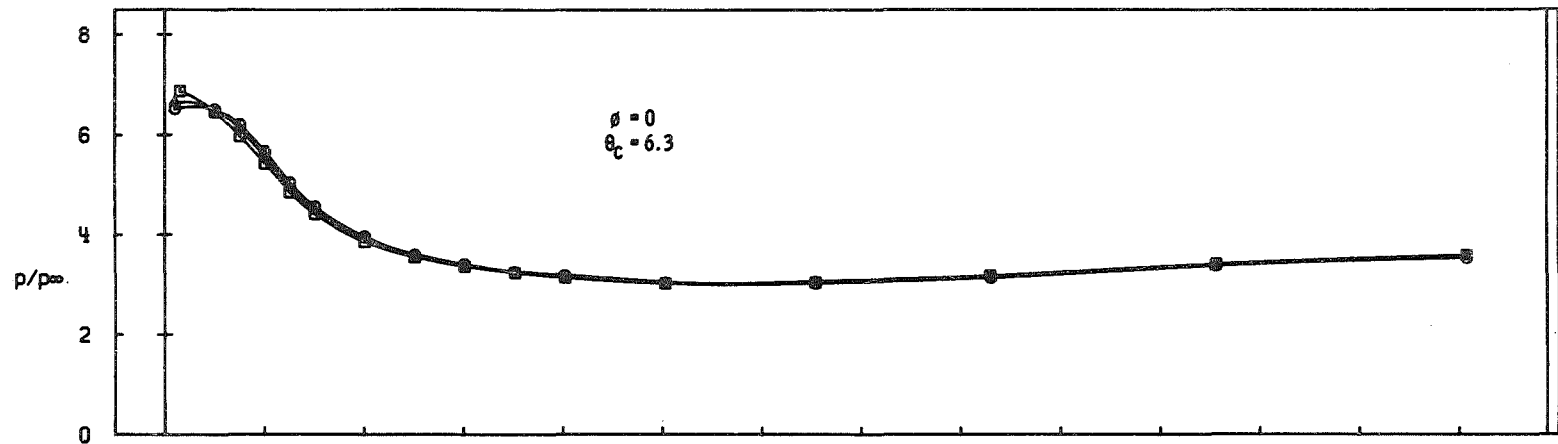


d. $a = 4$
Fig. 25 Concluded

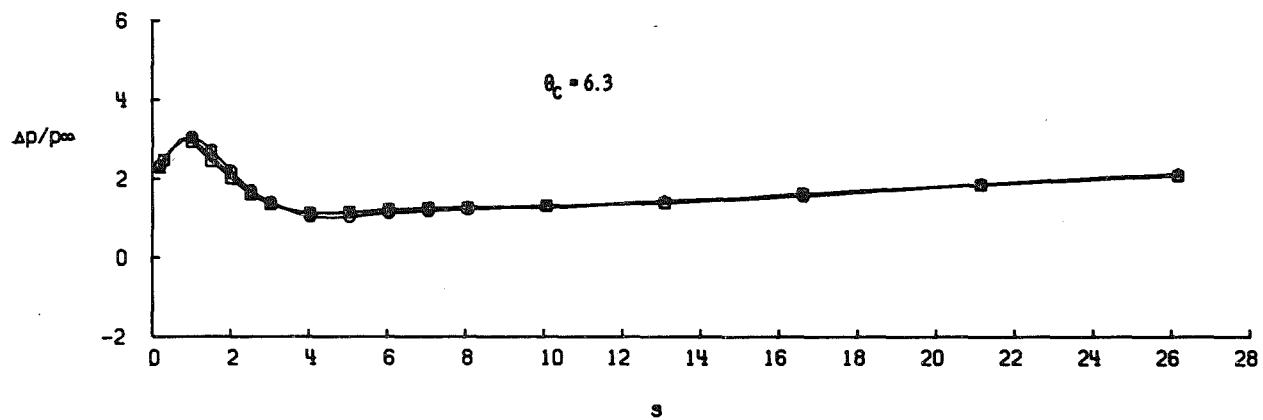


a. $\alpha = 0$

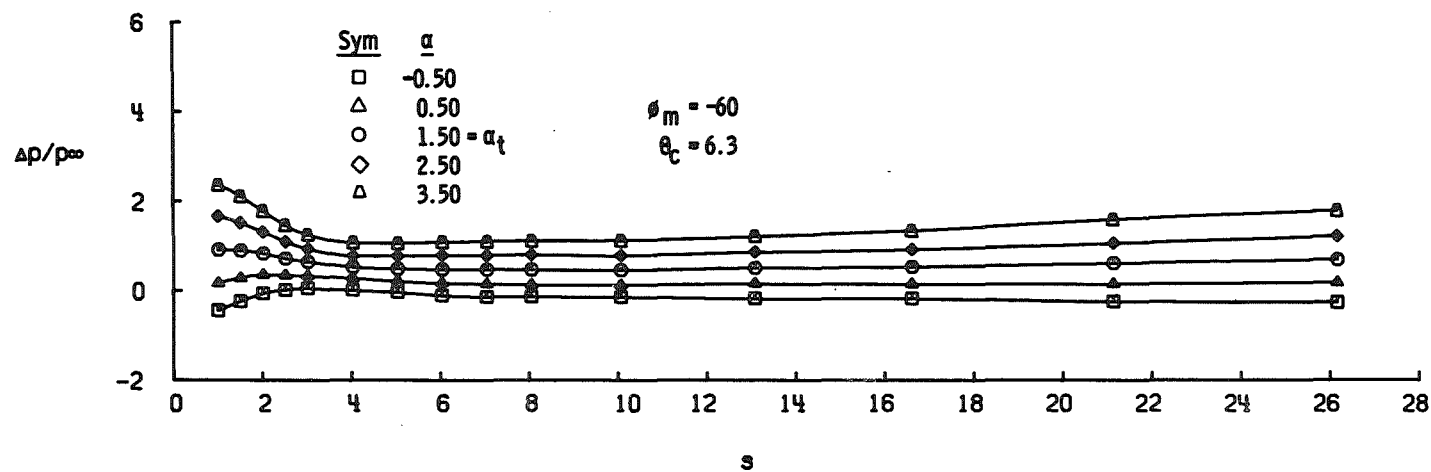
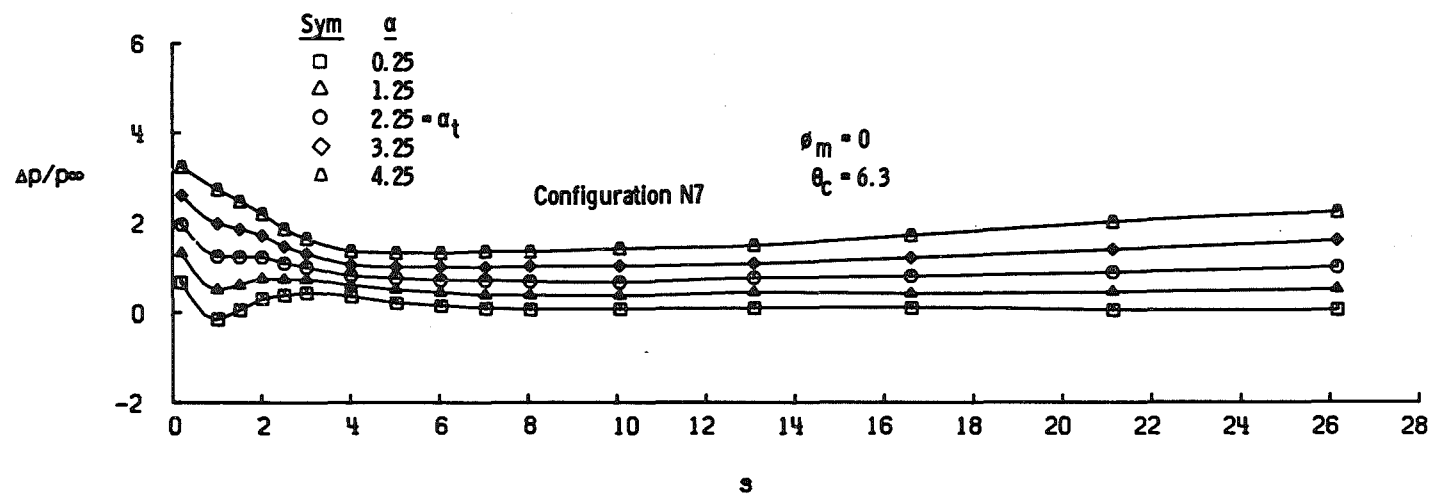
Fig. 26 Effects of Shoulder Radius (r_s) on the Main-Cone Windward and Leeward Pressure Distributions, $M_\infty = 8$



b. $\alpha = 4$
Fig. 26 Continued

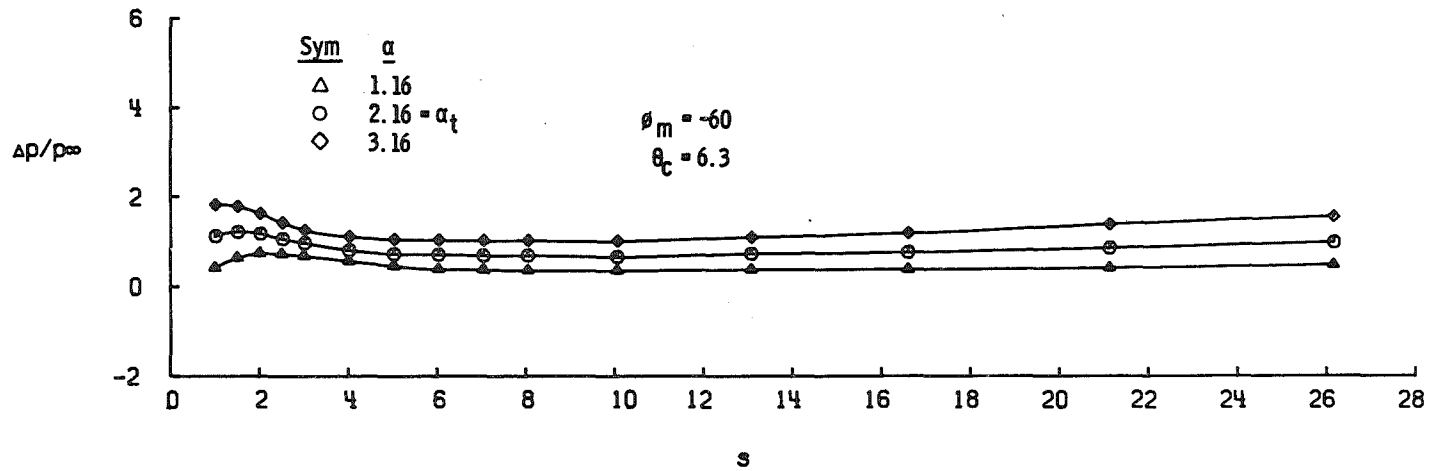
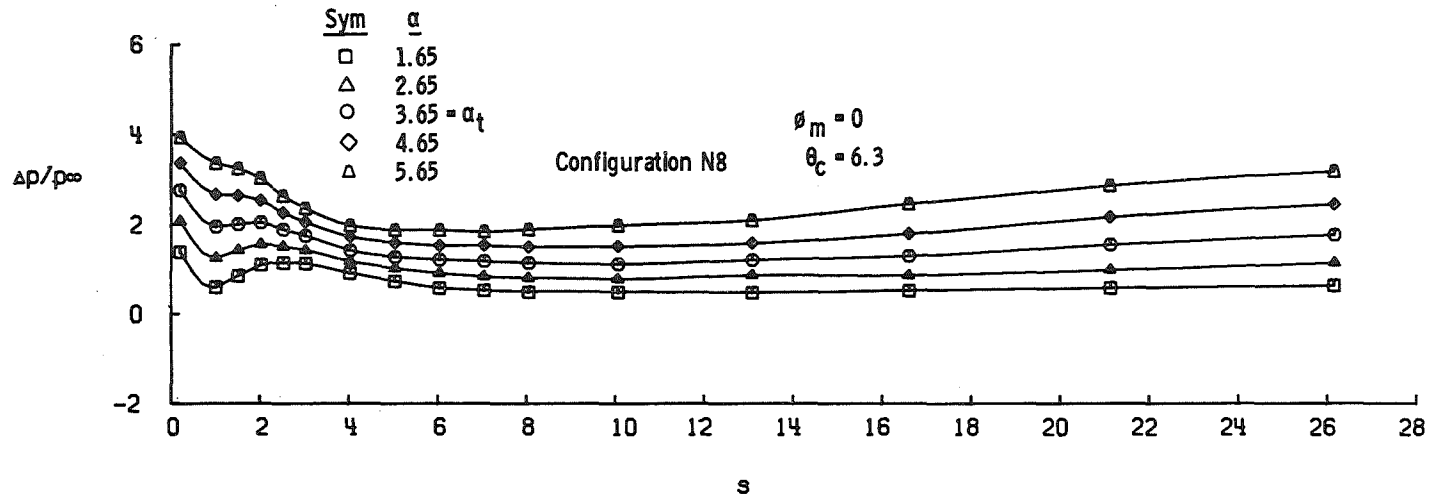


b. Concluded
Fig. 26 Concluded

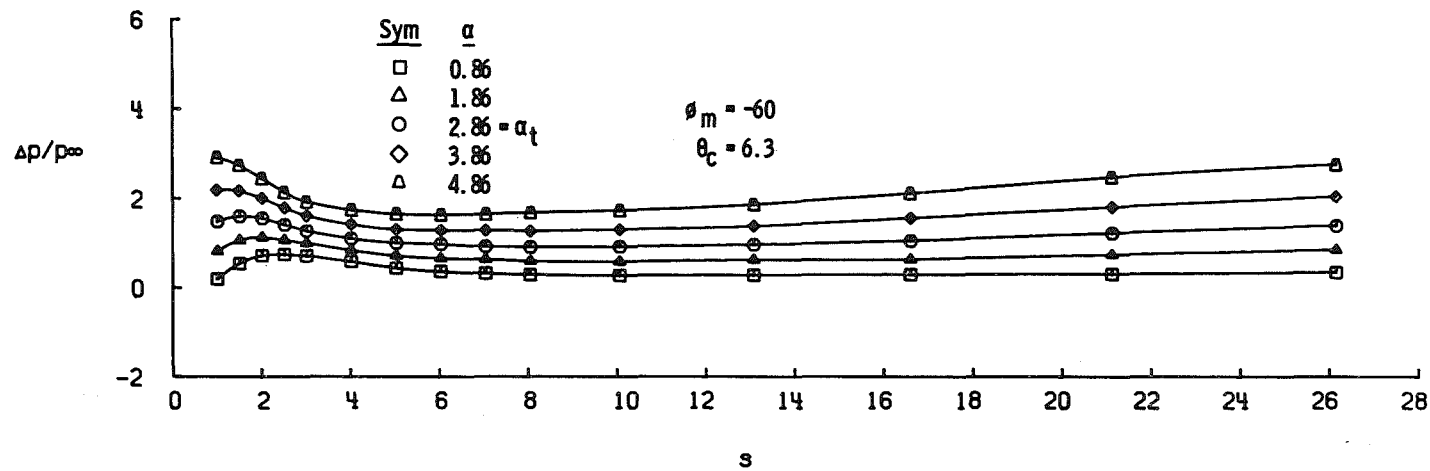
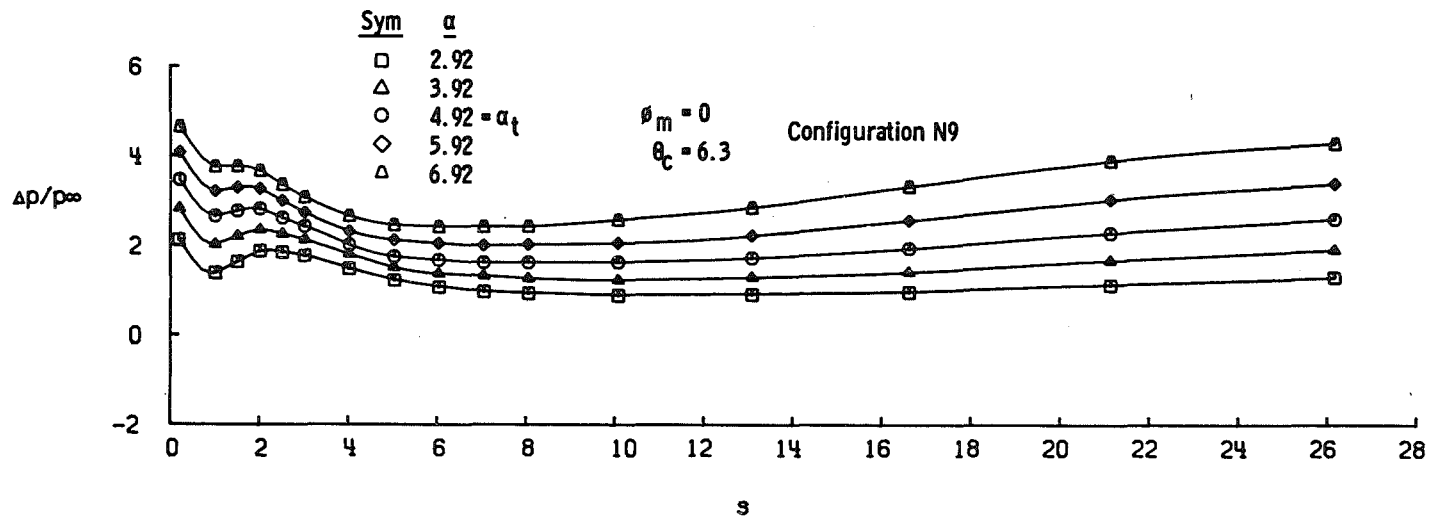


a. 6-deg Cant

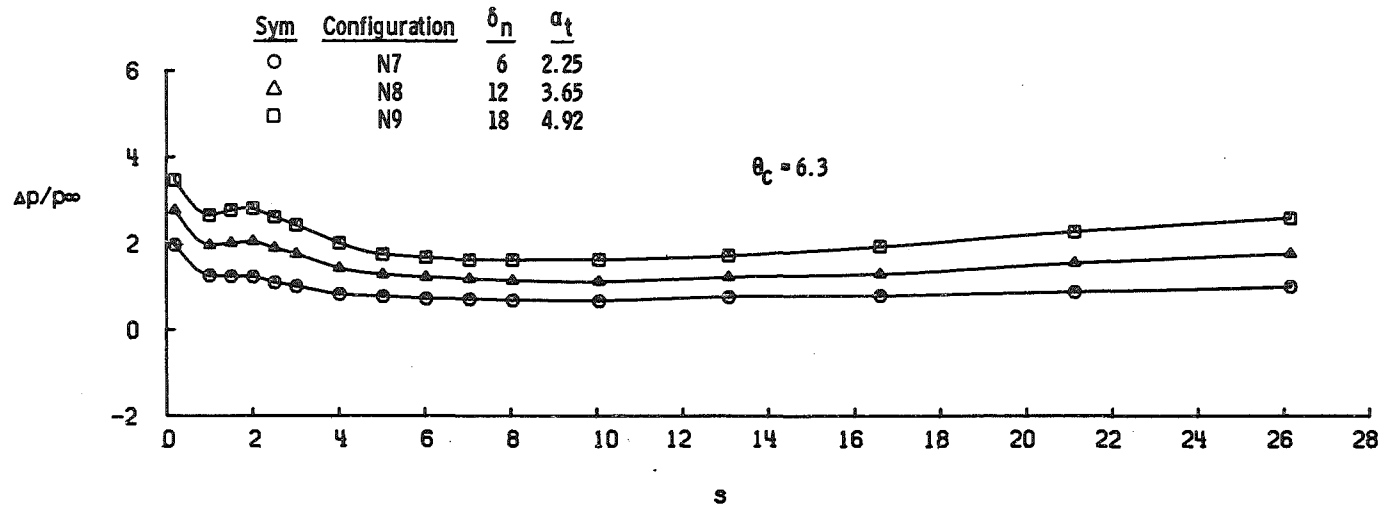
Fig. 27 Effects of Deviations from Trim Condition on the Main-Cone Differential Pressure Distributions for Asymmetrical Biconics, $M_\infty = 8$



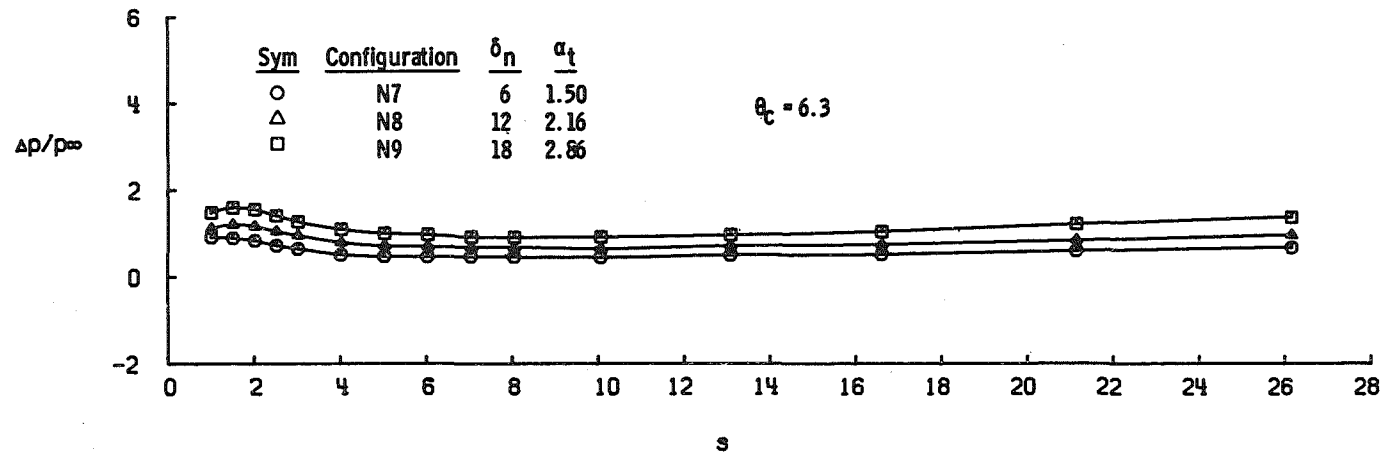
b. 12-deg Cant
Fig. 27 Continued



c. 18-deg Cant
Fig. 27 Concluded

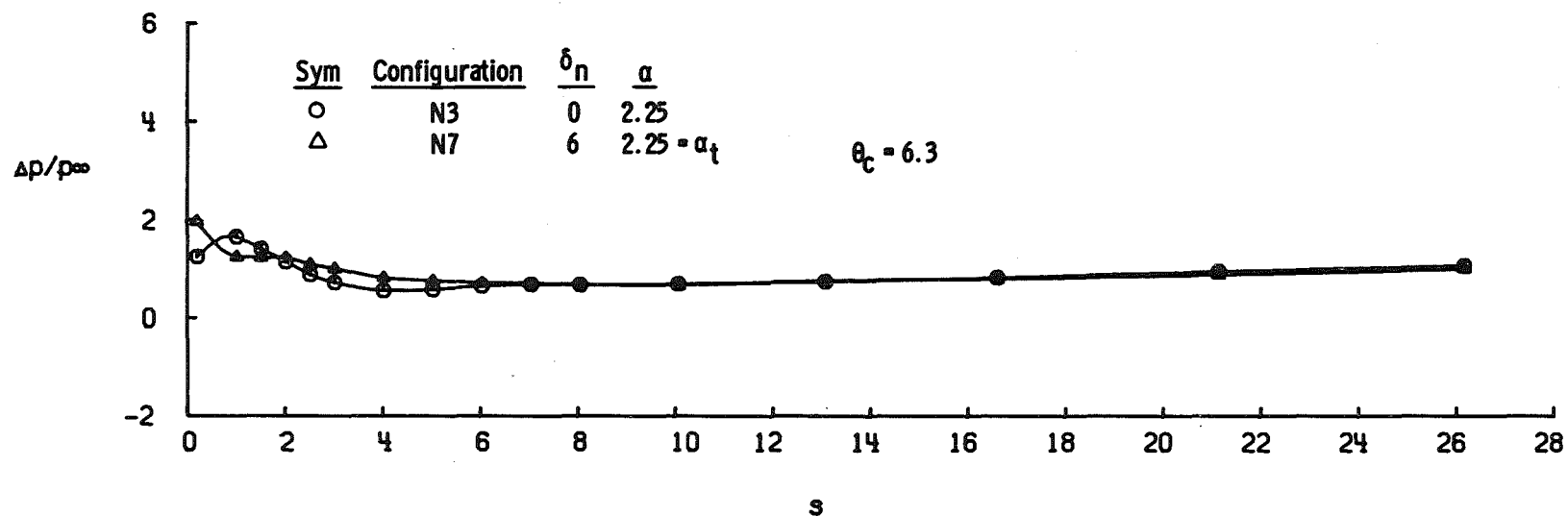


a. $\phi_m = 0$



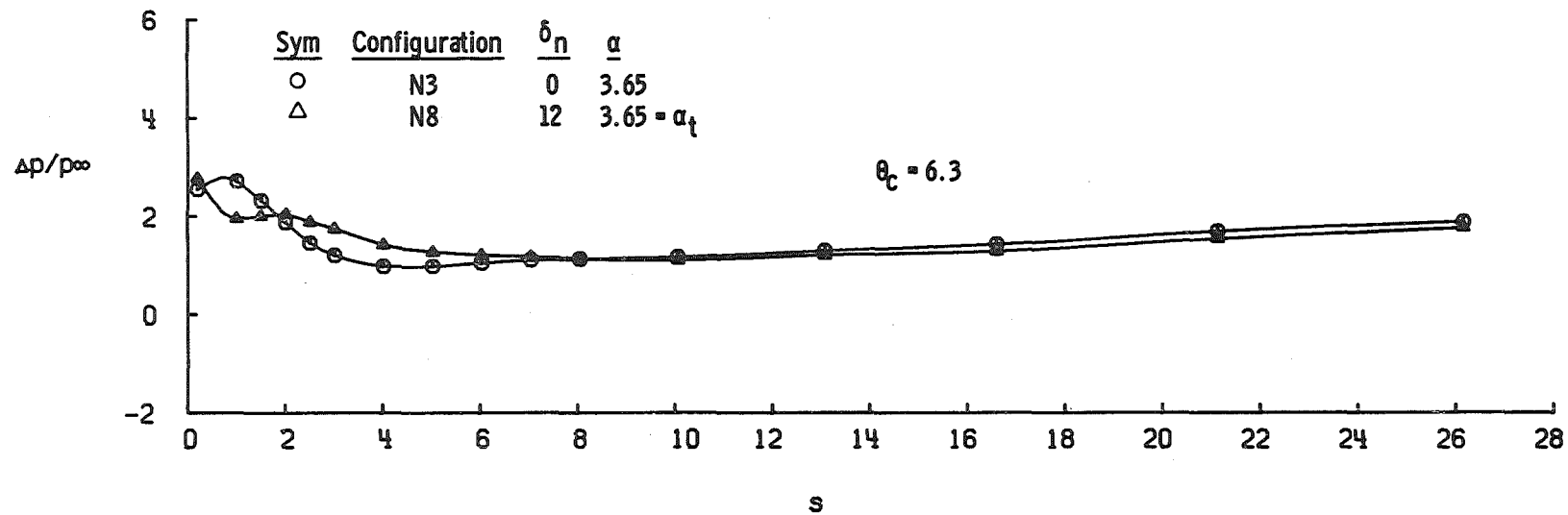
b. $\phi_m = -60$

Fig. 28 Comparisons of Aft-Cone Differential Pressure Distributions for Trimmed Asymmetrical Biconics, $M_\infty = 8$

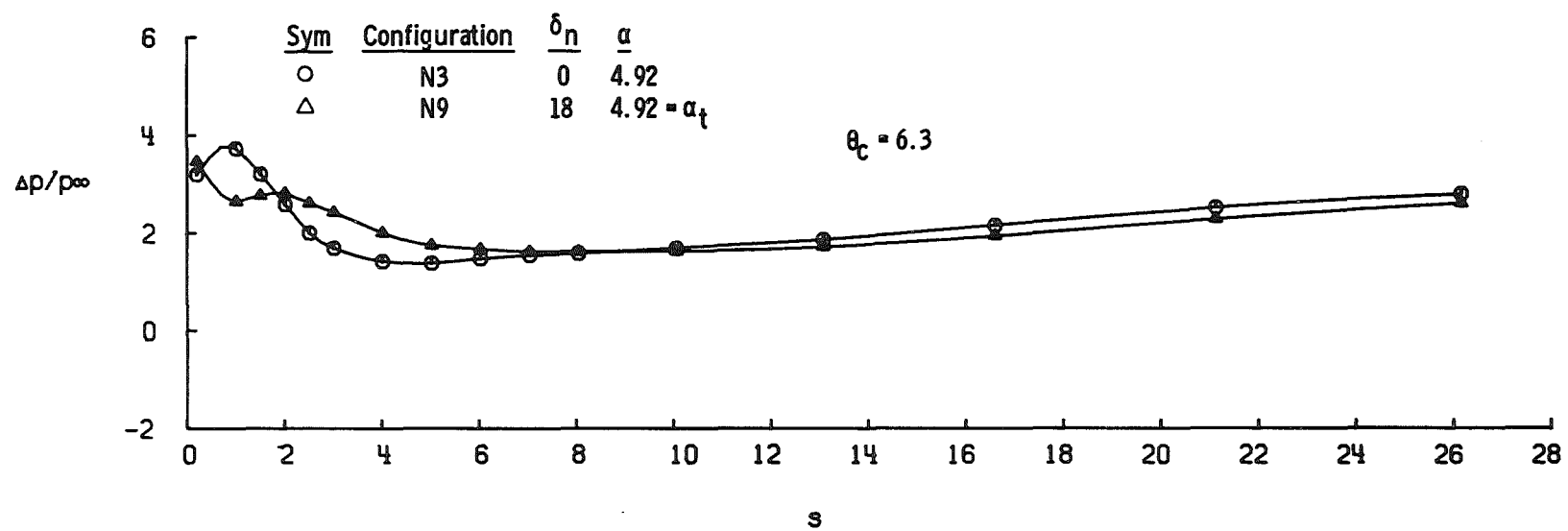


a. $\alpha = 2.25 = \alpha_t$ for Configuration N7

Fig. 29 Comparisons of Aft-Cone Differential Pressure Distributions for Symmetrical and Asymmetrical Biconics at the Asymmetrical Trim Angle, $M_\infty = 8$ and $\phi_m = 0$



b. $\alpha = 3.65 = \alpha_t$ for Configuration N8
Fig. 29 Continued



c. $\alpha = 4.92 = \alpha_t$ for Configuration N9
 Fig. 29 Concluded

TABLE I
TUNNEL B STATIC-FORCE TEST SUMMARY

θ_c	Configu- ration	ϕ_m	α
4.0	N3	0	α_1
4.0	N10		
6.3	N1		
	N2		
	N3		
	N4		
	N5		
	N6	0	α_2
		-30	
		-60	
		-90	
	N7	0	α_3
		-30	
		-60	
		-90	
	N8	0	α_3
		-30	
		-60	
		-90	
	N9	0	α_3
		-30	
		-60	
		-90	
	N10	0	α_1
9.0	N3	0	

Note: $M_\infty = 8$ and $\Delta\phi = 0$

α_1 : $\alpha = 0, \pm 0.5, \pm 1, \pm 2, \pm 3, \pm 4$, and ± 5 deg

α_2 : $\alpha = 0, \pm 0.5, \pm 1, \pm 2, \pm 3, \pm 4, \pm 5, \pm 6$, and ± 7 deg

α_3 : $\alpha = 0, \pm 0.5, \pm 1, \pm 2, \pm 3, \pm 4, \pm 5, 7, 9, 11$, and $\approx(\alpha_t \pm 0.5)$ deg

TABLE II
TUNNEL B PRESSURE TEST SUMMARY,
SYMMETRICAL CONFIGURATIONS

Configuration	α	$\phi_m = -30$	$\phi_m = 0$	$\phi_m = 30$
N1 ↓	0	-	x	x
	1.00	x	x	x
	2.00	x	x	x
	4.00	x	x	x
N2 ↓	0	x	x	x
	1.00	x	x	x
	2.00	x	x	x
	4.00	x	x	x
N3 ↓	0	-	x	-
	1.00	x	x	x
	2.00	x	x	x
	2.25	x	x	x
	3.65	x	x	x
	4.00	x	x	x
	4.92	x	x	x
N4 ↓	0	-	x	-
	1.00	x	x	x
	2.00	x	x	x
	4.00	x	x	x
N5 ↓	0	x	x	x
	1.00	x	x	x
	2.00	x	x	x
	4.00	x	x	x

Note: $M_\infty = 8$, $\theta_c = 6.3$ deg, and $\Delta\phi = 0$

TABLE III
TUNNEL B PRESSURE TEST SUMMARY, ASYMMETRICAL CONFIGURATIONS

Conf.	ϕ_m	α	ϕ_t		
			$\Delta\phi = -30$	$\Delta\phi = 0$	$\Delta\phi = 30$
N7	0	0.25	30	0	-30
		1.25			
		(2.25)			
		3.25			
		4.25			
	-30	0.25	0	-30	-60
		1.25			
		(2.25)			
		3.25			
		4.25			
	-60	-0.50	-30	-60	-90
		0.50			
		(1.50)			
		2.50			
		3.50			
	-90	-2.00	-60	-90	-120
		-1.00			
		(0)			
		1.00			
		2.00			
N8	0	-0.35	--	0	-30
		1.65	30		
		2.65			
		(3.65)			
		4.65			
	-30	5.65	--	-30	--
		7.65	--		
		-0.63	--	-30	--
		1.37	--		-60
		2.37	0		
		(3.37)			
		4.37			
		5.37	--		
		7.37	--		--

Conf.	ϕ_m	α	ϕ_t		
			$\Delta\phi = -30$	$\Delta\phi = 0$	$\Delta\phi = 30$
N8	-60	-1.84	--	-60	--
		0.16	--		--
		1.16	-30		-90
		(2.16)			
		3.16			
	-90	4.16	--		--
		6.16	--		--
		-4.00	--	-90	-120
		-2.00	-60		
		-1.00			
		(0)			
		1.00			
		2.00			
		4.00	--		--
N9	0	0.92	30	--	-30
		2.92		0	
		3.92			
		(4.92)			
		5.92			
	-30	6.92			
		8.92	0	--	-60
		2.45		-30	
		3.45			
		(4.45)			
	-60	5.45			
		6.45		--	
		0.86	-30	-60	-90
		1.86			
		(2.86)			
	-90	3.86			
		4.86			
		-1.00	-60	-90	-120
		(0)			
		1.00			

Note: $M_\infty = 8$ and $\theta_c = 6.3$ deg
() Denotes α_t Value Obtained from Static-Force Data

TABLE IV
TUNNEL F STATIC-FORCE TEST CONDITION*

p_{∞} , psia	ρ_{∞} , lbm/ft ³	T_{∞} , °R	U_{∞} , ft/sec	M_{∞}	q_{∞} , psia	Re_{∞} , ft ⁻¹	Re_{ℓ}	\bar{V}_{ℓ}	$p_{O'}$, psia	$T_{O'}$, °R	$H_{O'}$, Btu/lbm	$\dot{q}_{O'}$, Btu/ft ² -sec	$p_{O''}$, psia
0.0110	0.000286	100.6	7992	15.98	1.967	0.884×10^6	1.00×10^6	0.015	13,363	44.44	1300	120.0	3.658

*This is a reference condition used to correct all axial-force data for viscous interaction effects. It is typical of the conditions encountered.

TABLE V
TUNNEL F PRESSURE TEST CONDITIONS

Run No.	p_{∞} , psia	ρ_{∞} , lbm/ft ³	T_{∞} , °R	U_{∞} , ft/sec	M_{∞}	q_{∞} , psia	Re_{∞} , ft ⁻¹	Re_{ℓ}	\bar{V}_{ℓ}	p_o , psia	T_o , °R	H_o , Btu/lbm	\dot{q}_o , Btu/ft ² -sec	p'_o , psia
3748	0.0112	0.000316	92.4	7647	15.95	1.993	1.019×10^6	3.124×10^6	0.0084	12801	4097	1191	107.3	3.703
3749	0.0101	0.000303	87.1	7455	16.03	1.816	1.011×10^6	3.099×10^6	0.0085	11716	3919	1131	97.0	3.372
3750	0.0138	0.000354	101.7	7810	15.54	2.326	1.058×10^6	3.245×10^6	0.0080	13397	4260	1243	122.9	4.323
3751	0.0138	0.000345	104.3	8066	15.84	2.423	1.041×10^6	3.191×10^6	0.0083	15619	4498	1325	136.5	4.506
3752	0.0118	0.000324	95.0	7788	16.03	2.116	1.033×10^6	3.168×10^6	0.0084	14022	4226	1235	116.2	3.934
3753	0.0109	0.000296	95.8	7624	15.62	1.854	0.917×10^6	2.813×10^6	0.0087	10951	4099	1184	102.8	3.445
3754	0.0115	0.000312	96.1	7666	15.69	1.979	0.971×10^6	2.976×10^6	0.0085	11870	4130	1198	107.8	3.667
3755	0.0102	0.000316	84.1	7434	16.26	1.884	1.089×10^6	3.338×10^6	0.0083	12829	3884	1124	98.0	3.499

UNCLASSIFIED

Security Classification

DOCUMENT CONTROL DATA - R & D

(Security classification of title, body of abstract and indexing annotation must be entered when the overall report is classified)

1. ORIGINATING ACTIVITY (Corporate author)		2a. REPORT SECURITY CLASSIFICATION	
Arnold Engineering Development Center Arnold Air Force Station, Tennessee		UNCLASSIFIED	
3. REPORT TITLE		2b. GROUP	
FORCE AND PRESSURE TESTS ON CONES WITH SIMULATED ABLATED NOSES AT MACH NUMBERS 8 AND 16		N/A	
4. DESCRIPTIVE NOTES (Type of report and inclusive dates)			
Final Report - May 10 to September 7, 1971			
5. AUTHOR(S) (First name, middle initial, last name)			
J. S. Hahn and H. R. Little, ARO, Inc.			
6. REPORT DATE		7a. TOTAL NO. OF PAGES	7b. NO. OF REFS
April 1972		129	10
8a. CONTRACT OR GRANT NO.		9a. ORIGINATOR'S REPORT NUMBER(S)	
b. PROJECT NO.		AEDC-TR-72-52	
c. Program Element 63311F		9b. OTHER REPORT NO(S) (Any other numbers that may be assigned this report)	
d. System 627A		ARO-VKF-TR-72-11	
10. DISTRIBUTION STATEMENT Distribution limited to U.S. Government agencies only; this report contains information on test and evaluation of military hardware; April 1972; other requests for this document must be referred to Space and Missile Systems Organization/TRD-STINFO, AF Unit Post Office,			
11. SUPPLEMENTARY NOTES		12. SPONSORING MILITARY ACTIVITY	
Los Angeles, California 90045 Available in DDC		SAMSO (RSSE) Norton AFB, California 92409	
13. ABSTRACT			
<p>Results are presented from static-force tests and pressure distribution tests of conical bodies with various nose shapes which were chosen to simulate the estimated shapes obtained after significant ablation of the nose had taken place. The basic cone half-angle is 6.3 deg, and the nominal bluntness ratio is 0.25. Nose shapes tested consisted of symmetrical biconics with nose angles of 30, 40, and 50 deg and asymmetrical noses derived from the 50-deg biconic. Results were also obtained for a 50-deg symmetric biconic nose on 4.0- and 9.0-deg cones. The effect of changing the nose-to-cone shoulder radius was investigated on several configurations. Most of the data were obtained at Mach 8, and a limited amount of data was taken at Mach 16. The nominal Reynolds number was 3.1×10^6 based on the sharp cone length of the 6.3-deg pressure model. For the force tests, the angle-of-attack range was from -5 to 11 deg, and for the pressure tests, the angles of attack included the configuration trim angle and up to 4 deg on either side of the trim angle in increments of generally 1 deg. At Mach 8, data are given for the ablated nose shapes with the vehicle rolled -30, -60, and -90 deg.</p> <p>Distribution limited to U.S. Government agencies only; this report contains information on test and evaluation of military hardware; April 1972; other requests for this document must be referred to Space and Missile Systems Organization/TRD-STINFO, AF Unit Post Office, Los Angeles, California 90045.</p>			

UNCLASSIFIED

Security Classification

14.	KEY WORDS	LINK A		LINK B		LINK C	
		ROLE	WT	ROLE	WT	ROLE	WT
	force pressure tests conical bodies nose cones ablation Mach numbers						

AFSC
Arnold AFB Tenn

UNCLASSIFIED

Security Classification